REPORT DOCUMENTATION PAGE

Form Approved OMB NO. 0704-0188

The public reporting burden for this collection of information is estimated to average 1 hour per response, including the time for reviewing instructions, searching existing data sources, gathering and maintaining the data needed, and completing and reviewing the collection of information. Send comments regarding this burden estimate or any other aspect of this collection of information, including suggesstions for reducing this burden, to Washington Headquarters Services, Directorate for Information Operations and Reports, 1215 Jefferson Davis Highway, Suite 1204, Arlington VA, 22202-4302. Respondents should be aware that notwithstanding any other provision of law, no person shall be subject to any oenalty for failing to comply with a collection of information if it does not display a currently valid OMB control number.
PLEASE DO NOT RETURN YOUR FORM TO THE ABOVE ADDRESS.

1. REPORT DATE (DD-MM-YYYY)	2. REPORT TYPE	3. DATES COVERED (From - To)
21-05-2015	Final Report	1-Jun-2006 - 30-Sep-2014

4. TITLE AND SUBTITLE
Final Report: Monolithic Silicon Microbolometer Materials for Uncooled Infrared Detectors

5a. CONTRACT NUMBER
W911NF-06-2-0026

5b. GRANT NUMBER

5c. PROGRAM ELEMENT NUMBER
611102

6. AUTHORS
Mark Horn

5d. PROJECT NUMBER

5e. TASK NUMBER

5f. WORK UNIT NUMBER

7. PERFORMING ORGANIZATION NAMES AND ADDRESSES
Pennsylvania State University
Office of Sponsored Programs
110 Technology Center Building
University Park, PA 16802 -7000

8. PERFORMING ORGANIZATION REPORT NUMBER

9. SPONSORING/MONITORING AGENCY NAME(S) AND ADDRESS (ES)
U.S. Army Research Office
P.O. Box 12211
Research Triangle Park, NC 27709-2211

10. SPONSOR/MONITOR'S ACRONYM(S)
ARO

11. SPONSOR/MONITOR'S REPORT NUMBER(S)
50361-EL-MUR.32

12. DISTRIBUTION AVAILIBILITY STATEMENT
Approved for Public Release; Distribution Unlimited

13. SUPPLEMENTARY NOTES
The views, opinions and/or findings contained in this report are those of the author(s) and should not contrued as an official Department of the Army position, policy or decision, unless so designated by other documentation.

14. ABSTRACT
Final Report: Monolithic Silicon Microbolometer Materials for Uncooled Infrared Detectors. Includes two Ph.D. theses that were finished with the no-cost extension. One was entitled "Thin Film Materials and Devices for Resistive Temperature Sensing Applications" by Hitesh Basantani and the other entitled "Reactive sputter deposition of vanadium, nickel, and molybdenum oxide thin films for use in uncooled infrared imaging" by Yao Jin.

15. SUBJECT TERMS
microbolometer, infrared imaging, vanadium oxide, temperature sensing, biased-target deposition

16. SECURITY CLASSIFICATION OF:			17. LIMITATION OF ABSTRACT	15. NUMBER OF PAGES	19a. NAME OF RESPONSIBLE PERSON
a. REPORT	b. ABSTRACT	c. THIS PAGE			Mark Horn
UU	UU	UU	UU		19b. TELEPHONE NUMBER 814-865-0332

Report Title

Final Report: Monolithic Silicon Microbolometer Materials for Uncooled Infrared Detectors

ABSTRACT

Final Report: Monolithic Silicon Microbolometer Materials for Uncooled Infrared Detectors. Includes two Ph.D. theses that were finished with the no-cost extension. One was entitled "Thin Film Materials and Devices for Resistive Temperature Sensing Applications" by Hitesh Basantani and the other entitled "Reactive sputter deposition of vanadium, nickel, and molybdenum oxide thin films for use in uncooled infrared imaging" by Yao Jin.

Enter List of papers submitted or published that acknowledge ARO support from the start of the project to the date of this printing. List the papers, including journal references, in the following categories:

(a) Papers published in peer-reviewed journals (N/A for none)

Received	Paper
01/06/2014 26.00	Adem Ozcelik, Orlando Cabarcos, David L. Allara, Mark W. Horn. Vanadium Oxide Thin Films Alloyed with Ti, Zr, Nb, and Mo for Uncooled Infrared Imaging Applications, Journal of Electronic Materials, (10 2012): 0. doi: 10.1007/s11664-012-2326-9
01/06/2014 29.00	Hang-Beum Shin, David Saint John, Myung-Yoon Lee, Nikolas J. Podraza, Thomas N. Jackson. Electrical properties of plasma enhanced chemical vapor deposition a-Si:H and a-Si1?xCx:H for microbolometer applications, Journal of Applied Physics, (08 2013): 0. doi: 10.1063/1.4829013
04/09/2012 7.00	Dalong Zhao, Devin A. Mourey, Thomas N. Jackson. Low-Temperature Pulsed-PECVD ZnO Thin-Film Transistors, Journal of Electronic Materials, (11 2009): 0. doi: 10.1007/s11664-009-0995-9
04/09/2012 11.00	Jing Li, Bryan D. Gauntt, Elizabeth C. Dickey. Microtwinning in highly nonstoichiometric VOx thin films, Acta Materialia, (09 2010): 0. doi: 10.1016/j.actamat.2010.05.035
04/09/2012 10.00	Song Won Ko, Jing Li, Nikolas J. Podraza, Elizabeth C. Dickey, Susan Trolier-McKinstry. Spin Spray-Deposited Nickel Manganite Thermistor Films For Microbolometer Applications, Journal of the American Ceramic Society, (02 2011): 0. doi: 10.1111/j.1551-2916.2010.04097.x
04/09/2012 9.00	N.J. Podraza, D.B. Saint John, S.W. Ko, H.M. Schulze, J. Li, E.C. Dickey, S. Trolier-McKinstry. Optical and structural properties of solution deposited nickel manganite thin films, Thin Solid Films, (02 2011): 0. doi: 10.1016/j.tsf.2010.11.088
04/09/2012 8.00	Chandrasekaran Venkatasubramanian, Orlando M. Cabarcos, William R. Drawl, David L. Allara, S. Ashok, Mark W. Horn, S. S. N. Bharadwaja. Process-structure-property correlations in pulsed dc reactive magnetron sputtered vanadium oxide thin films, Journal of Vacuum Science & Technology A: Vacuum, Surfaces, and Films, (08 2011): 0. doi: 10.1116/1.3636372
04/10/2012 12.00	MingLiang Zhang, D. A. Drabold. The microscopic response method: Theory of transport for systems with both topological and thermal disorder, physica status solidi (b), (05 2011): 0. doi: 10.1002/pssb.201147036
04/10/2012 22.00	D. A. Drabold. Silicon: the gulf between crystalline and amorphous, physica status solidi (RRL) - Rapid Research Letters, (11 2011): 0. doi: 10.1002/pssr.201105444
04/10/2012 21.00	James P. Lewis, Pavel Jelínek, José Ortega, Alexander A. Demkov, Daniel G. Trabada, Barry Haycock, Hao Wang, Gary Adams, John K. Tomfohr, Enrique Abad, Hong Wang, David A. Drabold. Advances and applications in the FIREBALLab initio tight-binding molecular-dynamics formalism, physica status solidi (b), (08 2011): 0. doi: 10.1002/pssb.201147259
04/10/2012 20.00	Bin Cai, D. A. Drabold. Theoretical Studies of Structure and Doping of Hydrogenated Amorphous Silicon, MRS Proceedings, (07 2011): 0. doi: 10.1557/opl.2011.1095
04/10/2012 19.00	Mingliang Zhang, D A Drabold. The work done by an external electromagnetic field, Journal of Physics: Condensed Matter, (03 2011): 0. doi: 10.1088/0953-8984/23/8/085801

04/10/2012 18.00 Mingliang Zhang, D. Drabold. Comparison of the Kubo formula, the microscopic response method, and the Greenwood formula,
Physical Review E, (01 2011): 0. doi: 10.1103/PhysRevE.83.012103

04/10/2012 17.00 D. Drabold, Y. Li, B. Cai, M. Zhang. Urbach tails of amorphous silicon,
Physical Review B, (01 2011): 0. doi: 10.1103/PhysRevB.83.045201

04/10/2012 16.00 F. Inam, James P. Lewis, D. A. Drabold. Hidden structure in amorphous solids,
physica status solidi (a), (03 2010): 0. doi: 10.1002/pssa.200982877

04/10/2012 15.00 I. Santos, P. Castrillo, W. Windl, D. A. Drabold, L. Pelaz, L. A. Marqués. Self-trapping in B-doped amorphous Si: Intrinsic origin of low acceptor efficiency,
Physical Review B, (01 2010): 0. doi: 10.1103/PhysRevB.81.033203

04/10/2012 14.00 Ming-Liang Zhang, D. Drabold. Alternative Approach to Computing Transport Coefficients: Application to Conductivity and Hall Coefficient of Hydrogenated Amorphous Silicon,
Physical Review Letters, (10 2010): 0. doi: 10.1103/PhysRevLett.105.186602

04/10/2012 13.00 M.-L. Zhang, D. A. Drabold. Phonon driven transport in amorphous semiconductors: transition probabilities,
The European Physical Journal B, (08 2010): 0. doi: 10.1140/epjb/e2010-00233-0

11/03/2012 2.00 Devin A. Mourey, Dalong A. Zhao, Jie Sun, Thomas N. Jackson. Fast PEALD ZnO Thin-Film Transistor Circuits,
IEEE Transactions on Electron Devices, (02 2010): 0. doi: 10.1109/TED.2009.2037178

11/03/2012 3.00 E. C. Dickey, T. N. Jackson, N. J. Podraza, H.-B. Shin, D. B. Saint John, M.-Y. Lee, S. K. Ajmera, A. J. Syllaios. Influence of microstructure and composition on hydrogenated silicon thin film properties for uncooled microbolometer applications,
Journal of Applied Physics, (08 2011): 0. doi: 10.1063/1.3610422

11/03/2012 23.00 H. A. Basantani, S. Kozlowski, Myung-Yoon Lee, J. Li, E. C. Dickey, T. N. Jackson, S. S. N. Bharadwaja, M. Horn. Enhanced electrical and noise properties of nanocomposite vanadium oxide thin films by reactive pulsed-dc magnetron sputtering,
Applied Physics Letters, (2012): 0. doi: 10.1063/1.4731240

11/03/2012 24.00 N. J. Podraza, B. D. Gauntt, M. A. Motyka, E. C. Dickey, M. W. Horn. Electrical and optical properties of sputtered amorphous vanadium oxide thin films,
Journal of Applied Physics, (2012): 0. doi: 10.1063/1.3702451

11/03/2012 25.00 Heidi M. Schulze, David B. Saint John, Nikolas J. Podraza, Elizabeth C. Dickey, Susan S. Trolier-McKinstry, A. Feteira, Song Won Ko. Low Temperature Crystallization of Metastable Nickel Manganite Spinel Thin Films,
Journal of the American Ceramic Society, (08 2012): 0. doi: 10.1111/j.1551-2916.2012.05201.x

TOTAL: 23

Number of Papers published in peer-reviewed journals:

(b) Papers published in non-peer-reviewed journals (N/A for none)

Received	Paper

TOTAL:

Number of Papers published in non peer-reviewed journals:

(c) Presentations

Number of Presentations: 0.00

Non Peer-Reviewed Conference Proceeding publications (other than abstracts):

Received	Paper	
11/03/2012	1.00	Mark W. Horn , David L. Allara, Orlando M. Cabarcos, Hitesh A. Basantani, S. S. N. Bharadwaja, Jing Li, Bryan D. Gauntt, Sami Antrazi, Elizabeth C. Dickey. Comparison of ion beam and magnetron sputtered vanadium oxide thin films for uncooled IR imaging, Proc. SPIE 8012. 04-DEC-11, . : ,

TOTAL: **1**

Number of Non Peer-Reviewed Conference Proceeding publications (other than abstracts):

Peer-Reviewed Conference Proceeding publications (other than abstracts):

Received	Paper
01/06/2014	28.00 Hitesh A. Basantani, Hang-Beum Shin, T. N. Jackson, Mark W. Horn, Bjørn F. Andresen, Gabor F. Fulop, Charles M. Hanson, Paul R. Norton, Patrick Robert. Vertically integrated pixel microbolometers for IR imaging using high-resistivity VO, SPIE Defense, Security, and Sensing. 02-MAY-13, Baltimore, Maryland, USA. : ,
01/06/2014	27.00 Yao Jin, Hitesh A. Basantani, Adem Ozcelik, Tom N. Jackson, Mark W. Horn, Bjørn F. Andresen, Gabor F. Fulop, Charles M. Hanson, Paul R. Norton, Patrick Robert. High-resistivity and high-TCR vanadium oxide thin films for infrared imaging prepared by bias target ion-beam deposition, SPIE Defense, Security, and Sensing. 02-MAY-13, Baltimore, Maryland, USA. : ,
04/09/2012	5.00 B. D. Gauntt, J. Li, Orlando. M. Cabarcos, Hitesh. A. Basantani, Chandru. Venkatasubramanian, Srowthi. S. N. Bharadwaja, Nikolas. J. Podraza, Thomas. N. Jackson, Dave. L. Allara, Sami. Antrazi, Mark. W. Horn, Elizabeth. C. Dickey. Microstructure of vanadium oxide used in microbolometers, Infrared Technology and Applications XXXVII. 09-APR-11, Orlando, Florida, USA. : ,
04/09/2012	4.00 David. B. SaintJohn, Hang.-B. Shin, Myung.-Y. Lee, Elizabeth. C. Dickey, Nikolas. J. Podraza, Thomas. N. Jackson. Thin film silicon and germanium for uncooled microbolometer applications, Infrared Technology and Applications XXXVII. , Orlando, Florida, USA. : ,
04/09/2012	6.00 Song Won Ko, Jing Li, Myung-Yoon Lee, Elizabeth Dickey, Thomas Jackson, Susan Trollier-McKinstry. New materials for uncooled IR imaging: nickel manganite thin films grown by spin spray, Infrared Technology and Applications XXXVII. 09-APR-11, Orlando, Florida, USA. : ,
TOTAL:	**5**

Number of Peer-Reviewed Conference Proceeding publications (other than abstracts):

(d) Manuscripts

Received	Paper
TOTAL:	

Number of Manuscripts:

Books

Received Book

TOTAL:

Received Book Chapter

TOTAL:

Patents Submitted

Patents Awarded

Awards

Graduate Students

NAME	PERCENT_SUPPORTED	Discipline
Hitesh Basantani	0.00	
Yao Jin	0.00	
FTE Equivalent:	**0.00**	
Total Number:	**2**	

Names of Post Doctorates

NAME	PERCENT_SUPPORTED
FTE Equivalent:	
Total Number:	

Names of Faculty Supported

NAME	PERCENT_SUPPORTED

FTE Equivalent:
Total Number:

Names of Under Graduate students supported

NAME	PERCENT_SUPPORTED

FTE Equivalent:
Total Number:

Student Metrics

This section only applies to graduating undergraduates supported by this agreement in this reporting period

The number of undergraduates funded by this agreement who graduated during this period: 0.00
The number of undergraduates funded by this agreement who graduated during this period with a degree in science, mathematics, engineering, or technology fields:..... 0.00
The number of undergraduates funded by your agreement who graduated during this period and will continue to pursue a graduate or Ph.D. degree in science, mathematics, engineering, or technology fields:..... 0.00
Number of graduating undergraduates who achieved a 3.5 GPA to 4.0 (4.0 max scale):..... 0.00
Number of graduating undergraduates funded by a DoD funded Center of Excellence grant for Education, Research and Engineering:..... 0.00
The number of undergraduates funded by your agreement who graduated during this period and intend to work for the Department of Defense 0.00
The number of undergraduates funded by your agreement who graduated during this period and will receive scholarships or fellowships for further studies in science, mathematics, engineering or technology fields: 0.00

Names of Personnel receiving masters degrees

NAME

Total Number:

Names of personnel receiving PHDs

NAME
Hitesh Basantani
Yao Jin

Total Number: **2**

Names of other research staff

NAME	PERCENT_SUPPORTED

FTE Equivalent:
Total Number:

Sub Contractors (DD882)

Inventions (DD882)

Scientific Progress

see attachment

Technology Transfer

The Pennsylvania State University

The Graduate School

Department of Engineering Science and Mechanics

REACTIVE SPUTTER DEPOSITION OF VANADIUM, NICKEL, AND MOLYBDENUM OXIDE THIN FILMS FOR USE IN UNCOOLED INFRARED IMAGING

A Dissertation in

Engineering Science

by

Yao Jin

© 2014 Yao Jin

Submitted in Partial Fulfillment
of the Requirements
for the Degree of

Doctor of Philosophy

December 2014

The dissertation of Yao Jin was reviewed and approved* by the following:

Mark W. Horn
Professor in Engineering Science and Mechanics Department
Dissertation Advisor
Chair of Committee

Thomas N. Jackson
Robert E. Kirby Chair Professor in Electrical Engineering Department

S. Ashok
Professor in Engineering Science and Mechanics Department

Michael T. Lanagan
Professor in Engineering Science and Mechanics Department

Judith A. Todd
P. B. Breneman Department Head Chair
Head of the Department of Engineering Science and Mechanics

*Signatures are on file in the Graduate School

ABSTRACT

A vanadium oxide (VO_x) thin film is the most common imaging layer used in commercial uncooled focal plane arrays for infrared cameras. These VO_x thin films have an *x* value ranging from 1.3 to 2 and have low resistivity (0.1 to 10 Ω•cm), high temperature coefficient of resistance (TCR) (−2 to −3 %/K), and low 1/f noise. Reactive ion beam sputtering is typically used to deposit these VO_x thin films for commercial thermal imaging cameras. However, the reactive ion beam deposition system for the VO_x is reported to have less than desirable throughput and a narrow process window.

In this work, the potential for reactive pulsed-dc magnetron sputtering of nanocomposite VO_x thin films for microbolometer applications was investigated. VO_x thin films with resistivity from 10^{-4} to 10^5 Ω•cm with a TCR from 0 to -4.3 %/K were deposited by reactive sputtering from a metallic vanadium target in argon/oxygen mixtures with substrate bias. Magnetron sputtered VO_x shows bolometric properties comparable to those of commercial-grade IBD prepared VO_x. Important limitations for manufacturing implementation of reactive magnetron sputtering such as hysteresis oxidation and non-uniform oxidation of the vanadium target surface were evaluated. The VO_x film deposition rate, resistivity, and temperature coefficient of resistance were correlated to oxygen to argon ratio, processing pressure, target-to-substrate distance, and oxygen inlet positions. To deposit VO_x in the resistivity range of 0.1–10 Ω•cm with good uniformity and process control, it was found that a lower processing pressure, larger target-to-substrate distance, and an oxygen inlet near the substrate are useful. Other processing methods employing magnetron sputtering were investigated such as co-sputtering of V and V_2O_5 target, sputtering from a VC target, a V_2O_5 target, and a V_2O_x target but initial investigation of these methods did not yield a superior process to the simple sputtering of a pure metallic vanadium target.

Another technique, biased target ion beam deposition (BTIBD), was investigated for deposition VO_x thin films with potential alloy additions. In this BTIBD system, ions with energy lower than 25 eV were generated remotely and vanadium targets are negatively biased independently for sputtering. High TCR (<-4.5%/K) VO_x thin films have been reproducibly prepared in the resistivity range of 10^3-10^4 Ω•cm by controlling the oxygen partial pressure using real-time control with a residual gas analyzer. These high resistivity films may be useful in next generation uncooled focal plane arrays for through-film rather than lateral thermal resistors. This architecture could improve the sensitivity through the higher TCR without increasing noise normally accompanied by higher resistance. Processing parameters necessary to produce high TCR VO_x films and details on how this novel deposition tool operates are discussed. Addition of molybdenum and its effects on the VO_x thin films' electrical properties were also studied.

Using the BTIBD system, VO_x films in the resistivity range of 0.1-10 Ω•cm desired for current microbolometer application were difficult to produce. Pure molybdenum oxide (MoO_x) and nickel oxide (NiO_x) thin films were deposited by reactive biased target ion beam deposition and evaluated in a search for materials with a larger process latitude. MoO_x thin films were deposited with resistivity from 3 to 2000 Ω•cm and with TCR from -1.7 to -3.2 %/K. NiO_x thin film were deposited with resistivity from 1 to 300 Ω•cm and with TCR from -2.2 to -3.3 %/K. The thermal stability of these films was also investigated. It was found that biased target ion beam deposited high TCR MoO_x and NiO_x thin films are polycrystalline semiconductors and have good stability in air. Compared to commonly used VO_x thin films, MoO_x or NiO_x thin films may offer improved process control for resistive temperature sensors and a superior deposition rate. However, preliminary experiments indicate that these films might have relatively higher 1/f noise.

TABLE OF CONTENTS

LIST OF FIGURES

LIST OF TABLES

ACKNOWLEDGEMENT

I would like to thank the Army Research Office and Army Research Laboratory for sponsoring this work. This dissertation would not have been possible without their support.

My most sincere thanks go to my advisor and mentor Dr. Mark Horn. I would like to thank him for his trust, guidance, and encourage during these past four years. Dr. Horn has been very supportive and given me the freedom to proceed with the research in my own way. I very much appreciate Dr. Horn for carefully correcting my thesis, and his kind and patient instructions. I am honored to have Dr. Horn as my Ph.D. advisor.

I would also like to especially thank Dr. Thomas Jackson for being my role model as a mentor and a scientist. Dr. Jackson is one of the smartest and most knowledgeable people I know. He has always inspired me to a higher level of thinking with his tough, yet loving approach. Dr. Jackson not only taught me how to conduct research efficiently, but also to foster a can-do attitude. I appreciate his insightful suggestions on both a professional and personal level. I hope someday to become a successful engineer and scientist like him.

I would like to thank my colleagues (current and former): Hitesh Basantani, Adem Ozcelik, Haoyu Li, Myung-Yoon Lee, Yuanyuan Li, Kaige Sun, Yiyang Gong, Mike Motyka, David St. John et al. for stimulating discussions as well as a wide range of technical assistance. I especially would like to thank Hitesh for the EDS measurement, Adem for the Raman spectroscopy measurement, and Myung-Yoon for the 1/f noise measurement. I very much appreciate having them as my colleagues and friends.

I would like to thank Bill Drawl for helping me modify the Kurt Lesker sputtering tool and training me to use the 4Wave BTIBD system. I would also like to thank Nichole Wonderling and Gino Tambourine for assistance and discussion with XRD, and to thank Clark Trevor and

Julie Anderson for assistance with SEM and EDS. Thank you to Dr. Nikulas Podraza for his kind suggestions and assistance with SE models.

I would like to thank Dr. S Ashok and Dr. Michael Lanagan for serving as my thesis committee. Thank you for your insightful comments, questions, and suggestions.

I would finally like to thank my friends and family. Lanyun Gong and Yenwen Shao have been encouraging me throughout my graduate school life at Penn State. My thanks also go to Matt Edwards for helping me to correct my grammatical mistakes in my thesis. Matt also came up with critical questions and constructive advice to improve my oral defense. My parents, Yan Huo and Lianbo Jin, provided unconditional love, support, and care to me. Without them, I would not have made it this far.

Chapter 1

Introduction

Infrared (IR) imaging is one of the main methods used in night-vision devices. The IR radiation emitted from biological objects is in the range of 8-14 μm and can be detected by two kinds of detectors: photon and thermal detectors.[1] A photon detector is based on the interaction between incident photons and a sensing material's electrons. In order to reduce the noise effect caused by thermally generated carries and recombination, a photon detector is cooled by a bulky cooling system. Thermal detectors are based on a change in material property as a function of temperature caused by IR radiation. Thermal detectors can be based on thermoelectric effects, pyroelectric effects, and a change in resistivity with temperature [2]. The focus of this research is based on the resistive thermal detectors.

1.1 Microbolometers and Figures of Merit

Resistive microbolometers are thermal detectors with a sensing material that experience a change in resistance when absorbing incident IR radiation. A pixel of the device is freestanding and thermally isolated from the readout integrated circuitry (ROIC) by "standing" on a composite structure containing the electrically conductive legs. Figure 1-1 shows the schematic of a typical microbolometer pixel design. A microbolometer pixel typically includes a thin layer of sensing material (either metal or semiconductor), IR absorbing film, and an infrared reflecting layer below the active sensing layer to increase infrared absorption. The microbolometer pixel absorbs the IR and results in a temperature change, hence altering the sensing material resistance. The

change of resistivity is then detected by read-out circuitry in either the current or voltage signals through the metal legs. [2]

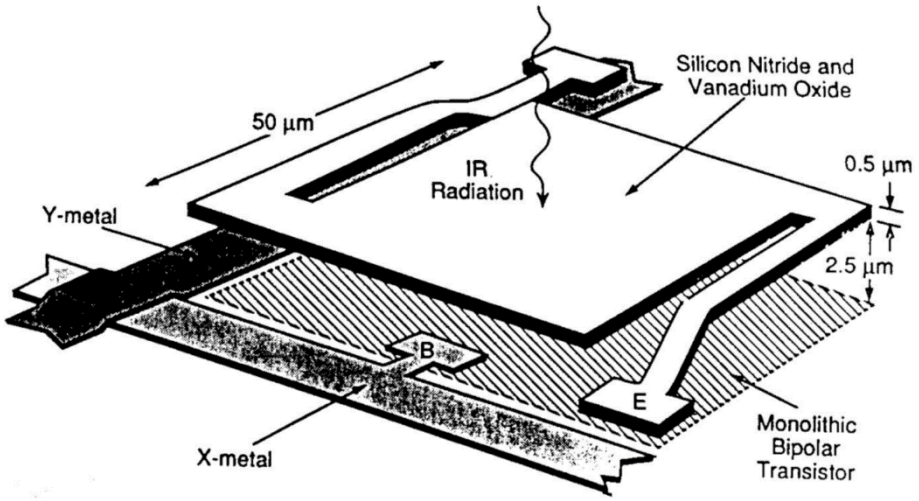

Figure 1-1. The schematic of a microbolometer pixel. [3]

In order to maximize the sensitivity of the pixel, the sensing material temperature coefficient of resistance (TCR) should be high. A metal thin film has a low, positive TCR whereas a semiconductor thin film has a TCR that is negative and significant, in the -1 to -6 % range. Eq.1-1 and 1-2 give the definition of the TCR value:

$$\%TCR = -\frac{E_a}{\left(k_B {T_{room}}^2\right)} \times 100\% \qquad Eq.1\text{-}1$$

$$E_a = \frac{d(lnR)}{d(1/k_B T)} \qquad Eq.1\text{-}2$$

where E_a is the thermal activation energy, k_B is Boltzmann constant, and T_{room} is room temperature (25°C) [2].

In order to reduce the power consumption during the operation, a lower resistance is often desired. Hence, a low room temperature resistivity sensing materials with high TCR should

be used. However, the sensing materials used for microbolometers are often limited by the noise of both the material and the read out circuitry being implemented. Four types of noise are seen in electrical properties: 1/f noise, Johnson noise, temperature fluctuation noise, and background fluctuation noise (Eq.1-3).

$$V^2_{total} = V^2_{Background} + V^2_{Temperature\ fluctuation} + V^2_{Johnson} + V^2_{1/f} \qquad Eq.\ 1\text{-}3$$

Of the four types of noise listed above, temperature fluctuation noise and background noise are related to the device design. The Johnson noise and 1/f noise (pink noise) are based on the material. For semiconductors, 1/f noise is often thought to be due to carriers trapping and un-trapping, which is a predominant noise at low frequency (1 Hz to 1 kHz). The 1/f noise is given by:

$$V_{1/f} = (kV_{bias}^2/f)^{1/2} \qquad Eq.\ 1\text{-}4$$

where f is the frequency that the noise is measured, V_{bias} is the bias applied during measurement, k is the 1/f noise parameter.

Johnson noise, on the other hand, is not dependent on frequency, and is attributed to free electrons random motion in a resistor:

$$V_{Johnson} = (4k_BTRB)^{1/2} \qquad Eq.\ 1\text{-}5$$

where k_B is the Boltzmann constant, T is measurement temperature, R is the total resistance of the pixel structure, and B is the noise bandwidth given $B = \frac{1}{2\Delta t}$ and Δt is the pulse bias duration.

Reducing the total resistance R can decrease the Johnson noise of a microbolometer. The 1/f noise is strongly dependent on the microbolometer resistor properties such as material, processing parameters, contact qualities, and so on [3]. In low frequency devices, 1/f noise can be higher than the Johnson noise, and become the dominating factor to limit the microbolometer sensitivity.

The responsivity *R* is one of the figures of merit that determines the effectiveness of microbolometer devices. *R* is a measure the ability of the infrared device to convert IR to a useful signal, given by the following equation:

$$R = \frac{\alpha\eta\beta i_b \alpha R_b}{G} \qquad \textit{Eq.1-6}$$

where η is the emissivity, i_b is the bias current, α is the TCR of the sensing material, R_b is the resistance, β is the areal fraction of the detector array covered by an active sensing material, and *G* is the thermal conductance of the supporting legs.

Another important figure of merit is the noise equivalent temperature difference (NETD), which describes the minimum temperature difference that can be detected by a microbolometer. NETD is related to the optical structure of device, read out circuitry, and sensing materials.

$$NETD \propto \frac{Noise}{TCR} \qquad \textit{Eq.1-7}$$

In order to minimize NETD to get the highest resolution, the total noise should be minimized and the responsivity should be maximized [2].

1.2 Vanadium oxide thin films as microbolometer sensing materials

Many materials have been investigated as the thermally active materials for resistive microbolometers. Metal thin films have been investigated as resistive microbolometers due to their CMOS (complementary metal-oxide-semiconductor) compatibility. Titanium is the most widely used metal for microbolometers. The TCR of titanium thin film is reported to be 0.26%/K. A 64×64 Ti based microbolometer array detector with a pixel size of 75×75 μm has production cost as low as $100 [4]. Though metal films have low noise and low cost, the low TCR limits its performance. High TCR semiconductor materials have been investigated as resistive

microbolometers, such as: VO_x [3],[5], hydrogenated amorphous Si (a-Si) [6],[7], yttrium barium copper oxide (YBaCuO) [8], and nickel oxide (NiO_x) [9], [10]. Among these materials, VO_x and a-Si based microbolometers have approximately 70% and 17% of the uncooled infrared imaging market share, respectively [11]. VO_x thin films have relatively low resistivity (0.1 to 10 Ω•cm) and high TCR (-2 to -3 %/K), whereas a-Si have relatively high resistivity (200 to 2500 Ω•cm) and higher TCR (-2.5 to -3.9 %/K) [3],[5],[7]. Both VO_x and a-Si based microbolometer pixel size reaches 17×17 μm^2, with NEDT about 50 milliKelvin [4],[11].

VO_x of various compositions for microbolometers has been prepared by many deposition methods, such as reactive ion beam deposition (IBD) [3], [5], reactive radio frequency (rf) sputtering [12], reactive dc sputtering [12], [13], and pulsed laser deposition (PLD) [14], [15]. However, vanadium has multiple valence states (+5,+4,+3,+2) and it can transition from one phase to another very quickly under different oxygen levels. This makes extremely difficult to fabricate single stable phases of VO_x thin films. Many vanadium oxide phases show metal-insulator transitions (MIT) at different temperatures such as V_2O_3, VO_2, and Magneli phases of VO_x which are between V_2O_3 and VO_2 as shown in Figure 1-2 [16]. The Magneli phases are described by V_nO_{2n-1} and n is an integer [17]. VO_2 is semiconducting at room temperature and then changes to metallic when temperature is higher than 68^oC [18]. The MIT temperature for V_2O_3 is 168 K (-105^oC) [17]. This drastic change in resistivity increases the responsivity of devices. However, the operation of the device requires a cooler and heater, which make V_2O_3 and VO_2 not suitable for uncooled microbolometers. In addition, the fast resistivity change may not be easily controlled by the readout circuitry. V_2O_5 is one of the most stable phases of VO_x. The resistivity for V_2O_5 is between 1E2 to 1E6 Ω•cm depending on the structure [19]. Though the TCR of V_2O_5 could be as large as -4.4 %/K (amorphous) [20],V_2O_5 is not suitable for the targeted resistivity range for pulse-biased microbolometer usage due to its high resistivity [2].

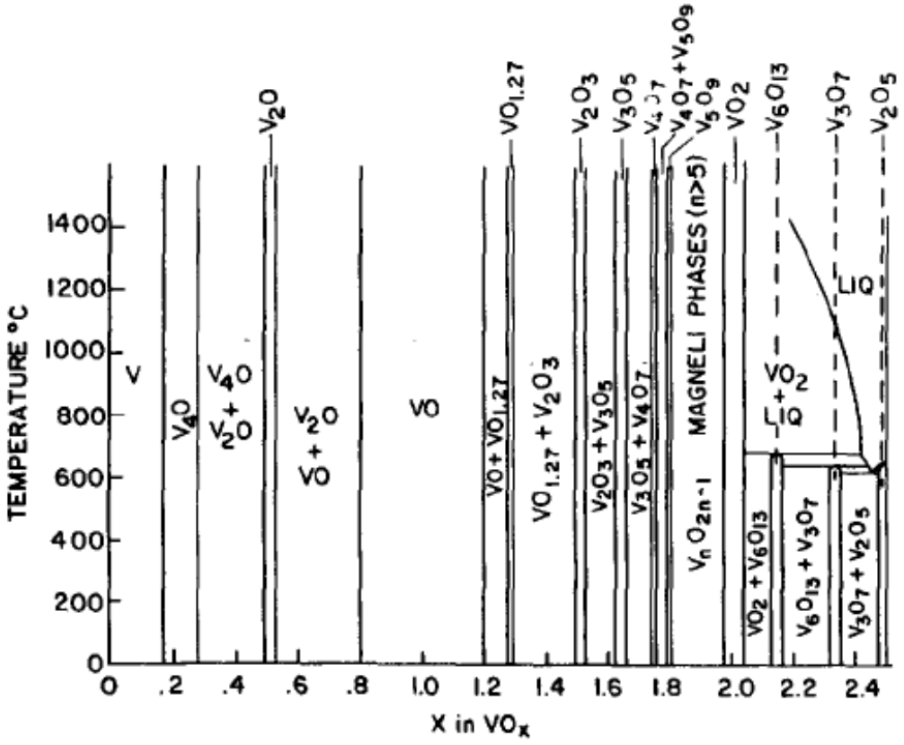

Figure 1-2. Phase diagram of VO_x system [16].

The VO_x thin films for microbolometers originally deposited by IBD have no phase transition near room temperature. The room temperature resistivity of VO_x prepared by IBD is from 4E-3 to 1 Ω•cm with TCR ranges from -0.65 to -3.5 %/K [21]. As shown in Figure 1-3 [3], higher TCR VO_x films inevitably show higher room temperature resistivity. The ideal x value of VO_x for microbolometer usage is between 1.75 and 2 [22], [23]. The deposited VO_x thin film properties can be largely influenced by deposition techniques and processing parameters. The deposited films should also exhibit good thermal and electrical stability.

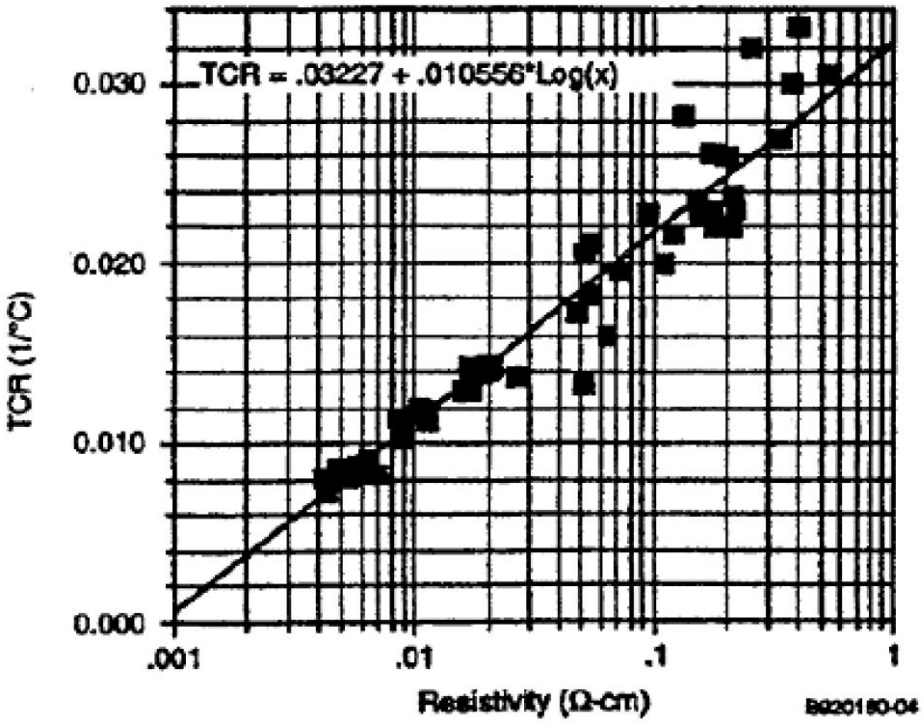

Figure 1-3. IBD prepared VO_x linear relationship of TCR vs. resistivity in log scale [3].

1.3 VO_x for microbolometers deposited by different fabrication methods

When used as microbolometer sensing materials, the VO_x thin films deposition temperatures should not exceed 400^oC due to the monolithic fabrication of microbolometer bridge structure on silicon readout circuitry [24].

Since the Honeywell patented VO_x prepared by reactive IBD method for microbolometers [25], IBD has been exclusively used to produce VO_x for commercial use. Wang et al. used reactive IBD to fabricate VO_x thin films with sheet resistance about 32 K Ω/sq and TCR -2.5 %/K [26]. A different Wang group [23] used IBD to deposit VO_x thin film that consisted of V_2O_5 and VO_2 with a sheet resistance of 50K Ω/sq and a TCR of -2.1 %/K. The post annealing in Ar at 400^oC caused the VO_x films to show a nonlinear relationship of log resistivity

versus temperature. Chain prepared VO_x by reactive ion beam deposition with different substrate temperature. The result shows that with increasing of substrate temperature, the deposited film grain size increases, which is consistent with the Thornton's structure zone model [27]. Chain also investigated the change in the VO_x thin film structure and optical properties when varying oxygen content in the reactive ion beam deposition with a metallic V target [28]. When the oxygen was low, the VO_x changed from an FCC crystal structure to a mixed oxide phase containing VO_2. As the concentration of oxygen was increased further, the VO_x became a mixed oxide with V_2O_5 and the grain orientation changes from preferential to randomly oriented. The oxygen content, ion beam energy and substrate temperature were found to have a great influence on the deposited VO_x composition and structure prepared by reactive IBD.

Deposition methods such as reactive rf sputtering and reactive dc sputtering are also investigated to produce VO_x for microbolometer usage. Luo et al. used reactive dc sputtering to prepare VO_x thin films and followed with in-situ thermal oxidation. The films as deposited were amorphous and after in-situ annealing in oxygen, they become nano-VO_2 with average grain size of 19 nm. The calculated TCR as deposited was -2 %/^oC and after 10 min of annealing, it increased to -3.1 %/^oC [29]. Lv et al. used facing V targets dc reactive sputtering to prepare VO_x thin films for microbolometer sensing materials [30]. The as-deposited VO_x had a room temperature sheet resistance of 30-80K Ω/sq and a TCR above -4.5 %/^oC. After being annealed in vacuum at 400 ^oC for 3 hours, the sheet resistance decreased to 20K Ω/sq but the TCR was still as high as -4.4 %/^oC. X-ray photoelectron spectroscopy (XPS) spectra show that the annealing in vacuum makes the V_2O_5 dissociate and results in large amounts of V^{4+} and V^{3+}, which the authors attribute as the cause of the increase of conductivity.

VO_x thin films have also been prepared by pulsed laser deposition (PLD) using a V_2O_5 target at room temperature. Though the prepared films have a high TCR of about -2.8%/K but the room temperature resistivity was as high as 1000 Ω•cm which makes it unsuitable for

microbolometer device sensing materials [31]. Due to the difficulty of controlling the fabrication of the VO_x composition and phase, a multilayer structure consisting of V_2O_5 and V was prepared by reactive magnetron rf sputtering at room temperature without oxygen. The as-deposited multilayer VO_x thin films were further annealed at 300^{o}C to make the oxygen diffuse from the V_2O_5 to the metallic V layer. By adjusting the thickness of the V and V_2O_5 thin films, the VO_x resistivity varied from 4-30 Ω•cm with TCR from -1.8%/K to -2%/K [32].

In 2006, Penn State was awarded a multidisciplinary university research initiative (MURI) supported by The Army Research Office to investigate sensing materials for uncooled microbolometers. VO_x thin films for infrared imaging have been prepared by magnetron pulsed dc reactive sputtering method, [13], [33]–[37] and show similar or even superior properties compared to VO_x prepared by IBD as shown in Figure 1-4 [35].

The Penn State group determined that the desired VO_x thin films' microstructure in the interested resistivity and TCR range is a nanocomposite, where there are FCC VO_x ($0.8<x<1.3$) nanocrystalline domains embedded in an oxygen rich VO_x amorphous matrix [38]. The growth conditions in the chamber were found to have great influences on the deposited film composition and electrical properties [39]. The presence of a nano-twin structure has been observed in VO_x thin films prepared by both magnetron sputtering and IBD [40]. The rf substrate self-bias applied on VO_x films during deposition makes the films denser with a higher concentration of nano-twins, which is more similar to IBD prepared samples. The microstructure of VO_x deposited by different methods is shown in Figure 1-5. Enhanced electrical properties of VO_x prepared with substrate bias were also reported [36]. Without substrate bias, the as-deposited films are porous; however, post-deposition process such as ex-situ annealing in oxygen/nitrogen, and implantation of hydrogen/helium can improve TCR and resistivity of these as-deposited VO_x films [41]. In an effort to improve thermal stability and possibly TCR, transition metals have been incorporated into the VO_x thin films. There were no significant effects on the films microstructure and little

improvement in the films electrical properties. However, by adding the transition metals in VO_x thin films, the thermal stability of deposited films was improved [37].

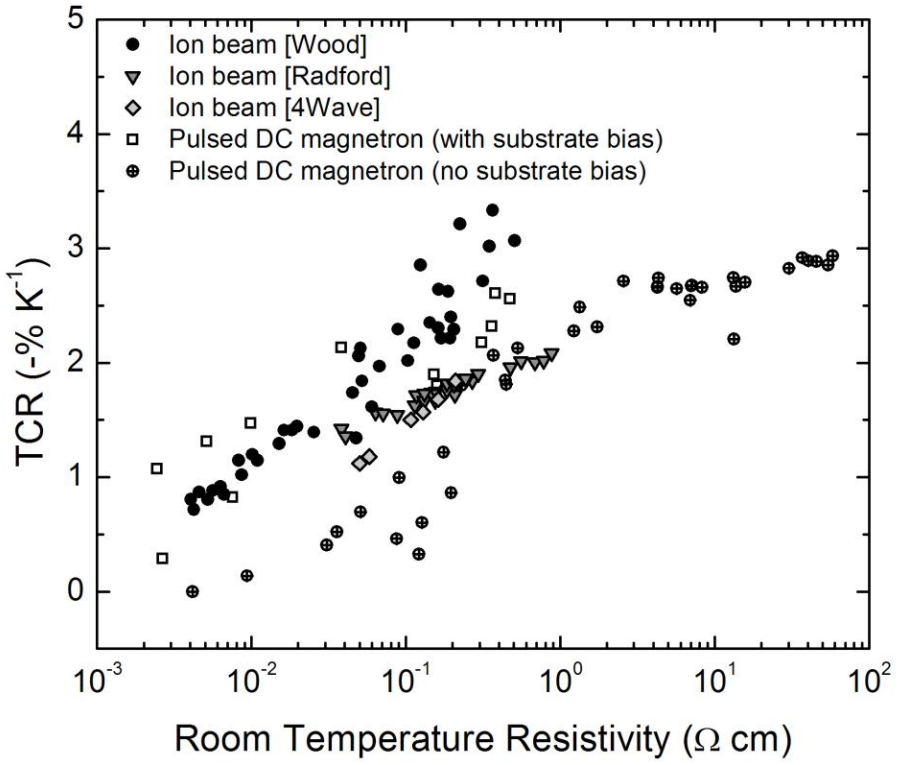

Figure 1-4. TCR vs. room temperature resistivity for VO_x films that were prepared by different deposition methods [35].

Besides VO_x, our group at Penn State University also investigated other materials for microbolometer applications, such as: hydrogenated silicon (Si:H) [42], polycrystalline SiGe [43], nickel magnetite ($NiMnO_x$) [44][45]. The bolometric properties such as: resistivity, TCR, and 1/f noise of these materials prepared by different deposition techniques are compared.

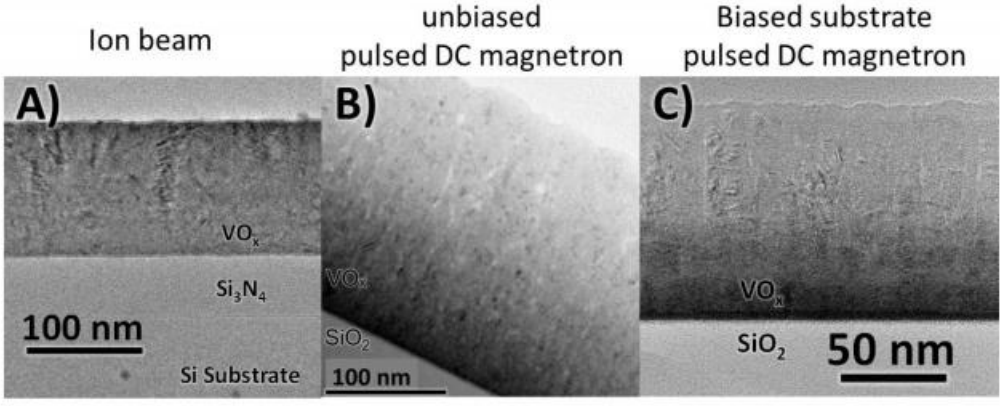

Figure 1-5. Bright field TEM pictures of VO_x prepared by different deposition methods: ion beam deposition, unbiased magnetron sputtering, and biased magnetron sputtering [35].

Table 1-1 lists resistivity, TCR, and 1/f noise comparison of these microbolometer sensing materials. The 1/f noise and TCR are related, and the general rule is higher TCR materials have higher resistivity and 1/f noise. As shown in Eq. 1.7, in the same TCR range, lower 1/f noise is needed to get higher NETD. At TCR range from -2 to -2.5 %/K, IBD and biased magnetron sputtered VO_x have lower 1/f noise. At TCR range from -3 to -4 %/K, a-Si and PECVD nanocrystalline and amorphous Ge:H show lower 1/f noise. However, high TCR (<-4.5%/K) VO_x thin films have not yet been investigated, which needs to be further investigated.

1.4 Biased target ion beam deposition

In this work, a new technique: biased target ion beam deposition (BTIBD) is investigated and used to deposit microbolometer-sensing materials. This section introduces how a BTIBD system works and summarizes the work has been reported by using this unique technique.

BTIBD combines ion beam deposition and sputter deposition. In a BTIBD system, an ion beam is remotely generated and the targets are negatively biased to promote sputtering. The energy and distribution of the ion beam is mainly dependent on the ion source since the plasma

sheath toward the negatively biased target is small [49], [50]. This allows for the independent control of the generation of ion beam and biased target sputtering. The control of the ion beam energy and sputtered species energy make this technique have the potential to have good repeatability and uniformity. The Ar+ ions generated remotely in a BTIBD system typically have energies lower than 25 eV (lower than the sputter threshold of vacuum materials). At such a low energy, the contamination that will be introduced to the deposited thin films from vacuum system and other non-biased targets can be kept to a minimum. The sputter yield for some elements as a function of incident Ar+ energy is shown in Figure 1-6, and most of these element sputtering yield is less than 0.01 when incident Ar+ ion (normal to the surface) energy is lower than 30 eV [51].

Table 1-1. Resistivity, TCR, and 1/f noise values for various microbolometer sensing materials.

Materials (MURI)	Resistivity (Ω•cm)	TCR (-%/K)	1/f Noise $(k \times Volume)$	References
IBD (nc+a) VO_x	0.1 to 1	2	10^{-22}	[3][36]
Magnetron sputtered (nc+a) VO_x	0.001 to 1	0.2 to 2.6	10^{-28} to 10^{-22}	[36], [46]
Nickel Manganite	630	2.9	10^{-21}	[44]
PECVD a-Si:H doped	100 to 3000	2.0 to 3.6	10^{-22} to 10^{-17}	[42]
PECVD a-Ge:H	12,000 to 50,000	2.8-5	10^{-20} to 10^{-17}	[43][47]
PECVD (nc+a)Ge:H	750 to 4,500	1.8 to 6.3	10^{-20} to 10^{-18}	[48]

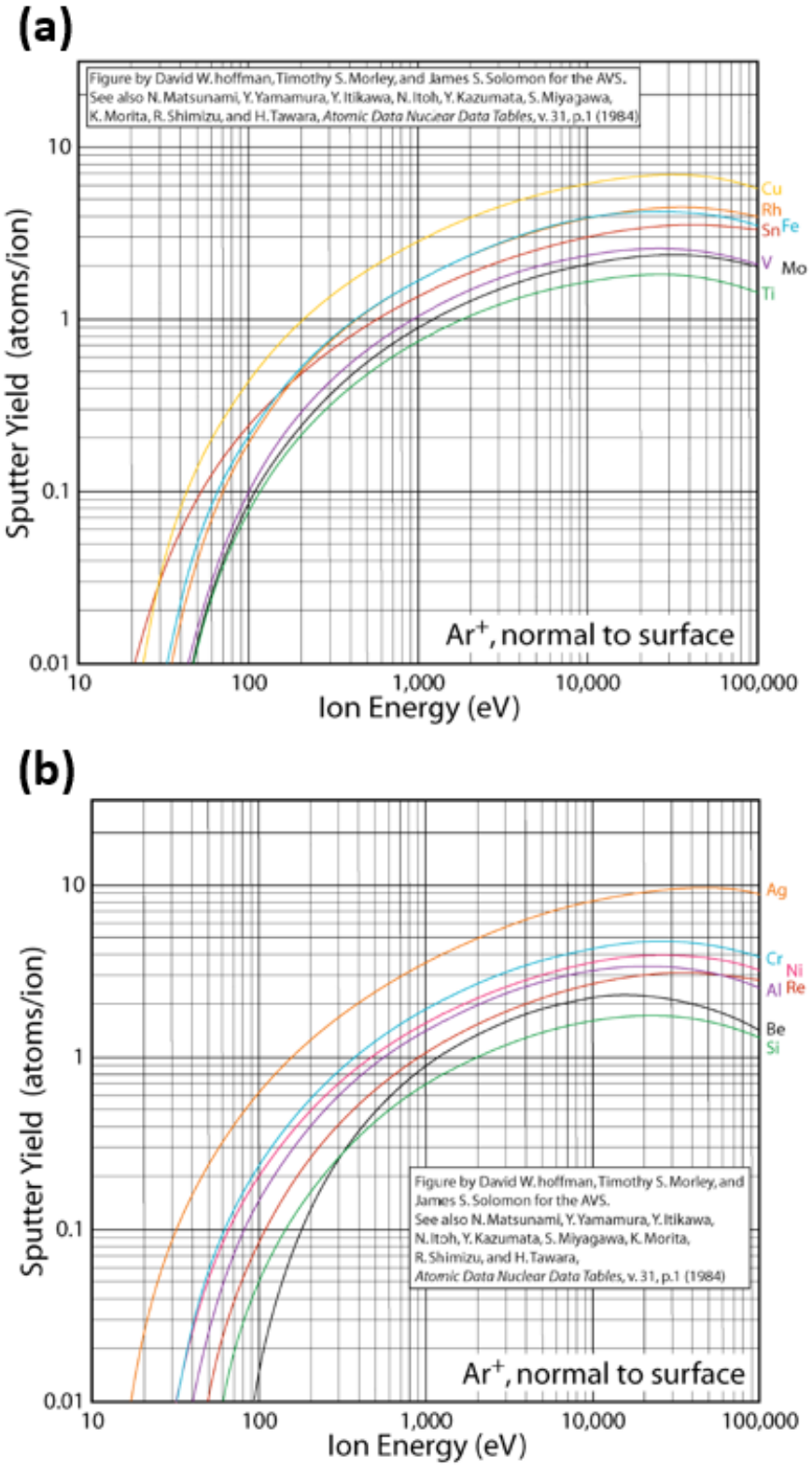

Figure 1-6. Sputter yield for some elements: Ar ions normal to the surface [51].

Based on this novel technique, 4WAVE Inc. has built a Laboratory Alloy and Nanolayer Sputtering system (LANS) and an Ion Beam Assisted Biased Target Deposition Sputtering System (IABTD) and (as shown in Figure 1-7).

4W-LANS system used in this work has also been used to prepare thin films for different applications. Gallium nitride (GaN) has been deposited on sapphire wafers using the BTIBD technique. A mixture of Ar and N_2 was introduced on to the end hall to generate plasma. Ar flow rate was fixed at 30 SCCM and N_2 flow rate varied from 3 SCCM to 30 SCCM. The liquid Ga target was biased with -850 V for 11 μs and +10 V for 3 μs. However, the prepared GaN thin films have poor structural and optical properties [52].

Amorphous rare earth substituted Bismuth Iron Garnet was also prepared by reactive sputter deposition using four metallic targets: Bi, Dy, Fe and Al in 4W-LANS system. The target voltage was -850 V with pulse width/period of 3 μs /14 μs. The composition of the $BiDyFeAlO_{12}$ garnet films was calculated by the single-metal oxide deposition rates with certain oxygen partial pressure from 1E-5 Torr to 5E-5 Torr monitored by a residual gas analyzer (RGA). The processing pressure was fixed at 6.4E-4 Torr. The $BiDyFeAlO_{12}$ garnet films were later annealed in oxygen for an hour at 650^{o}C. After annealing, the amorphous film turned to poly-crystalline with a saturation magnetization and coercivity comparable to those films prepared by other methods [49].

4W-LANS reactive BTIBD is also used to deposit vanadium dioxide thin films. Single-phase VO_2 thin films were grown on Al_2O_3 at 450^{o}C substrate temperature. A metallic vanadium target was used and biased with 11 μs -900 V and 3 μs +20 V. It has been found that Ar flow rate at 80 SCCM with a mixture of Ar/O_2 80/20 gas flow rate at 5 SCCM gives the optimized growth of $VO_{2.5}$ [53]. Cr doped VO_2 thin films $V_{1-x}Cr_xO_2$ (x between 0.1 and 0.2) were also prepared by

the same group by using reactive BTIBD technique in 4W-LANS system. The films show high crystalline quality and low surface roughness [54].

A more sophisticated structure of BTIBD with a second ion source as ion assist has also been developed. The 4W-IABTD has been used to prepare: Giant magnetoresistive (GMR) multilayer spin-valves [55], diamond-like carbon(DLC) thin films corporation with Co, Ti, Ni, and W [56], [57], as well as magnetic tunnel junction(MTJ) with naturally oxidized AlO_x barriers [58].

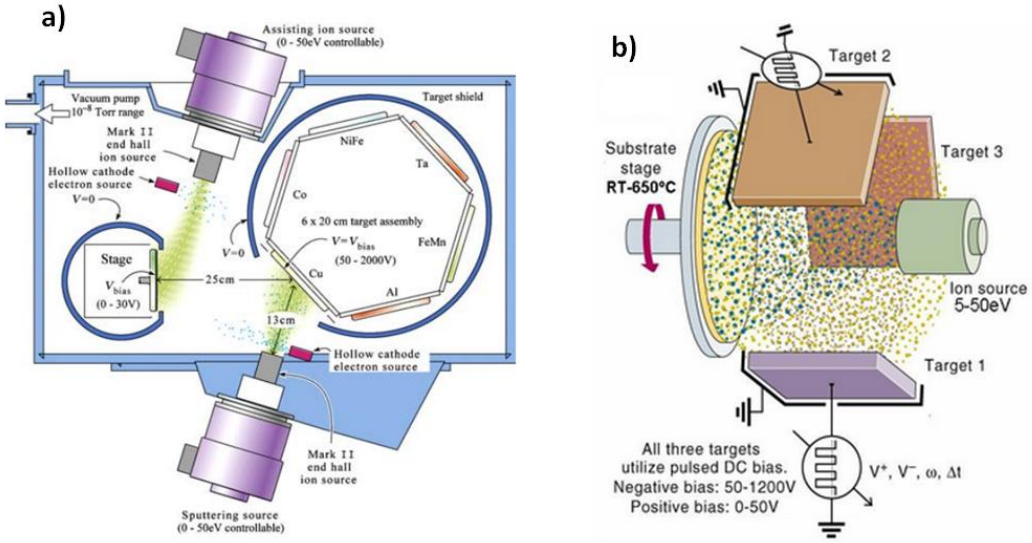

Figure 1-7. Schematic of (a) 4Wave IABTD system and (b) 4Wave BTIBD system [59]

In this thesis, 4W-LANS BTIBD system with off-axis geometry was used to prepare transition metal oxide thin films. More details of this system will be discussed in Chapter 2.

1.5 Thesis outline

This thesis explores the potential of reactive sputtering of VO_x, NiO_x, and MoO_x thin films for microbolometer applications. In the past, ion beam deposition has been exclusively used to fabricate commercial VO_x thin films for microbolometer sensing materials due to its good process controllability. However, IBD has low throughput. Our group has proven that magnetron pulsed-dc reactive sputtering of VO_x with substrate bias has similar or enhanced electrical properties to IBD VO_x. However, there are important limitations for manufacturing implementation due to its inherent process non-uniformity. In this work, we try to answer the questions as follows:

1). Can magnetron pulsed-dc sputtering be an alternative method to IBD to prepare VO_x thin films for microbolometers. Are there ways to improve process controllability and improve yield?

2). Can high TCR VO_x thin films be prepared with good thermal stability and relatively low 1/f noise? How do they compare to other high TCR materials?

3). Can other sensing materials with good bolometric properties and easier process control than VO_x be developed for microbolometer applications?

Chapter 2 of this thesis describes the processing and analysis methods used in this work, includes deposition techniques, thin film properties characterization, and device fabrication. The operation details of the new deposition technique (biased target ion beam deposition) are also discussed. Chapter 3 details experiments designed to evaluate the potential of magnetron reactive sputtering of VO_x thin films. The process controllability was improved by varying different processing parameters such as sputtering target, processing pressure, oxygen to Ar inlet ratio, substrate bias, reactive gas inlet position, substrate to target position etc. Chapter 4 introduces the high resistivity high TCR vanadium oxide thin films prepared by reactive biased target ion beam

sputtering. The potential usage of these materials for a through-film structure microbolometer pixel was investigated. Chapter 5 describes the fabrication and characterization of high TCR nickel oxide and molybdenum oxide thin films as potential microbolometer sensing materials prepared by biased target ion beam deposition. The correlation of these film properties to processing conditions was studied. Aging tests and post-annealing effects on deposited films were also investigated. The 1/f noise of NiO_x is compared to VO_x thin films and other sensing materials investigated. Chapter 6 summarizes the results obtained in this thesis work and proposes possibilities for future work.

Chapter 2

Experimental Methods

This chapter includes experimental methods for depositing and characterizing the thin films studied in this thesis. In this work, metal oxide thin films were deposited by both reactive magnetron sputtering and biased target ion beam deposition using various processing parameters. Post-deposition processes such as rapid thermal annealing (RTA) were used to evaluate the metal oxide thin film thermal stability. The thin films were characterized by profilometry, spectroscopic ellipsometry (SE), grazing incident x-ray diffraction (GIXRD), Raman spectroscopy, and energy-dispersive X-ray spectroscopy (EDS). Electrical properties of deposited films were analyzed by the transmission line measurement (TLM) method.

2.1 Reactive magnetron pulsed direct current (dc) sputtering

2.1.1 Reactive magnetron pulsed-dc sputtering issues

Magnetron pulsed-dc sputtering is a physical vapor deposition method can be used to deposit electrically insulating materials directly or through a reactive sputtering process of metal targets where reaction products are electrically insulating. In conventional dc sputtering, a metallic target (cathode) has negative potential compare to the substrate and chamber walls. For pressures between 1 mTorr and 10 Torr, The potential difference causes electrons to accelerate from cathode to anode. The electron gains enough kinetic energy to sufficiently ionize the gas molecules in the chamber by inelastic collisions, which leads to a cascade process such that stable plasma is sustained. The positive gas ions (typically Ar+) then accelerate toward the cathode and when they have sufficient energy, sputter target atoms into the gas phase. The sputtered target

atoms deposit on the chamber wall and substrate. In magnetron guns, magnets are placed under the targets create a crosswise magnetic field over the cathode and largely increase the electrons travel path thereby increasing the probability of ionizing collisions by trapping electrons in orbits near the targets. Using a magnetron gun decreases the minimum pressure necessary to sustain the plasma to about 1 mTorr from something closer to 10 mTorr.

Reactive sputtering from a metal target enables compound deposition with lower target fabrication cost and higher deposition rate [60]. In reactive sputtering, the reactive gas is added to the Ar sputtering gas to form a compound film on the substrate. The deposited film composition and deposition rate is sensitive to the supply of reactive gas. In this technique, as the reactive gas supply increases, the target can become "poisoned" with an electrical insulator layer that forms on the target surface. This insulating layer then permits Ar+ ions to build-up positive charge which then repulses positive ions from further bombarding the target and decreases the sputtering rate. Pulsed-dc sputtering helps to overcome this charging issue by adding a short positive pulse to draw electrons to neutralize the charged target. A pulsed-dc bias on the target is shown in Figure 2-1: the negative portion of a duty cycle causes normal sputtering and the positive portion neutralizes the charged target.

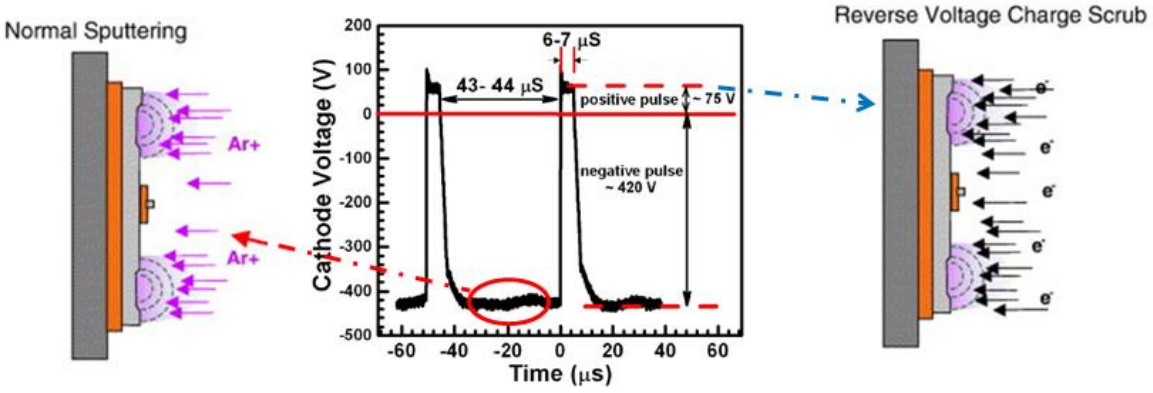

Figure 2-1. Schematic of a pulsed-dc sputtering process. Replotted from Ref [61] and Ref [62].

In reactive sputtering with a metallic target, a process hysteresis behavior is typical, that is to say that the sputtering rate is dependent on whether or not the reactive gas flow has been increased or decreased. The hysteresis loop for deposition rate can be monitored directly by an in-situ quartz-crystal deposition-rate monitor or indirectly by measuring the cathode current/voltage on the target.

Figure 2-2 shows the hysteresis loop of the cathode voltage with constant sputtering power and partial pressure of non-reactive gas [63]. At low reactive gas flow rate, the deposited film is metal-rich. With further increasing of reactive gas flow rate, the gas-metal compound forms on the target surface and sputtering rate drops abruptly at f_{r1}, the sputtered film is gas-rich. By reducing reactive gas flow rate, the sputtering rate won't increase until f_{r2}, where the compound layer on target surface is removed and metal is exposed. The hysteresis effect leads to process instability and should be eliminated in a manufacturing environment.

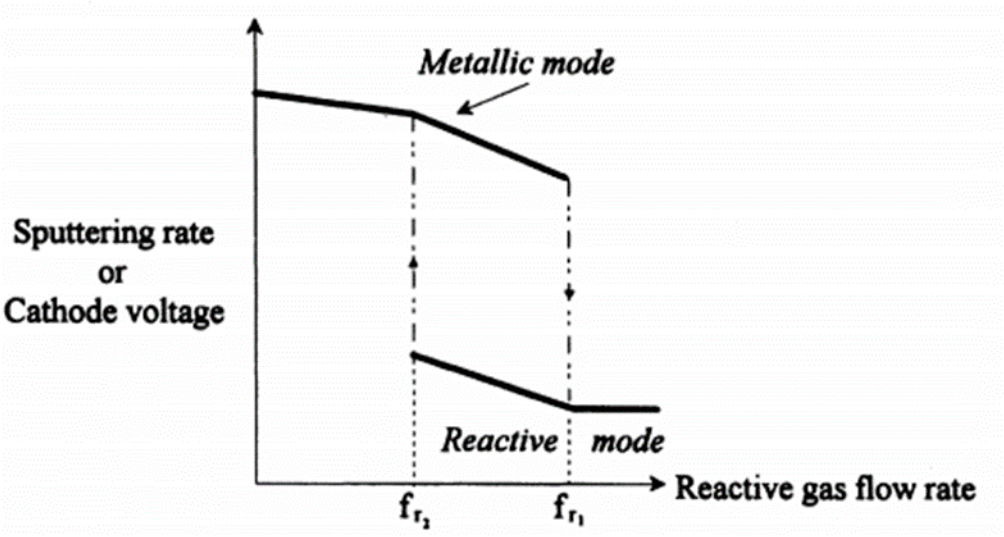

Figure 2-2. The hysteresis loop of reactive magnetron sputtering [63].

In addition to the hysteresis effect in reactive sputtering, there is another undesirable feature of magnetron sputtering. The magnetron introduces non-uniform sputtering of cathode due to non-uniform plasma density across the target surface. The discharge current density is

higher in the racetrack region compared to other regions. This leads to different sputtering rate across the target, which can be averaged in a not reactive environment, but it also caused a variation in the sputtered species during reactive deposition [63]. The target sputtering rate, R_{sput}, and oxidization rate $R_{ox,}$ are site-dependent across the target as shown in Figure 2-3 (a). Figure 2-3(b) shows that when reactive gas flow rate is high, R_{ox} is larger than R_{sput} and the target is covered by oxide layer (the degree of the oxide coverage Θ_{ox} is 1). With decreasing oxygen flow rate, the oxide coverage Θ_{ox} decreases until the racetrack of target surface has no oxide layer (the degree of the oxide coverage Θ_{ox} is 0). When Θ_{ox} is between 0 and 1, at the discharge region the oxide layer is continuously formed and destroyed. The R_{sput} and R_{ox} vary across the discharge region and the difference leads to possibility three different states exist simultaneously on target: fully oxidized, partially oxidized, and fully metal. The non-uniform poisoning of target may lead to non-uniformity of deposited films, both in rate and composition.

2.1.2 Experimental equipment

Some of the VO_x thin films studied in this thesis were deposited in a Kurt J. Lesker CMS-18 sputtering system. The system has three 3-inch magnetron sputtering sources and allows for substrate temperature control and RF biasing (Figure 2-4). VO_x thin films were deposited by reactive pulsed-dc magnetron sputtering from a 3-inch metallic vanadium target (99.99% V) onto 6-inch silicon wafers covered with 100 nm of thermal oxide. The deposition time was kept constant at 900 seconds. The pulsed dc power was maintained at 300 W with a 20 KHz pulse frequency and a 5 μsec pulse width using a dc magnetron power source (MDX 1000) with a SparKLE 20 pulse generator. The voltage-pulse waveform is shown in Figure 2-1. The system can accommodate 2 additional 3-inch targets which can be powered by rf power source (RFX-6000) for co-sputtering.

During all VO_x film depositions in this system, a negative substrate self-bias voltage of approximately -240 V developed using 25W of 13.56 MHz RF power was used. The total gas ($Ar + O_2$) flow rate was held at 18 SCCM with a downstream throttle valve used to adjust the deposition pressure. The target-to-substrate distance (throw distance) was set at either 4 or 8 inches by moving the target position with respect to the substrate. Oxygen with 99.99% purity was introduced into the process chamber either near the substrate or near the target; Ar was introduced into the chamber near the target. Both the oxygen and Ar flow rates were controlled by MKS mass flow controllers. The O_2 to Ar (O_2/Ar) inlet ratio was varied from 0.05 to 0.15. The chamber was pumped down to a base pressure of about 8E-7 Torr before each deposition.

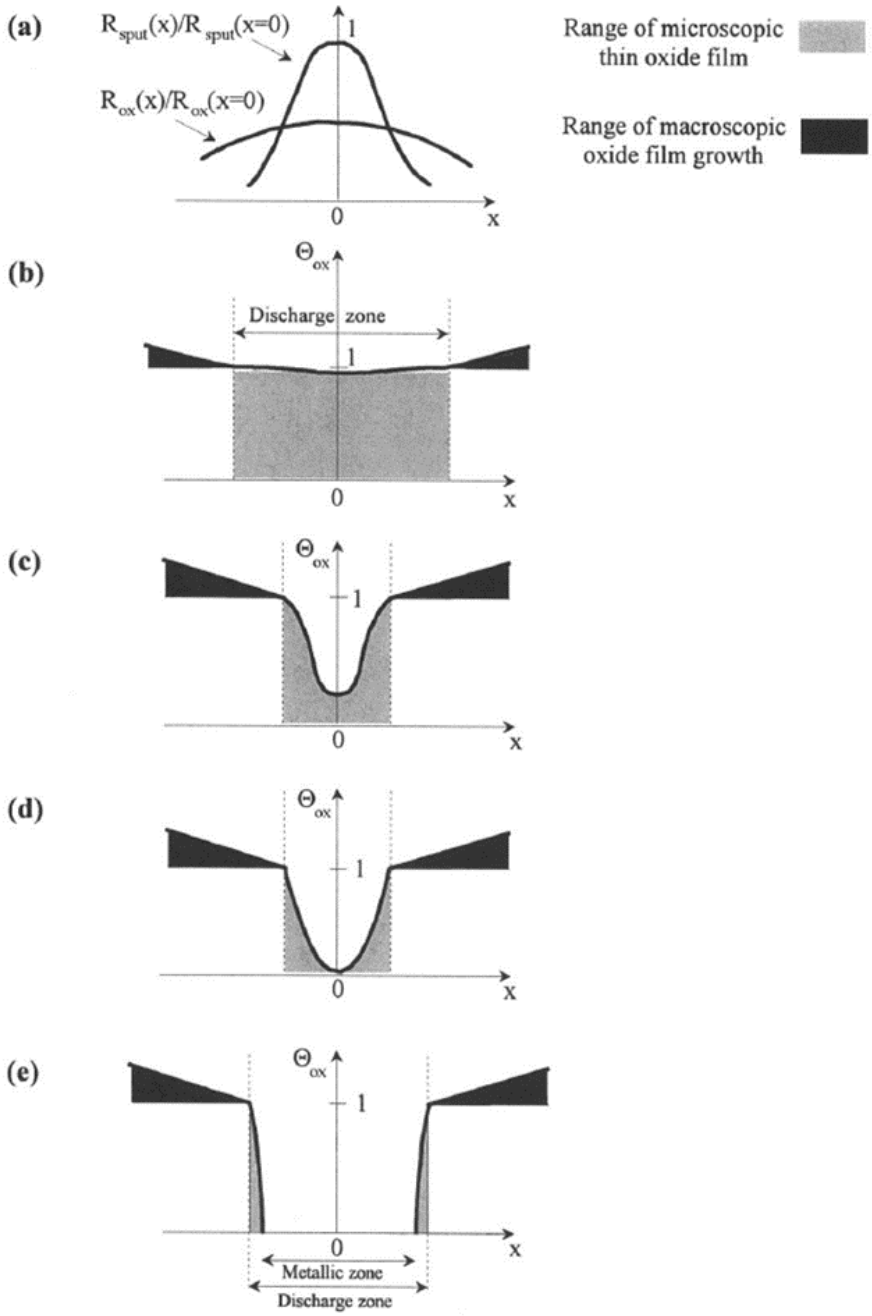

Figure 2-3. Differential poisoning of the target around the racetrack. (a) Comparison between the normalized metal sputter rate and oxidization rate at racetrack. (b) Target is fully oxidized; the racetrack is fully covered with oxide thin film. (c) to (e) Oxide thin film layer coverage is decreasing when rO_2 is decreasing. The cathode current of target is recovered gradually back to highest value. Graph is from reference [63].

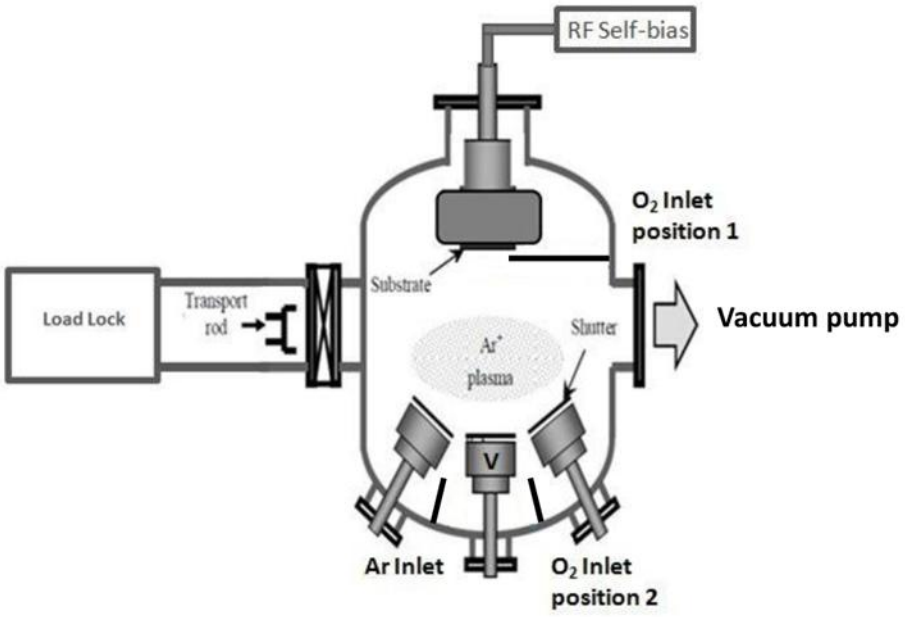

Figure 2-4. Schematic of Kurt J. Lesker magnetron sputtering system.

2.2 Biased target ion beam deposition

2.2.1 Biased target deposition

An alternative to magnetron reactive pulsed-dc sputtering used in this work is a novel technique called biased target ion beam deposition (BTIBD). As mentioned in Chapter 1, unlike magnetron sputtering, this technique utilizes a remote ion source to produce a low energy plasma which is then used to sputter up to three different targets simultaneously by independently applying a dc or pulsed-dc voltage to the targets. This section discusses both how the ion beam generated and how the sputtering is promoted by controlling the biased targets.

2.2.1.1 Low energy ion beam generation

In order to generate a low energy plasma with enough ions to illuminate the whole target, an un-focused "ion beam" is produced by a broad beam ion source. This kind of ion source requires an external electron source to produce electrons for ionization and neutralization of the ion beam. The generated electrons from the cathode-neutralizer are accelerated crossing the magnetic-field lines in the ion source anode to cause ionization. The diagram of end-hall ion beam source with a HC electron source is shown in Figure 2-5. Broad-beam ion sources include Kaufman-type gridded source and the Hall-effect gridless sources. There are two basic gridless ion sources: closed-drift ion source and end-hall ion source [64], [65]. The BTIBD systems used in this thesis was built by 4Wave Inc. and utilizes an end-hall ion source with hollow cathode (HC) electron source. Though HC is more complex than a filament source and is more expensive, the HC has much longer lifetime typically over 500 hours with noble gases. The schematic diagram of an end-hall ion source (EH1000 ion source by Kaufman and Robinson, Inc.) is shown in Figure 2-6 (a) and (b). The detailed ion source used in 4Wave BTIBD system is shown in Figure 2-6(c).

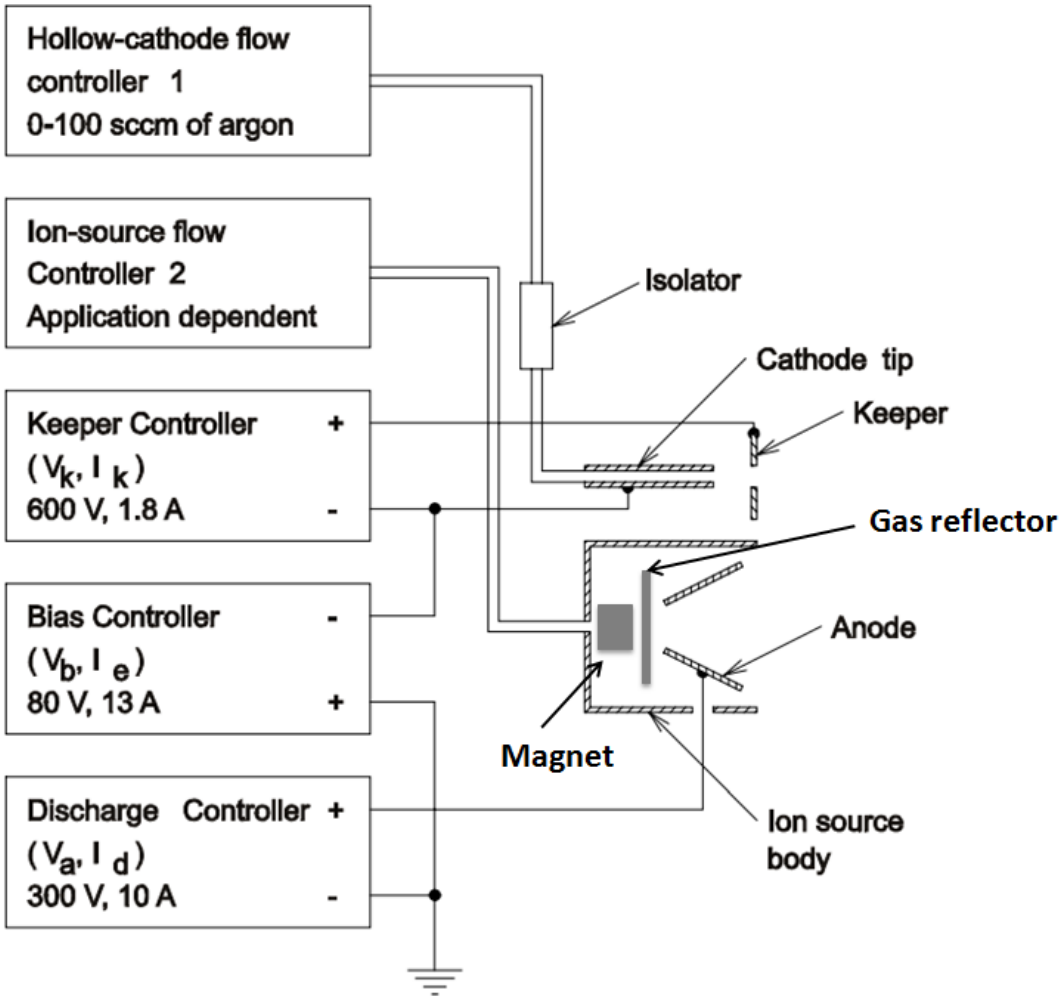

Figure 2-5. Re-plot schematic diagram of end-hall ion beam source with a HC electron source from reference [66].

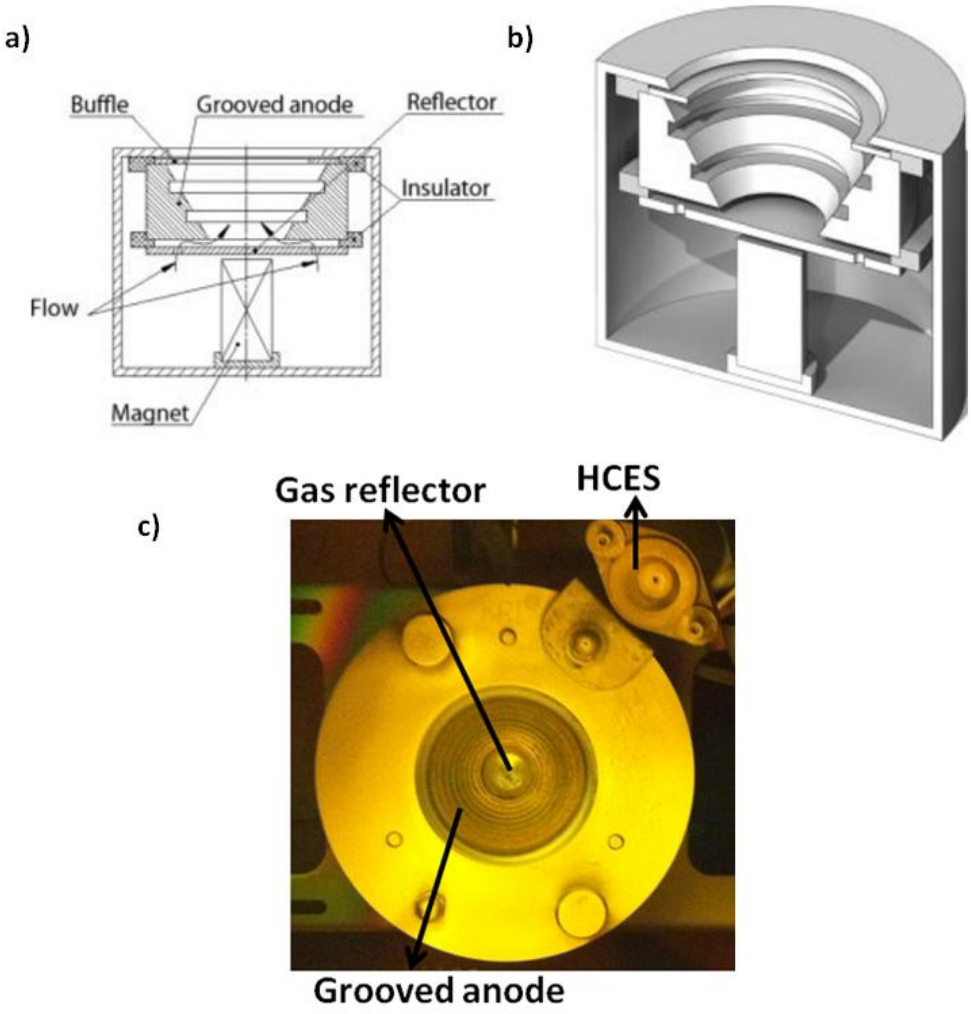

Figure 2-6. (a) and (b) show cross-section schematics of end-hall ion source with grooved anode [67]; (c) shows a top-view picture of this ion source assembled with HC electron source (HCES).

As shown in Figure 2-6 (a) and (b), a permanent magnet is placed under the gas reflector. The electrons provided by HC move in circles toward to the anode due to the magnetic field at the anode, hence the probability of collision between electrons and working gas molecules increase. The ions are generated by the ion source move along the applied electrical field without influence by the magnetic field. The extra electrons produced by the HC neutralize the ions to make quasi-neutrality, where the density of electrons and ions are approximately equal in a broad ion beam. It

should be mentioned that when background pressure is below 1 mTorr, the recombination of electrons and ions is not significant [67].

The working gas to produce plasma could be a noble gas such as argon or xenon. Other working gases such as hydrogen, nitrogen, and oxygen can also be used for reactive processes. The grooved anode and the baffle are designed to reduce "poisoning" of anode from reactive gases and prevent sputtered particles from depositing on anode which is shown in Figure 2-6 (c) [67] and reducing ion current generation.

2.2.1.2 Important characterization values of the ion beam

The ion sources have non self-sustained regime and a self-sustained regime. For the self-sustained regime, the discharge voltage between anode and cathode (walls) is high enough (above 300 V) to generate electrons from conductor surfaces for ion and electron collisions. However, the non self-sustained regime, where the discharge voltage is lower, an external electron source is needed to provide electrons [68]. The BTIBD system operates the ion source at a non self-sustained regime in order to keep the ion beam at low energy (<25 eV) to prevent ions sputtering vacuum system materials. The ion beam current I_i and mean value of ion beam energy E_i are the most two important values for the ion beam thin film deposition.

The end-hall ion source design such as the dimension of discharge channel, magnetic field value, gas distribution system, etc. have an influence on the ion beam current as a function of discharge voltage. However, with the certain ion source (EH 1000), the processing parameters of the end-hall ion source and HC such as: emission current of HC electron source, discharge current, discharge voltage, working gas type, working gas flow rates, total processing pressure have great influences on the produced ion beam [67].

In order to keep the mean energy of the plasma as small as possible so as to reduce unwanted impurities in the film, care must be taken to choose the proper processing parameters. It has been reported that the coefficient of the ion beam energy transformation from the discharge voltage to an ion beam mean energy is related to the neutralization of the ion beam. When the ion beam is properly neutralized, whereas the emission current from an external electron source is equal to discharge current, the ion beam mean energy produced by the end-hall ion source is 60-70% of the discharge voltage with a broad energy distribution. When the emission current is lower than the discharge current, the ion beam is under neutralized, and the ion beam mean energy is only 10-50% of the discharge voltage. This coefficient will increase when the emission current is higher than the discharge current [65], [67].

In addition to the neutralization of ion beam, working gas flow rates have effects on this coefficient as well. At the discharge current, higher working gas flow rates lead to lower discharge voltage. It is reported that at the same discharge current, when discharge voltage is lower than 50 V, the increasing of discharge voltage leads to increase of ion beam current. When discharge voltage is higher than 50 V, the ion beam current does not change too much with the discharge voltage increasing, and mainly change as a function of discharge current [67].

Other values of ion beam are also important to thin film deposition, such as: ion beam divergence, distribution of ion beam energy, the coefficient of the working material utilization, the ratio of ionized particles flying into chamber to flying back into a reflector, and so on. For the end-Hall ion source, 70-80% of ions of the neutralized ion beam have a half-angle α of 40^{o}-60^{o} from the ion source axis. The large ion beam divergence enables the uniform illumination of negatively biased targets for sputtering for the system used in this thesis since the targets are 90 degrees with respect to the source axis [50], [65], [67].

2.2.1.3 Biased target deposition

In the BTIBD system, the target is negatively biased, with either direct current for conductors or pulsed dc (or rf) for dielectrics. The plasma sheath is around 2mm, which is around a few Debye lengths when pressure is about 1 mTorr. Once the target is applied with negative bias, the ions bombarding the target surface energy is the sum of ions kinetic energy E_o and the potential energy gained to the target qV_b [67]:

$$E = E_o + qV_b \qquad Eq.\ 2.1$$

Unlike magnetron sputtering, there is no magnet under targets, so the erosion of target is uniform, and furthermore, magnetic materials (such as Ni, Fe, Co etc.) are more easily sputtered by this technique. For pure metal sputtering, the target is applied with negative dc potential. For dielectric targets and/or reactive sputtering of metal targets, pulsed dc is applied on targets for reactive sputtering.

2.2.2 Experimental equipment

A 4Wave-LANS system was used to deposited vanadium oxide, nickel oxide, and molybdenum oxide thin films. As shown in Figure 2-7, in this system, up to three 4-inch targets could be sputtered simultaneously with voltage varies from -300 to -800 V. The pulse period (full duty cycle) was 100 μsec whereas the pulse width (time duration applied with +5 V power) varied from 1-90 μsec. For vanadium oxide thin film deposition, three V targets with 99.99% purity were used for co-sputtering. For molybdenum oxide and nickel oxide thin films, a single Mo or Ni target (99.99%) was utilized.

For all the depositions, the HC Ar flow rate was fixed at 10 SCCM whereas the ion source Ar flow rate was varied from 60 to 100 SCCM. In order to keep the ion beam energy

lower than 25 eV, the discharge voltage should be less than 45 V. The discharge current was fixed at 7.5 Amp, and the ion beam current is about 1.8 Amp (25% of discharge current). The processing pressure was based on the total Ar flow rate (no active control) and typically varied from 7 to 1.2 mTorr.

A residual gas analyzer (RGA) is installed on the top of processing pressure to monitor and control a reactive gases partial pressure during deposition. The reactive gas could be either maintained at certain partial pressure from RGA feedback controller or at certain flow rates by gas flow controller. The oxygen partial pressure varied from 5E-7 to 6E-6 Torr and the oxygen was introduced into the chamber either near the ion source or near the target position 1.

As shown in Figure 2-7, a shield was used to prevent cross-contamination among targets during co-sputtering. The picture of this system was taken facing the end-hall ion source. The 4-inch substrate holder and load lock are not shown. As discussed previously, the deposited films deposition rate and stoichiometry is not only controlled by reactive gas, but also by pulse frequency and applied potential. Because of the off-axis design, the low energy ion beam secondarily conditions the deposited films if a physical block is not put on the shielding to prevent direct line of sight between the ion source and the substrate.

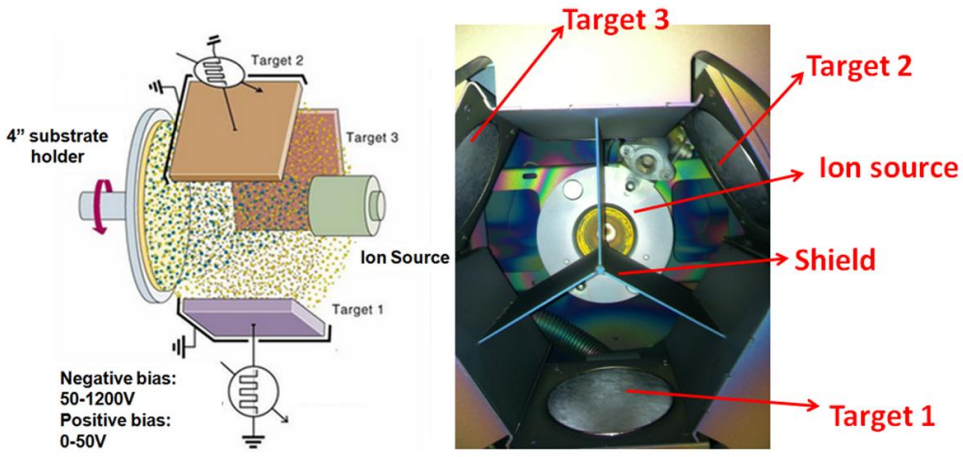

Figure 2-7. Schematic and picture of the 4Wave LANS chamber.

2.3 Rapid thermal annealing (RTA)

A series of annealing experiments were done to assess the deposited oxide thin film thermal stability of resistivity and TCR. As shown in Figure 2-8, a homemade rapid thermal annealing system was used to post-anneal the deposited oxide thin films. The ambient gas (99.99% Ar or O_2 gas) was fed into the tube furnace at the flow rate of 2 L/min. The furnace was first preheated to 350^{o}C. The samples were placed on a graphite boat and inserted into the tube for 20 min annealing. After annealing, the samples were moved to the end of the tube and cooled to room temperature in an Ar ambient.

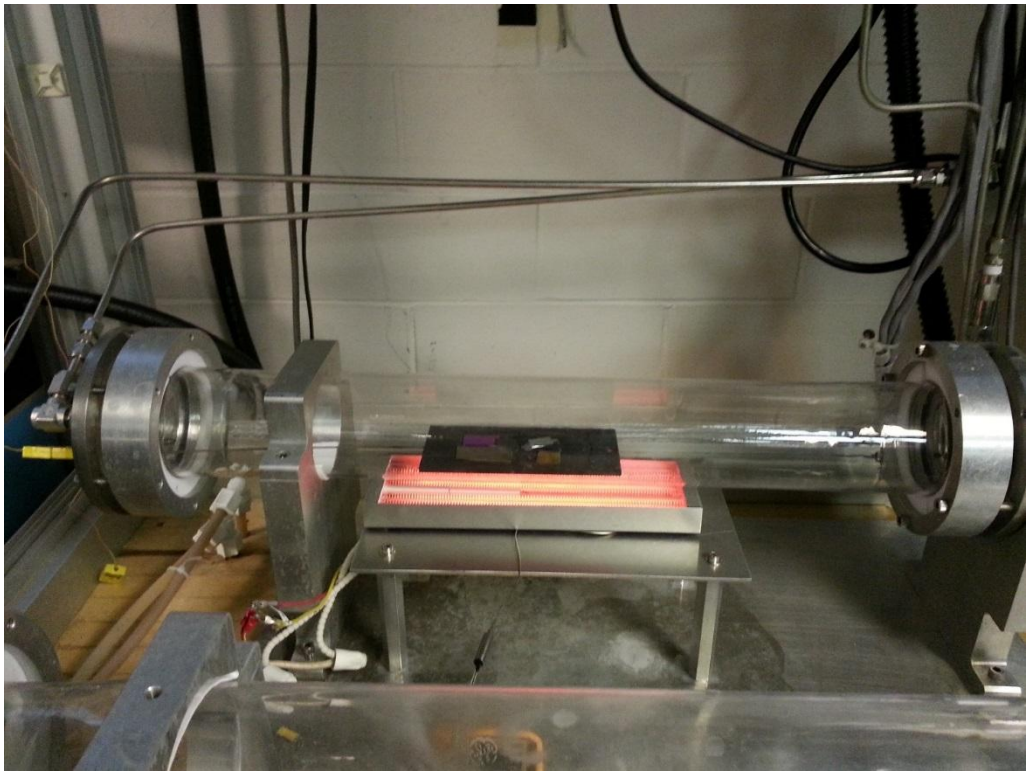

Figure 2-8. Picture of homemade RTA used for annealing experiments.

2.4 Grazing incidence X-ray diffraction (GIXRD)

Grazing incidence x-ray diffraction utilizes the technique of x-ray diffraction with a small incident angle to in order to increase the probability of evaluating a thin film's crystallinity. In this work, the incident beam angle was fixed at 1^{o} and the detector angle was scanned so that the 2θ angles varied from 5^{o} to 70^{o}. This geometry reduces diffraction signal from the substrate and limits the penetration depth of X-rays to be about 100 Å.

As shown in Figure 2.9, in this work, a PANAnalytic Pro X'Pert MPD with Cu $K\alpha_1$ (λ=1.54 Å) radiation was used to collect the x-ray diffraction pattern. The collected data was analyzed by using the MDI JADE 9 software.

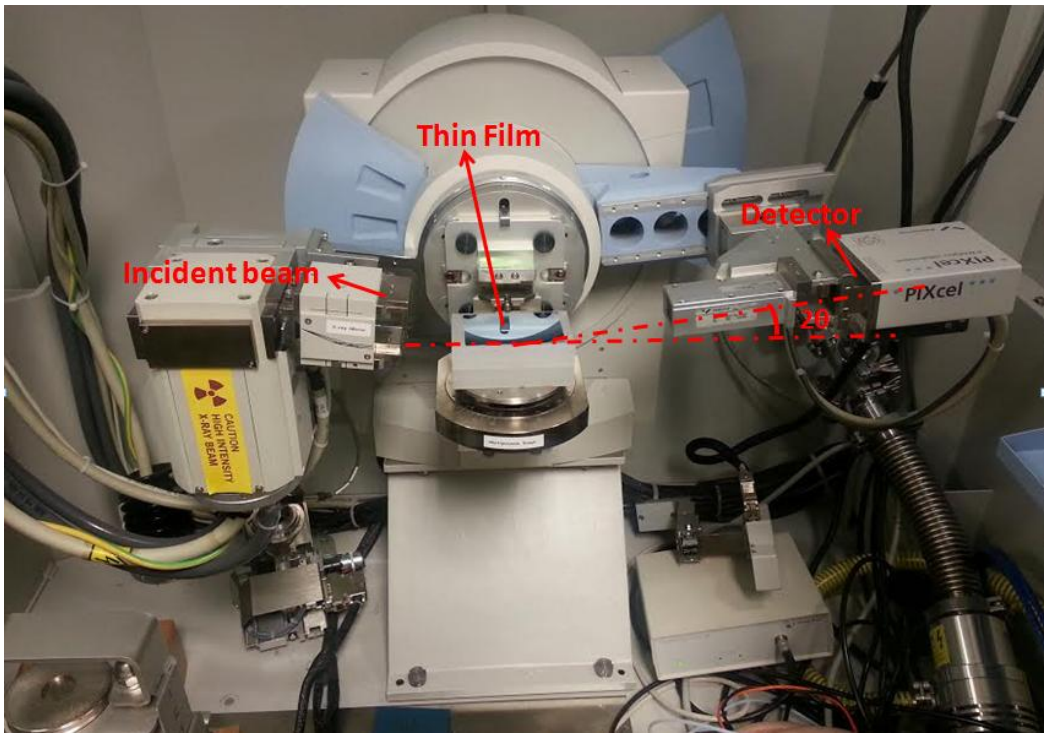

Figure 2-9. Picture of the GIXRD instrument used in this work.

2.5 Raman spectroscopy

Raman spectroscopy is a vibrational spectroscopy technique used to analyze chemical composition and structure of the materials. This technique is based on the frequency shifting of a monochromatic light caused by inelastic scattering by the sample. Raman spectra provide a spectral fingerprint of each molecule and can be analyzed both qualitatively and quantitatively.

In this work, the Raman spectra of a vanadium target and vanadium oxide thin films were collected using a Renishaw inVia Raman Microscope (Renishaw Inc., Gloucestershire, UK) with backscattering geometry. A HeNe (632.5 nm) laser was used as excitation source with a power around 5 mW, and a 100x microscope objective lens with a numerical aperture of 0.9 was used to collect the data. Since a silicon wafer was used as substrate, reference spectrum of Si was collected and subtracted from all the spectra.

2.6 Energy-dispersive X-ray spectroscopy (EDS)

Energy dispersive x-ray spectroscopy is a technique used to analyze and identify the elements in a sample. EDS utilizes the x-ray spectrum emitted by a sample surface bombarded by a high-energy focused electron beam. The incident electron beam excites an electron from an inner shell to an outer shell of an atom, and another electron from a higher energy shell fills the hole and release an x-ray. The number and energy of the x-ray photons are measured for both qualitative and quantitative analysis. Elements with atomic number from 4 to 92 can be detected.

In this work, the elemental analysis of metal oxide thin films was made by EDS spectroscopy using a field emission scanning electron microscope (NanoSEM 630). The collected data was analyzed by AZtecEnergy EDS analysis software (Oxford Instruments). Due to the statistical and analytical errors, the analytical accuracy is estimated about ± 5% (at%).

2.7 Surface profilometry

The deposited film thickness was measured by a Tencor Alpha-step 500 surface profilometer. The step was created by a Kapton tape or colloidal graphite at the center of wafer. After the film deposition, Kapton tape or the colloidal graphite was carefully removed by acetone. The height of the resulted step was measured using 50 μm to 2 mm scan lengths across the step. The reported thickness was typically an average by repeated measurements for different spots as well as different scanning direction. In addition to profilometry, the deposited metal oxide thin film thickness was also estimated from spectroscopic ellipsometry. The measured film thickness has a typical error$< \pm 2\%$.

2.8 Spectroscopic ellipsometry (SE)

As a non-destructive optical characterization method, spectroscopic ellipsometry is not only used to measure the thickness of thin films, but also provides optical information of a sample. The polarization of the incident light beam changes after interacting with a sample, and the change of the amplitude ratio Ψ and the phase difference Δ are measured and quantified by further modeling. The sample thickness and optical properties can be extracted from the model.

In this work, a J.A. Woollam Co. RC2 multichannel spectroscopic ellipsometry with dual-rotating compensator was used to attain ex-situ and real time in-situ data. For ex-situ measurement, the light incidence angle was varied from 50^o to 80^o with a step of 10^o. A Xe lamp and a Quartz Tungsten Halogen lamp installed in the RC2 instrument enable large spectral range from 0.73 to 5.15 eV (1700-240 nm). Figure 2-10 shows the photographs of RC2 instrument for ex-situ measurement.

The collected data of the deposited films were fitted to a model that contains a four-layer structure as shown in Figure 2-11. The Bruggman effective medium approximation (EMA) was used to calculate surface roughness as a mixture of 50% top bulk metal oxide layer and 50% voids.

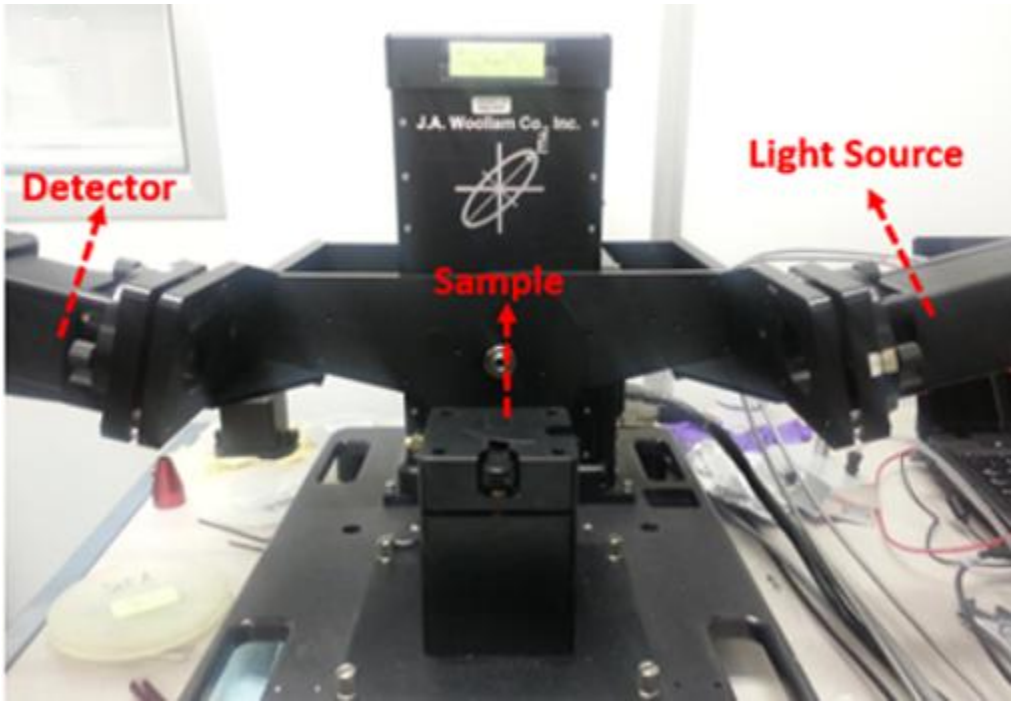

Figure 2-10. Picture of J.A. Woollam RC2 SE instrument for ex situ measurement on the variable angle base.

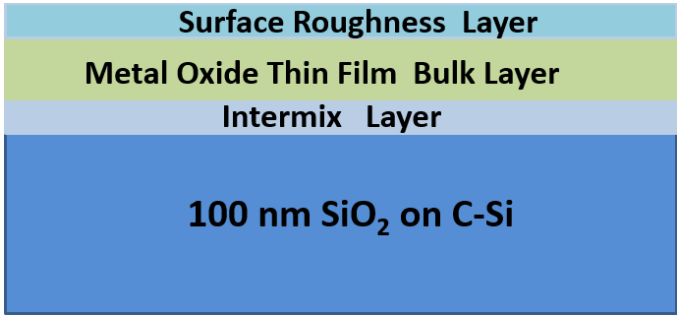

Figure 2-11. Cartoon of the model structure with four layers.

2.9 Electrical properties characterization

Resistivity and temperature coefficient of resistance (TCR) of deposited thin films were measured by two methods. A four-point probe instrument was used to measure films sheet resistant and TCR mapping (usually 49 points for a 6 inch wafer) if the films sheet resistance below 800k Ω/square. Transmission line measurements of film resistivity were also conducted using 100-nm-thick Ti contacts sputtered through a stencil mask onto the deposited thin film surface.

The resistance R between two Ti electrodes was calculated by I-V measurement with voltage from -5 to 5 V. The room temperature resistivity ρ was calculated by:

$$R = \frac{R_{sh} d_i}{W} + 2\frac{R_c}{W} \qquad \textit{Eq. 2.2}$$

$$R_{sh} = w \times slope \qquad \textit{Eq. 2.3}$$

$$\rho = t \times R_{sh} \qquad \textit{Eq. 2.4}$$

where R_{sh} is the sheet resistance of thin film, R_c is the contact resistance between the thin film and the contact, d_i is the spacing between electrodes, w is electrodes length, and t is the thin film thickness. Figure 2-12 shows the TLM pattern and fitting graph to calculate film resistivity and contact resistance.

The resistance R was measured on a two-point micro-probe station at temperatures ranging from 20-80^{o}C with a step of 2^{o}C, and the room temperature TCR values were calculated using the Eq 1-1 and 1-2. The calculated TCR values typically have an error of $\pm$10%.

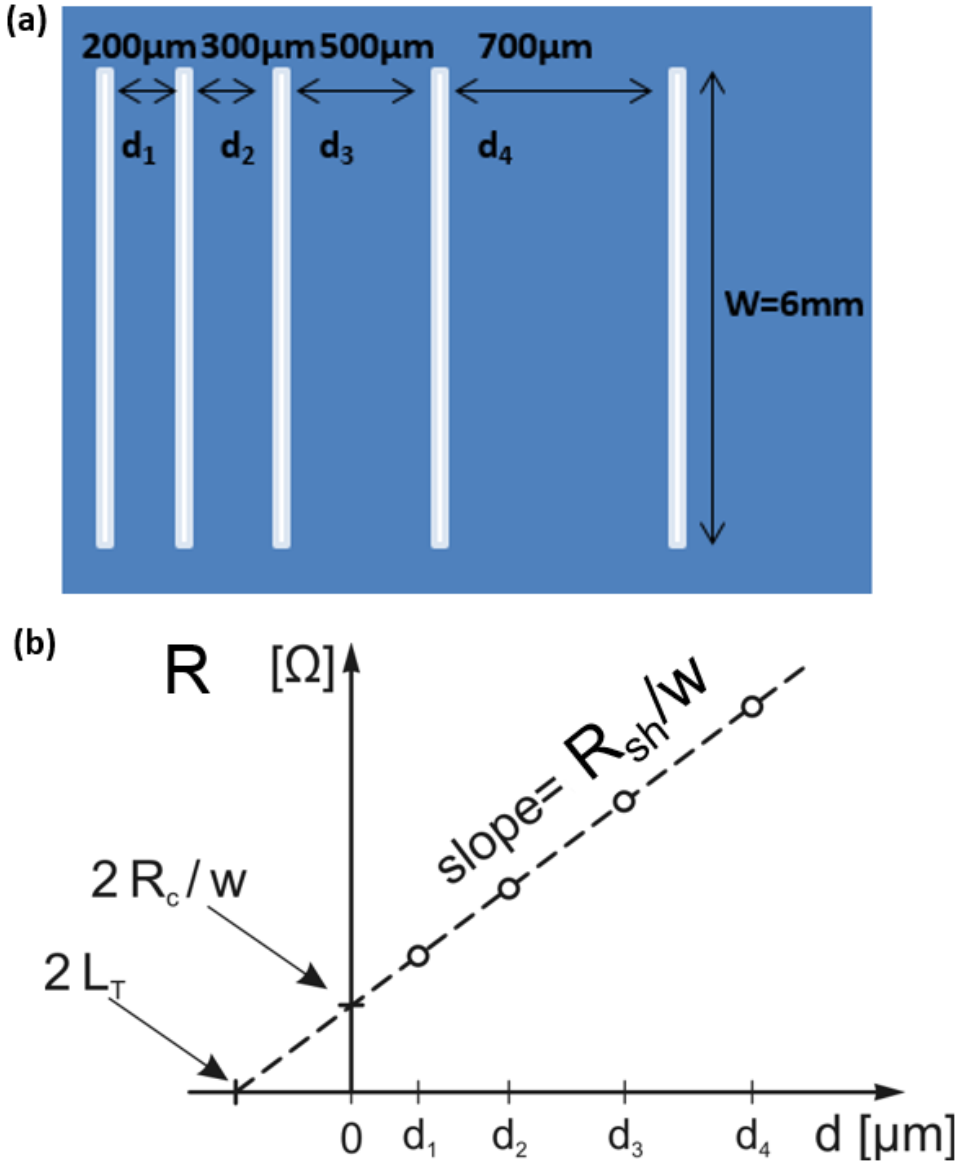

Figure 2-12. (a) Cartoon and (b) graph of TLM pattern used to calculate thin film resistivity.

2.10 Photolithography

Photolithography is a process of transferring patterns on a mask to a thin film. In this work, the smallest features were 1µm × 1µm and contact photolithography with 365 nm (i-line)

ultraviolet light source (LED array) was used to make patterns. Figure 2.14 shows the picture of the contact mask aligner used in this work (Karl Suss MA56 aligner).

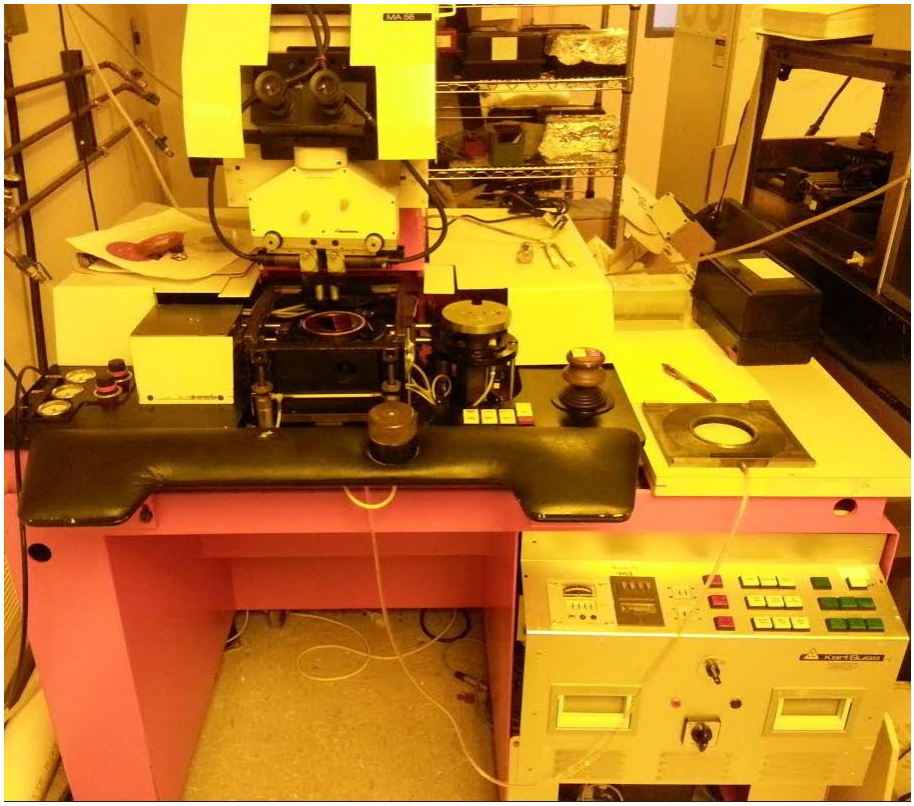

Figure 2-13. A picture of Karl Suss M56 mask aligner.

Photolithography recipe varies for different oxide thin films and device structures. Wet etching was first tried to pattern NiO_x film. Different etchants such as ammonium hydroxide, nitric acid, and sulfuric acid (at 60^{o}C) have been tried to pattern NiO_x thin films, and they did not etch NiO_x films. CAN (ceric ammonium nitrate) at different temperatures also have been tried. The etch rate of NiO_x by high concentration of CAN (1:1) is very slow at room temperature (1nm/min), whereas at 60^{o}C the etch rate increases to about 1nm/sec. However, high concentration CAN at 60^{o}C also etches the protecting photoresist (1811) very fast. Thus, in this work, NiO_x active layers were patterned by a lift-off process. The processing recipe steps are

listed in Appendix A. Figure 2-14 shows the comparison between etching and lift-off patterning of NiO_x thin films. The photolithography masks were designed by Myung-Yoon Lee, a graduate student in Jackson Electronics Research Group at The Pennsylvania State University.

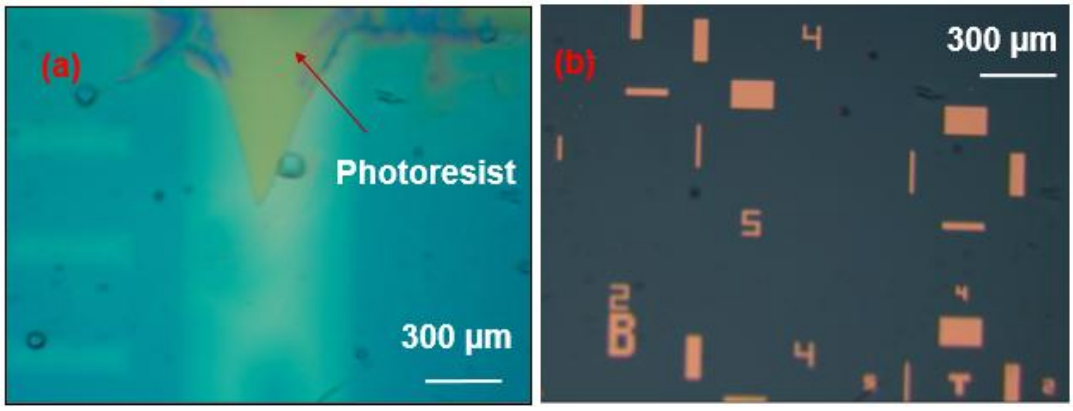

Figure 2-14. NiO_x active layer patterned by (a) CAN etching at 60°C for 3 min and (b) double-layer lift off process.

2.11 1/f noise measurement

As mentioned in Chapter 1, unlike the Johnson noise, the 1/f noise is dependent on material properties and processing parameters rather than just the film resistance. The low frequency 1/f noise for microbolometer sensing materials was extracted by using Hooge-Vandamme relation [69]:

$$Log(\frac{S_I(f)}{I_{bias}^2}) = Log\,\frac{\alpha_H}{n \times V} - \beta Log(f) \qquad \textit{Eq.2-5}$$

where I_{bias} is the measured sample current, $S_I(f)$ is the spectral current density and f is the frequency. $S_I(f)/I_{bias}^2$ is the power spectra density (PSD). α_H is the Hooge's parameter, n is the carrier concentration, V is the measured thin film sample volume, and β is the slope of measured *1/f* noise. It is hard to independently measure the VO_x [46] and NiO_x carrier concentration. In

order to compare 1/f noise among different materials, a normalized Hooge's parameter $\frac{\alpha_H}{n}$ is used as the property of interest.

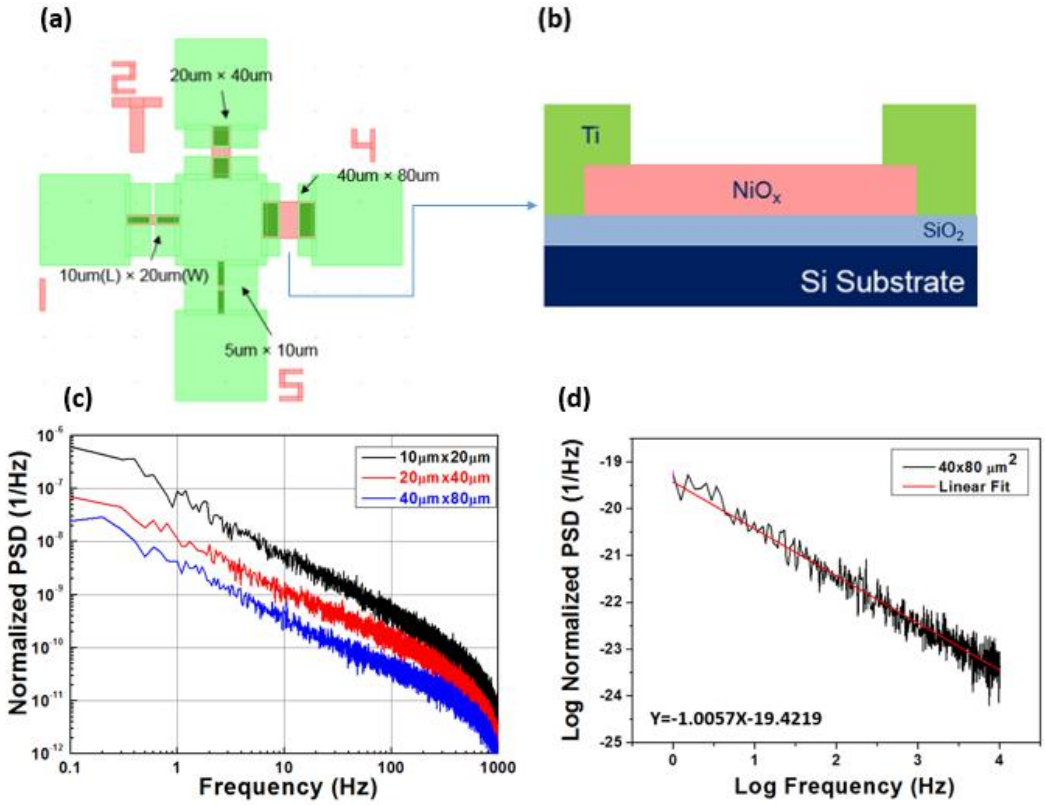

Figure 2-15. (a) and (b) Top and cross-section view of noise patterns; (c) volume dependence of PSD; and (d) Plot of log (PSD) versus log (frequency) to extract normalized Hooge's parameter α/n.

As shown in Figure 2-15, the 1/f noise of different volumes of a patterned NiO_x film were measured, and the normalized PSD data is inversely proportional to the sample volume, which correlates to Eq. 2-5. The normalized Hooge's parameter can be extracted by a linear fit to PSD versus frequency, in a log-log scale. The slope of the fitted line is about -1, again, confirming 1/f noise is measured. The intercept of this linear fit on Y-axis is used to extract the normalized Hooge's parameter. The NiO_x noise shown in this work was measured and analyzed by Myung-Yoon Lee.

Chapter 3

Reactive Magnetron Pulsed-dc Sputtering of Vanadium Oxide

As mentioned in the introduction, VO_x thin films deposited by reactive magnetron pulsed-dc sputtering with RF substrate bias have increased film density, improved TCR, and reduced 1/f noise when compared with those that do not use substrate bias. However, reactive magnetron sputtering is a complex process and the inherent non-uniform sputtering of the target as well as the specifics of the system being used must be taken into consideration. In this chapter, the potential of reactive pulsed-dc magnetron sputtering as an alternative to reactive ion beam sputtering to prepare VO_x microbolometer thin films is investigated. Different processing parameters such as processing pressure, total gas flow rates, target to substrate throw distance, and gas delivery effects on process control and film uniformity are analyzed. We also report on other methods also have been tried in a "quick-and-dirty" way to find out if they might be useful to the microbolometer industry to improve process controllability and overall yield. These processing methods include co-sputtering of V and V_2O_5 targets, reactive sputtering from a VC target, V_2O_5 target, V_2O_x target, and H_2 introduced into chamber plasma during deposition.

3.1 VO_x thin films prepared by sputtering of metallic V target

3.1.1 The effects of processing pressure

VO_x thin films were deposited with -240 V (25 W rf) substrate bias at 1, 5, and 10 mTorr pressure and with O_2/Ar inlet ratios of 0.08, 0.1, and 0.12. The oxygen inlet position was near the substrate and the throw distance was 8 inches. As shown in Figure 3-1 (a), for low O_2/Ar inlet ratios, the VO_x deposition rate is higher at higher processing pressure. As the O_2/Ar inlet ratio

increases, the deposition rate of VO_x decreases, and the decrease is greater at higher processing pressure. The deposited film resistivity and TCR values are shown in Figure 3-1(b). Resistivity and TCR increase with O_2/ Ar inlet ratio increase and the resistivity change is greater at higher processing pressure.

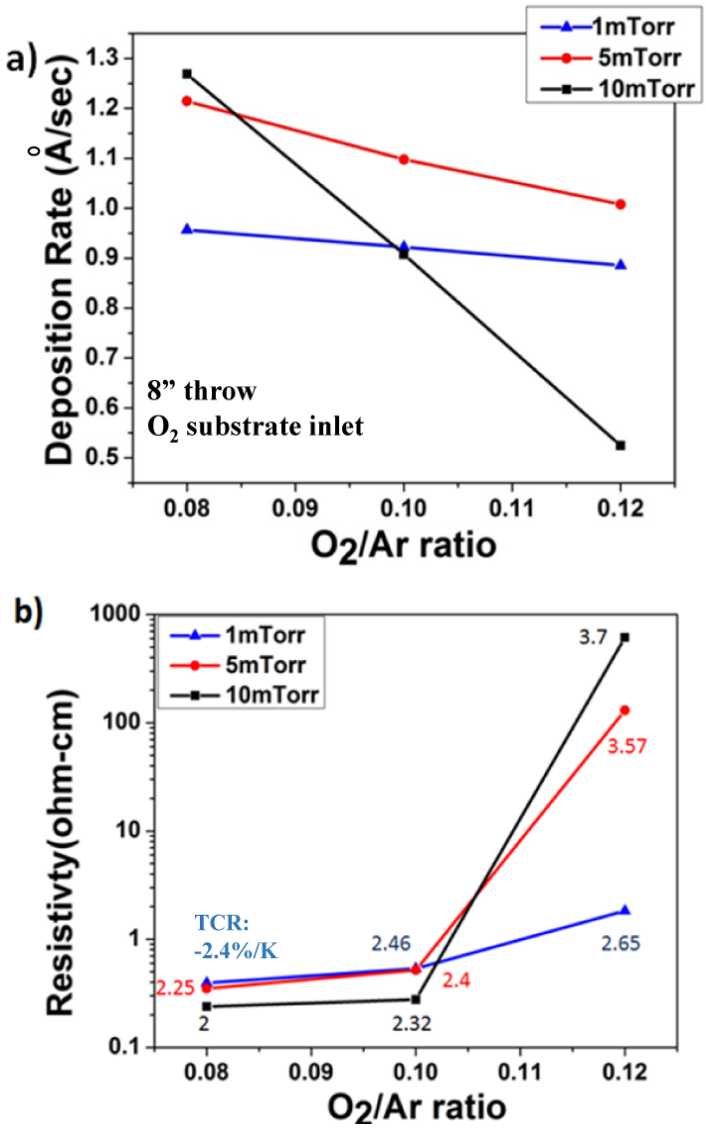

Figure 3-1. VO_x films deposited at different pressures as a function of O_2 to Ar inlet ratio with -240V substrate bias at an 8 inch throw distance with oxygen inlet position near the substrate. (a)VO_x film deposition rate and (b) resistivity and TCR values.

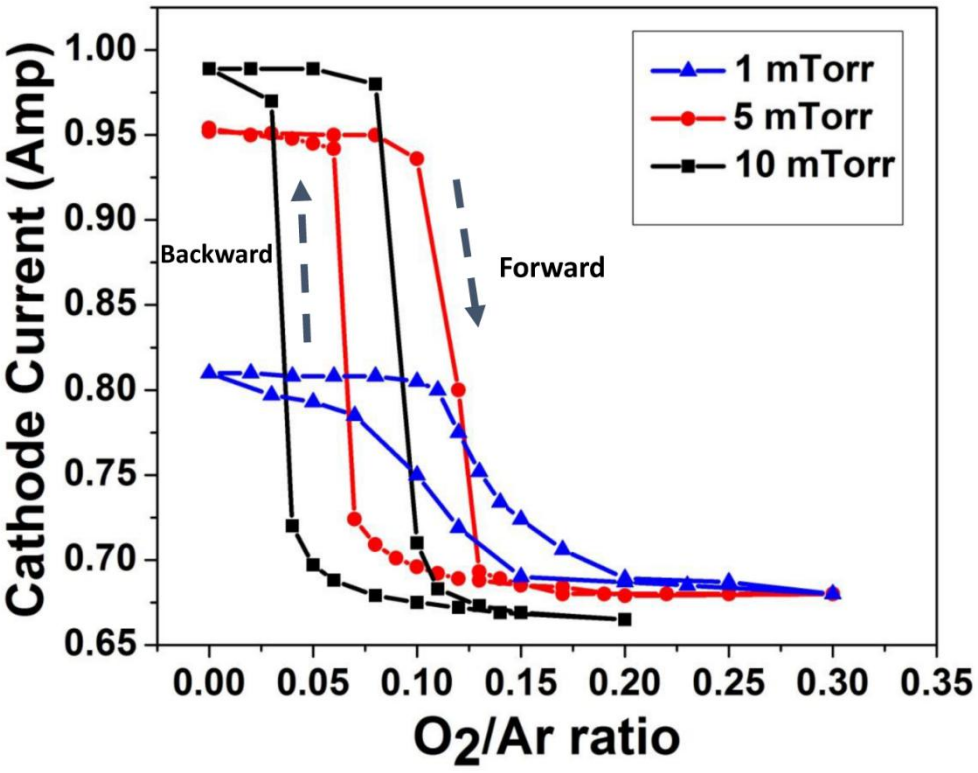

Figure 3-2. Hysteresis curves of vanadium target cathode current versus O_2 to Ar inlet ratio, for 300 W pulsed DC, -240 V substrate bias, a total gas flow rate of 18 SCCM, throw distance of 8 inches, with oxygen inlet position near the substrate, and total pressures of 1, 5, and 10 mTorr.

To understand VO_x thin film property changes with increasing of O_2 /Ar inlet ratio, the vanadium metal target oxidation was assessed by monitoring the target cathode current. As shown in Figure 3-2, the dependence of the cathode current with varying O_2/ Ar inlet ratio is hysteretic. The dependence can be divided into three regions: a metallic zone at low O_2/Ar inlet ratio, where the target is initially oxidized and the cathode current is large; an oxidized zone at high O_2/Ar inlet ratio, where the target surface is oxidized and the cathode current is low, and; an intermediate zone, where the target surface is transitioning from metallic to oxidized and the cathode current is larger than for the oxidized target surface, but smaller than for the initially oxidized surface. The target hysteretic characteristic was observed before [62].

During reactive sputtering, the O_2 gas has, in general, three possible outcomes: some is consumed by the target surface, some is consumed by reaction with vanadium at the substrate and chamber walls, and some is pumped out of the vacuum chamber [60]. In the metallic zone, the available oxygen is insufficient to significantly oxidize the V target and the measured cathode current is approximately the same as with no O_2 input. Ions are drawn from the magnetron plasma, the cathode current is approximately constant during the entire negative pulse time, and the sputter deposition rate is high. In the oxidized zone, the available oxygen is sufficient to fully oxidize the vanadium target surface. Because the conductivity of the surface VO_x is low, the Ar/O_2 ion flux charges the target surface, the cathode current decreases rapidly during the target negative pulse time, and the deposition rate is reduced compared to the metallic target. The strength of the metal-oxide bonds for the oxidized target surface may also reduce the sputter yield, further reducing the deposition rate [61]. Between the metallic zone and oxidized zone is an intermediate zone, where the V target is partially oxidized [62] As shown in Figure 3-2, the intermediate zone occurs for O_2/Ar inlet ratio from 0.07 to 0.2 at 1 mTorr, 0.06 to 0.12 at 5 mTorr, and 0.04 to 0.1 at 10 mTorr. A comparison of Figures 3-1 and 3-2 shows that films with the resistivity required for microbolometer use are deposited with the cathode current in or near the intermediate zone, where the target surface is transitioning from metallic to oxidized. At higher deposition pressure (5 and 10 mTorr), the transition from metallic to oxidized target surface is abrupt and control is difficult. Reducing the deposition pressure to 1 mTorr leads to a more gradual change from metallic to oxidized target surface and allows better control of deposited film properties. The results indicate that lower pressure (1 mTorr) is useful for reproducible deposition of VO_x films in the 0.1 to 10 Ω•cm resistivity range.

3.1.2 The effects of total gas flow rate

If the pumping speed is fixed by the adjusting the throttle valve, the processing pressure changes as a function of total gas flow rate. As shown in Figure 3-3, the hysteresis curves of the V target among different total gas flow rates are compared. The higher of the pressure and total gas flow rate, the higher of the cathode current. This may be due to more Ar^+ bombarding to the target. Higher total gas flow rate means at the same O_2/Ar inlet ratio, the oxygen flow rate is higher, which may lead to the faster oxidization of the target. On the other hand, higher total gas flow rate recovers the oxidized target faster. This may explain the hysteresis curve is slimmer when total gas flow rate is higher. Though the higher pressure indicates higher deposition rate, the fast transition between metallic zone to oxidized zone leads to poor process controllability.

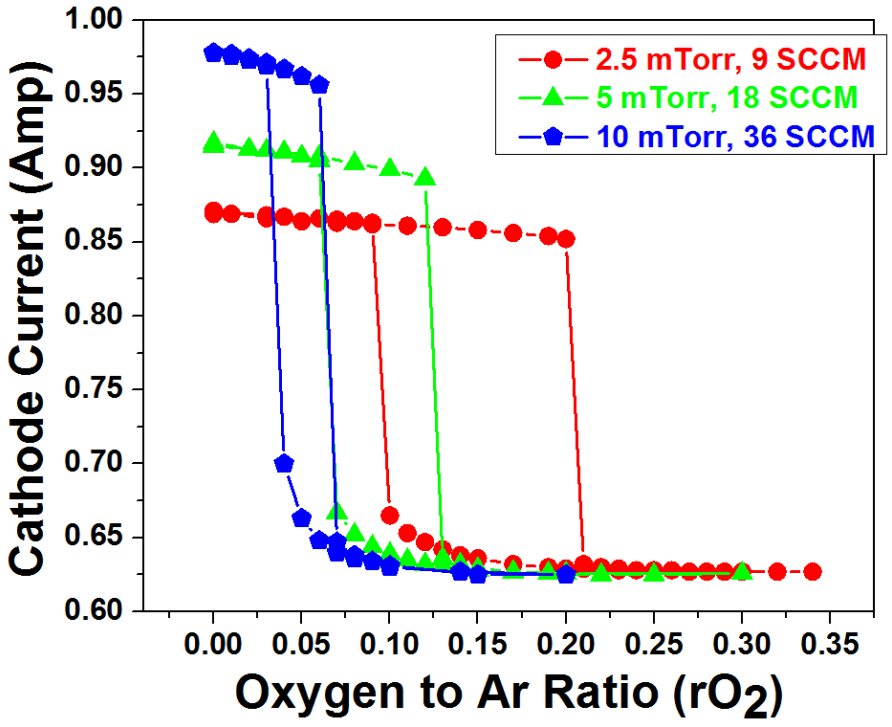

Figure 3-3. Vanadium target hysteresis curve comparison with different total gas flow rate. The pumping speed is fixed. Throw distance is 8 inch. The oxygen inlet position is near substrate and pulsed dc power applied on target is 300 W. Substrate bias voltage is -240 V.

3.1.3 Gas delivery and throw distance effects

The effects of target to substrate throw distance and oxygen inlet position were also investigated. During deposition, the pulsed dc power was fixed at 300 W and the processing pressure was 5 mTorr with a total gas flow rate of 18 SCCM. The film deposition time was 900 seconds and the substrate was rotated at 20 rpm. The substrate bias was fixed at -240 V and the throw distance was changed by moving the V target position.

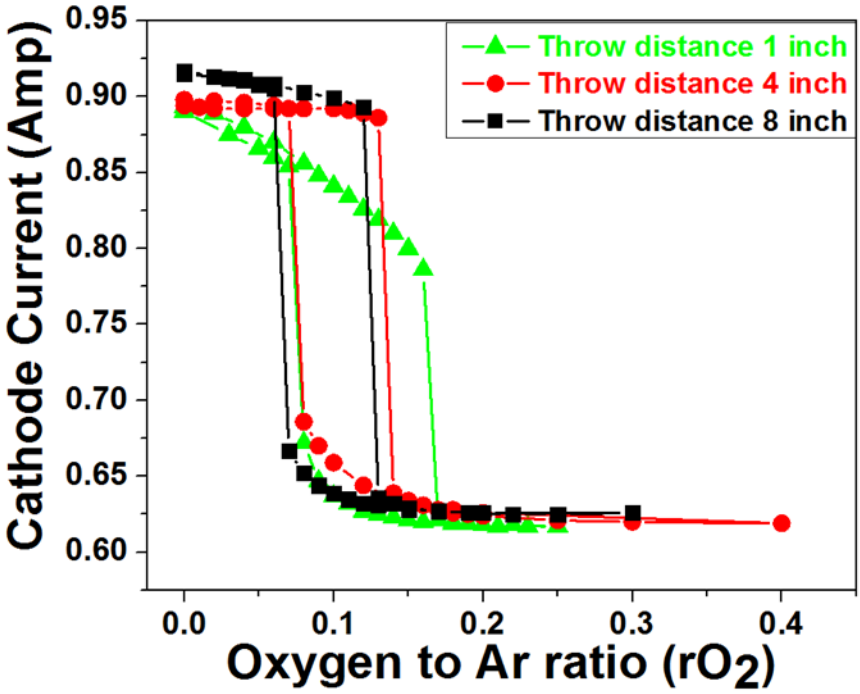

Figure 3-4. Vanadium target hysteresis curve comparison for different throw distances. Total gas flow rate of 18 SCCM. Throw distance varies from 1 inch, 4 inch, to 8 inch. The oxygen inlet position is near substrate. Processing pressure is 5 mTorr and pulsed dc power applied on target is 300 W. Substrate bias voltage is -240 V.

Figure 3-4 shows the hysteresis curves with different throw distances. Target hysteresis curve has wider window when throw distance is shorter. This indicates that the throw distance has influences on the conditioning of target. When throw distance is 1 inch, the intermediate zone is when O_2/Ar inlet ratio is between 0.05 and 0.15. With increasing of the throw distance, this

intermediate zone width changes to between 0.08 and 0.14 when throw distance is 4 inch, and 0.07 to 0.12 when throw distance is 8 inch. At the metallic zone, the higher throw distance has higher cathode current.

In the CMS-18 deposition system, the target shutter was closed for pre-conditioning of the target. However, the target condition changes once the target shutter is opened for film deposition. This leads to the composition of the initial layer of deposited film being less controllable and more variable. Thus, a substrate shutter rather than the target shutter should be used to improve the controllability of the sputtering process.

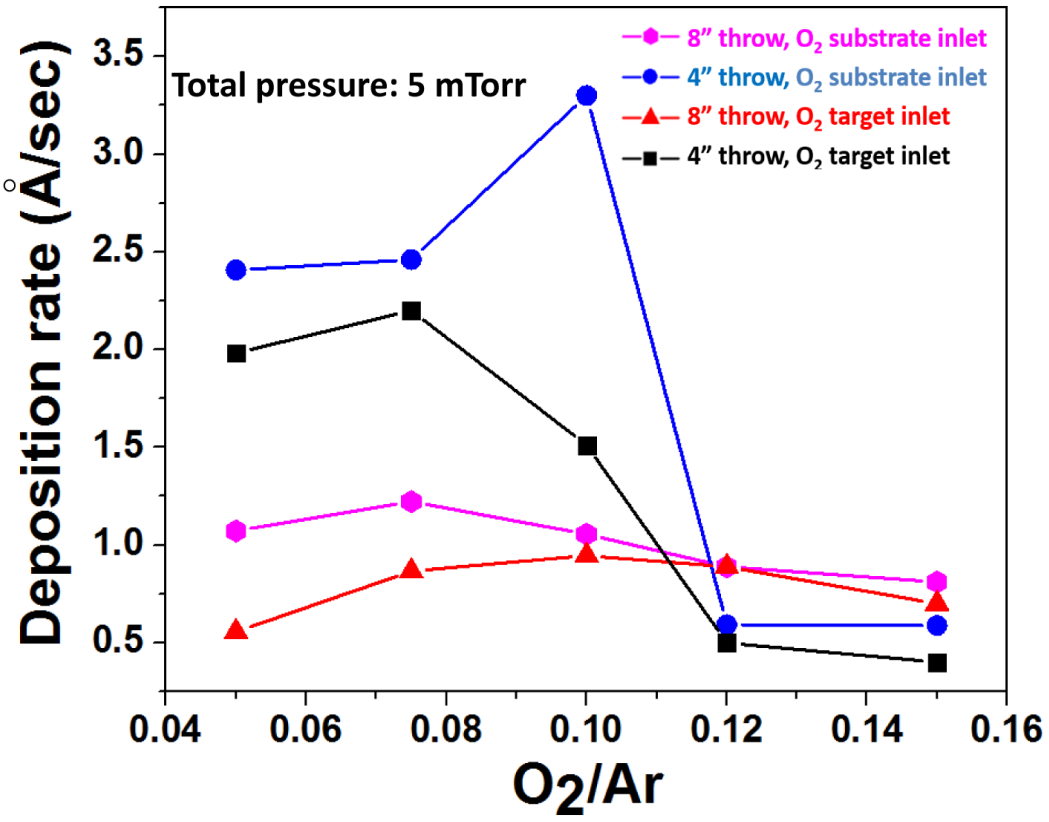

Figure 3-5. VO_x thin films deposition rate for two different oxygen inlet positions at different target to substrate throw distances (4 inch or 8 inch), with the oxygen inlet either near the substrate or near the target.

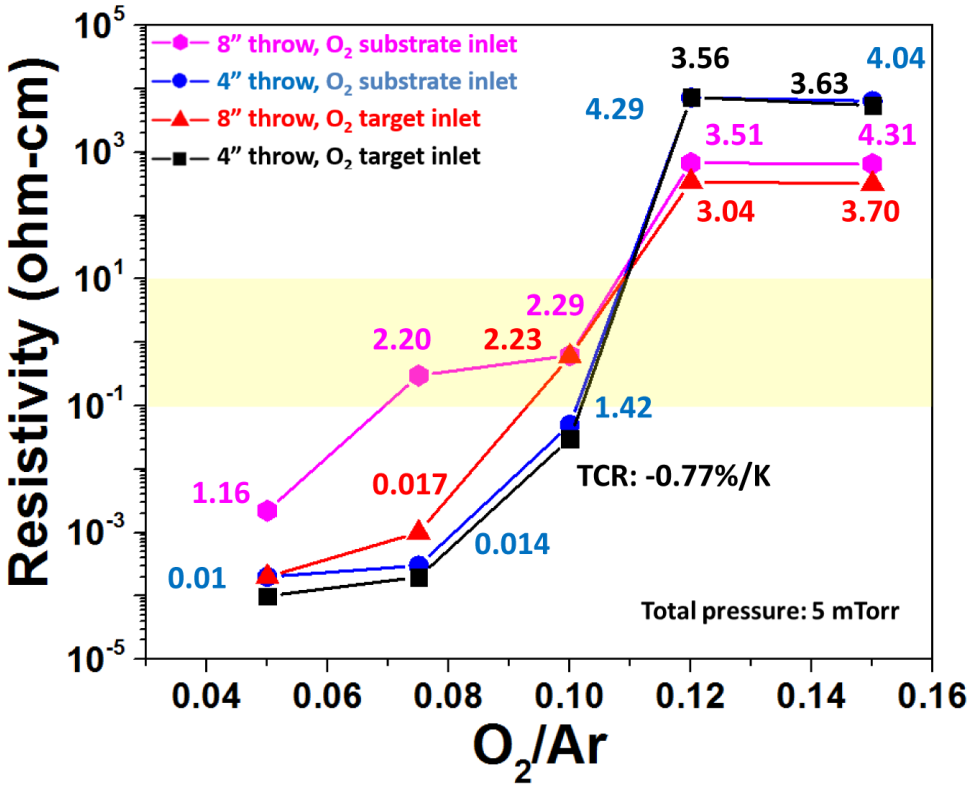

Figure 3-6. VO_x thin film resistivity and TCR for two different oxygen inlet positions at different target to substrate throw distances (4 inch or 8 inch), with oxygen inlet either near substrate or near target. The yellow region shows the resistivity range of interest from 0.1 Ω•cm to 10 Ω•cm.

Figures 3-5 and 3-6 show the VO_x thin film deposition rate, resistivity and TCR values for VO_x thin films prepared at different throw distances and oxygen inlet positions. As shown in Figure 3-5, at a fixed throw distance (either 4 inch or 8 inch), before the V target is fully oxidized (O_2/Ar inlet ratio <0.12), the deposition rate, resistivity and TCR values of VO_x films are higher when the oxygen inlet is near the substrate. Introducing oxygen near the substrate tends to favor greater oxidation at the substrate thus increasing film resistivity, while keeping the target surface more metallic than for the same O_2 ratio near the target. At high O_2/Ar inlet ratio (>0.12), the target is in the oxidized zone and the deposition rate and the VO_x film resistivity are similar for oxygen introduced near the target or near the substrate.

Figure 3-5 shows that at the lowest O_2/Ar inlet ratio, the target is in the metallic zone, and the film deposition rate is a strong function of throw distance, with larger throw distance leading to lower deposition rate. This is primarily a geometric effect, but there is also a target surface composition component. Introducing oxygen near the target leads to greater target oxidation and lower sputtering rate, so for both 4" and 8" throw distance the deposition rate is lower for oxygen introduction near the target.

As the O_2/Ar inlet ratio increases the film deposition rate first increases then decreases. The film deposition rate is a function of both the target surface oxidation and additional vanadium oxidation either in the sputtering ambient or at the substrate surface. To first order, the sputtering rate correlates with the target cathode current. From the target hysteresis curve (Figure 3-4), the sputtering rate should decrease with increasing O_2/Ar ratio. The increasing deposition rate shown in Figure 3-5 results from increasing oxidation of the depositing vanadium, that is, the film composition is changing as more oxygen is incorporated. Figure 3-6 shows that film resistivity increases greatly (> 3 orders of magnitude) as the O_2/Ar inlet ratio increases from 0.05 to 0.15, consistent with more fully oxidized vanadium. For 8" throw distance, with increasing O_2/Ar inlet ratio the increase in film thickness that results from increasing oxidation approximately counters the decreasing sputter rate and the deposition rate changes relatively little. For 4" throw distance, the increased target surface oxidation from the substrate bias plasma leads to a decreased sputtering rate that dominates, and for O_2/Ar inlet ratio greater than 0.12 the deposition rate is lower than for the larger throw distance.

The results show that when the vanadium metal target is not fully oxidized (in the metallic zone and intermediate zone), both throw distance and oxygen inlet position play important roles in the deposition rate and electrical characteristics of pulsed dc sputtered VO_x thin films. This provides a tool to deposit VO_x films in the desired resistivity range. By using a long throw distance and introducing oxygen near the substrate, it is possible to increase the sputter

ambient and substrate vanadium oxidation to increase the deposited film resistivity to the desired range while maintaining the vanadium sputtering target surface in the stable metallic zone.

3.1.4 The analysis of non-uniform oxidization of V target

As discussed in Chapter 2, during reactive magnetron sputtering, the plasma density is non-uniform across the target surface, and the discharge current density is higher in the racetrack region formed by the target magnetic field. For non-reactive sputtering, this leads to a sputtering rate that varies widely across the target surface and results in a racetrack erosion pattern for well-used targets. For reactive sputtering, the varying plasma density and sputtering rate can also lead to variations in the target surface composition [60], [63]. For example, for a constant O_2/Ar inlet ratio in the metallic or intermediate zone, higher sputtering rate leads to less target surface oxidation because the available oxygen is not sufficient to oxidize the rapidly eroding target surface. Where the sputtering rate is lower the target surface will be relatively more oxidized. As described earlier, the oxidized target surface leads to a further reduction in sputtering rate. Thus, for reactive magnetron sputtering the target surface composition is expected to be non-uniform.

Figure 3-7 shows the top-view picture and cross-section schematic of a well-used vanadium target. The racetrack region (valley) has higher consumption compared to other regions (hills). After being sputtered with 300 W of power for 15 minutes and an O_2/Ar inlet ratio equal to 0.15, the non-uniform oxidization across the vanadium target was analyzed by Raman spectroscopy in order to evaluate the stoichiometry at different spots on the target.

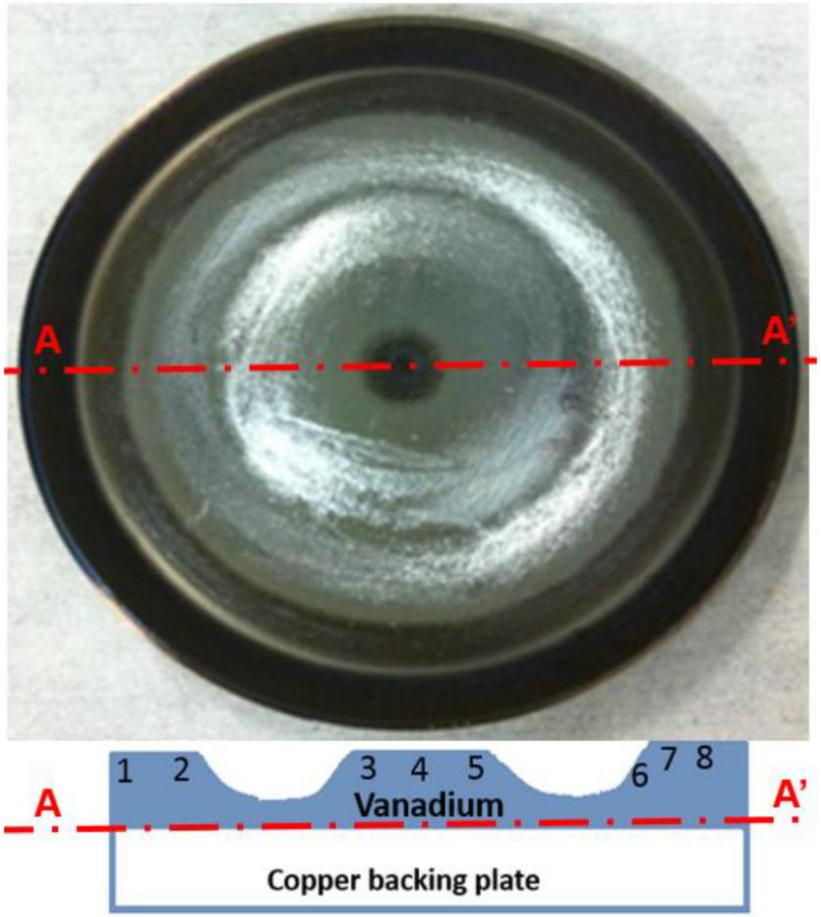

Figure 3-7. Top view and cross-section of V target. The cross-section shows positions analyzed by Raman spectroscopy.

As shown in Figure 3-8, points 1, 4 and 8 have similar Raman features. The low frequency peaks at 275 cm^{-1} suggest the existence of defective FCC nanocrystalline domains as found in previous studies correlating TEM and Raman results for numerous VO_x films [33], [36], [41]. The high frequency feature of points 4 and 8 at around 930 cm^{-1} suggest the existence of V^{5+}=O consistent with polycrystalline V_2O_5 V^{5+}=O stretching peak. The high frequency peak of point 1 shifts to 890 cm^{-1} which suggest the existence of V^{4+} double bonded to oxygen[35][70]. These target surface areas are strongly oxidized. Points 3 and 5 only show peaks at 275 $cm^{-1}$are somewhat less oxidized. Points 2, 6, and 7 show no obvious Raman VO_x features, indicating that these target surface areas are metallic.

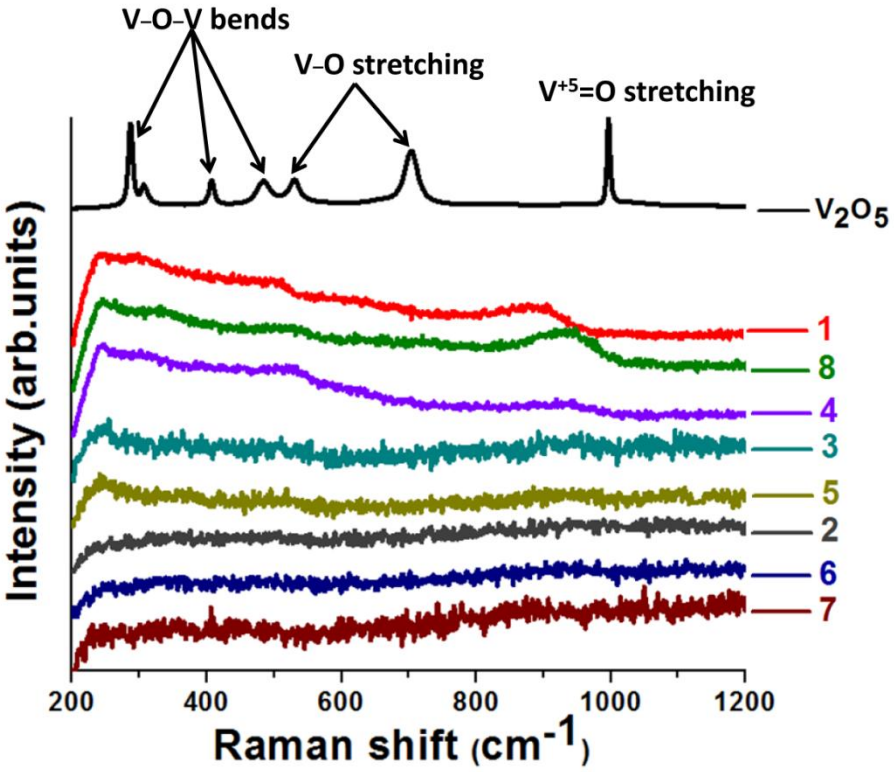

Figure 3-8. Raman spectroscopy analysis of different positions across the V target. Measured positions are shown in Figure 3-7.

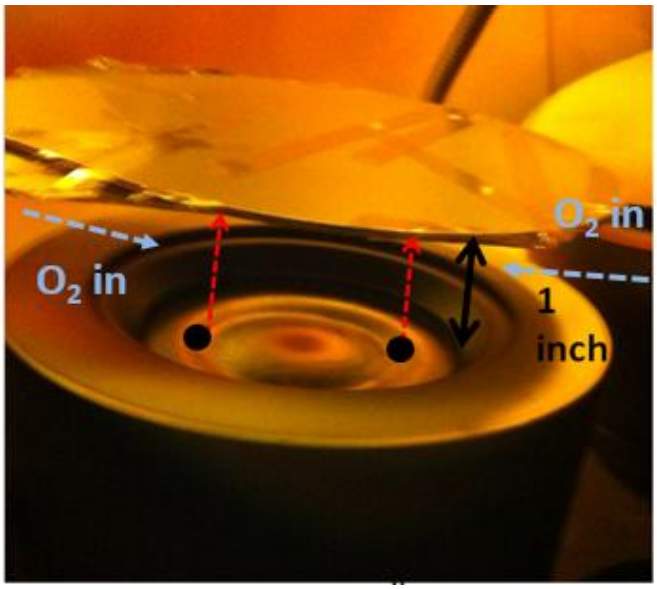

Figure 3-9. Picture of non-rotated substrate mounted on the target shutter with 1-in throw distance.

To study the V target non-uniform sputtering and composition effects on the deposited VO_x thin films, non-rotated and rotated films were prepared at different throw distances at 5 mTorr. As shown in Figure 3-9, non-rotated substrate was mounted on the target shutter to collect data for 1-inch throw distance. For the 1-inch throw distance the oxygen was introduced in near the target with O_2/Ar inlet ratio equal to 0.15. As shown in Figure 3-10, the resistivity of the deposited film is lower at the center and higher at the edges. This is expected, because in this close spaced sputtering configuration, gas that reaches the target center must pass through the edge region. In doing so much of the oxygen is consumed and the oxygen-depleted Ar that reaches the target center results a lower resistivity for the sputtered VO_x thin film. The non-rotated and rotated films at 4-inch and 8-inch throw distance were deposited with an O_2/Ar inlet ratio equal to 0.1 on 6 inch wafers with oxygen inlet near the substrate. The resistivity of a non-rotated VO_x film varied from 0.02 to 0.2 Ω•cm at a 4-inch throw distance, and from 0.4 to 0.8 Ω•cm at an 8-inch throw distance. The deposited films' uniformity can be further improved by rotating the substrate during deposition. At a 4-inch throw distance, the rotated film resistivity varied from 0.017 to 0.07 Ω•cm, whereas at an 8-inch throw distance film resistivity varied from 0.6 to 0.86 Ω•cm. The resistivity mapping of non-rotated and rotated samples at different throw distance are shown in Figure 3-11. This suggests the longer throw distance allows target non-uniformities to be averaged and results in improved uniformity of deposited films.

Figure 3-12 shows the TCR of VO_x films deposited by reactive pulsed-dc magnetron sputtering is comparable to films deposited by ion beam deposition. The results demonstrate that by optimizing process parameters, reactive pulsed-dc magnetron sputtering can be an industrial alternative for depositing VO_x films for microbolometers.

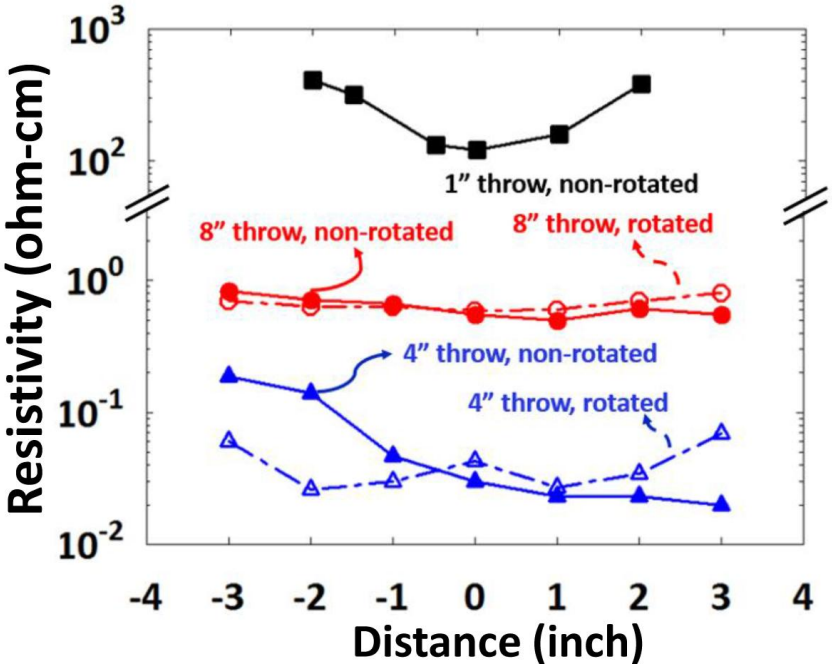

Figure 3-10. Resistivity uniformity for VO_x films prepared at different throw distances (1 inch, 4 inch, and 8 inch).

At 1 inch throw distance, VO_x deposited on 4 inch non-rotated substrate at O_2/Ar=0.15. At 4 and 8 inch throw distances, VO_x deposited on non-rotated and rotated 6 inch wafers at O_2/Ar=0.1.

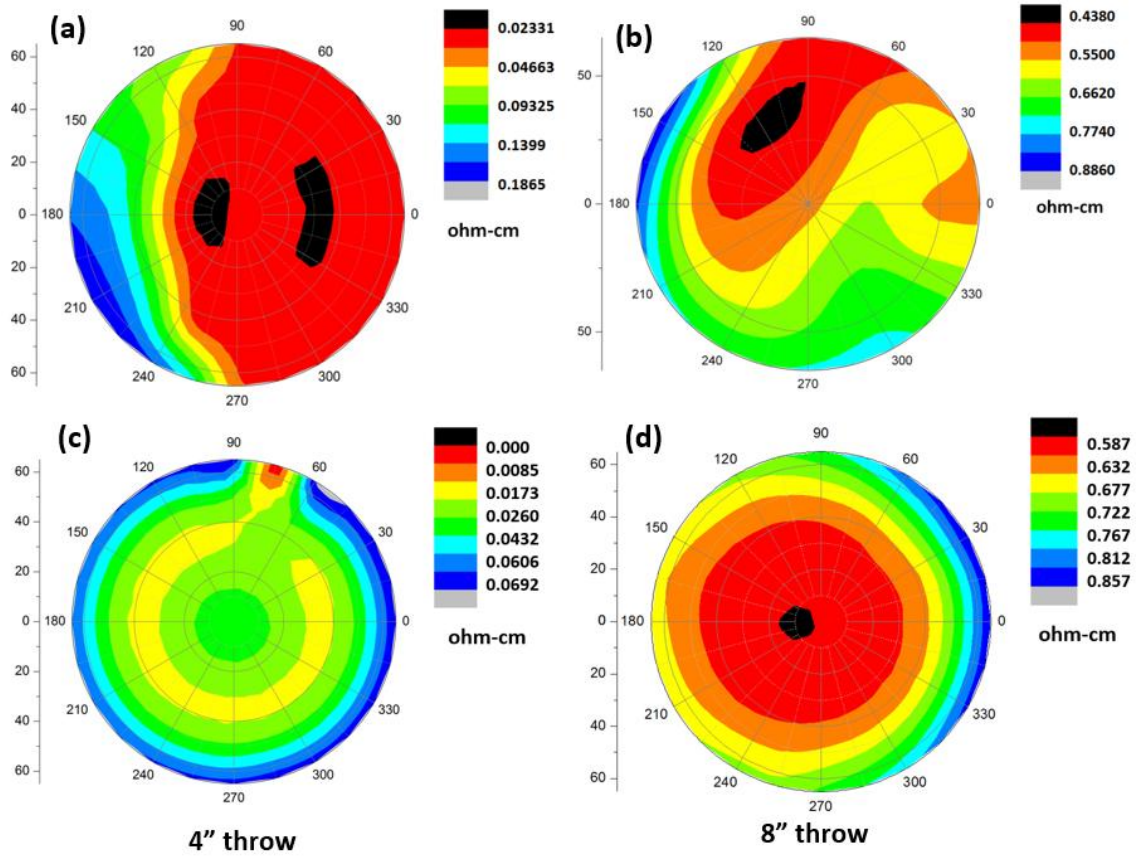

Figure 3-11. Resistivity mapping of VO_x films when oxygen inlet position near substrate at a (a) 4 inch throw distance non-rotated (b) 8 inch throw distance non-rotated (c) 4 inch throw distance rotated and (d) 8 inch throw distance rotated. The oxygen to Ar inlet ratio is 0.1 and substrate bias is -240V.

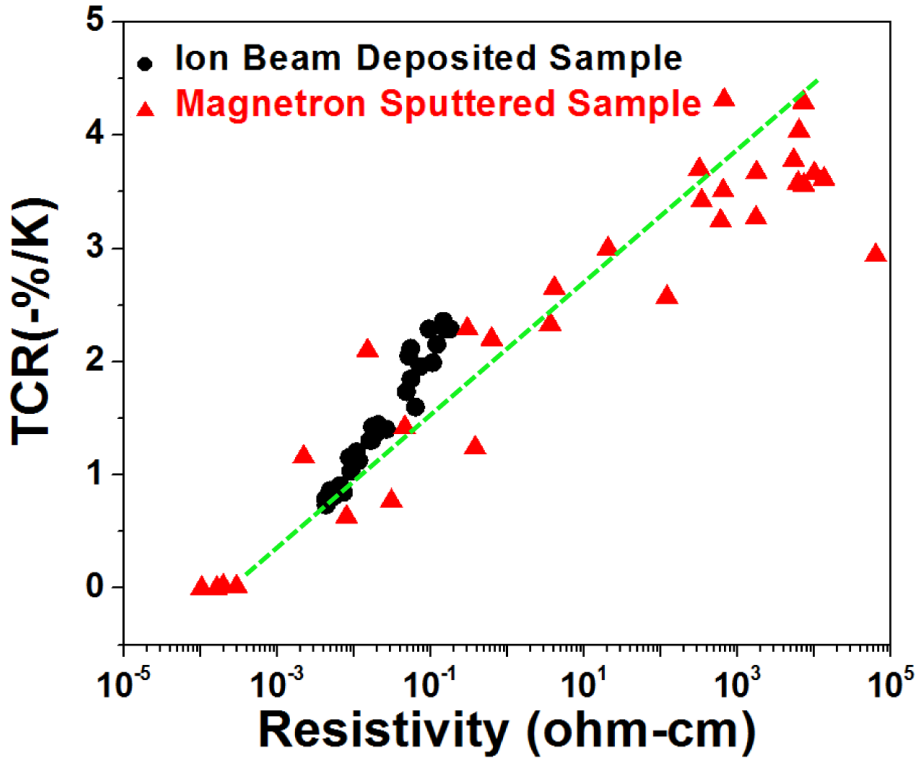

Figure 3-12. TCR versus resistivity of VO_x thin films prepared by ion beam deposition1 and reactive pulsed-dc magnetron sputtering

3.2 VO_x thin films deposited by co-sputtering of V and V_2O_5 targets

The target hysteresis, non-uniform oxidization of metallic target surface, oxygen delivery effects, throw distance, and processing pressure all influence the controllability of the sputtering process. Previous work has shown that the process window is very narrow for depositing VO_x thin films of a specific composition by using one metallic V target in the magnetron pulsed dc reactive sputtering process. Will the co-sputtering of metallic target and oxide target improve the controllability and repeatability of the process? With low oxygen flow rate, the V target is sputtering low resistivity FCC VO_x constituent and the V_2O_5 target is sputtering high resistivity amorphous V_2O_5 constituent. In this section, the VO_x were deposited from metallic V and V_2O_5

targets by co-sputtering, and different processing parameters such as substrate bias and oxygen flow rates were varied.

In this set of experiments, the V target was pulsed dc biased by 300 W and V_2O_5 was applied with 200 W of rf power. The processing pressure was fixed 5 mTorr and total gas flow rate was 18 SCCM. The throw distance was 8 inch and oxygen inlet was introduced through a gas ring 1 inch below substrate.

The deposited films resistivity and TCR values were mapped with and without substrate bias. The oxygen to Ar ratio is 0.05 and the V target was in the metallic regime. Figure 3-13 (a) and (b) show that without substrate bias, the deposited film resistivity varying from 2.25-1.72 Ω•cm whereas TCR from negative 2.92-2.36 %/K from wafer center to perimeter. This phenomenon corresponds to Gauntt's [39] observation of a VO_x sample deposited by one V target in reactive environment without substrate bias when rotation speed is 10 rpm. Because rO_2 is 0.05 and V target is at the metallic regime, the sputtering rate of V target is larger than V_2O_5 target. The deposited film is mainly determined by the sputtered V species reacting with O_2 on substrate. The decreasing of resistivity from center to edge is presumed to be due to the different time for reaction to occur on the substrate [39]. As is the usual trend, the TCR is decreasing when film resistivity decreases.

Figure 3-13 (c) and (d) show the deposited films with substrate bias and all the other processing conditions are the same. From the wafer center to perimeter, the resistivity varies from 0.21-0.42 Ω•cm. This opposite behavior suggests that the rf self-bias on substrate is affecting the substrate during the deposition. With substrate bias, the lower resistivity VO_x region shows higher TCR values, indicating the change of microstructure of VO_x and enhanced electrical properties.

Although using dual targets for co-sputtering has the potential to improve the repeatability of process by controlling the V target in metallic regime, the resistivity and TCR

mapping indicates that the deposited film on a 6-inch wafer is not uniform, even when the substrate is rotated at 10 rpm. Will the uniformity across the wafer be improved by increasing of oxygen to Ar ratio? As shown in Figure 3-14, when the rO_2 increases to 0.075, the film deposition rate increases to 1.8 Å/sec, which is 35% higher than that for a film sputtered from single V target under the same processing parameters. However, when rO_2 further increases to 0.1, the film deposition rate decreases indicating the beginning of oxidization of the V target. In order to prevent the V target from being oxidized and keep the higher deposition rate, rO_2 should not be greater than 0.1. When the rO_2 is fixed at 0.075, the VO_x film deposited by co-sputtering resistivity and TCR values are mapped. By comparing Figure 3-15 (a) and (b) to Figure 3-13 (c) and (d), the VO_x deposited with $rO_2 = 0.075$ shows better uniformity compared to the one deposited $rO_2 = 0.05$. Figure 3-11 shows the resistivity versus TCR values of VO_x thin films deposited by co-sputtering of V and V_2O_5 targets under different conditions, showing comparable properties with VO_x prepared by Wood using IBD [3].

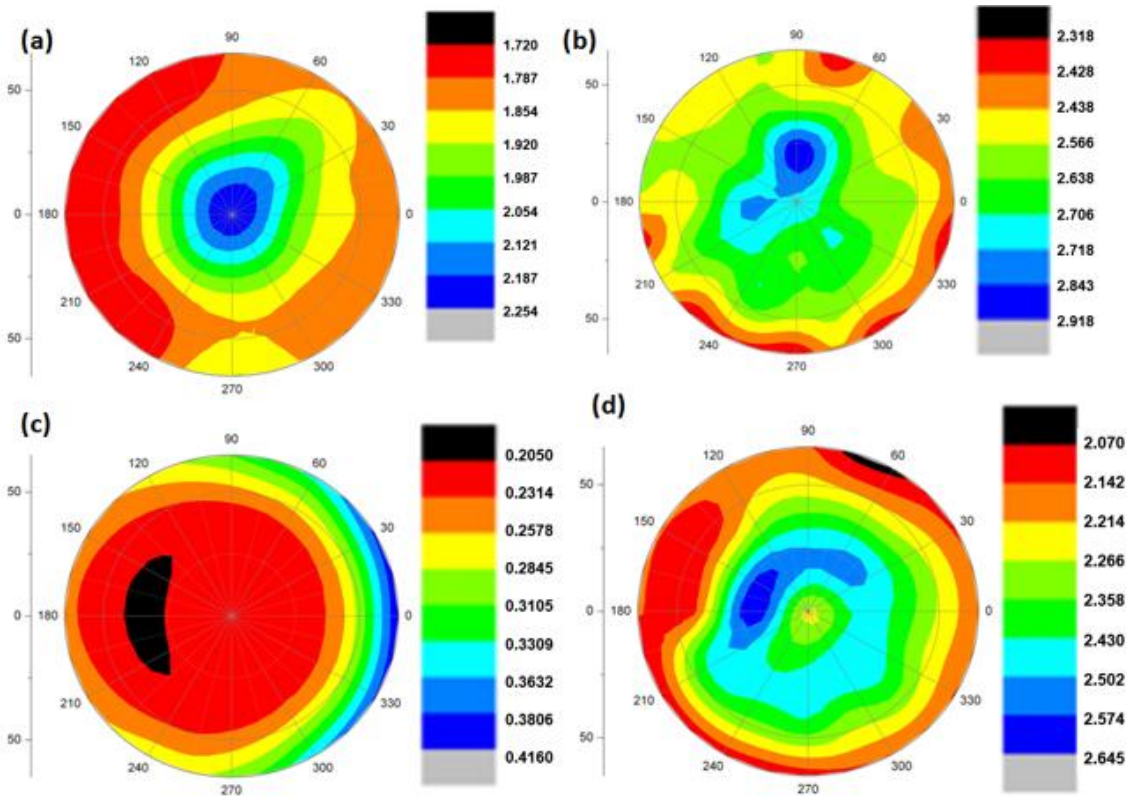

Figure 3-13.6 inch wafer mapping of VO_x deposited by co-sputtering of V and V_2O_5 targets, rO_2 is 0.05 and substrate is rotated at 10 rpm: (a) resistivity and (b) TCR mapping without substrate bias; (c) resistivity and (d) TCR mapping with 25 W substrate bias. Resistivity unit is Ω•cm and TCR unit is -%/K.

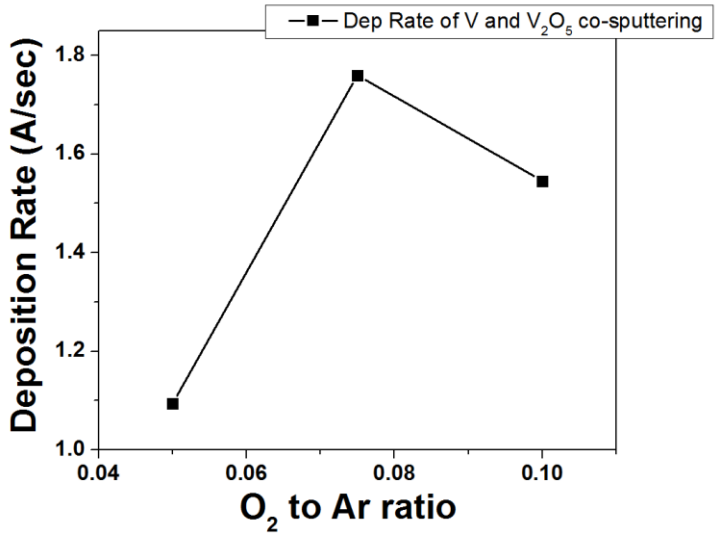

Figure 3-14. The VO_x films deposition rates (measured at the center of 6" wafer) change as a function of rO_2, deposited by V and V_2O_5 co-sputtering.

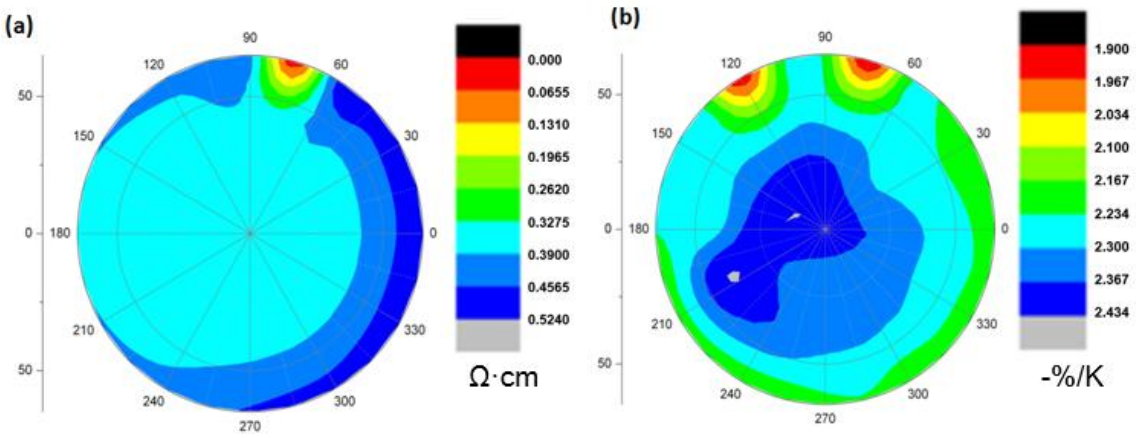

Figure 3-15. VO_x films (a) resistivity and (b) TCR mapping deposited by V and V_2O_5 co-sputtering when rO_2 is 0.075.

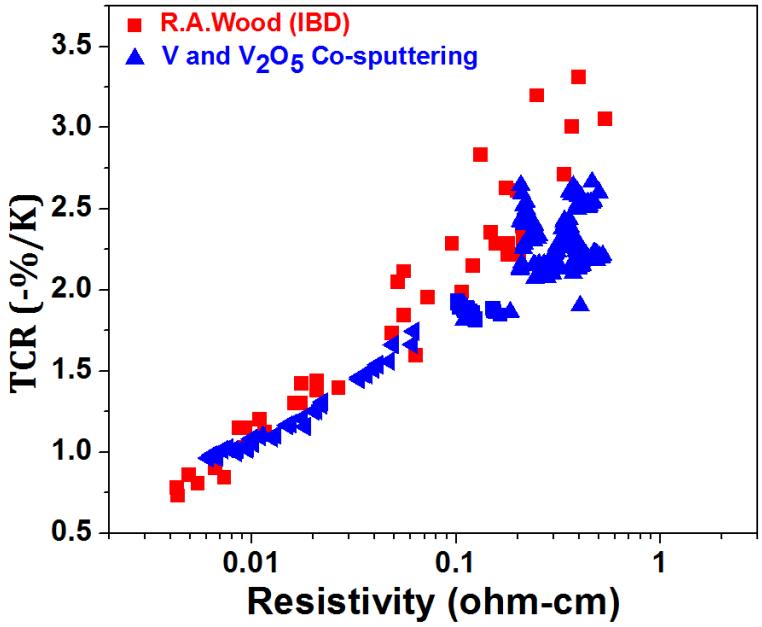

Figure 3-16. TCR vs. Resistivity of VO_x films deposited by co-sputtering of V and V_2O_5 targets show comparable properties with VO_x prepared by Wood IBD method [3].

3.3 VO_x thin films deposited using a vanadium carbide (VC) target

In addition to co-sputtering from metallic V and V_2O_5 target, different targets such as vanadium carbide (VC), and vanadium oxide (V_2O_x) were also investigated to sputter VO_x thin films for infrared imaging. In the first section, VO_x thin films were sputter deposited from a vanadium carbide (VC) target on 100nm thermal oxide substrates. All the films were deposited for 900 sec and the VC target was pulsed dc biased with 300 W of power. The substrate was rf biased by -240 V (25W). The total gas flow rate was fixed at 18 SCCM whereas the processing pressure was 5 mTorr.

As shown in Figure 3-17, similar to metallic V target, the VC target shows hysteresis behavior by varying the oxygen to Ar inlet ratio. Even though the power applied on the target remained the same, the cathode current of the VC target current was lower than the pure V target due to lower conductivity (about half of pure V target) [71], indicative of lower deposition rate. Table 3.1 shows the deposition rate, resistivity, and TCR values of VO_x deposited from the VC target with oxygen to Ar ratio varied from 0.05 to 0.2. Though the cathode current and deposition rate change gradually, the deposited VO_x resistivity increases abruptly from metallic to high resistive. The poor process control and low deposition rate suggest that reactive sputtering from a VC target may not be a good option to deposit VO_x for microbolometers.

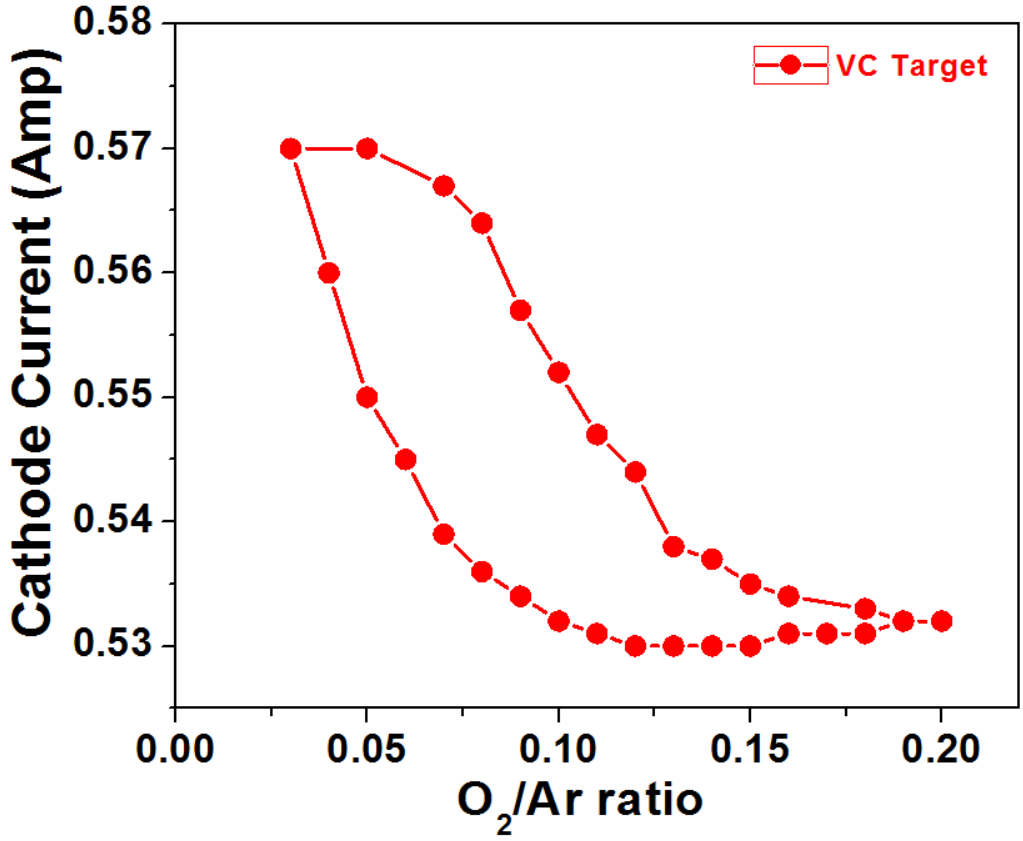

Figure 3-17. Hysteresis loop of the VC target monitored by cathode current

Table 3-1. Deposition rate, resistivity, and TCR values of VO_x sputtered from a VC target

O_2/Ar ratio	Deposition Rate (Å/sec)	Resistivity (Ω•cm)	TCR (%/K)
0.05	0.8	9.13E-4	+0.18
0.1	0.7	8.9E4	-0.35
0.2	0.7	2.9E4	-4.01

3.4 VO_x thin films deposited from a V_2O_5 target or a V_2O_x target

Previous study shows that increasing the substrate bias on VO_x thin films (reactive sputtered from a V target) increases film internal strain by nanotwin formation; and the resistivity, TCR and film growth rate keep decreasing with increasing substrate bias [46]. In order to avoid the process complexity introduced by reactive sputtering, in this section, the substrate bias effects on VO_x thin films sputtered from a V_2O_5 target and a V_2O_x target without additional O_2 is discussed. Four samples were deposited from a V_2O_5 target applied with 300 W RF power at different substrate bias. Total Ar gas flow rate was at 18 SCCM and processing pressure was 5 mTorr.

Figure 3-18 shows the deposition rate, resistivity, and TCR decrease with an increasing of substrate bias. The deposition rate of VO_x by a V_2O_5 target with 25 W substrate bias is about 1/3 of the rate when using a V target under the same conditions. Figure 3-13 also shows that the film with resistivity at 0.1 Ω•cm only has a TCR of -0.4 %/K, which is much lower than its counterpart (-2.5 %/K) deposited by reactive sputtering of a metallic V target. The low deposition rate and poor bolometric properties of these samples suggest it is not an optimal method for industrial fabrication.

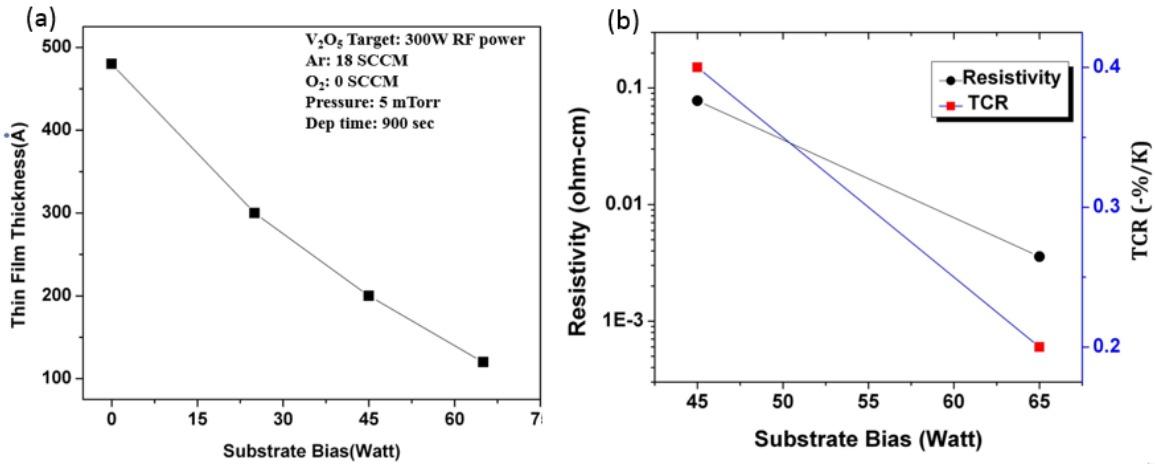

Figure 3-18. VO_x thin film thickness, resistivity and TCR values sputtered from the V_2O_5 target change as a function of substrate bias.

VO_x thin films sputter deposited from a V_2O_x target at different substrate bias were also studied. Before the films were deposited, the hysteresis behaviors of the V_2O_x target were assessed by monitoring the cathode current. The V_2O_x target was pulsed-dc biased with 300 W power and oxygen to Ar ratio varied from 0 to 0.25. As shown in Figure 3-19, under three different processing pressures (1, 5, and 20 mTorr), the cathode current shows no obvious hysteresis behavior as a function of oxygen to Ar inlet ratio, indicative of good process control. However, the target current is lower than the metallic target under the same processing parameters, suggesting lower deposition rate. Though there is no hysteresis behavior of the V_2O_x target, similar to the metallic V target, the cathode current of the target change more gradual with increasing of oxygen to Ar ratio, indicating better control of deposited film composition and resistivity.

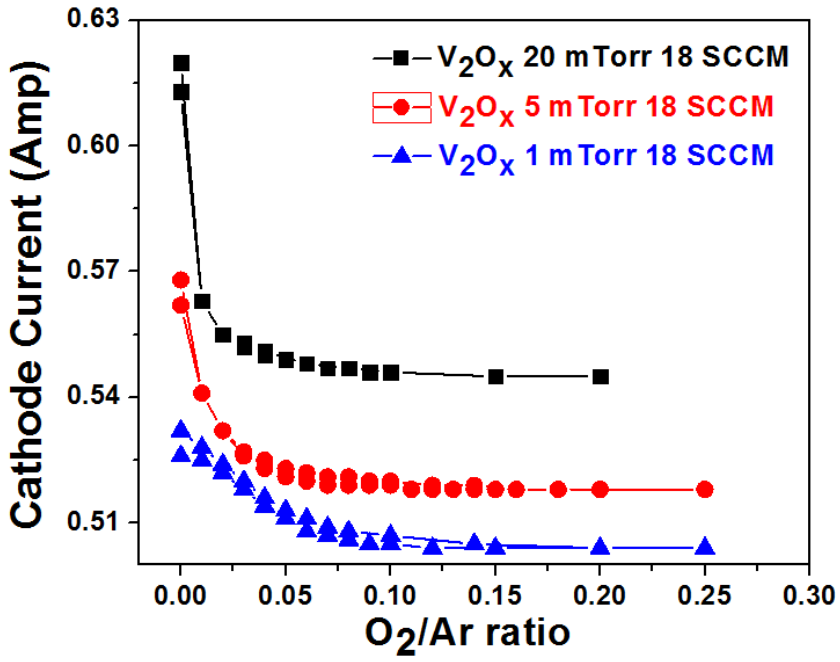

Figure 3-19. Hysteresis curve of V_2O_x target under different processing pressures.

Figure 3-20 shows the VO_x thin films deposited from the V_2O_x target with different substrate bias. Similar to VO_x deposited from the V_2O_5 target, the increasing of substrate bias during deposition decreases deposited films resistivity and TCR. The resistivity of the film deposited at 45 W substrate bias is 0.03 Ω•cm and the TCR is -1.3 %/K, which about half of the VO_x is prepared with pure V target at the same resistivity. Even though the V_2O_x target suggests possible good process controllability, the VO_x thin film deposited from this target have lower deposition rate and limited TCR value compared to the one prepared from the metallic V target.

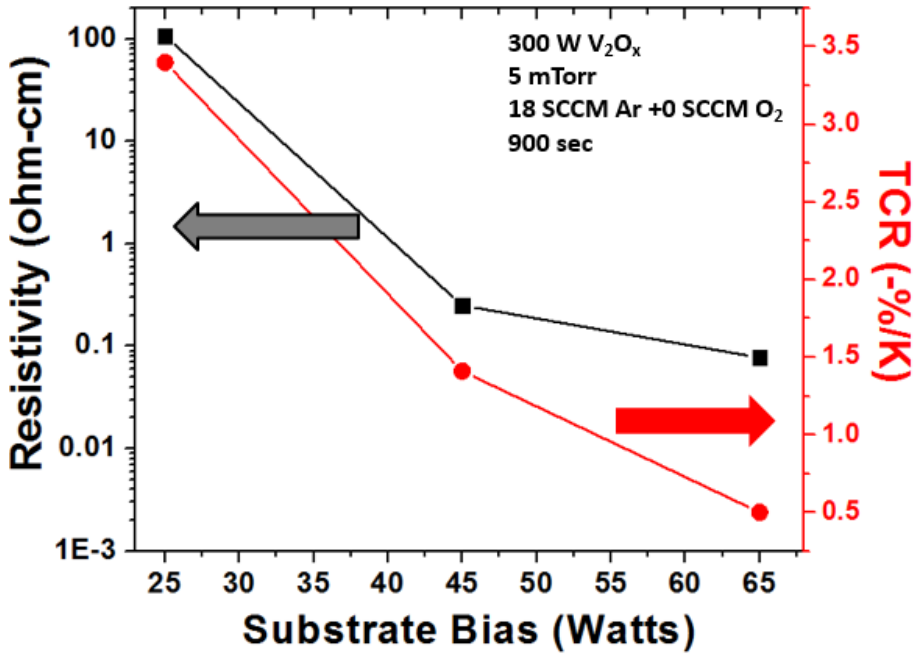

Figure 3-20. Resistivity and TCR values of VO_x thin films sputter deposited from V_2O_x target with different substrate biases.

3.5 VO_x thin films reactive sputtered from a V target with oxygen and hydrogen

Previous study shows post-deposition H+ implantation to deposited VO_x thin films increase both film resistivity and TCR. [41] In this section, in order to study the hydrogen effects

on VO_x thin films properties, two samples were prepared with and without hydrogen introduced into the plasma during deposition. Both of these VO_x samples were reactive sputtered from the metallic V target with 300 W pulsed-dc power supply and -240 V substrate bias at 5 mTorr. The first sample was deposited in a mixture of Ar and O_2, and the total flow rate was 18 SCCM and O_2/Ar inlet ratio was 0.05. The second sample was deposited with the same processing parameters except H_2 was introduced into the chamber during deposition, and both H_2/Ar and O_2/Ar ratio was 0.05.

As shown in Figure 3-21, the resistivity versus TCRs of these two samples (different points measured across 6-in wafer) were plotted and compared to ion beam deposited sample. The graph shows that though the resistivity does not change much with introducing of H_2 during deposition, the TCR reduced about 20-25%, which is unsuitable for microbolometer usages. This result is quite different from the earlier report of H+ implantation.

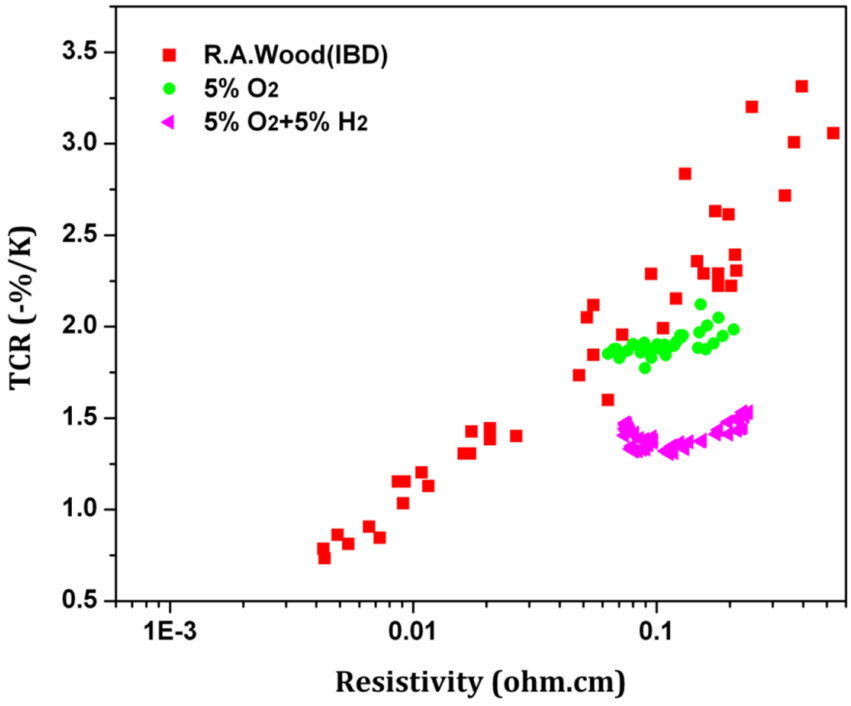

Figure 3-21. TCR versus resistivity of VO_x thin films prepared by ion beam deposition and reactive pulsed-dc magnetron sputtering.

3.6 Conclusion

In this Chapter, the potential for reactive pulsed-dc magnetron sputtering of nanocomposite VO_x thin films for microbolometers was discussed. Processing pressure, throw distance, and the delivery of oxygen have large effects on the deposition rate and electrical properties of VO_x films. To deposit uniform VO_x with characteristics suitable for thermal images long throw distance and oxygen inlet position near the substrate are useful. Lower processing pressure leads to more gradual transition of target surface oxidization and better control of deposited film properties, but also results in lower deposition rate. Reactive co-sputtering of metallic V and V_2O_5 target increase the vanadium oxide thin film deposition rate and also improve film uniformity, which might be an alternative industrial method to prepare VO_x microbolometer thin films.

Different methods were also investigated in a "quick-and-dirty" way improve processing controllability. However, the VO_x prepared from a V_2O_5 target, V_2O_x target, and VC target show lower deposition rate and limited bolometric properties compared to the ones reactive sputter deposited from a metallic V target. Introducing of hydrogen into chamber plasma during deposition reduces as-deposited VO_x TCR values but not resistivity. These initial results did not provide any results that would indicate that they are more suitable for microbolometer industry to fabricate VO_x thin films than the reactive sputtering of a vanadium target with Ar and oxygen.

Chapter 4

High Resistivity and High TCR VO_x Thin Films Prepared by Biased Target Ion Beam Deposition

In this chapter, VO_x thin films were prepared by the biased target ion beam deposition system (BTIBD) mentioned in Chapter 2. Unlike magnetron sputtering, this system utilizes uniform sputtering of targets implying a more uniform stoichiometry of sputtered species. As mentioned in Chapter 2, a lower energy plasma (<25 eV) is remotely generated by an end-Hall ion source, the three targets are independently biased by three pulsing units, and the oxygen partial pressure is controlled by a residual gas analyzer installed on the top of processing chamber. The independent controllability of the ion source, target, and reactive gas of the BTIBD system provides flexibility in the processing parameters that can be used to engineer deposited film properties. In this work, the deposited film deposition rates and electrical properties are varied by controlling the oxygen partial pressure, oxygen inlet position, source Ar flow rates, target pulse width, and target bias voltage. Results for VO_x thin films doped with Mo are also investigated. VO_x films deposited by BTIBD system show high TCR (<-4.5%/K), high resistivity (>1000 Ω•cm) and good thermal stability. These prepared high resistivity and high TCR VO_x thin films are candidates as active sensing layers for vertical-structure pixels of microbolometers, which will be discussed in the last section of chapter.

4.1 The effects of oxygen partial pressure and oxygen inlet position

VO_x thin films were prepared by the BTIBD system in a mixture of Ar and O_2 ambient. Three metallic V targetswith 99.99% purity were pulsed-dc biased at -800 V with 10 kHz pulse repetition rate and 1μsec pulse width. The end-Hall ion source discharge current was set to be 7.5 Amp and discharge voltage was about 40 V. The oxygen partial pressure (ppO_2) was monitored

and controlled by a residual gas analyzer and was varied from 5E-7 to 2.6E-6 Torr. The total chamber pressure was set by the Ar and O_2 flows (no active pressure control) and was approximately 0.74 mTorr. The ion source and hollow cathode Ar flow were 60 and 10 SCCM respectively. The trends for the as-deposited VOx thin films deposition rate, resistivity, and TCR as a fuction of oxygen partial pressure, and oxygen inlet position is discussed.

Figure 4-1 (a) and (b) show that when oxygen is introduced through the ion source, the cathode current for the three targets, the deposition rate, and the electrical properties of the deposited VO_x change as a function of ppO_2. With increasing ppO_2, the cathode current decreases linearly, indicating continous oxidation of all three targets. The film deposition rate is related to the target bias current. When the oxygen inlet position is near targetposition 1, a similar trend has been observed (Figure 4-1(c)). Though the target cathode current and film deposition rate decrease gradually with increasing the oxygen partial pressure, the film resistivity increasesabruptly from 1E-3 to 1E3 Ω•cm with only a 1E-7 Torr increase of ppO_2.When oxygen is introduced through the ion source, the resistivity threshold is at an oxygen partial pressure of 6E-7 Torr, and 8E-7 Torr when oxygen is near target position 1. This may be because when the oxygen inlet is in the end-Hall source, the target is oxidized faster due to a higher oxygen species energy since oxygen is used as working gas with Ar. However, unlike magnetron reactive sputtering that was discussed in Chapter 3, the oxygen inlet position does not effect the as-deposited VO_x propreties significantly. Figure 4-1 shows that the as-deposited VO_x films have resistivity in the range of 2E3 Ω•cm to 1E5 Ω•cm and TCR from -3.9 %/K to -5.2 %/K. The VO_x films with resistivity lower than 1E-3 Ω•cm have TCR than -0.06 %/K, which is not of interest for microbolometer applications.

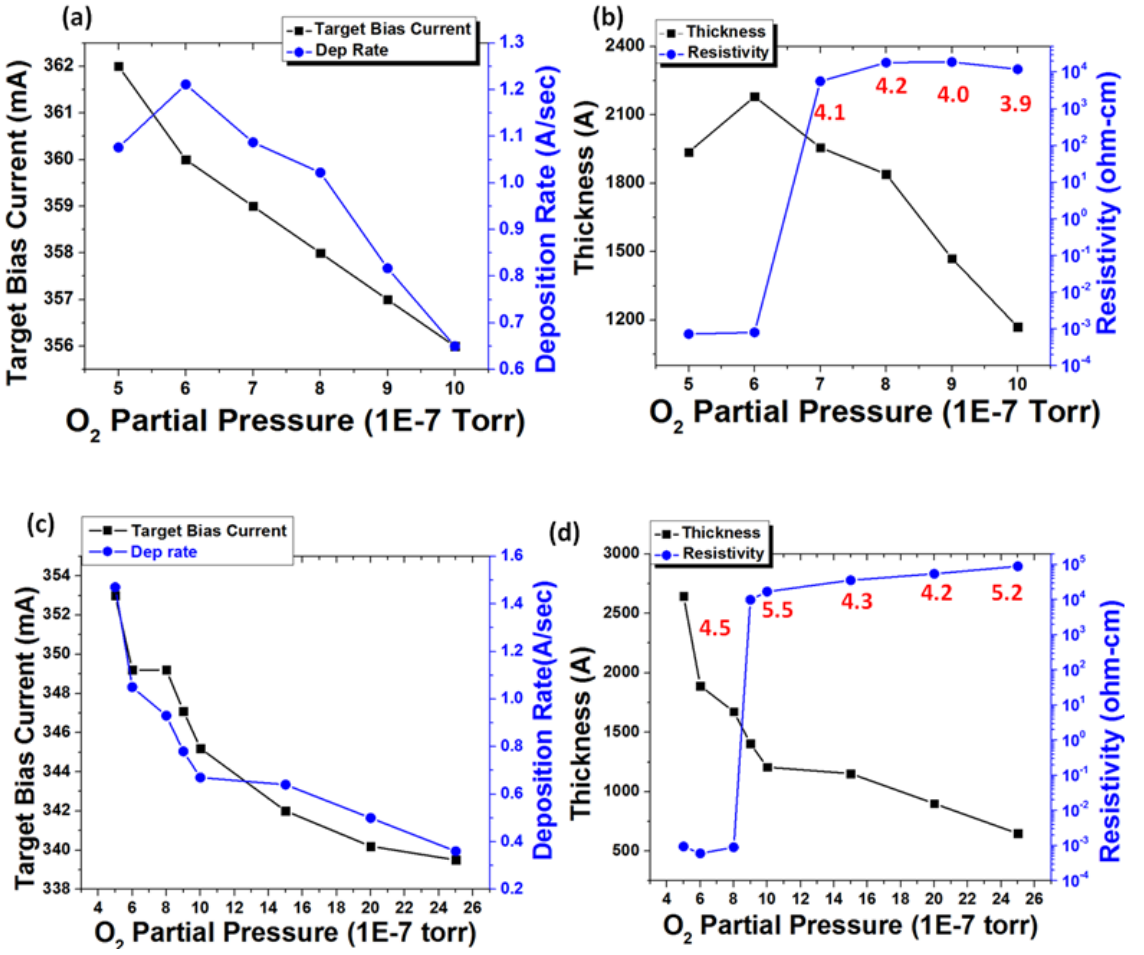

Figure 4-1. VO_x thin films properties change as a function of oxygen partial pressure: a) and b) when oxygen inlet at end-hall; b) and c) oxygen inlet near target VO_x thin films deposited with three V targets with substrate bias voltage -800 V and pulse width/pulse period 1 µsec/100 µsec. The HC flow rate is 10 SCCM whereas the ion source Ar flow rate is 60 SCCM. The discharge current is 7.5 Amp and discharge voltage is around 40 V. The numbers in red are the TCR values with unit of -%/K.

4.2 The effects of source Ar flow rate (processing pressure)

As mentioned in Chapter 2, the Ar+ ions generated by the ion source are about 60-70% of the ion source discharge voltage. Since in our BTIBD system the ion source discharge current is fixed to be 7.5 Amp, the discharge voltage is a function of source Ar flow rate: the higher the Ar flow rate the lower the discharge voltage. In this section, the effects of source Ar flow rate on deposited VO_x thin film deposition rate and electrical properties are discussed. Similar to last section, three V targets were biased with -800 V with 10 kHz frequency and 1μsec pulse width. Hollow cathode Ar flow was 10 SCCM, and source Ar flow rate was set to be 30 SCCM and 80 SCCM. Ion source discharge current was fixed at 7.5 Amp. The discharge current was 7.5 Amp and discharge voltage was around 70 V when source Ar was 30 SCCM and 35 V when source Ar was 80 SCCM. Oxygen was introduced near target position 1.

Figure 4-2 (a) shows that when the source Ar flow rate is 30 SCCM, with increasing ppO_2, the deposition rate first increases then decreases. The initial increase of the deposition rate suggests the three V targets have not fully oxidized yet, and the sputtered V species actively react with oxygen in the chamber plasma and near the substrate. Further increase of ppO_2 leads to oxidization of the three V targets and hence, decrease of film deposition rate. Again, the film resistivity increases abruptly from about 1E-3 to 2000 Ω•cm when ppO_2 increases from 1.2E-6 to 1.3E-6 Torr. Figure 4-2(b) shows that at high source Ar flow rate (80 SCCM), the film deposition rate decreases continuously with increasing ppO_2, and the resistivity again increases from 1E-3 to 1E3 Ω•cm when ppO_2 changes from 7E-7 to 8E-7 Torr. The result shows that the resistivity threshold increases to higher ppO_2 with an increase in the source Ar flow rate. This is probably due to higher Ar flow rate depletes the oxygen concentration near the V target surface at the same ppO_2. Thus higher ppO_2 is needed to fully oxidize the target surface.

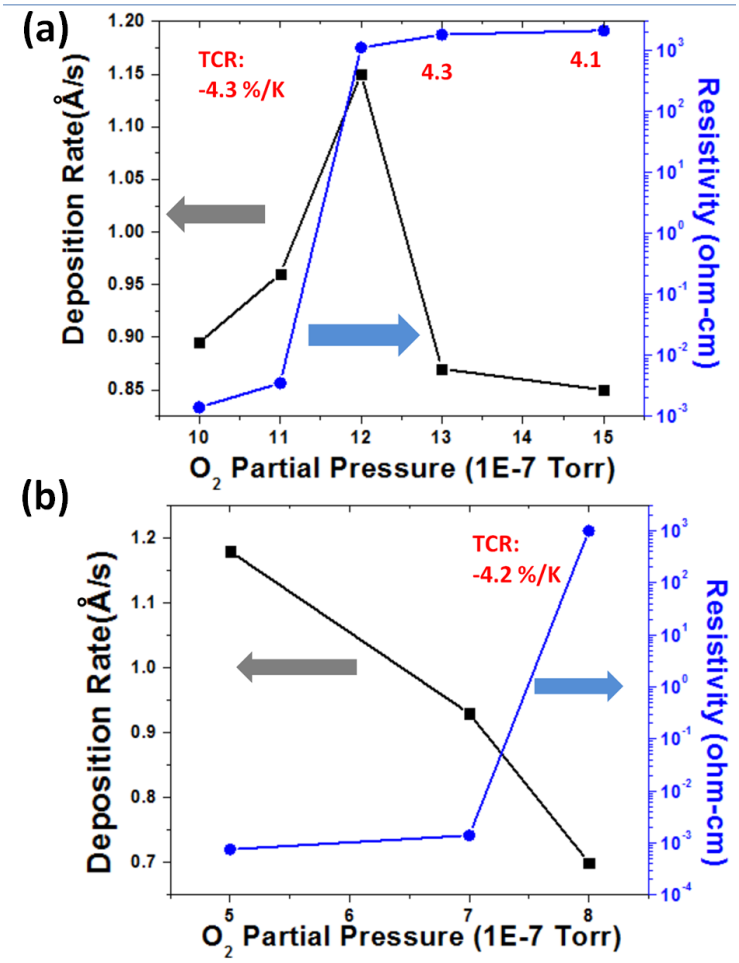

Figure 4-2. VO_x thin films properties change as a function of oxygen partial pressure (a) Source Ar flow rate set to be 30 SCCM (total pressure 4.7E-4 Torr) (b) source Ar flow rate set to be 80 SCCM (total pressure 8.9E-4 Torr). Oxygen inlet position is near target 1. VO_x thin films deposited with three V targets with substrate bias voltage -800 V and pulse width/pulse period 1 µsec/100 µsec. The HC flow rate is 10 SCCM whereas the source Ar flow rate is either to be 30 SCCM or 80 SCCM.

4.3 The effects of target bias voltage

In order to investigate the effect of bias voltage on the composition and electrical properties of VO_x films, the voltage of all three targets was varied from -300 V to -800 V. The oxygen inlet was fixed near Target 1, and the hollow cathode Ar flow rate was 10 SCCM while the source Ar was 60 SCCM.

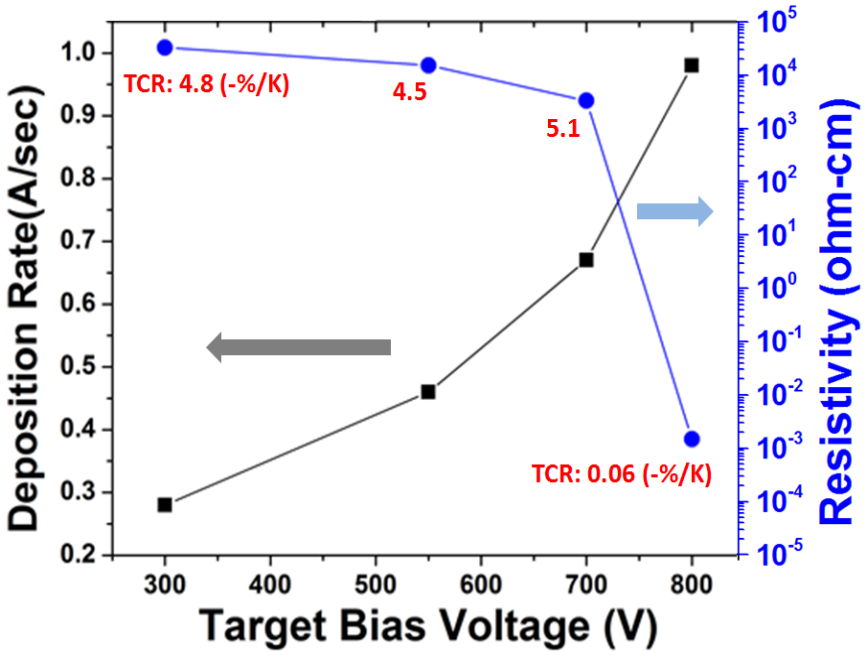

Figure 4-3. VO_x film deposition rate and resistivity change as a function of increasing target bias voltage.

Figure 4-3 shows when all three targets pulse width/pulse period is 1/100 µsec and ppO_2 remains at 8E-7 Torr, the deposition rate increases as a function of target bias voltage. The increase in deposition rate is likely due to higher bombardment energy of Ar^+ which leads to a higher sputtering yield. When bias increases from -300 V to -700 V, the VO_x films resistivity drops two orders of magnitude, indicating the increasing target bias voltage removes the oxide layer of oxidized targets more efficiently thereby allowing lower valence or more metallic V species arrive at the substrate surface. When target bias voltage increases form -700 V to -800 V, the deposited film resistivity dramatically drops from 1E3 Ω•cm to 1E-3 Ω•cm. This is corresponding to previous observation and indicates the strong threshold for sputtering of metal versus oxide, which is typical in reactive sputtering. For this ppO_2, VO_x films made with a bias between -300 and -700 V have a TCR higher than -4.5%/K are prepared with resistivity higher than 2E3 Ω•cm.

4.4 The effects of pulse width on biased targets

Results from last few sections show that in this BTIBD system, even when adjusting ppO_2, oxygen inlet position, source Ar flow rates, and target bias voltage, it is hard to prepare VO_x thin films in the resistivity range of 0.01-10 Ω•cm. In Chapter 3 we discussed that the co-sputtering deposited VO_x films from the metallic V and V_2O_5 targets showed good bolometric properties in the resistivity range of 0.01 to 10 Ω•cm. This begs the question can the composition and properties of BTIBD prepared VO_x thin films be controlled by using multi-target co-sputtering? By controlling the pulse width of three targets, the surface oxidized level of the target surface can be controlled. Thus, in this section, three V targets were biased at the same voltage but with a different pulse width individually. All the three targets were biased with -800 V at a 10 kHz frequency, and the pulse width was used to control the sputtered species from different targets. The oxygen was introduced near target position 1 and the ppO_2 was fixed at 8E-7 Torr. The source Ar and hollow cathode Ar were 60 and 10 SCCM respectively, and the processing pressure was about 0.74 mTorr. The source discharge current was fixed at 7.5 Amp and the discharge voltage was about 40 V. The pulse width of the three targets varied from 1 to 20 μsec, individually.

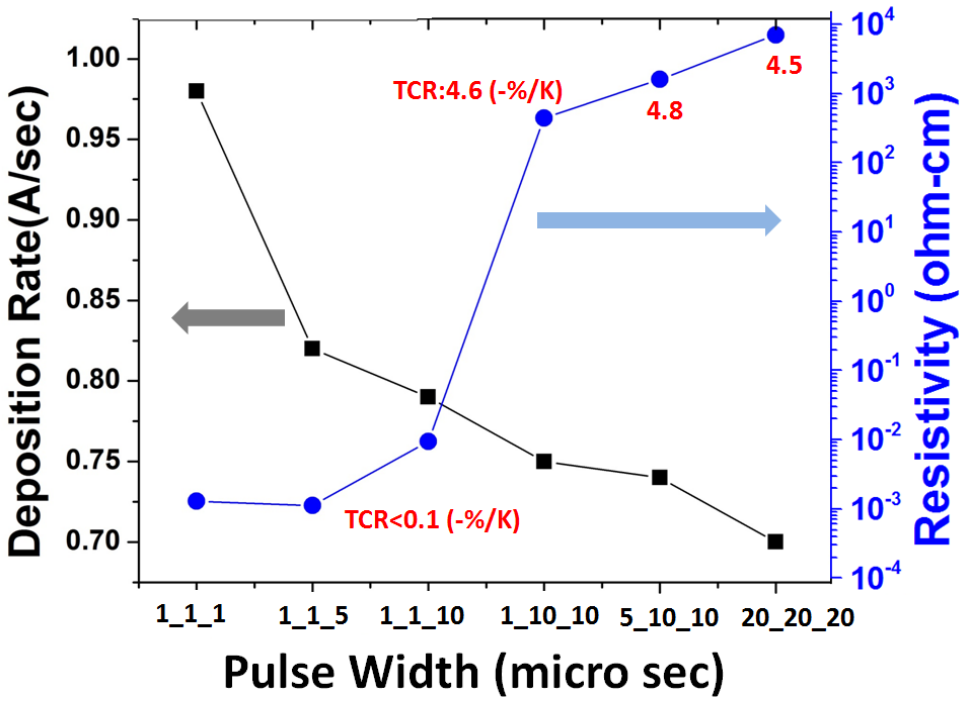

Figure 4-4. VO_x thin films properties change as a function of pulse width applied on different targets: VO_x deposition rate and resistivity change as a function of different pulse width of biased targets.

As shown in Figure 4-4, when all three targets are pulsed with a 1 µsec pulse width, the deposited VO_x film is metallic (6E-4 Ω•cm). When all three targets are pulsed with a width of 20 µsec, the deposited film has high resistivity (1E4 Ω•cm). With increasing of the pulse width, the films resistivity increases. When one target is applied with a 10 µsec pulse and the two other targets are pulsed with a 1 µsec pulse, the deposited film is not uniform across the 4 inch wafer. The film resistivity was found to be about 0.01 Ω•cm at center, and 350 Ω•cm at the edge. This set of experiments did not produce films in the desired resistivity range.

Another set of experiments were done by varing target pulse width at higher proessing pressure (1.74 mTorr). Because there was no active control of the processing pressure in this system, the flow rates of hollow cathode Ar and source Ar were increasesd to 100 SCCM each (highest value). In this set of experiments, the oxygen inlet position was moved back to the ion

source and the ppO_2 was fixed at 5E-7 Torr (before the targets were fully oxidized, refer to Figure 4-1 (a)). The target bias voltage was still -800 V with 10 kHz frequency. The ion source discharge current was 7.5 Amp and discharge voltage was about 35 V with 100 SCCM source Ar flow rate.

The three target pulse width varied from 1 to 15 µsec. When all three target pulse width is at 1 µsec, the deposited VO_x film is uniform and has a resistivity of 5E-4 Ω•cm. When the three target pulse width is 5, 8, 10 µsec respectively, the deposited film is non-uniform, even with 20 rpm substrate rotation. As shown in Figure 4-5, at the center the film resistivity is ~3E-3 Ω•cm and at the edge is 8.7 Ω•cm. The film edge thickness is ~15% higher than the center. The result indicates that even a sample can be prepared in the resistivity range of 0.01-10 Ω•cm, the film has poor uniformity.

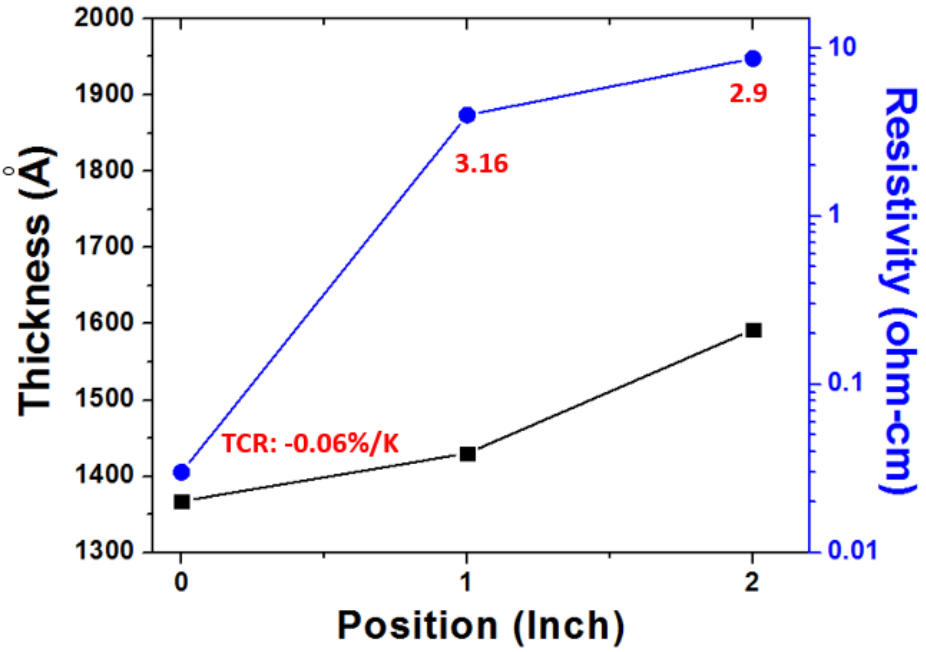

Figure 4-5. A non-uniform VO_x film sample resistivity, TCR, and thickness varied from film center to edge.

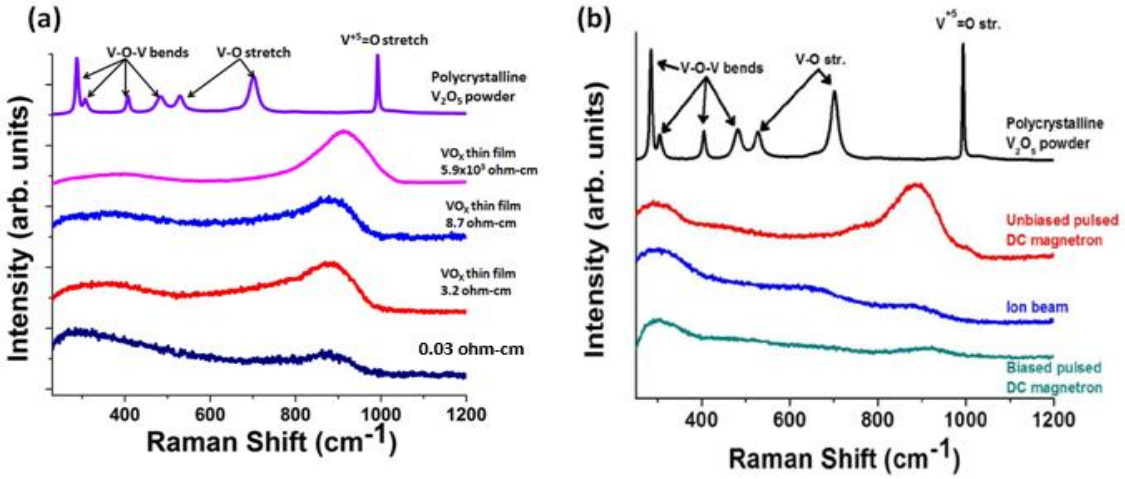

Figure 4-6. Raman spectra of (a) VO_x thin films prepared by BTIBD system and (b) VO_x thin films prepared by other techniques [35].

Raman spectroscopy was used to study the structure of the non-uniform sample which is shown in Figure 4-5. From the sample center to edge, the resistivity is 0.03 Ω•cm, 3.2 Ω•cm, and 8.7 Ω•cm. From Figure 4-6 (a) we can tell with from the center to edge, the intensity of V-O-V bends at 295 cm^{-1} decreases and V^{5+} =O double stretch intensity at 890 cm^{-1} increases. The peak shows at 295 cm^{-1} is observed to correlate to the FCC nanocrystalline domains, which decreases the film resistivity[35] . Figure 4-6(b) shows the Raman spectra of VO_x prepared by ion beam deposition and magnetron pulsed dc sputtering with and without substrate bias. It shows that low resistivity VO_x prepared by BTIBD has the similar features to the samples prepared by IBD and magnetron pulsed dc sputtering with substrate bias. The Raman spectrum of the high resistivity sample with resistivity of 5.9E3 Ω•cm only shows the strong peak of V^{5+} double bond and moves to high frequency at about 920 cm^{-1}. From the non-uniform sample's Raman spectra, we believe that in the film center there is more FCC nanocrystalline domains than the edge. At this high pressure, the plasma is not as uniform, thus the formation of the nanocrystalline material may be due to a high-energy tail of source Ar+ ions bombarding the sample. This extra energetic argon may reduce the amount of oxygen that is bonded when compared to the edge.

The results from this set of experiments suggest that when using this BTIBD system in this configuration, it is hard to prepare uniform nanocomposite VO_x films with resistivity in 0.01-10 Ω•cm across a 4" wafer. By using beam blocker may be able to prevent the high energy Ar+ bombard to the substrate and improve film uniformity. However, it might also prevent FCC nanocrystalline domains formation in the deposited films. Further experiments would have to be made at different bias voltages, ppO_2 and pulse widths to better determine whether this method is capable of making films in the low resistivity range currently used in microbolometers.

4.6 $(Mo/V)O_x$ thin films properties and thermal stability

It has been shown in previous work using magnetron sputtering that adding molybdenum in the 0.01-1 Ω•cm VO_x thin films prepared by magnetron pulsed-dc sputtering improves the films electrical properties and thermal stability [37]. In order to study the properties of $(Mo/V)O_x$ alloy films prepared by BTIBD system, one Mo target and two vanadium targets were co-sputtered to get alloyed films.

In the experiment, all three targets were powered with -800 V and the pulse frequency was 10 kHz. The two V targets had a pulse width fixed at 1 μsec and the pulse width of the Mo was varied from 30 μsec to 95 μsec in order to control the Mo composition in alloy films. One pure VO_x control film was deposited at the same processing parameters but without Mo target turned on. Figure 4-7 shows the $(Mo/O)O_x$ alloy film deposition rate and electrical properties as a function of Mo pulse width. The Mo to V ratio was measured by EDS with error of ±5%.

When Mo target was turned off, the pure VO_x thin films were deposited. Table 4.1 shows that the deposition rate of alloy films and the Mo content increases when the pulse width of the Mo target decreases (or the sputtering portion of the full duty cycle increases). When the ppO_2 is controlled at 1E-6 Torr by the residual gas analyzer feedback controller, the oxygen flow rate

increases with decreasing the pulse width of the Mo target. This indicates that the sputtered Mo species are actively reacting with O_2 in the plasma during deposition. The alloy films resistivity increases when Mo to V ratio increases, and surprisingly when the Mo/V ratio is about 2, the film resistivity is as high as 2E-5 Ω•cm. However, when the Mo content in the alloy films further increases, it is expected that the films resistivity will eventually drop to a low resistivity corresponding to MoO_x thin films.

Table 4-1. Mo to V atomic ratio changes as a function of Mo target pulse width. Mo to V atomic ratio was measured by EDS spectrum elemental analysis with ±5% error.

Mo target pulse width (μsec)	Mo/V atomic ratio	O_2 flow rate during deposition (SCCM)	Film deposition rate (Å/sec)
Off	0	3.3	0.50
95	0.04	3.3	0.51
90	0.08	3.4	0.57
70	0.38	3.5	0.65
30	1.90	3.8	1.59

The alloy films as well as the pure VO_x control film were annealed in Ar atmosphere for 10 min at 350^{o}C in order to evaluate their thermal stability at temperatures that they might experience during device processing. Figure 4-8 shows that after annealing, both the VO_x film and the alloy films resistivity and TCR values do not change dramatically. BTIBD prepared high resistivity VO_x thin films are amorphous from GIXRD pattern with x value in the range of 2.2-2.4, measured by Rutherford back scattering [72]. Compared to the high resistivity (>1000 Ω•cm) amorphous VO_x prepared by magnetron pulsed-dc sputtering without substrate bias, the BTIBD prepared VO_x shows better thermal stability [41]. This is probably because the BTIBD prepared VO_x thin films show a relatively high density (3.93g/cm^3). The increased density of BTIBD

prepared VO_x thin films may be caused by two reasons: low processing pressure (according to Thornton's structure zone model), and secondary conditioning by Ar+ ions directly bombard to the film during deposition.

By adding Mo in the high resistivity VO_x thin films, the film deposition rate increases dramatically, without significantly changing the films electrical properties and thermal stability. This suggests that the high throughput, high resistivity and high TCR $(Mo/V)O_x$ alloy films could be an alternative sensing material in vertically integrated pixel microbolometers. However, the electrical noise of these alloy films needs to be further investigated.

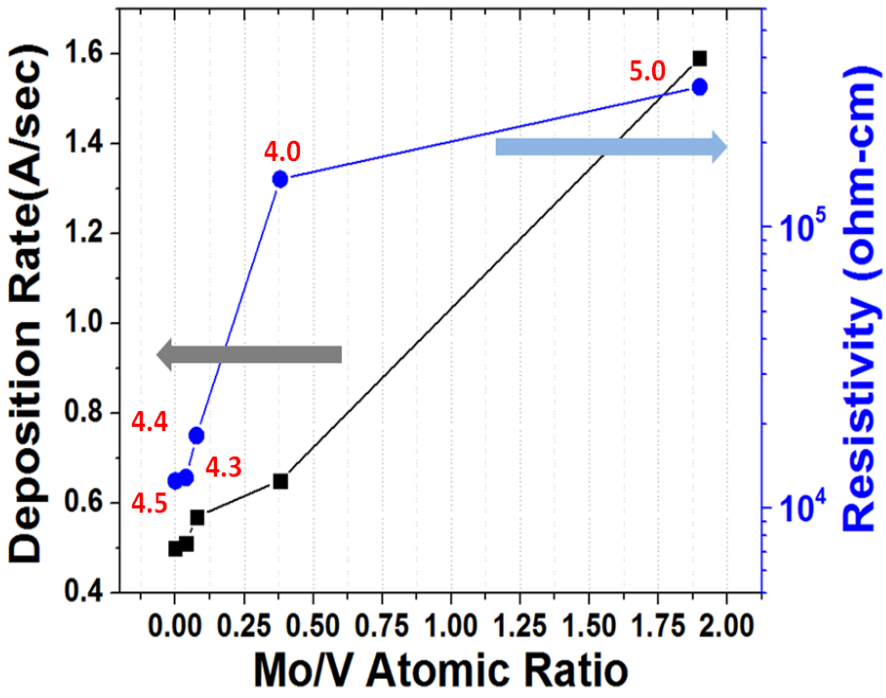

Figure 4-7. $(Mo/V)O_x$ alloy films deposition rate and resistivity change as a function of Mo content. The red numbers are the TCR values. The ppO_2 is fixed at 1E-6 Torr.

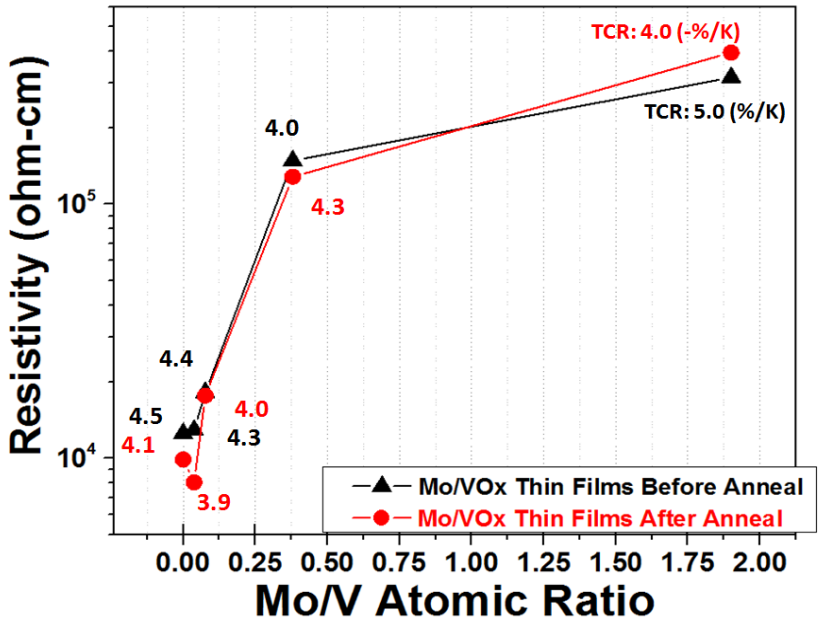

Figure 4-8. Resistivity and TCR values comparison before anneal and after 10 minutes anneal in Ar atmosphere for 350°C.

Figure 4-9 plots TCR versus resistivity for VO_x films prepared by different techniques. The VO_x and $(Mo/V)O_x$ films with resistivity higher than 1E3 Ω•cm and TCR higher than -4 %/K can be reproducibly fabricated using BTIBD. High resistivity VO_x thin films prepared by BTIBD show higher TCR and better thermal stability than VO_x and a-Si:H films [43] prepared by other techniques.

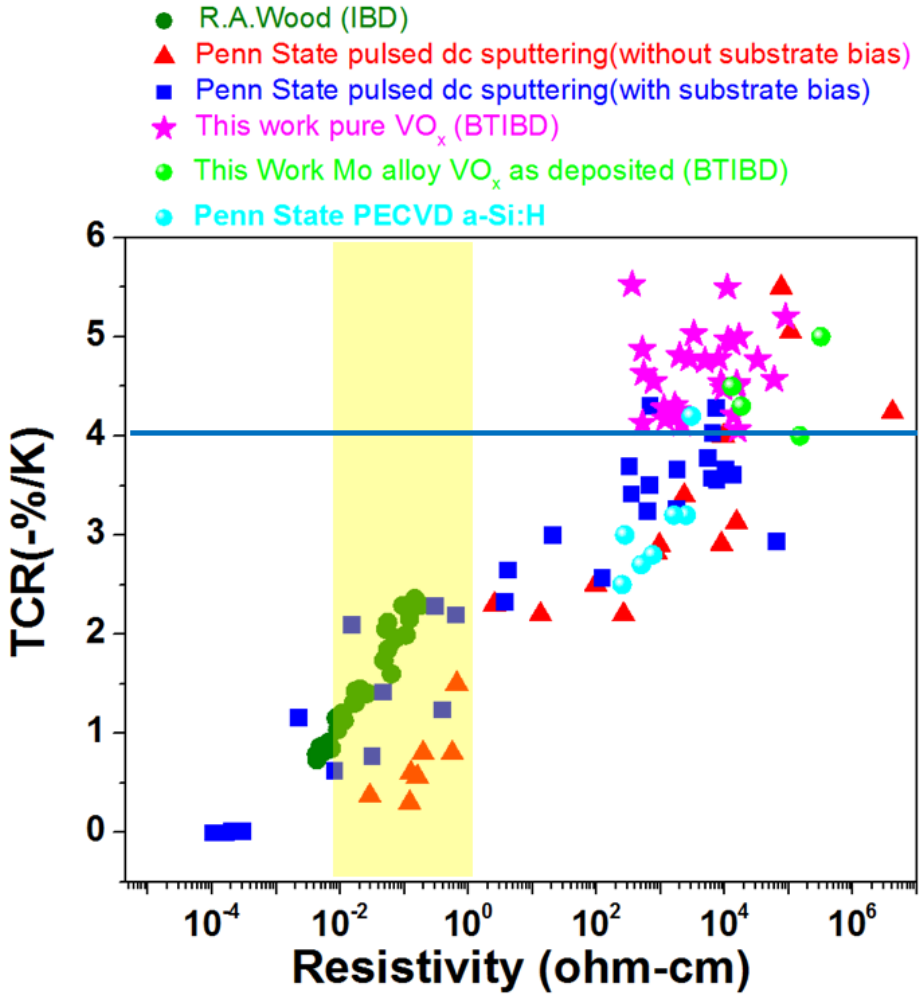

Figure 4-9. TCR versus resistivity of VO_x prepared by different methods as well as a-Si:H prepared by PECVD [3],[42].

4.7 1/f noise of high TCR VO_x films and through-film resistor structure for uncooled microbolometers

As mentioned Chapter 1, the conventional uncooled microbolometer pixel structure uses a lateral resistor configuration. Higher resolution requires smaller pixels (state-of-art pixel size is 17 μm×17 μm). However, smaller pixels result less responsivity due to smaller area for absorbing photons. In order to increase the active layer responsivity, higher TCR is desired. Unfortunately,

higher TCR materials inevitably have higher resistivity and 1/f noise. For a lateral resistance structure, the higher resistance of the sensing materials leads to higher Johnson noise, which may limit the microbolometers performance. Hence, a vertical resistor structure has been proposed which is capable of using high resistivity, high TCR sensing materials without introducing high electrical noise associated with high resistance [72]. Figure 4-10 shows the cross-section schematics of conventional lateral structure and vertical structure [72].

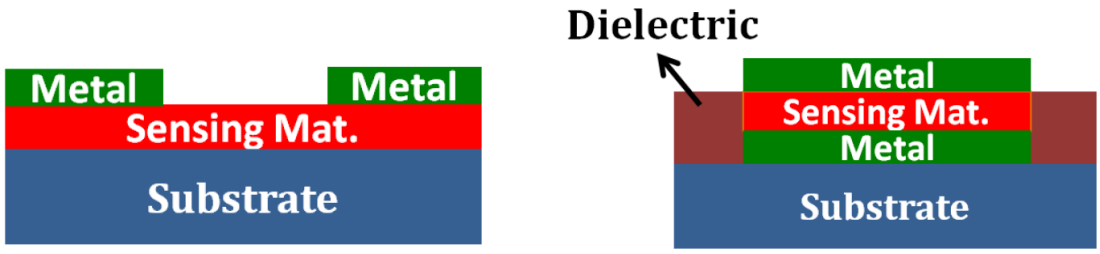

Figure 4-10. The left is the conventional lateral resistance pixel design and the right is the new vertical resistance pixel design [72].

The through-film devices made with BTIBD prepared VO_x have been reported by Basantani et al. in 2013. To measure the through-film resistivity, TCR, and also electrical noise of the BTIBD prepared VO_x films, the films were patterned by photolithography. The VO_x resistivity was extracted from the resistance measurement of different contact areas between top and bottom metal contacts. As shown in Figure 4-11, the deposited VO_x film resistance increases linearly with "1/contact area", and the through-film resistivity is equal to the slope of the line divided by film thickness. For the same VO_x material, the measured through-film resistivity is 30% higher than the lateral-film resistivity. One reason for this might be that there is a high resistivity intermixed layer of TiO_2 between bottom Ti metal and deposited VO_x. However, the measured TCR and normalized Hooge's parameter α_H/n are the same for both the lateral and through-film configuration. Figure 4-12 shows the normalized Hooge's parameter versus TCR values of VO_x prepared by different methods, as well as other sensing materials for bolometers developed by our group. It again shows the general trend that higher TCR VO_x films have higher

1/f noise in addition to higher resistivity as mentioned previously. Compare to PECVD prepared a-Ge and a-Si, at the same TCR range, BTIBD prepared VO_x show lower 1/f noise, suggesting possible higher NETD and better performance.

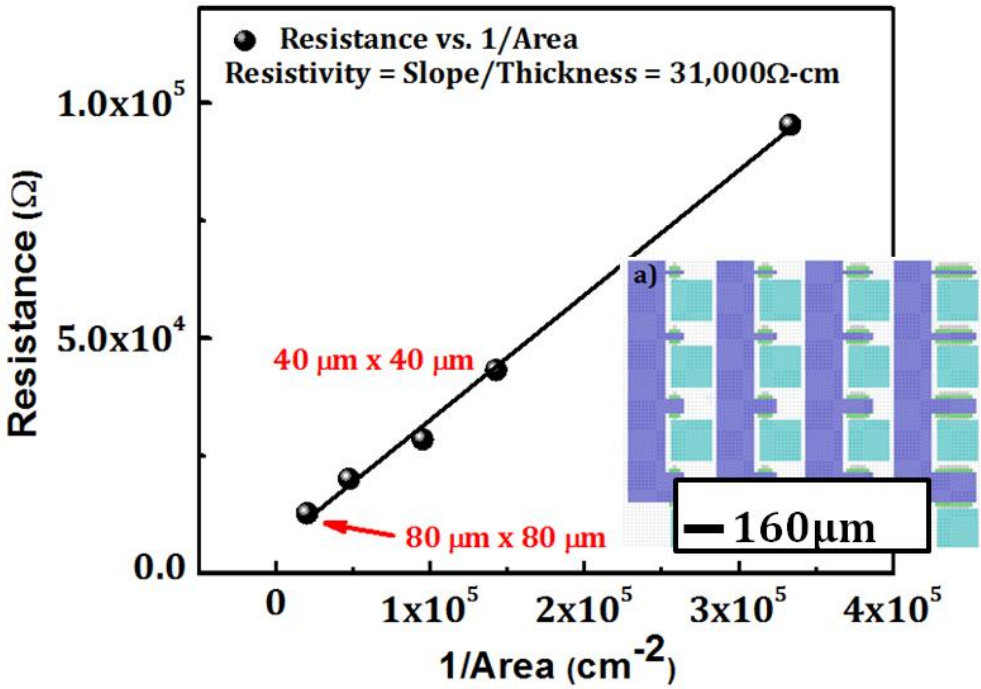

Figure 4-11. BTIBD prepared VO_x through-film resistance change as a function of 1/contact area [72].

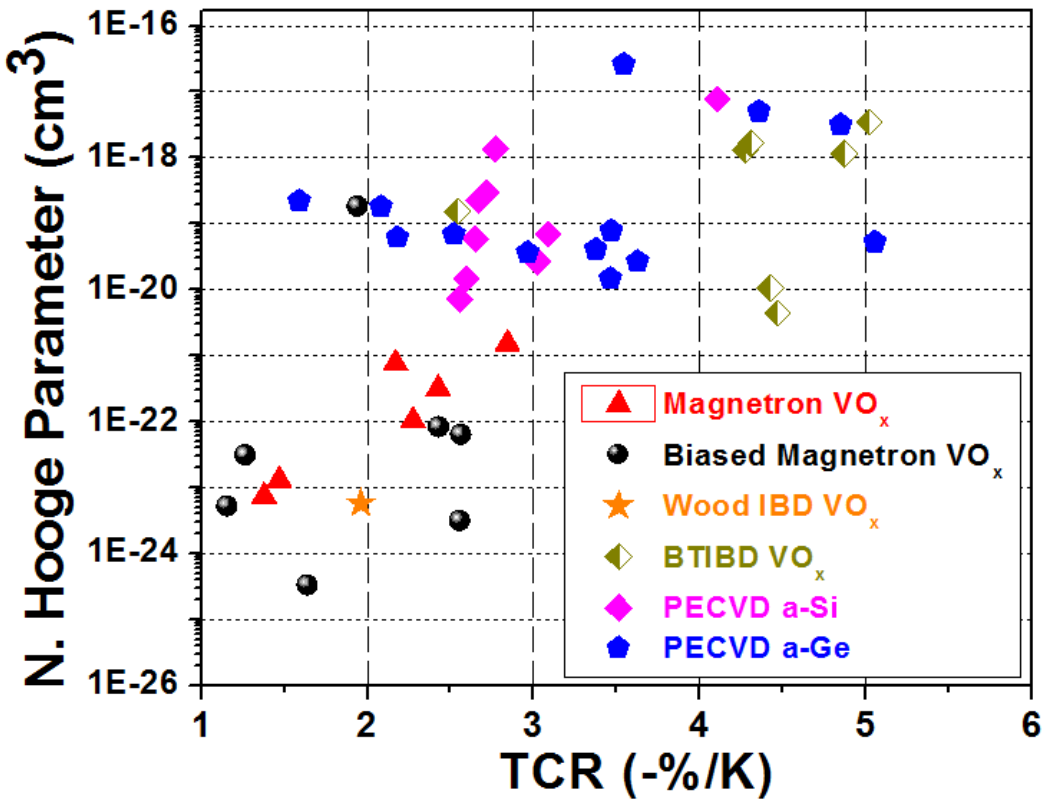

Figure 4-12. Normalized Hooge's parameters versus TCR of VO_x prepared by different methods, replotted from Ref [72].

4.8 Conclusion

In this Chapter, VO_x thin films with TCR <-4.5%/K in the resistivity range of 1E3 to 1E5 Ω•cm have been reproducibly deposited by using the BTIBD system. Different processing parameters such as oxygen partial pressure, oxygen inlet position, processing pressure, target bias voltage, and pulse width and their effect on the electrical properties of VO_x thin films has been investigated. Mo doped VO_x thin films show much higher deposition rates and good thermal stability when compared with similar resistivity undoped VO_x thin films. BTIBD prepare VO_x films show higher TCR and lower 1/f noise compared to other high TCR materials. The results

suggest that BTIBD prepared VO_x are possible better candidates to next generation of uncooled focal plane arrays that would incorporate through-film resistive bolometer structures.

Though high TCR (<-4.5 %/K) VO_x can be easily made in this BTIBD system, it is hard to prepare uniform nanocomposite VO_x films with resistivity in 0.01-10 Ω•cm. The previous study [37] and the result in this Chapter show that adding Ni and Mo in VO_x thin films did not significantly affect the electrical properties of the deposited VO_x thin films. This led to further investigation into the bolometric properties of NiO_x and MoO_x, which would be further detailed in Chapter 5.

Chapter 5

Nickel Oxide and Molybdenum Oxide Thin Films Prepared by Biased Target Ion Beam Deposition

As discussed in Chapter 4, using BTIBD, it is hard to deposit uniform vanadium oxide thin films which have a resistivity in the range of 0.01 to 10 Ω•cm typical of what is used currently in IR microbolometer applications. In this chapter, biased target ion beam deposited (BTIBD) nickel oxide (NiO_x) and molybdenum oxide (MoO_x) thin films have been investigated for microbolometer applications. The NiO_x and MoO_x thin film deposition rate, electrical properties, structural and optical properties, as well as thermal stability will be discussed in this Chapter. NiO_x and MoO_x thin film process control and electrical properties will be compared to the VO_x thin films presently used in industry and those discussed in this thesis.

5.1 NiO_x prepared by BTIBD system

5.1.1 Experiment details

NiO_x thin films have been reported as microbolometer active sensing layers. The methods to fabricate NiO_x thin films for infrared imaging include: reactive magnetron pulsed dc sputtering, reactive rf sputtering and heat treatment of sputtered Ni thin films in oxygen atmosphere [9], [10]. Potential advantages of using NiO_x thin films as infrared imaging sensing materials include: 1) low number of phases (NiO and Ni_2O_3) compared to VO_x which makes it is easy to reproducibly fabricate; 2) resistivity is easy to engineer by controlling the nickel vacancies and oxygen interstitial; 3) fabrication method is cheap and compatible to the CMOS process; 4) relatively low 1/f noise has been reported for a poly-crystalline structure [9].

In this work, NiO_x thin films were reactively sputter deposited from a 99.99% metallic Ni target in an O_2/Ar ambient in the BTIBD system. The source and HC Ar flow rate were 80 SCCM and 10 SCCM respectively. The total processing pressure was about 7E-4 Torr. Ion source discharge current and voltage was 7.5 Amp and 45 V. The Ni target was pulsed dc biased at -800 V with 10 kHz pulse repetition rate and 1μsec pulse width. The deposition rate and electrical properties of NiO_x thin films were studied with a function of the oxygen partial pressure (ppO_2) and total processing pressure.

To study the NiO_x film thermal stability, one set of samples was annealed in air on hot plate at 250°C for 10 minutes. The other set of samples was simply stored in sample boxes in the laboratory for 250 days (8 months) with no effort to control the ambient after which the resistivity and TCR were measured. These 250 day-old samples were annealed at 350°C for 20 minutes in an Ar or O_2 ambient, and resistivity and TCR again measured.

5.1.2 NiO_x thin film deposition rate and electrical properties

NiO has a rock salt crystal structure and is reported to be a p-type semiconductor [73], [74]. Resistivity of NiO_x thin films can be controlled by adjusting the Ni to O ratio [75], [76]. In this work, the biased target ion beam deposited NiO_x thin film properties were engineered by varying the ppO_2 from 2E-7 to 6E-6 Torr. As shown in Figure 5-1, as the oxygen partial pressure increases, the deposited NiO_x thin film deposition rate increases. For NiO_x deposition, nickel oxidation can occur at the target, in the plasma-filled chamber ambient, and at the substrate. The increase of deposition date indicates that at a lower oxygen partial pressure, the Ni target is not significantly oxidized yet, and the reaction mainly happens in the plasma ambient or at the substrate. The large increase of NiO_x resistivity suggests the film changes from Ni rich to a more oxidized state. However, further increase of ppO_2 leads to a decrease in deposition rate which

may be due to an increase in oxidation of the Ni target surface. Further increase in the oxygen partial pressure results in a continued decrease in the deposition rate, indicating increased oxidation of the Ni target surface. Unlike VO_x, further increase of oxygen partial pressure leads to a decrease in the NiO_x thin film resistivity; this has been attributed to an increase in the oxygen interstitial concentration [75] [76]. In this work, the as-deposited NiO_x thin film resistivity ranges from 1 to 300 Ω•cm with TCR from -2.2 to -3.3 %/K as the oxygen partial pressure is varied from 6×10^{-6} to 1×10^{-6} Torr. Notably, the NiO_x thin film resistivity varies slowly and monotonically with the oxygen partial pressure in this range and the film characteristics are easily controlled. Compare to BTIBD prepared VO_x thin films discussed in Chapter 4, BTIBD prepared NiO_x thin films show a much larger process latitude with respect to oxygen partial pressure and a better overall deposition rate than VO_x thin films (at a ppO_2=2E-6 Torr, the deposition rate of NiO_x from a Ni target is 10 times of VO_x sputtered from a single V target).

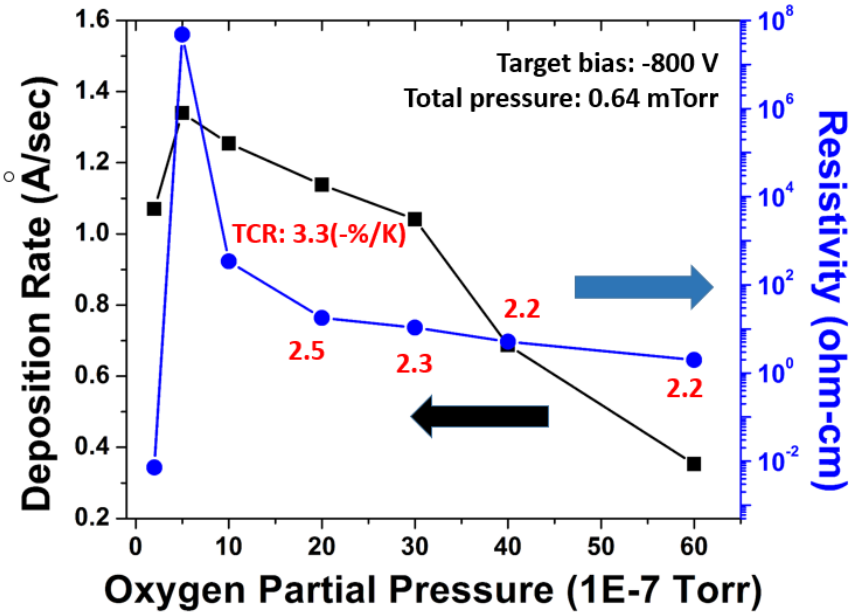

Figure 5-1. Biased target ion beam deposition prepared NiO_x thin films deposition rates, resistivity and TCR change as a function of ppO_2.

The deposition rate and electrical properties of as-deposited NiO_x thin films can also be engineered by total processing pressure. In our BTIBD system, the processing pressure is not actively controlled so the total processing pressure is varied by varying the source Ar flow rates. However, by increasing the source Ar flow rates, the end-Hall discharge voltage decreases, as well as the Ar+ ion energy which is approximately 60% of the discharge voltage. A set of experiments was performed where the oxygen partial pressure was fixed at 6E-6 Torr and the source Ar flow rates was varied from 60 to 100 SCCM yielding a processing pressure from 0.6 to 1.6 mTorr. As shown in Figure 5-2, by increasing of the processing pressure, the film deposition rate and the resistivity decreased. The decrease of deposition rate may due to more collision of sputtered species before deposited on the substrate (shorter mean free paths) or a reduced number of Ar ions available for sputtering because of the higher background pressure. The lowest resistivity of as-deposited NiO_x thin films is about 0.5 Ω•cm with TCR of -2.0 %/K.

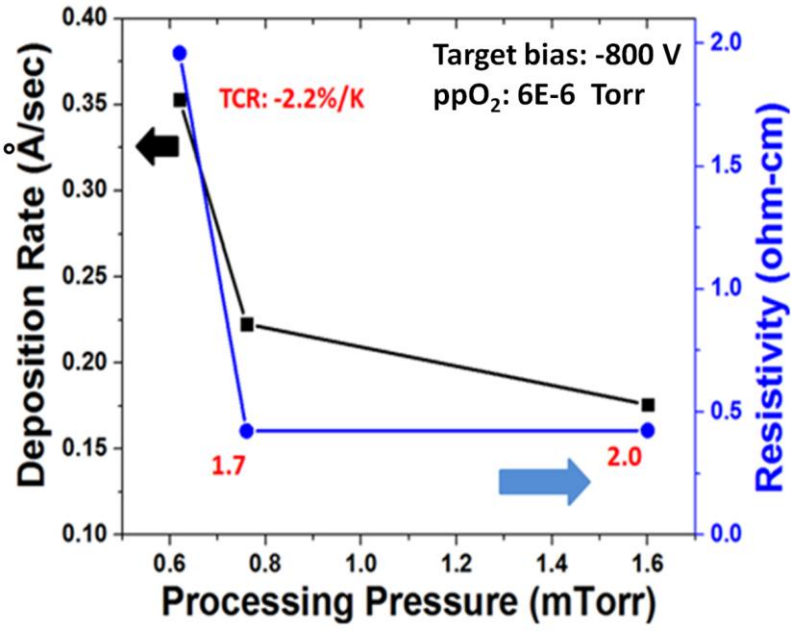

Figure 5-2. BTIBD prepared NiO_x thin films deposition rates, resistivity and TCR change as a function of total processing pressure.

5.1.3 Aging effects and thermal stability of NiO_x thin films

Aging effects and thermal stability of NiO_x thin films have also been studied. The resistivity and TCR were measured after the as-deposited films were annealed in air on a hot plate at 250^{o}C for 10 minutes. Another set of as-deposited films was simply stored in sample boxes in the laboratory with no effort to control the ambient. The resistivity and TCR of the 250 day-old samples were measured. They were also annealed at 350 °C for 20 minutes in an Ar or O_2 atmosphere, and resistivity and TCR again measured. As shown in Figure 5-3, the NiO_x resistivity and TCR electrical properties change little after 250 days of storage. After annealing at low temperature (250^{o}C) for a short time, the film electrical properties do not change much either. However, the changes after inert gas annealing, in either Ar or O_2 at 350^{o}C for a longer time are very large, with a factor of 10^2 to 10^4 increase in film resistivity and a significant increase (40-50%) in TCR. Interestingly, the changes with annealing are similar for both Ar and O_2 ambient. The increase in film resistivity and TCR are somewhat larger for annealing in O_2 than for Ar, perhaps indicating more complete oxidation. However, the difference that results from the annealing ambient is small compared to the difference between annealed and as-deposited films. This would suggest that the change in NiO_x properties during annealing is probably due to the evolution of the microstructure rather than a change in composition.

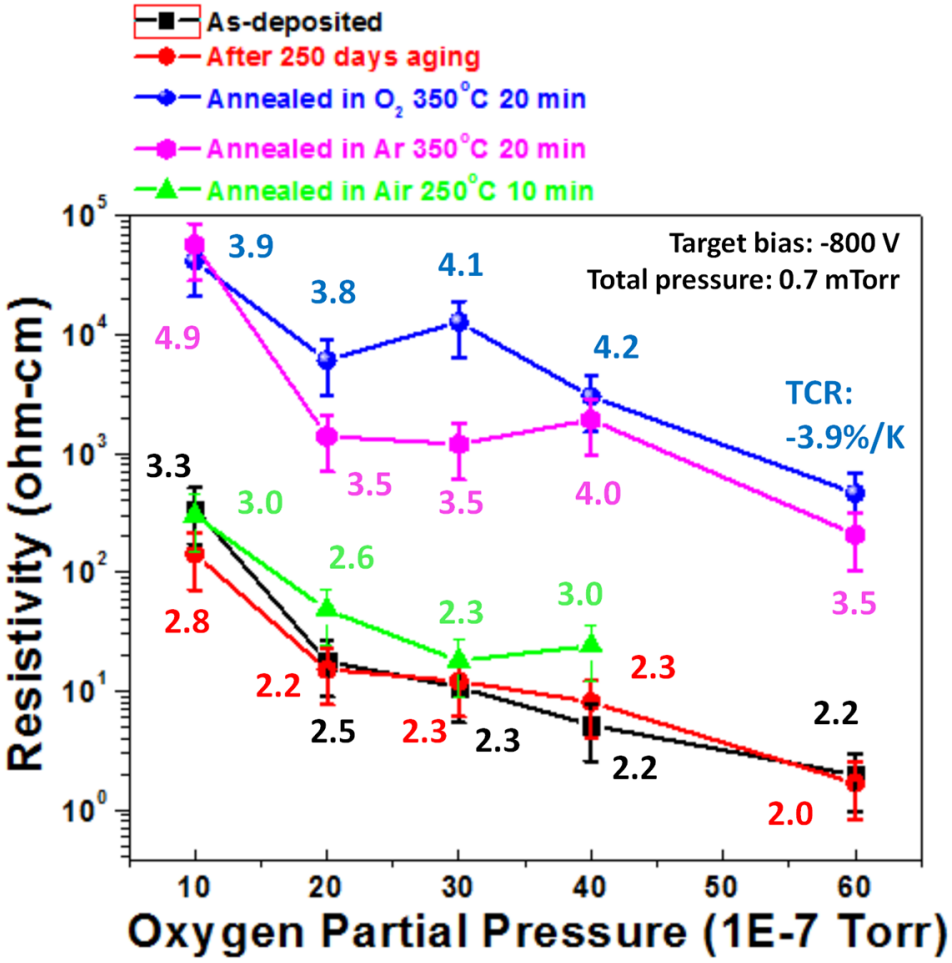

Figure 5-3. NiO_x thin film resistivity and TCR values comparison for films that were as-deposited, after exposed to air for 250 days, and after annealing.

5.1.4 Structure analysis of NiO_x thin films

Figure 5-4 shows GIXRD results for as-deposited NiOx thin films. All the films deposited in the oxygen partial pressure range studied are polycrystalline. As the oxygen partial pressure increases, the GIXRD data suggests that the film texturing and stress change. For oxygen partial pressure from 2E-7 to 5E-7 Torr, the NiO (111) peak increases and is larger than the (200) peak. For larger oxygen partial pressure the (111) peak decreases and the (200) peak dominates. The (200) peak position also moves to smaller angle, which may be due to increasing

stress. To measure the stress in the NiO_x thin films, film surface curvature was measured by profilometry before and after NiO_x deposition. The measured average compressive stress of a 56 nm thick NiO_x prepared at ppO_2=4E-6 Torr is approximately 800 MPa. The same sample was used to calculate the average grain size. The average grain size was calculated using the Scherrer formula:

$$L = \frac{K\lambda}{\beta \cos\theta} \qquad \textit{Eq. 5.1}$$

where L is average crystallite size, β is the peak width of the diffraction peak profile at half maximum height in 2θ axis (in radians), λ is the X-ray wavelength in nanometer, and K is a constant related to crystallite shape. In this work, K is taken as 0.9, and λ is 0.15 nm (Cu K-alpha). Table 5-1 shows the parameters measured by software and the calculated crystallite sizes from three peaks (As shown in Figure 5-5). The average grain size is about 5.7 nm in this film. Similarly, the grain size of this sample after annealing in Ar at 350 ℃ was also calculated and found to be about 7 nm (Table 5-2). The NiO_x thin film GIXRD peak intensity and calculated grain size before and after annealing show no significant difference. However, the GIXRD peak position shifts to higher angle, which may due to the stress change in thin film. This stress may be partly responsible for the large increase of resistivity after annealing.

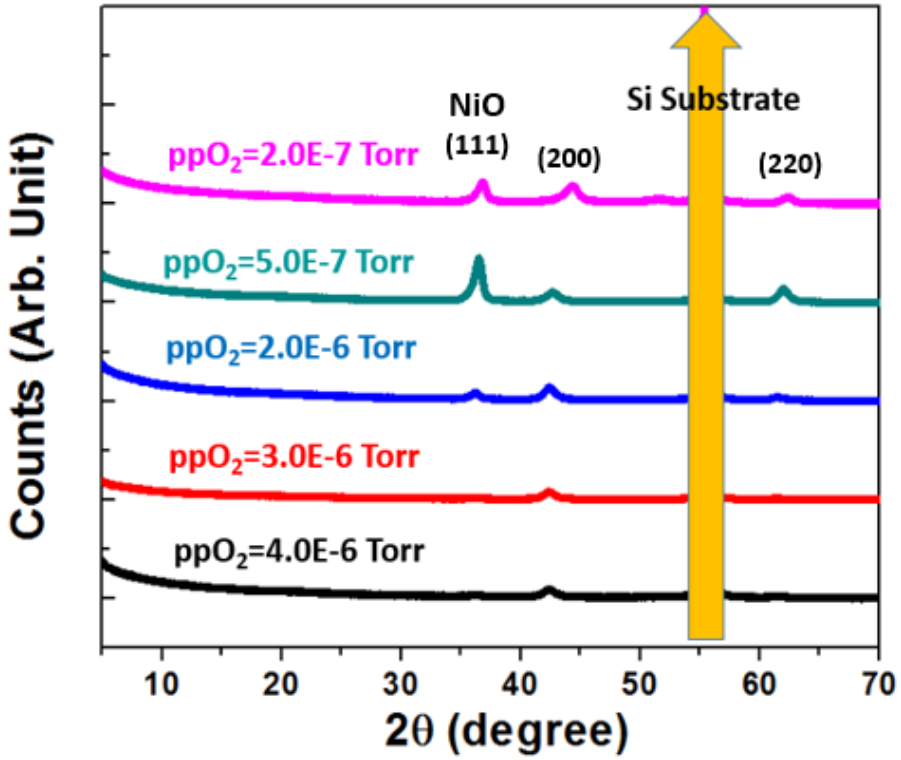

Figure 5-4. GIXRD pattern of as-deposited NiO_x thin films prepared at different ppO_2.

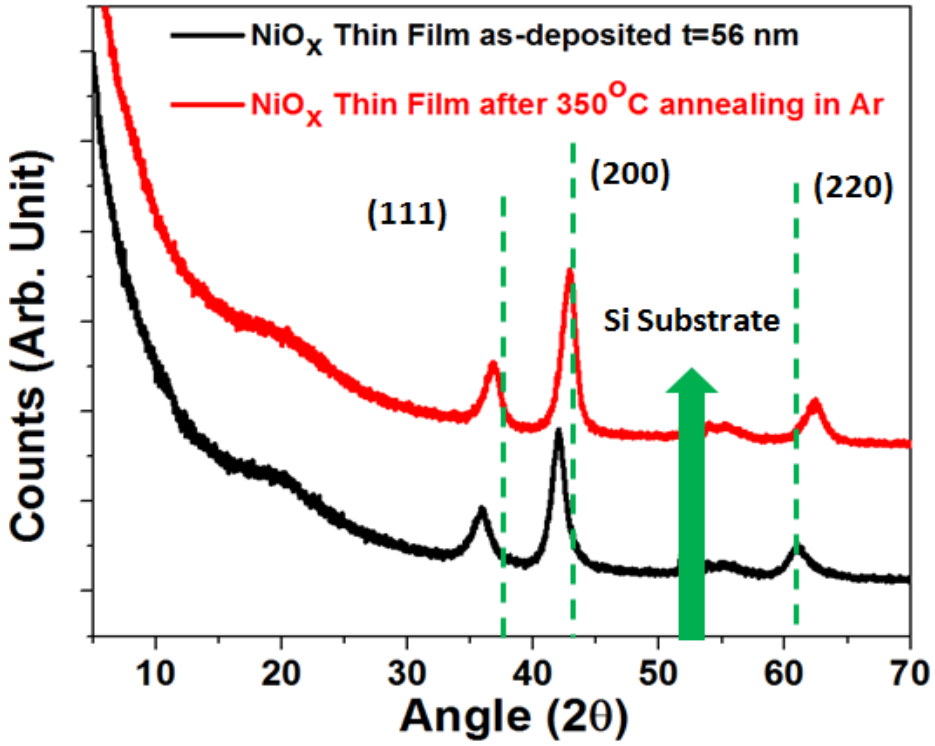

Figure 5-5. GIXRD comparison of a 56-nm-thick NiO_x thin film before and after annealing. This sample was used to calculate the average grain size and average stress. This film was prepared with 60 SCCM source Ar, 4E-6 Torr oxygen partial pressure, and -800 pulsed dc target bias with 100 µsec pulse period and 1 µsec pulse width. Oxygen inlet position was near Ni.

Table 5-1. Parameters from GIXRD measurement and calculated crystallite size of as-deposited NiO_x thin film:

Ref Angle (2θ)	Ref (h k l)	Ref d(Å)	Angle (2θ)	FWHM	Ln(1/cos θ)	Ln(FWHM)	L_1(nm)
37.20	(111)	2.4	35.87	1.31°	0.049	-3.779	6.382
43.23	(200)	2.1	42.03	1.20°	0.068	-3.869	7.118
62.79	(220)	1.5	60.97	1.37°	0.149	-3.729	6.702

Table 5-2. Parameters from GIXRD measurement and calculated crystallite size of NiO_x thin film annealed in Ar at 350°C for 20 min:

Ref Angle (2θ)	Ref (h k l)	Ref d(Å)	Angle (2θ)	FWHM	Ln(1/cos θ)	Ln(FWHM)	L_1(nm)
37.20	(111)	2.4	36.79	1.25°	0.052	-3.822	6.68
43.23	(200)	2.1	42.89	1.15°	0.071	-3.906	7.41
62.79	(220)	1.5	62.47	1.30°	0.156	-3.786	7.15

5.1.5 Optical properties of NiO_x thin films

The optical properties of as-deposited NiO_x were extracted from ex-situ ellipsometry measurement. Ellipsometric spectra were collected at room temperature at an angle of incidence of 70° using a dual rotating compensator multichannel instrument. Least squares regression analysis with an unweighted error function were combined to fit experimental ellipsometric spectra to a structural model consisting of a semi-infinite crystal silicon (c-Si) wafer substrate, ~100 nm of thermally grown silicon dioxide (SiO_2), NiO_x bulk thin film, and surface roughness. The optical response of the surface roughness layer is represented using a Bruggeman effective

medium approximation consisting of fixed 0.5 NiO_x bulk film and 0.5 void volume fractions. The surface roughness for all these NiO_x samples are less than 2 nm. As shown in Figure 5-6(a), the ex-situ refractive index n and extinction coefficient k of as-deposited NiO_x prepared at different ppO_2 were compared. At 633nm, the refractive index of as-deposited NiO_x ranges from 2.43 to 2.35 with ppO_2 from 1E-6 to 6E-6 Torr. Absorption coefficient (Figure 5-6 (b)) was calculated by equation $\alpha=4\pi k/\lambda$ where *k* is the extinction coefficient and λ is the wavelength of incident light.

At low energy (<3 eV), the observed α for NiO_x increases in amplitude with increasing oxygen partial. Similar to semiconducting VO_x [77], the amplitude of the absorption coefficient for NiO_x decreases with increasing resistivity. The optical properties for NiO_x films prepared here fall within the range reported in literature [78], [79] . Significant absorption below the reported NiO band gap near 3.0-4.0 eV is observed and indicates that non-stoichiometry may give rise to multiple Ni valence states in the film [78], [80]–[82].

The optical properties of NiO_x before and after annealing have been also investigated. The same sample (NiO_x 56 nm thick) which was described in last section was analyzed by ex-situ SE before and after annealing in Ar or O_2 at 350 ℃ for 20 min, respectively. Figure 5-7 shows that after annealing, the absorption coefficient at lower energy levels decreases, corresponding to the previous observation: α decreases with increasing film resistivity. However, there is no difference between α of NiO_x annealed in Ar and O_2, which agrees the previously mentioned observation for annealing that the film resistivity has little difference after annealing in Ar or O_2.

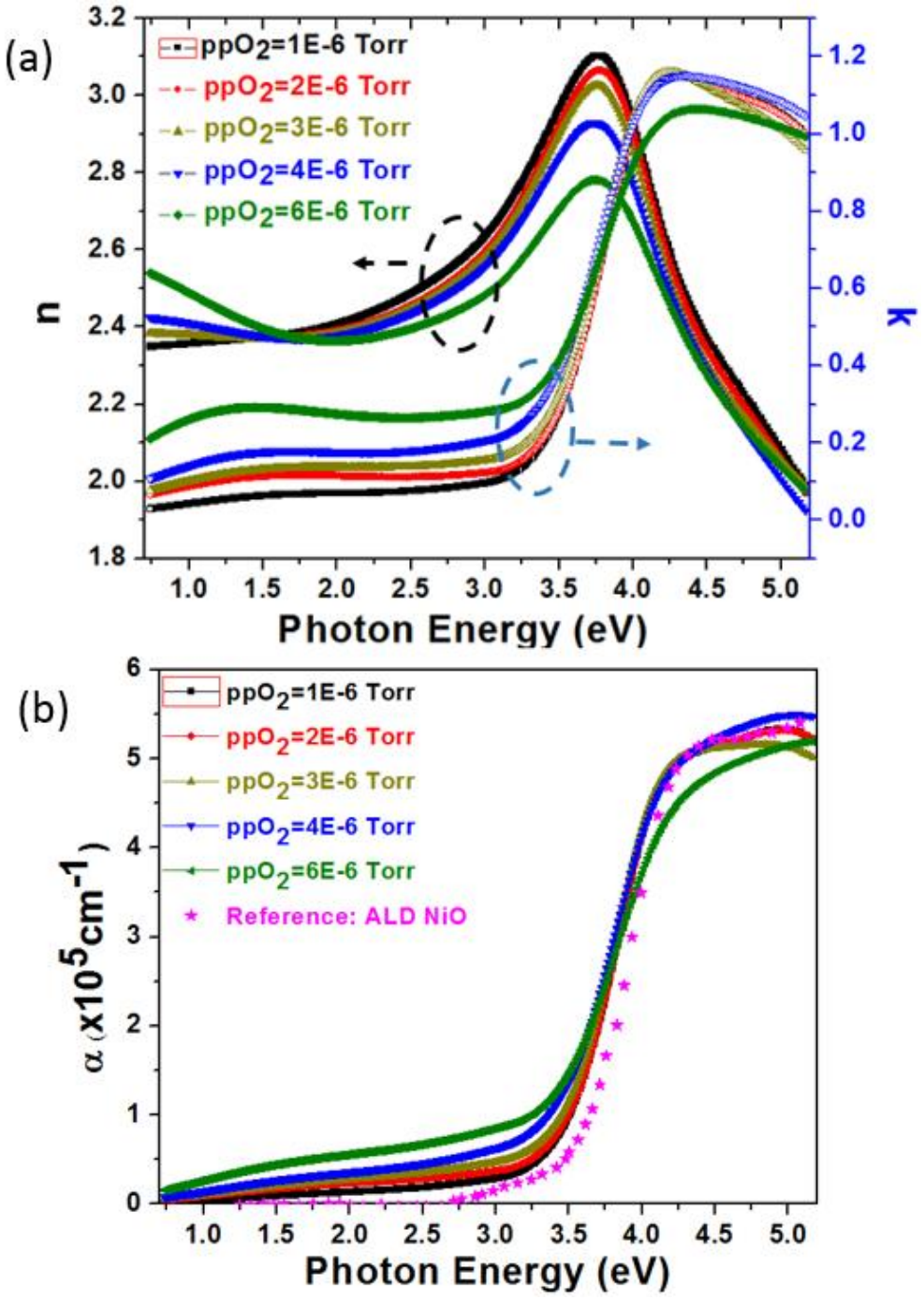

Figure 5-6. Plot of (a) *n* and *k* versus hv and, (b) absorption coefficient α versus $h\nu$ for as-deposited NiO_x thin films prepared at different ppO_2, compared to atomic layer deposited (ALD) NiO [78].

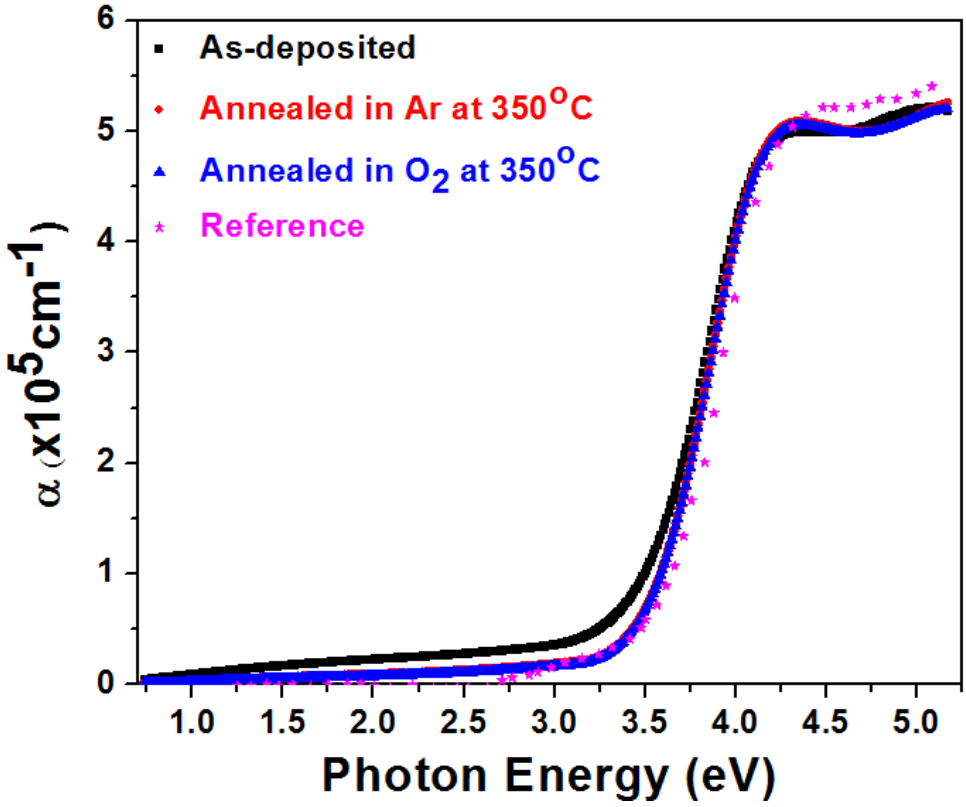

Figure 5-7. Plot of α versus hν for as-deposited NiO_x thin films, after annealed in Ar, and annealed in O_2 at 350°C for 20 min. Reference from [78]

5.2 MoO_x thin films prepared by BTIBD system

In chapter 4, it was shown that for high resistivity and high TCR VO_x films, the addition of large amount of Mo in the VO_x thin films did not significantly change the electrical properties of the films. This section describes experiments designed to determine whether pure MoO_x thin films can be used as a potential microbolometer sensing material.

5.2.1 Experimental details

MoO_x thin films were deposited on thermally oxidized silicon substrates by the BTIBD system using a mixture of Ar and O_2. Molybdenum (Mo) target with 99.99% purity were pulsed dc biased at -800 V with 10 kHz pulse repetition rate and 1μsec pulse width. The ion source discharge current was held at 7.5 Amp and the ion beam current was about 1.5 Amp, and the ion source discharge voltage was kept below 45 V. The ion source Ar flow rate is 80 SCCM and HC flow rate is 10 SCCM, whereas the processing pressure was about 0.7 mTorr.

As with the nickel oxide films described in the previous section, to investigate the deposited films thermal stability, the resistivity and TCR values were measured again after MoO_x films were exposed to natural atmosphere for 250 days. In addition, these 250-day-old samples were measured again after being annealed in the RTA system at 350 ℃ in Ar atmosphere for 20 minutes.

5.2.2 MoO_x thin films electrical properties

MoO_x thin films were reactively sputter deposited from a 99.99% metallic Mo target in an O_2/Ar ambient in the biased target ion beam deposition system. The oxygen partial pressure was varied from 1E-6 to 2E-6 Torr. As shown in Figure 5-8, as the oxygen partial pressure increases, the deposited MoO_x thin film resistivity increases from 3E-4 to 2000 Ω·cm. For MoO_x deposition, molybdenum oxidation can occur at the target, in the plasma-filled chamber ambient, and at the substrate [60]. When the oxygen partial pressure is low (1E-6 Torr), the deposited films are metallic (3E-4 Ω·cm resistivity and small, positive TCR). When the oxygen partial pressure increases to 1.3E-6 Torr, the MoO_x resistivity increases to 3 Ω•cm with a negative TCR of -2.2%/K. Figure 5-8 shows that the film deposition rate approximately doubles as the oxygen

partial pressure increases from 1E-6 Torr to 1.3E-6 Torr. The increase in deposition rate suggests that the Mo target surface is not significantly oxidized and most of the oxidation takes place either in the chamber ambient or at the substrate. Further increase of oxygen partial pressure leads to increasing film resistivity and TCR, and decreasing deposition rate. The deposited film resistivity increases slowly with increasing oxygen partial pressure and thus allows easier control of film resistivity in the region of interest. This is in contrast to VO_x films deposited in our biased target ion beam deposition system, where the deposited film resistivity changes from metallic (3E-4 Ω•cm) to high resistivity (>1000 Ω•cm) for an oxygen partial pressure change of <1E-7 Torr. The decrease in deposition rate for oxygen partial pressure >1.3E-6 Torr is likely due to the reduced sputter yield as the molybdenum target surface becomes increasingly oxidized.

Figure 5-9 shows that similar to the VO_x and NiO_x thin films, the MoO_x thin films show a linear decrease of log (Resistance) with increasing of temperature from 290 K to 350 K, suggesting MoO_x thin films are also potential candidates for bolometer applications. They have the addition advantages of having a much higher deposition rate than that of VO_x.

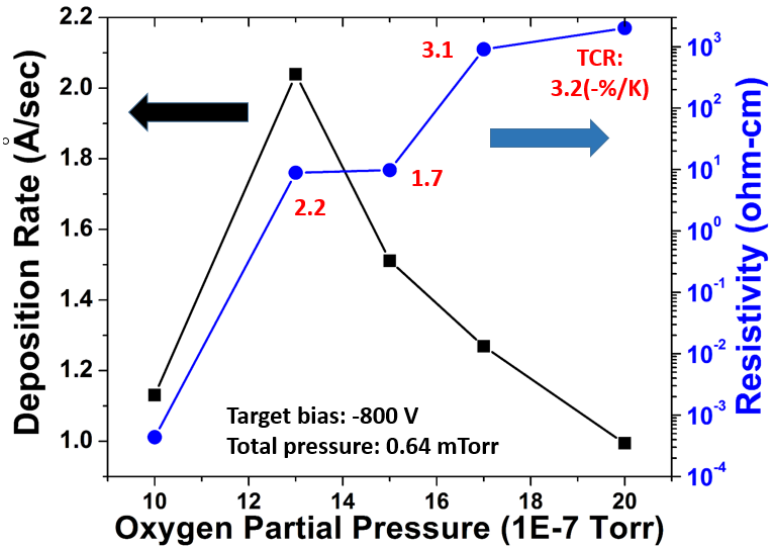

Figure 5-8. Deposition rate and electrical properties of MoO_x with different ppO_2

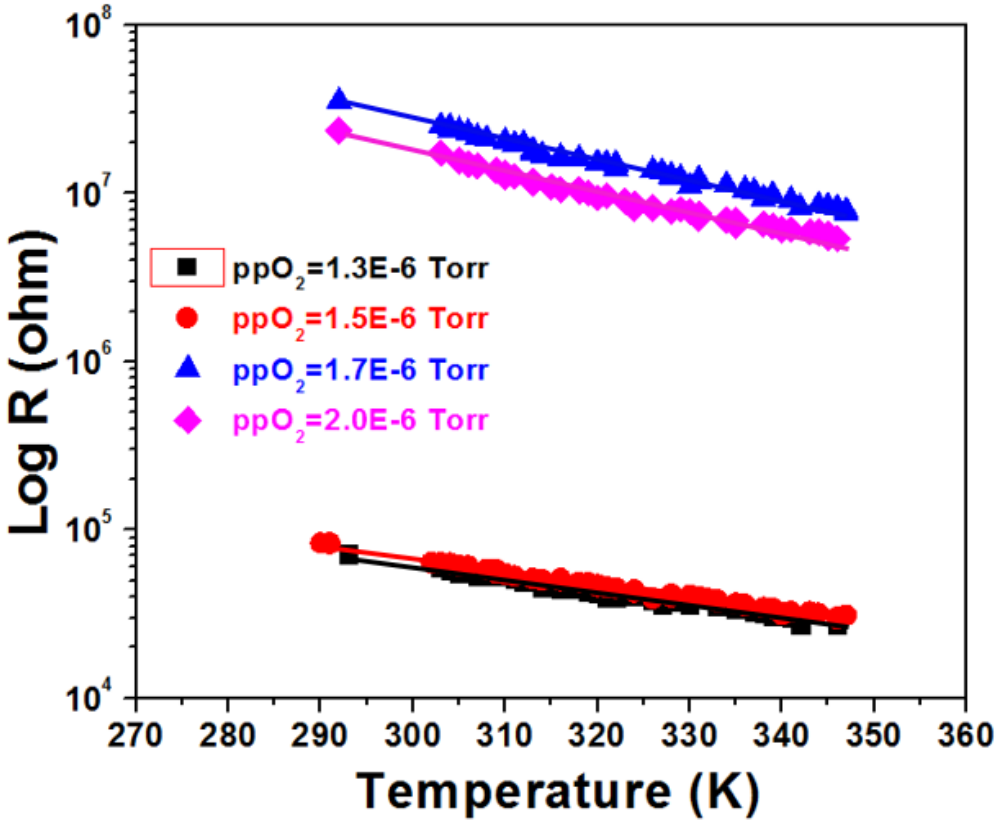

Figure 5-9. Plot of Log(R) vs. Temperature, MoO_x prepared with different ppO_2.

5.2.3 Aging effects and thermal stability of MoO_x thin films

The resistivity and TCR of the MoO_x thin films was measured after deposition and again after 250 days. Similar to the NiO_x samples, during this time the samples were simply stored in sample boxes in the laboratory with no effort to control the ambient. The 250 day-old samples were also annealed at 350°C for 20 minutes in an Ar ambient, and resistivity and TCR again measured. As shown in Figure 5-10, similar to NiO_x thin films, the MoO_x resistivity and TCR electrical properties change little after 250 days of storage. However, the changes after inert gas annealing are very large, with a factor of 10^2 to 10^4 increase in film resistivity. Films with the highest resistivity had non-linear contacts and it was therefore hard to measure TCR; for films

with lower resistivity, TCR increases by about 25 % after the inert gas anneal, which is not as much as seen for NiO_x films. Annealing in oxygen ambient may lead to more complete oxidation and higher film resistivity of MoO_x films, which is not desirable for microbolometer applications.

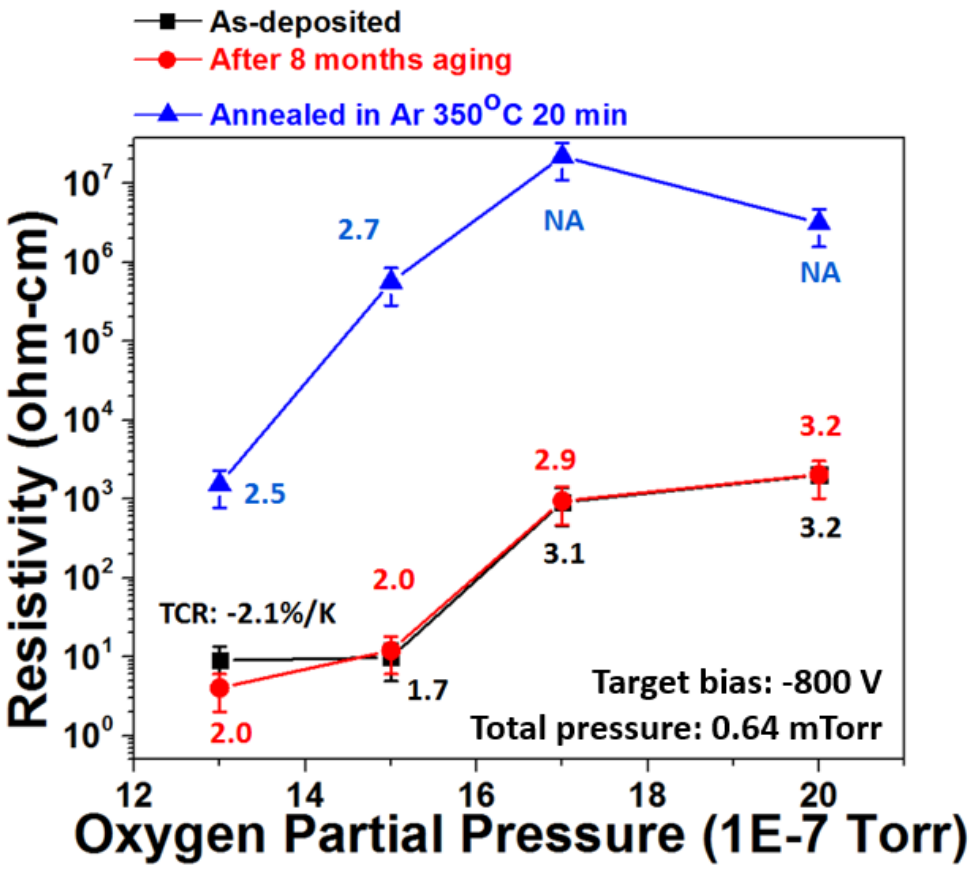

Figure 5-10. MoO_x thin film resistivity and TCR values comparison among as-deposited, after exposed to air for 250 days, and after annealing.

5.2.4 Structure analysis of MoO_x thin films

Figure 5-11 shows the GIXRD pattern of as-deposited MoO_x thin films prepared at different oxygen partial pressures. As shown in Figure 5-11, for an oxygen partial pressure of 1E-

6 Torr, the metallic sample has peaks corresponding to MoO_2, but shifted from the expected position. The shift of the peaks suggests significant stress developed in the deposited thin film. MoO_2 is metallic with a low resistivity about 1E-4 Ω•cm [83][84] so the combination of film resistivity and x-ray characterization indicate that this film is either MoO_2 or a mixture of MoO_2 and Mo. As the oxygen partial pressure is increased, the MoO_2 peaks decrease and peaks corresponding to MoO_3 appear. The MoO_3 peaks are broad, indicating small grain size, possibly in an amorphous matrix. The GIXRD characteristics change little with further increase in oxygen partial pressure, consistent with previous reports that showed little change in thin film x-ray characteristics for sputtering over a range of large oxygen partial pressure [83], [85], [86] Although the x-ray characteristics change little, the film resistivity increases from 0.9 to 2000 Ω•cm as the oxygen partial pressure increases from to 1.3E-6 to 2E-6 Torr.

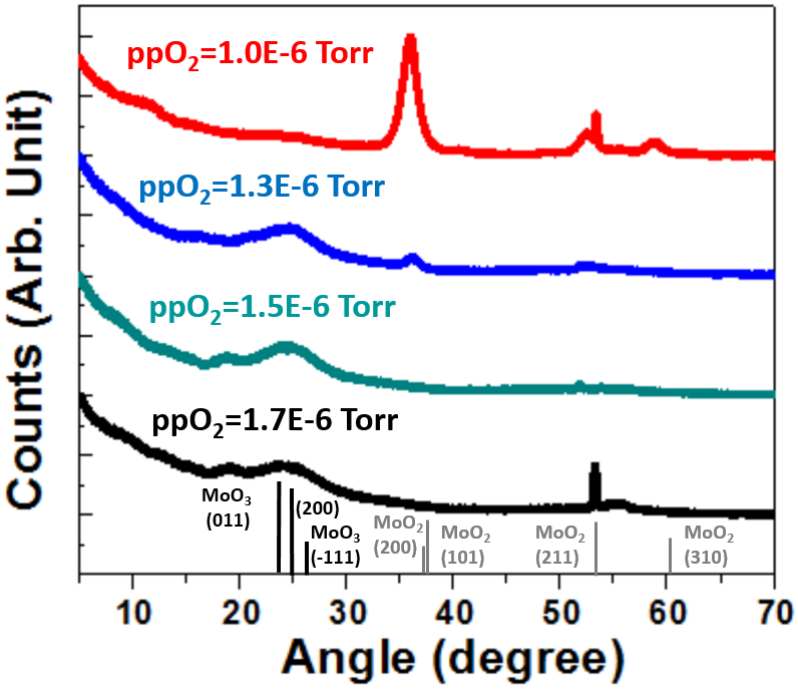

Figure 5-11. GIXRD pattern of as-deposited MoOx thin films prepared at different oxygen partial pressures. The reference peaks in this picture are corresponding to MoO_2 (Tetragonal) and MoO_3 (Monoclinic). The peak at 54° with the oxygen partial pressure of 1E-6 and 1.7E-6 Torr is believed due to Si substrate.

5.2.5 Optical properties of MoO_x thin films

The as-deposited MoO_x thin films optical properties were deduced by the ex-situ SE measurement. As shown in Figure 5-12, MoO_x film prepared at oxygen partial pressure at 1E-6 Torr exhibits a Drude feature, indicating the metallic behavior. This observation agrees the film low resistivity (3E-4 Ω•cm).

All MoO_x films prepared at oxygen partial pressure >1.0E-6 Torr in this work do not exhibit a Drude feature, indicating semiconductor like behavior. Negative values of TCR for these films are consistent with this observation. These MoO_x film refractive index at 633 nm varies from 1.7 to 2.3 as the oxygen partial pressure increases from 1.3E-6 to 2.0E-6 Torr, which is similar to a previous report [87]. As shown in Figure 5-12(b), there is significant absorption at photon energy from 3.5 to 4.2 eV, which is similar to the reference. There is also absorption at photon energy <3.0 eV, and the absorption coefficient α decreases in amplitude with increasing oxygen partial pressure. Film resistivity also increases with oxygen partial pressure for MoO_x in this range. A similar feature has been observed in disordered mixed valence VO_x thin films, which also decreases in amplitude with increasing film resistivity [77], [88]. Although different trends are observed between oxygen partial pressure and film resistivity for these MoO_x and NiO_x films, the behavior of the low energy feature in the optical properties correlates with film resistivity for both cases. The low energy absorption of non-stoichiometric MoO_x may indicate that the feature originates from a distribution in the valence states of Mo. These low energy absorption features support the idea that mixed-valence states are present, considering that the band gap of MoO_3 has been reported near 2.9-3.4 eV [87][89], and MoO_2 is metallic [90].

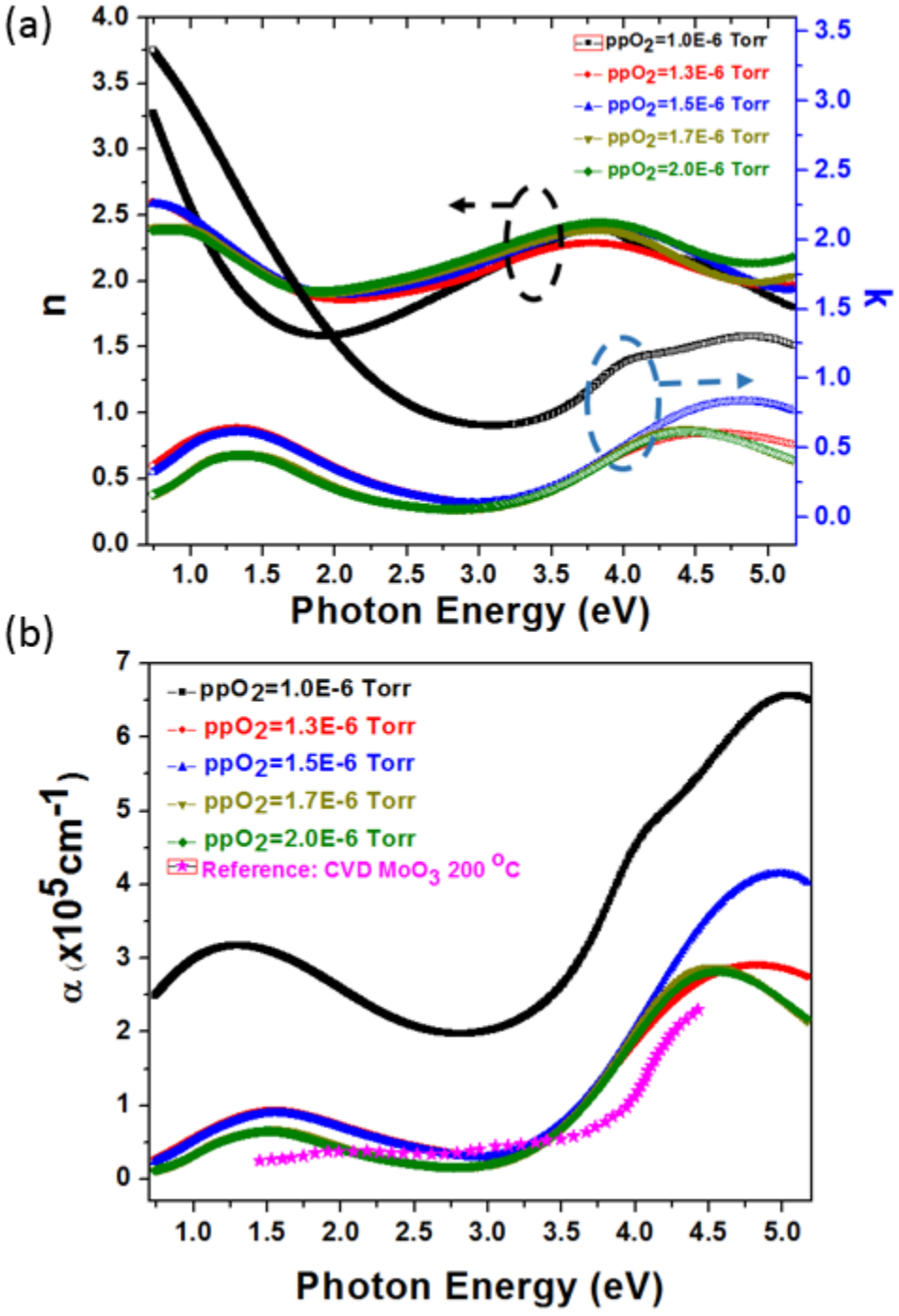

Figure 5-12. Plot of (a) n and k versus hν and, (b) absorption coefficient α versus hν for as-deposited MoO_x thin films prepared at different ppO_2 [87].

5.3 1/f noise measurement

To evaluate the 1/f noise of BTIBD prepared NiO_x thin films, one NiO_x sample with resistivity was prepared at an oxygen partial pressure of 4E-6 Torr. The measured film resistivity is 29.7 Ω•cm with a TCR of -2.5 %/K. The calculated normalized Hooge's parameter of this sample is 6.58E-19 cm^3.

Figure 5-13 shows the normalized Hooge's parameter comparison of various sensing materials investigated by our group. The 1/f noise of BTIBD prepared NiO_x is larger than that of VO_x, and is similar to PECVD a-Si. Other group reported the k value of 1/f noise of reactive sputtered NiO_x thin film was 9.7E-12 with a resistivity of 33.6 Ω•cm and TCR of -3.33 %/K [91]. However, the volume information of this sample was not included in the report. Thus, no direct comparison to the BTIBD prepared NiO_x film can be made.

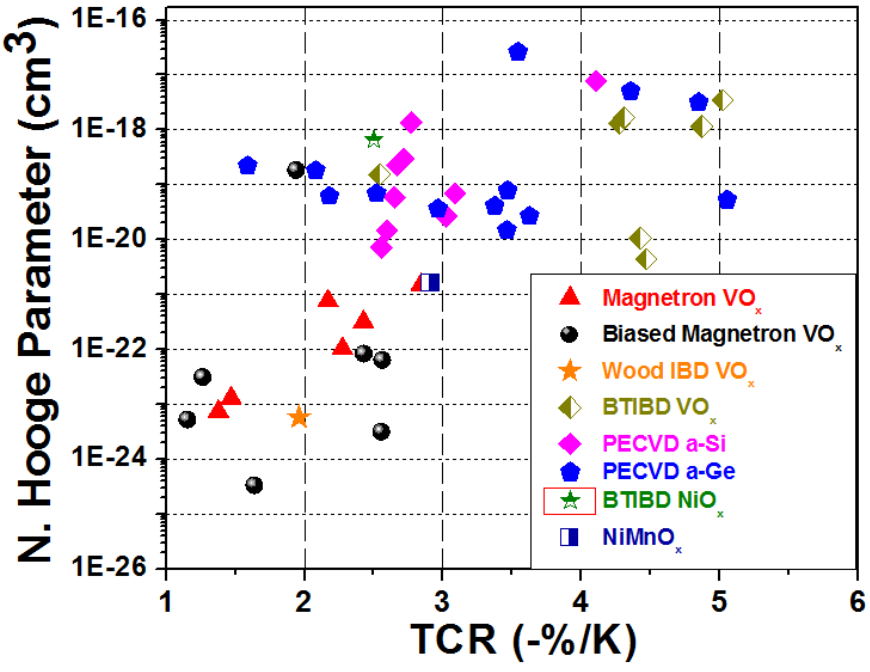

Figure 5-13. TCR versus normalized Hooge's parameter comparison among: VO_x prepared by ion beam deposition, pulsed dc magnetron sputtering, biased target ion beam deposition, PECVD a-Si, PECVD a-Ge, and BTIBD NiO_x.

5.4 Conclusion

In this Chapter, high TCR NiO_x and MoO_x thin films were prepared by our biased target ion beam deposition system. The deposition rate and electrical properties of as-deposited NiO_x and MoO_x thin films are dependent on processing parameters such as the oxygen partial pressure and processing pressure. The resistivity of as-deposited NiO_x thin films is 1 to 300 Ω•cm with a temperature coefficient of resistance (TCR) from -2.2 %/K to -3.3 %/K; the resistivity of as-deposited MoO_x thin films is 3 to 2000 Ω•cm with TCR from -1.7 %/K to -3.2 %/K. Figure 5-13 shows TCR verses resistivity for a variety of thin films. NiO_x and MoO_x show comparable bolometric properties to device-grade VO_x in the resistivity range of 0.1 to 100 Ω•cm. Compared to BTIBD prepared VO_x, the resistivity for both NiO_x and MoO_x varies slowly over a relatively large range of oxygen partial pressure, permitting easier control of film characteristics than for VO_x thin films. XRD characteristics and optical absorption analysis suggests that both the NiO_x and MoO_x thin films show short range order and are semiconductor. The thermal stability of NiO_x and MoO_x thin films was also studied. The result shows that both NiO_x and MoO_x thin films show good long term stability in natural atmosphere. After rapid thermal annealing, both NiO_x and MoO_x electrical properties change significantly. The NiO_x properties after annealing in Ar as compared to O_2 do not show dramatic difference, indicating that the change in properties during annealing is probably due to the evolution of the microstructure rather than a change in composition. In order to use NiO_x and MoO_x thin films as microbolometer sensing materials, the annealing effects on the film properties should be further investigated.

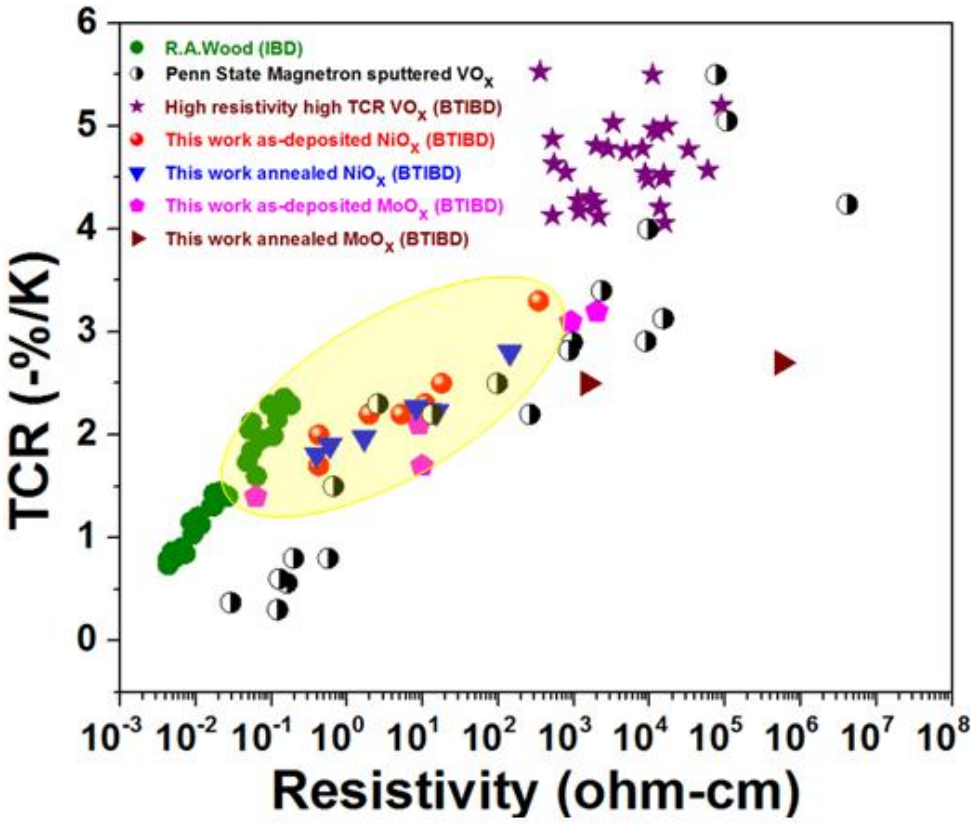

Figure 5-14. Resistivity versus TCR comparison among: VO_x prepared by ion beam deposition, pulsed dc magnetron sputtering, biased target ion beam deposition, and biased target ion beam deposited NiO_x and MoO_x.

Chapter 6

Conclusion

6.1 Conclusion

Nanocomposite vanadium oxide thin films with properties suitable for microbolometer devices have been prepared by reactive magnetron pulsed-dc sputtering with substrate bias. Reactive magnetron sputtering from a metallic V target is an inherently non-uniform process due to target hysteretic characteristics and the non-uniform oxidization across target surface. The hysteretic oxidation of the V target surface was assessed by measuring the average cathode current under different total O_2/Ar flow rates, processing pressure, and target-to-substrate distance. Non-uniform oxidation of the V target surface was analyzed by Raman spectroscopy. The VO_x thin film deposition rate, resistivity, and TCR values were greatly affected by the oxygen to Ar inlet ratio, processing pressure, throw distance, and the geometry of the delivery of reactive gas. The target hysteresis curve suggests that lower processing pressure leads to a more gradual transition of the V target surface oxidation which translates into better control of deposited film properties in the transition region of the hysteresis loop. It was found that a larger throw distance and an oxygen inlet near the substrate improve the as-deposited VO_x uniformity and process control. However, lower processing pressure and longer throw distance result in lower deposition rate. The overall conclusion for magnetron sputtered films is that once processing conditions are well understood and characterized, the deposited nanocomposite VO_x thin films show comparable bolometric properties to commercial ion beam deposited VO_x. These results suggest that reactive pulsed-dc magnetron sputtering can be an industrial alternative for depositing VO_x films for microbolometers and potentially offer advantages in terms of deposition rate and machine costs of a magnetron sputter system over one using an ion beam.

In Chapter 3, co-sputtering from a pure V target and a V_2O_5 target in the magnetron sputtering system was also investigated. Similar to reactive sputtering from a metallic V target, VO_x thin film TCR/resistivity was improved by applying 25 W substrate bias during the co-sputtering process. By varying the oxygen to Ar ratio, the film deposition rate was 35% higher than the one sputtered from a single V target, and the film uniformity was also improved. VO_x thin films prepared by co-sputtering from a V and V_2O_5 target showed comparable bolometric properties to VO_x prepared by IBD.

Other variations of magnetron reactive sputtering to deposite VO_x films were also explored for example, sputtering from a VC target, sputtering of a V_2O_5 or a V_2O_x target with various substrate biases, and reactive sputtering from a V target with H_2, O_2, and Ar mixtures. However, the results for the limited experiments performed did not indicate that these offered any advantages for fabricating VO_x thin films for microbolometer applications, due to either low deposition rate or limited TCR/resistivity combination.

In Chapter 4, a new method for making VO_x films was introduced BTIBD. High TCR (<-4.5%/K) high resistivity (1E3 to 1E5 Ω•cm) VO_x thin films were produced by the biased target ion beam deposition system. Compare to the high TCR (<-4%/K) VO_x films prepared by magnetron sputtering, the BTIBD prepared VO_x films had lower room temperature resistivity. Due to the low processing pressure (<1 mTorr) and the secondary condition of Ar+ ions to the substrate, these BTIBD prepared high TCR VO_x films were denser than their counterparts prepared by magnetron sputtering, and hence had better thermal stability. The addition of Mo in VO_x thin films significantly increased film deposition rate, which is desirable for commercial preparation of microbolometer sensing films. After annealing, the high TCR $(Mo/V)O_x$ thin film electrical properties changed little, suggesting good thermal stability. GIXRD results indicated that high TCR VO_x and $(Mo/V)O_x$ thin films were x-ray amorphous. These high TCR high resistivity VO_x and $(Mo/V)O_x$ thin films have the potential to be used as the sensing materials for

a through-film microbolometer pixel design. By using the through-film pixel design, high TCR VO_x can be utilized without introducing high Johnson noise, which is usually correlated to film resistance.

Although in the BTIBD system many processing parameters can be varied to engineer the deposited film properties, unfortunately, making films in the 0.1-10 Ω•cm range proved to be difficult. By increasing the oxygen partial pressure less than 1E-7 Torr, the VO_x film resistivity increased abruptly from 1E-4 Ω•cm to over 1000 Ω•cm. Other processing parameters such as the vanadium target bias voltage, pulse width, total processing pressure have been varied, however, it was still difficult to produce uniform VO_x thin films in the range of 0.01 to 10 Ω•cm.

Due to the difficult process control encountered for magnetron sputtering and BTIBD of VO_x thin films, other metal oxide thin films such as NiO_x and MoO_x thin films were investigated as potential microbolometer imaging layer materials as detailed in Chapter 5. BTIBD prepared as-deposited NiO_x thin film resistivity varied from 1 to 300 Ω•cm with TCR from -2.2 to -3.3 %/K, and as-deposited MoO_x thin film resistivity was found to vary from 3 to 2000 Ω•cm with TCR from -1.7 to -3.2 %/K, Similar to VO_x thin films, higher room temperature resistivity MoO_x and NiO_x films showed higher TCR values. BTIBD prepared NiO_x and MoO_x have TCR comparable to VO_x in the resistivity range of 0.1 to 100 Ω•cm.

GIXRD and spectroscopic ellipsometry were used to study the structure and optical properties of BTIBD prepared MoO_x and NiO_x thin films with different oxygen partial pressure. GIXRD results indicated that the room temperature resistivity of as-deposited MoO_x were amorphous. By increasing the oxygen partial pressure, the as-deposited MoOx thin film structure appeared to change from MoO_2 to MoO_3, and the MoO_3 peaks were broad. Though GIXRD characteristics changed little with further increasing of oxygen partial pressure, the room temperature resistivity of the as-deposited film increased over 2000 times. GIXRD results indicated that the as-deposited NiO_x films were polycrystalline. The film texture changed and the

compressive stress increased with an increase oxygen partial pressure, all other parameters remaining the same.

The optical properties extracted from the ellipsometry measurement suggested that the MoO_x prepared at low oxygen partial pressure (1E-6 Torr) had metallic like feature, and MoO_x prepared at higher oxygen partial pressure showed semiconductor like behavior. The absorption coefficient α at low energy (< 3eV) decreased with increasing of resistivity and oxygen partial pressure. Similar to semiconducting MoO_x and VO_x, the amplitude of the low energy feature for NiO_x decreases with increasing resistivity. Both of the BTIBD prepared semiconducting MoO_x and NiO_x optical index fell within the range reported in literatures. However, significant absorption below the reported band gap for both MoO_x and NiO_x indicated the existence of multiple valence states of Mo and Ni in the films.

Notably, by using the reactive BTIBD method, NiO_x and MoO_x thin film deposition had a much larger process window than VO_x in the regions with properties of interest for microbolometers. As mentioned earlier, process control was very difficult for low resistivity VO_x thin films deposited by reactive biased target ion beam deposition; films transitioned from metallic to high resistivity with a very small change in oxygen partial pressure. By contrast, MoO_x and NiO_x film properties were easily varied by controlling the oxygen partial pressure, and it was expected that process control for other deposition techniques such as diode or magnetron sputtering to be simpler for MoO_x and NiO_x than for VO_x. Measurement of aging effects suggested both MoO_x and NiO_x electrical properties have good long term stability. After annealing, MoO_x film resistivity increased significantly with TCR increasing only 25%. Similar to MoO_x, NiO_x film resistivity increased ~1000 times after annealing, but the TCR values also doubled. GIXRD showed that the annealing had little change in NiO_x film microstructure, but significant change in film stress. In the same TCR range, he measured 1/f noise of one NiO_x

sample was similar to that of PECVD a-Si, and higher than that of VO_x. The simple process control and the high TCR make MoO_x and NiO_x films of interest for microbolometer applications.

6.2 Future work

In this thesis it has been shown that reactive pulsed-dc magnetron sputtering can be an industrial alternative for depositing VO_x films for microbolometers provided the system is well understood and the processing parameters carefully monitored. The study of throw distance effects on deposited films properties was at fixed pressure (5 mTorr). It would be interesting to see how the throw distance affects the target hysteresis behavior and the deposited VO_x films properties at lower processing pressure (1 mTorr). As shown in this work, lower processing pressure leads to more gradual oxidation of the V target, but also results in lower deposition rate. However, the combination of the shorter throw distance and lower processing pressure may provide both good process control and relatively good deposition rate, which will be a useful guide for incorporating a VO_x deposition process using a magnetron sputtering system in the commercial microbolometer industry.

Vanadium oxide thin films prepared by reactive magnetron co-sputtering from a V and V_2O_5 targets have shown preliminary interesting results: comparable resistivity/TCR combination to IBD prepared VO_x, higher deposition rate, and improved film uniformity. In this work, the V target was pulsed-dc biased was fixed at 300 W whereas the V_2O_5 target was rf-biased at 200 W, and the total processing pressure was at 5 mTorr. The V:O ratio in the plasma and in the film during deposition can be further tailored by varying the power supplied to these two targets, the O_2 to Ar inlet ratio, and the total processing pressure. It may be possible to optimize the processing parameters and reach good process uniformity, high throughput, and good repeatability.

It has been shown that the process control is difficult for preparing VO_x in the range of 0.01-10 Ω•cm by uniform sputtering from V target, either in an RF diode system [92] or a BTIBD system. However, in all these systems, the oxygen supply was controlled either by fixed oxygen gas flow rates or fixed oxygen partial pressure during the deposition. As shown in Figure 6.1, a preliminary study in our group on an RF diode system showed that at a 2.5% oxygen supply content, the oxygen partial pressure increased by approximately 100%. A similar phenomenon has been observed in the BTIBD system: at a fixed oxygen partial pressure, the oxygen flow rate changed during the deposition. This may be the reason that it is hard to repeatedly produce VO_x in the range of 0.01-10 Ω•cm. One way to overcome this problem would be to employ a closed-loop control between the feed in oxygen content and the target cathode current (target surface oxidation) or film deposition rate (deposited film composition). In addition to the oxygen supply, the target power/voltage, and pulse width/frequency could also be used to closed-loop to better control the deposition process.

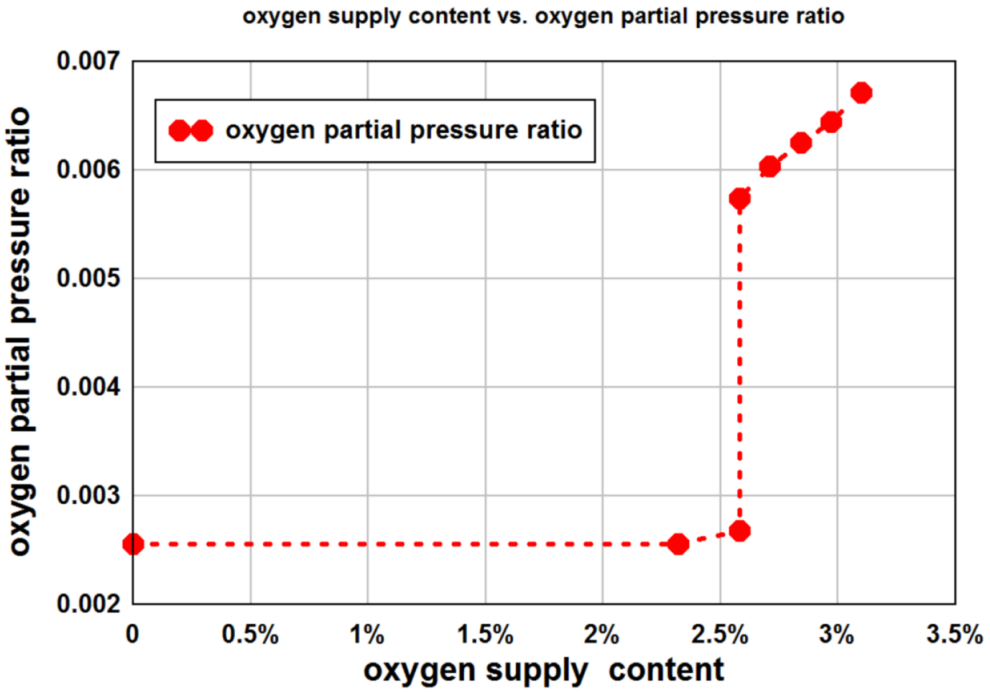

Figure 6-1. RGA measured oxygen partial pressure changes as a function of oxygen supply content (gas flow rates ratio of $O_2/(O_2+Ar)$, the Ar flow rate was fixed at 62 SCCM). (Plotted by Haoyu Li, measured in a rf diode system)

The 1/f noise behavior of BTIBD prepared high TCR high resistivity VO_x thin films has been studied and compared to PECVD prepared high TCR a-Ge and a-Si thin films by our group [48]. However, high TCR $(Mo/V)O_x$ thin films through-film resistivity, TCR and 1/f noise have not been investigated yet. Since $(Mo/V)O_x$ thin films have good thermal stability and much higher deposition rate than pure VO_x thin films, it is suggested that future work compare the 1/f noise of $(Mo/V)O_x$ thin films to other high TCR materials as candidates for next generation high sensitivity microbolometer with through-film structure pixels.

BTIBD prepared high TCR MoO_x and NiO_x have shown comparable TCR/resistivity combination to IBD prepared VO_x thin films. However, due to the off-axis geometry in our BTIBD system, the deposition rate is relatively low. Since the process control of NiO_x and MoO_x electrical properties was easy by varying oxygen partial pressure, it would be promising to prepare MoO_x and NiO_x by rf diode or magnetron sputtering, or in a BTIBD system that was optimized for throughput by having the substrate parallel to the target. Even though the GIXRD characteristics showed that no significant change of NiO_x thin film microstructure before and after annealing, cross-section SEM or TEM might be useful to further understand the microstructure evolution by annealing. The measured 1/f noise of a NiO_x was similar to a-Si. However, as one of the important bolometric properties, the 1/f noise of MoO_x and NiO_x thin films should be further extensively studied. The correlation between MoO_x/NiO_x film 1/f noise to the material composition, microstructure, and band structure should be investigated. It will be interesting to see how the 1/f noise of MoO_x and NiO_x effects by different processing parameters and post-annealing treatment.

Thin NiO_x and MoO_x films have been reported as useful hole injection layers for organic light-emitting diodes (OLED) [93], [94],[95] and anode buffer layers in organic photovoltaic cells

(OPV) [96], [97] to improve device efficiency and stability. The BTIBD prepared NiO_x and MoO_x thin films are potentially interesting for this application. They have a large range of electrical properties, ultra-smooth film surface over a broad range of composition (<2 nm), and good long term electrical properties stability. Due to these properties, it would be interesting to investigate the structural and electrical functionality of BTIBD prepared NiO_x and MoO_x in OLED and OPV devices.

Appendix A

Lithography Steps to Pattern NiO_x Thin Films

1. Clean SiO_2 wafer using acetone, rinse with IPA, and blow dry.
2. Spin 495 PMMA C4 at 4000 rpm for 30 sec (~1micron).
3. Bake at 160^{o}C for 10 min.
4. Spin 1811 photoresist at 4000 rpm for 40 sec (~1 micron).
5. Soft bake at 90^{o}C for 90 sec.
6. Use bright field active layer isolation mask and exposure for 50 sec.
7. Reverse bake in NH_3 at 90^{o}C for 60 min.
8. Put samples under flood exposure for 75 sec.
9. Develop in 5:1 DI water:351 solution for about 40 sec or until appropriately developed, rinse with DI water and blow dry.
10. Remove residual resist at 1811 and PMMA interface by using oxygen RIE for 3 min.
11. Expose the sample under deep UV for 400 sec.
12. Develop in toluene for 1 min and blow dry.
13. Remove residual resist between PMMA and oxide layer below.
14. Deposit NiO_x thin films.
15. Lift off in acetone, rinse with IPA and blow dry.
16. Spin LOR 5B at 4000 rpm for 40 sec .
17. Bake at 160^{o}C for 5 min.
18. Spin 1811 photoresist at 4000 rpm for 45 sec.
19. Soft bake at 90^{o}C for 90 sec.
20. Use top metal liftoff mask align, and expose for 53 sec.
21. Develop in 3.5:1 DI water: 351 solution for 90 sec or until appropriately developed (see double line), rinse with DI water and blow dry.

22. Sputter deposit 100 nm of Ti.
23. Anneal sample at 120^{o}C for 5 min.
24. Liftoff on hotplate in NMP (N-Methyl-2-pyrrolidone), clean with IPA and blow dry.

Appendix B

Study of BTIBD System Processing Parameters Effects

As mentioned in Chapter 2, in this 4-Wave LANS BTIBD system, the ion source, the biased targets, and reactive gas partial pressure can be independently controlled. In this section, processing parameters of the ion source and the biased targets are investigated. Target bias current is used to evaluate the process stability.

First, the discharge current and the ion source Ar flow rate effects on the ion source discharge bias and target bias current were studied. In this system, the ion source discharge power supply was set at the constant-current mode of operation and the highest discharge voltage could not exceed 100 Volts (the average ion beam energy is lower than 60 eV).

In this set of experiments, the working gas was Ar and three targets (V, Si, and Ti) were biased. The neutralizer (Neut.) keeper current was set to 1.5 Amp and Neut. bias current was 0.5 Amp higher than the ion source discharge current (keep the plasma neutralized). The applied power on all three biased targets was -800 Volts and the pulse width was 1 μsec, whereas the pulse period was 100 μsec (10 kHz pulse frequency).

Figure B-1 shows the discharge voltage and target bias current change as a function of the discharge current.

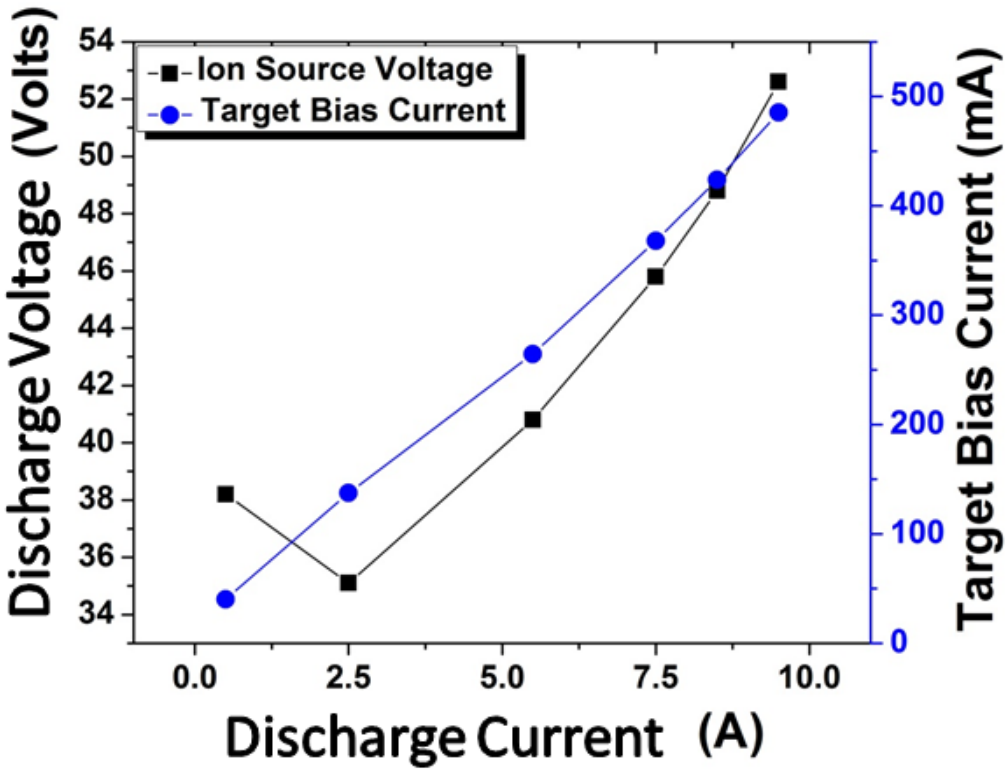

Figure B-2. HC Ar flow rate is 9 SCCM, source Ar flow rate is 60 SCCM and oxygen flow rate is 0 SCCM. The total pressure is around 0.7 mTorr. The discharge voltage and target bias current change as a function of discharge current.

Figure B-1 shows that with a fixed ion source Ar flow rate (60 SCCM), the discharge voltage increases as the ion source discharge current increases. Increasing the discharge current also leads to an increase in the target bias current. When discharge current varies from 0.5 Amp to 9.5 Amp, the target bias current increases from 40 mAmp to 483 mAmp, suggesting an increase of the target sputtering rate.

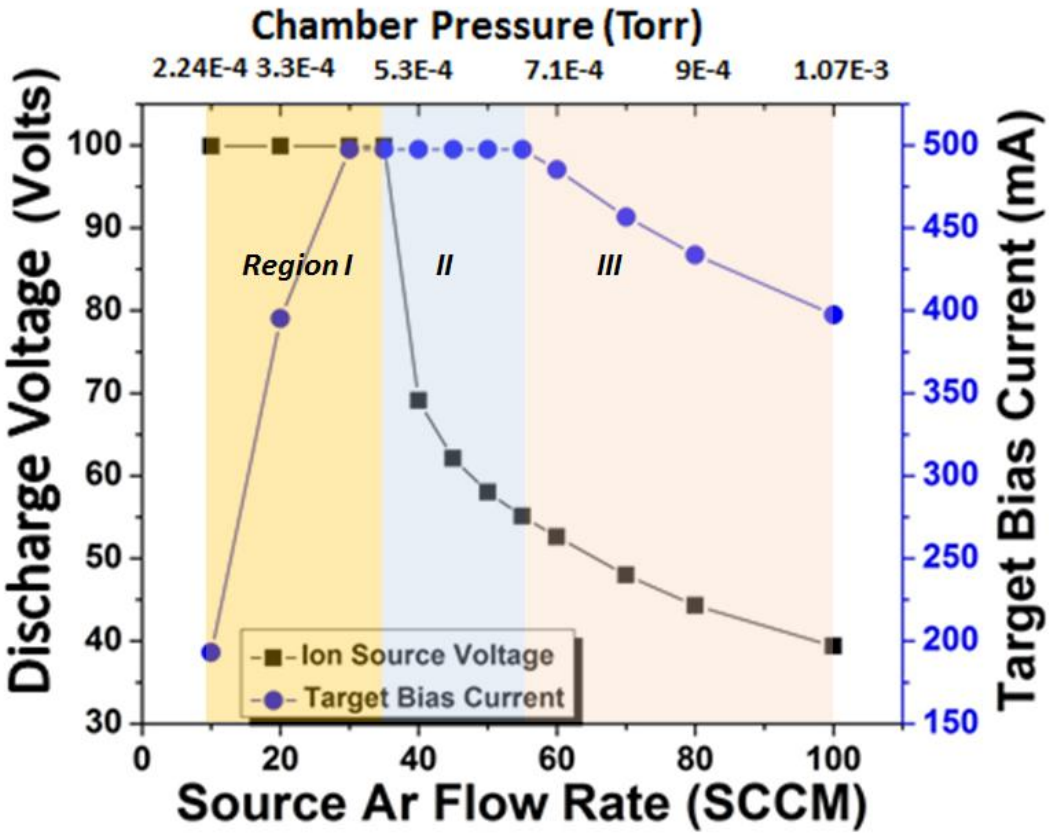

Figure B-3. HC Ar flow rate is 9 SCCM and discharge current is 9.5 Amp (Neut. Bias current 10 Amp). Discharge voltage and target bias current change as a function of source Ar flow rate.

Figure B-2 shows that at a fixed ion source discharge current (9.5 Amp), the discharge voltage and target bias current also change as a function of the source Ar flow rate. Different from the ion source discharge power supply, the target bias power supply is set at the constant-voltage mode of operation and the total target bias current cannot exceed 500 mAmp. As shown in Figure B-2, in Region I, the source Ar flow rate is between 8 SCCM to 35 SCCM, the ion source voltage exceeds the set point (100Volts), and the discharge current and the target bias current is not stable. In this region, the target bias current is limited by the ion source. In Region II, when the source Ar is between 40 to 55 SCCM, the ion source current can be maintained stably at 9.5 SCCM, and the discharge voltage drops as the source Ar flow rate increases. Though

the ion source is stable in this region, the target bias current reaches its highest value (500 mAmp) which causes an instability at the target bias set point voltage (-800 Volts). In Region III, when the source Ar flow rate is greater than 60 SCCM, the target bias voltage is stable at -800 Volts. Further increasing the source Ar flow leads to a decrease of the discharge voltage and the target bias current. The result suggests that the source Ar flow rate should be maintained in Region III to operate the ion source and bias target stably. To reach the highest target bias current (highest sputtering rate), the source Ar should be the lowest value in the Region III (different ion source discharge current will have different value).

With fixed ion source parameters, the parameters of the biased target were also investigated. In this set of experiments, the HC Ar was fixed at 9 SCCM and source AR flow rate was 60 SCCM. The Neutralizer keeper current was 1.5 Amp, and ion sources charge current was 9.5 Amp whereas the discharge voltage was about 45 Volts.

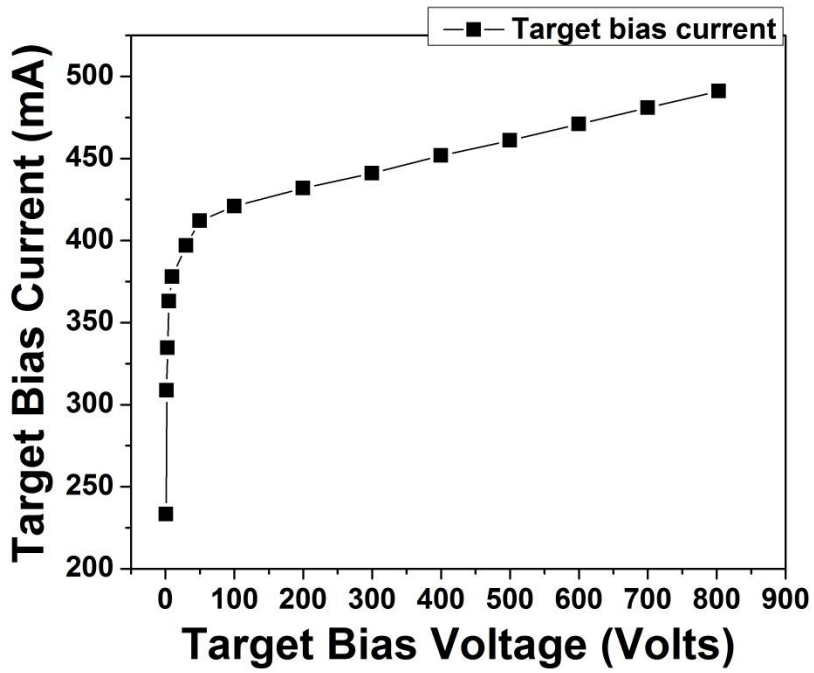

Figure B-3. When pulse width is 1 μsec and pulse period is 100 μsec, the target bias current change as a function of negative target bias voltage.

As shown in Figure B-3, when the target bias voltage changes from 0 to -100 Volts, the target bias current increases quickly. When target bias voltage further increases from -100 V to -800 V, the target bias current increases linearly.

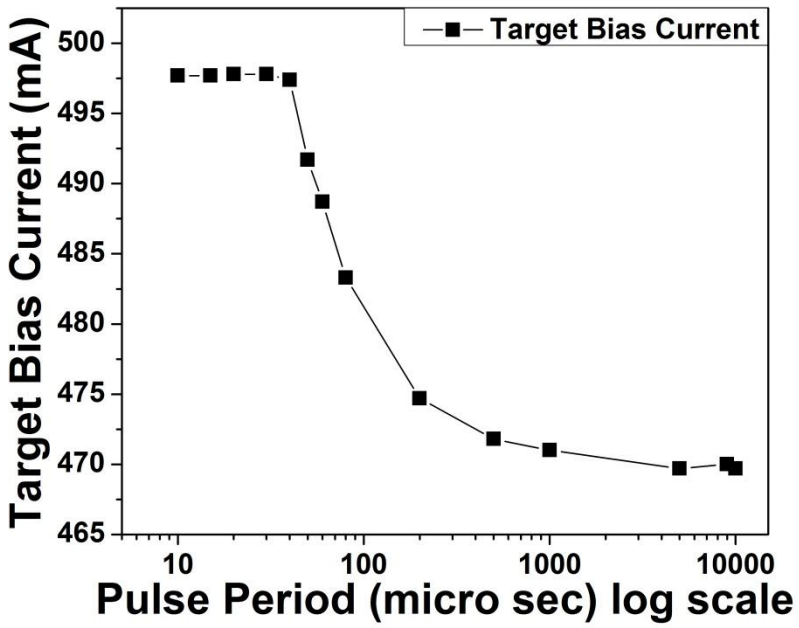

Figure B-4. Target bias current changes as a function of pulse period (frequency) when pulse width is fixed at 1 μsec.

Figure B-4 shows that the when the pulse width is fixed at 1 μsec and the target bias voltage at -800 Volts, the target bias current change as a function of pulse period. When the pulse period is lower than 30 μsec, the target bias current does not change as the pulse period increases. Further increasing the pulse period leads to a decrease of the target bias current. This result indicates that a shorter pulse period (higher frequency) leads to higher target bias current, suggesting a higher target sputtering rate. However, due to the voltage overshoot when the

positive pulse is applied, the pulse period should not be too short in order to improve the film deposition controllability and repeatability.

Bibliography

[1] T. Zaveri, M. Zaveri, I. Makwana, and H. Mehta, "An optimized region-based color transfer method for night vision application," *2010 Int. Conf. Signal Image Process.*, pp. 96–101, Dec. 2010.

[2] P. W. Kruse, V. Tt, R. Enhancement, O. Lithography, A. K. Wong, O. Design, and B. H. Walker, *Uncooled Thermal Imaging: Arrays, Systems and Applications.* 2001.

[3] R.A.Wood, *Monolithic Silicon Microbolometer Arrays*. San Diego : Academic Press. 1997.

[4] T. Akin, "CMOS-based Thermal Sensors," in *Advanced Micro and Nanosystems*, vol. 2, 2005, pp. 479–512.

[5] W. Radford, D. Murphy, M. Ray, S. Propst, A. Kennedy, J. Kojiro, J. Woolaway, and K. Soch, "320 x 240 silicon microbolometer uncooled IRFPAs with on-chip offset correction ," *Infrared Detectors and Focal Plane Arrays IV, SPIE, Orlando, FL.* vol. 2746, pp. 82–92,1996.

[6] A.J. Syllaios, T.R. Schimert, R.W.Gooch, W. L. McCardel, B.A. Ritchey, "Amorphous Silicon Microbolometer Technology," in *Mat. Res.Soc.Symp.*,vol. 609, 2000, pp. 1–6.

[7] T. Schimert, C. Hanson, J. Brady, T. Fagan, M. Taylor, W. McCardel, R. Gooch, M. Gohlke, and A. J. Syllaios, "Advances in small-pixel, large-format α-Si bolometer arrays," in *Advances in small-pixel, large-format α-Si bolometer arrays*, vol. 7298, 2009,pp. 72980T1-5.

[8] M. Almasri, S. Member, D. P. Butler, and S. Member, "Self-Supporting Uncooled Infrared Microbolometers With Low-Thermal Mass," *Journal of Microelectromechanical Systems*, vol. 10, pp. 469–476, 2001.

[9] Y. S. Lee, D. S. Kim, Y.-C. Jung, and H. C. Lee, "Electric characteristic of nickel oxide film for the mirobolometer," in *Proc. of SPIE Infrared Technology and Applications XXXVII*, vol. 8012, pp. 80121P7, May 2011.

[10] D. S. Kim, I. W. Kwon, C. H. Hwang, H. C. Lee, and Y. S. Lee, "Properties of reactively sputtered nickel oxide films as a microbolometer sensing material," in *Proc. SPIE 7660 Infrared Technology and Applications XXXVI*, 2010,pp. 76601B.

[11] A. Rogalski, "Infrared Detectors for the Future." *ACTA Physica Polonica A.*, vol. 116, pp.389-405, 2009.

[12] Y. S. Yoon, J. S. Kim, and S. H. Choi, "Structural and electrochemical properties of vanadium oxide thin films grown by d.c. and r.f. reactive sputtering at room temperature," *Thin Solid Films*, vol. 460, pp. 41–47, Jul. 2004.

[13] N. Fieldhouse, S. M. Pursel, M. W. Horn, and S. S. N. Bharadwaja, “Electrical properties of vanadium oxide thin films for bolometer applications: processed by pulse dc sputtering,” *J. Phys. D. Appl. Phys.*, vol. 42, pp. 055408, Mar. 2009.

[14] J. Zhang, J. M. Mcgraw, J. Turner, and D. Ginleyt, “Charging Capacity and Cycling Stability of VO Films Prepared by Pulsed Laser Deposition,” *Journal of The Electrochemical Society*, vol. 144, No. 5, pp. 1630–1634, 1997.

[15] M. Soltani, M. Chaker, E. Haddad, R. V. Kruzelecky, and D. Nikanpour, “Optical switching of vanadium dioxide thin films deposited by reactive pulsed laser deposition,” *J. Vac. Sci. Technol. A Vacuum, Surfaces, Film.*, vol. 22, pp. 859, 2004.

[16] C. H. Griffiths, “Influence of stoichiometry on the metal-semiconductor transition in vanadium dioxide,” *J. Appl. Phys.*, vol. 45, pp. 2201, 1974.

[17] U. Schwingenschlögl, and V. Eyert, “The vanadium Magnéli phases VnO2n-1,” *Ann. Phys.*, vol. 13, pp. 475–510, Sep. 2004.

[18] J. B. Goodenough, “The Two Components of the Crystallographic Transition in VO_2,” *Journal of Solid Stae Chemistry*, vol. 3, Issue 4, pp. 490–500, 1971.

[19] J. Bullot, O. Gallais, M. Gauthier, and J. Livage, “Semiconducting properties of amorphous V2O5 layers deposited from gels,” *Appl. Phys. Lett.*, vol. 36, pp. 986, 1980.

[20] T. Allersma, “Structure and Physical Properties of Solid and Liquid Vanadium Pentoxide,” *J. Chem. Phys.*, vol. 46, pp. 154, 1967.

[21] R.A.Wood, “Uncooled thermal imaging with monolithic silicon focal planes,” in *SPIE 2020* I*nfrared Technology XIX 322*, 1993, pp. 322–329.

[22] V. R. Mehta, S. Shet, N. M. Ravindra, a. T. Fiory, and M. P. Lepselter, “Silicon-integrated uncooled infrared detectors: Perspectives on thin films and microstructures,” *J. Electron. Mater.*, vol. 34, pp. 484–490, May 2005.

[23] S. B. Wang, S. B. Zhou, G. Huang, and X. J. Yi, “VOx thin films obtained by ion beam sputtering and oxidation process,” *Surf. Coatings Technol.*, vol. 191, pp. 330–334, Feb. 2005.

[24] R. Cole, B. Higashi, R. Ridley, J. Wood, “Integrated vacuum packaging for low-cost light-weight uncooled microbolometer arrays,” in *SPIE 4369 Infrared Technology and Applications XXVII*, 2001, vol. 4369, pp. 235–239.

[25] B E Cole, C.J. Zins, “Flexible high performance microbolometer detector material fabricated via controlled ion beam sputter deposition process,” U.S. Patent 6322670 B2, Nov. 27, 2001.

[26] H. Wang, X. Yi, S. Chen, S. He, and X. Fu, “Reactive Ion Beams Sputtering of Vanadium Oxides Films for Uncooled Microbolometer,” *Int. J. Infrared Millimeter Waves*, vol. 26, pp. 421–431, Feb. 2005.

[27] E. E. Chain, “The influence of deposition temperature on the structure and optical properties of vanadium oxide films,” *J. Vac. Sci. Technol. A Vacuum, Surfaces, Film.*, vol. 4, pp. 432, May 1986.

[28] E. E. Chain, “Effects of oxygen in ion-beam sputter deposition of vanadium oxide,” *J. Vac. Sci. Technol. A Vacuum, Surfaces, Film.*, vol. 5, pp. 1836, Jul. 1987.

[29] Z. Luo, Z. Wu, T. Wang, W. Li, and Y. Jiang, “Effects of oxygen content on the microstructures and optical properties of thermochromic vanadium oxide thin films,” *Philos. Mag.*, vol. 92, pp. 471–479, Feb. 2012.

[30] Y. Lv, M. Hu, M. Wu, and Z. Liu, “Preparation of vanadium oxide thin films with high temperature coefficient of resistance by facing targets d.c. reactive sputtering and annealing process,” *Surf. Coatings Technol.*, vol. 201, pp. 4969–4972, Feb. 2007.

[31] R. T. Rajendra Kumar, B. Karunagaran, D. Mangalaraj, S. K. Narayandass, P. Manoravi, M. Joseph, and V. Gopal, “Pulsed laser deposited vanadium oxide thin films for uncooled infrared detectors,” *Sensors Actuators A Phys.*, vol. 107, pp. 62–67, Oct. 2003.

[32] H. K. Kang, Y. H. Han, H. J. Shin, S. Moon, and T. H. Kim, “Enhanced infrared detection characteristics of VO[sub x] films prepared using alternating V[sub 2]O[sub 5] and V layers,” *J. Vac. Sci. Technol. B Microelectron. Nanom. Struct.*, vol. 21, pp. 1027, 2003.

[33] B. D. Gauntt, E. C. Dickey, and M. W. Horn, “Stoichiometry and microstructural effects on electrical conduction in pulsed dc sputtered vanadium oxide thin films,” *J. Mater. Res.*, vol. 24, pp. 1590–1599, Jan. 2011.

[34] N. J. Podraza, B. D. Gauntt, M. a. Motyka, E. C. Dickey, and M. W. Horn, “Electrical and optical properties of sputtered amorphous vanadium oxide thin films,” *J. Appl. Phys.*, vol. 111, pp. 073522, 2012.

[35] O. M. Cabarcos, H. A. Basantani, S. S. N. Bharadwaja, J. Li, B. D. Gauntt, S. Antrazi, E. C. Dickey, D. L. Allara, and M. W. Horn, “Comparison of ion beam and magnetron sputtered vanadium oxide thin films for uncooled IR imaging,” In SPIE 8012 Infrared Technology and Applications XXXVII,2011,pp. 80121.

[36] H. A. Basantani, S. Kozlowski, M.-Y. Lee, J. Li, E. C. Dickey, T. N. Jackson, S. S. N. Bharadwaja, and M. Horn, “Enhanced electrical and noise properties of nanocomposite vanadium oxide thin films by reactive pulsed-dc magnetron sputtering,” *Appl. Phys. Lett.*, vol. 100, pp. 262108, 2012.

[37] A. Ozcelik, O. Cabarcos, D. L. Allara, and M. W. Horn, “Vanadium Oxide Thin Films Alloyed with Ti, Zr, Nb, and Mo for Uncooled Infrared Imaging Applications,” *J. Electron. Mater.*, vol. 42, pp. 901–905, Oct. 2012.

[38] B. D. Gauntt, J. Li, O. M. Cabarcos, H. a. Basantani, C. Venkatasubramanian, S. S. N. Bharadwaja, N. J. Podraza, T. N. Jackson, D. L. Allara, S. Antrazi, M. W. Horn, and E. C. Dickey, "Microstructure of vanadium oxide used in microbolometers," in SPIE 8012 Infrared Technology and Applications XXXVII, 2011, pp. 80123T.

[39] B. D. Gauntt, "The nano-composite nature of vanadium oxide thin films for use in infrared microbolometer," Ph.D. disertation, The Pennsylvanai State University, Pennsylvania, USA, 2011.

[40] J. Li, B. D. Gauntt, and E. C. Dickey, "Microtwinning in highly nonstoichiometric VOx thin films," *Acta Mater.*, vol. 58, pp. 5009–5014, Sep. 2010.

[41] C. Venkatasubramanian, "Preparation, characterization and post-deposition modification of pulsed-dc magnetron sputtered vanadium oxide thin films for microbolometer appliations," Ph.D. disertation, The Pennsylvania State Unviersity, Pennsylvania, USA, 2010.

[42] D. B. Saint John, H.-B. Shin, M.-Y. Lee, S. K. Ajmera, a. J. Syllaios, E. C. Dickey, T. N. Jackson, and N. J. Podraza, "Influence of microstructure and composition on hydrogenated silicon thin film properties for uncooled microbolometer applications," *J. Appl. Phys.*, vol. 110, pp. 033714, 2011.

[43] D. B. Saint John, H.-B. Shin, M.-Y. Lee, E. C. Dickey, N. J. Podraza, and T. N. Jackson, "Thin film silicon and germanium for uncooled microbolometer applications,"in *SPIE 8012 Infrared Technology and Applications XXXVII*, 2011, pp. 80123U.

[44] S. Won, J. Li, M. Lee, E. Dickey, and T. Jackson, "New Materials for Uncooled IR Imaging : Nickel Manganite Thin Films Grown by Spin Spray," in *SPIE 8012 Infrared Technology and Applications XXXVII*, 2011, pp. 80123S.

[45] S. W. Ko, J. Li, N. J. Podraza, E. C. Dickey, and S. Trolier-McKinstry, "Spin Spray-Deposited Nickel Manganite Thermistor Films For Microbolometer Applications," *J. Am. Ceram. Soc.*, vol. 94, pp. 516–523, Feb. 2011.

[46] H. A. Basantani, "Effect of RF substrate bias on vanadium oxide thin films during reactive pulsed dc magnetron sputter deposition," M.S. thesis, The Pennsylvania State University, Pennsylvania, USA, 2011.

[47] D. B. Saint John "Optical and Electrical Characterization of High Resistivity Semiconductors for Constant-bias Microbolometer Devices," Ph.D. dissertation, The Pennsylvania State University, Pennsylvania, USA, 2012.

[48] H. A. Basantani, D. B. Saint John, N. J. Podraza, T. N. Jackson, and M. W. Horn, "Evaluation of 1/f noise in prospective IR imaging thin films," in *Proc. SPIE 9070 Infrared technology and Applications XL*, 2014, pp. 90701P.

[49] D. Baldwin, M. Martyniuk, and R. C. Woodward, "Synthesis Route to Garnet and Perovskite Thin Films via Quad-Reactive Co-Sputter Deposition of Amorphous Non-

Equilibrium Alloy Oxides and Subsequent Annealing," in *Proc. 52 nd Annual Technical Conference*,2009, pp. 15–18, DOI: ISSN 0737-5921.

[50] T. L. Hylton, B. Ciorneiu, D. a. Baldwin, O. Escorcia, J. Son, M. T. McClure, and G. Waters, "Thin film processing by biased target ion beam deposition," *IEEE Trans. Magn.*, vol. 36, pp. 2966–2971, 2000.

[51] "Sputter yield for different elements." Internet: http://www.iuvsta.org/IUVSTA_Educational_Material.html.[Oct.21 2014]

[52] D. A. Baldwin, D. Jena, N. Dame, and S. Bend, "Progress on Gallium Nitride Semiconductor Growth by Plasma Sputtering," in *Proc. 51st annual Technical Conference*, 2008, pp.20-22, DOI: ISSN 0737-5921.

[53] K. G. West, J. Lu, J. Yu, D. Kirkwood, W. Chen, Y. Pei, J. Claassen, and S. a. Wolf, "Growth and characterization of vanadium dioxide thin films prepared by reactive-biased target ion beam deposition," *J. Vac. Sci. Technol. A Vacuum, Surfaces, Film.*, vol. 26, pp. 133, 2008.

[54] K. G. West, J. Lu, L. He, D. Kirkwood, W. Chen, T. P. Adl, M. S. Osofsky, S. B. Qadri, R. Hull, and S. a. Wolf, "Ferromagnetism in Rutile Structure Cr Doped VO2 Thin Films Prepared by Reactive-Bias Target Ion Beam Deposition," *J. Supercond. Nov. Magn.*, vol. 21, pp. 87–92, Jan. 2008.

[55] H. N. G. Wadley, X. W. Zhou, and J. J. Quan, "Biased Target Ion Beam Deposition of Spin-valves", Internet: http://www.4waveinc.com/BTD%20of%20Spin-valves_030823.pdf, [Oct.21 2014].

[56] P. V. Bharathy, D. Nataraj, P. K. Chu, H. Wang, Q. Yang, M. S. R. N. Kiran, J. Silvestre-Albero, and D. Mangalaraj, "Effect of titanium incorporation on the structural, mechanical and biocompatible properties of DLC thin films prepared by reactive-biased target ion beam deposition method," *Appl. Surf. Sci.*, vol. 257, pp. 143–150, Oct. 2010.

[57] P. VijaiBharathy, Y.-Y. Chang, D. Nataraj, Q. Yang, S.-M. Yang, D. Mangalaraj, L. Yang, and T. J. Webster, "Effect of nickel incorporation on structural, nanomechanical and biocompatible properties of amorphous hydrogenated carbon thin films prepared by low energy biased target ion beam deposition," *Thin Solid Films*, vol. 519, pp. 1623–1628, Dec. 2010.

[58] W. Chen, D. N. H. Nam, J. Lu, K. G. West, and S. a. Wolf, "Effects of target bias voltage in magnetic tunnel junctions grown by ion beam deposition," *J. Appl. Phys.*, vol. 106, pp. 013905, 2009.

[59] H. N. G. Wadley, X. W. Zhou, and J. J. Quan, "Biased Target Ion Beam Deposition of GMR Multilayers," Internet: http://www.virginia.edu/ms/research/wadley/Documents/Publications/Biased.Target.Ion.Beam.Deposition.of.GMR.Multilayers.pdf, [Oct.21, 2014].

[60] S. Berg and T. Nyberg, “Fundamental understanding and modeling of reactive sputtering processes,” *Thin Solid Films*, vol. 476, pp. 215–230, Apr. 2005.

[61] W. D. Sproul, D. J. Christie, and D. C. Carter, “Control of reactive sputtering processes,” *Thin Solid Films*, vol. 491, pp. 1–17, Nov. 2005.

[62] C. Venkatasubramanian, O. M. Cabarcos, W. R. Drawl, D. L. Allara, S. Ashok, M. W. Horn, and S. S. N. Bharadwaja, “Process-structure-property correlations in pulsed dc reactive magnetron sputtered vanadium oxide thin films,” *J. Vac. Sci. Technol. A Vacuum, Surfaces, Film.*, vol. 29, pp. 061504, 2011.

[63] I. Safi, “Recent aspects concerning DC reactive magnetron sputtering of thin films: a review,” *Surf. Coatings Technol.*, vol. 127, pp. 203–218, May 2000.

[64] H. R. Kaufman, “Broad-beam ion sources: Present status and future directions,” *J. Vac. Sci. Technol. A Vacuum, Surfaces, Film.*, vol. 4, pp. 764, May 1986.

[65] S. Kaufman, “Broad-Beam Industrial Ion Sources Technical Note KRI-01,”Internet: http://www.ionsources.com/PDF/TN-01%20BB%20Industrial%20Ion%20Sources%209-06.pdf, 2006, [Oct. 21, 2014].

[66] F. Collins, “EH1000 ION SOURCE MANUAL HCES VERSION EH1000 ION SOURCE MANUAL,” 2003.

[67] V. V Zhurin, *Industrial Ion Sources: Broadbem Gridless Ion Source Technology*, Wiley-VCH Verlag GmbH & Co. KGaA., 2012, pp. 203–205.

[68] V. V. Zhurin, H. R. Kaufman, J. R. Kahn, and T. L. Hylton, “Biased target deposition,” *J. Vac. Sci. Technol. A Vacuum, Surfaces, Film.*, vol. 18, pp. 37, 2000.

[69] F.N. Hooge, T. G. M. Kleinpenning, and L.K.J. Vandamme, “Experimental studies on 1/f noise,” Rep. Prog. Phys. vol. 44, pp.479, 1981.

[70] L. Abello, E. Husson, Y. Repelin, and G. Lucazeau, "Vibrational-spectra and valence force-field of crystalline V2O5," *Spectrochimica Acta Part A-Molecular and Biomolecular Spectroscopy*, vol. 39, pp. 641-651, 1983.

[71] M. Y. Liao, Y. Gotoh, H. Tsuji, and J. Ishikawa, “Deposition of vanadium carbide thin films using compound target sputtering and their field emission,” *J. Vac. Sci. Technol. A Vacuum, Surfaces, Film.*, vol. 23, pp. 1379, 2005.

[72] H. A. Basantani, H.-B. Shin, T. N. Jackson, and M. W. Horn, “Vertically integrated pixel microbolometers for IR imaging using high-resistivity VO_x,” in *Proc. SPIE 8704 Infrared Technology and Applications XXXIX*, 2013, pp. 87041A.

[73] M. A. K. and E. Z. K. V I Anisimov, “Band-structure description of Mott insulators,” *J. Phys. Condens. Matter*, vol. 39723, pp. 3973–3987, 1990.

[74] J. E. K. and J. M. Honig, “SELECTED ELECTRICAL AND THERMAL PROPERTIES OF UNDOPED NICKEL OXIDE,” 1978.

[75] S. Nandy, U. N. Maiti, C. K. Ghosh, and K. K. Chattopadhyay, “Enhanced p-type conductivity and band gap narrowing in heavily Al doped NiO thin films deposited by RF magnetron sputtering.,” *J. Phys. Condens. Matter*, vol. 21, pp. 115804, Mar. 2009.

[76] W.L. Jang, Y.M. Lu, W.S. Hwang, T.L. Hsiung, and H. P. Wang, “Point defects in sputtered NiO films,” *Appl. Phys. Lett.*, vol. 94, pp. 062103, 2009.

[77] N. J. Podraza, B. D. Gauntt, M. a. Motyka, E. C. Dickey, and M. W. Horn, “Electrical and optical properties of sputtered amorphous vanadium oxide thin films,” *J. Appl. Phys.*, vol. 111, pp. 073522, 2012.

[78] H. L. Lu, G. Scarel, M. Alia, M. Fanciulli, S.-J. Ding, and D. W. Zhang, “Spectroscopic ellipsometry study of thin NiO films grown on Si (100) by atomic layer deposition,” *Appl. Phys. Lett.*, vol. 92, pp. 222907, 2008.

[79] and H. L. Jun-Woo Park, Kwang Nam Choi, Seoung Ho Baek, Kwan Soo Chung, “Optical Properties of NiO Thin Films Grown by Using Sputtering Deposition and Studied with Spectroscopic Ellipsometry,” *J. Korean Phys. Soc.*, vol. 52, pp. 1868–1876, 2008.

[80] M. A. Guziewicz, J. A. Grochowski, M. I. Borysiewicz, and E. L. Kaminska, “Electrical and optical properties of NiO films deposited by magnetron sputtering,” Optica Applicata, vol. 41, pp. 431-440, 2011.

[81] G. A. Sawatzky and J.W. Allen, “Magnitude and origin of the band gap in NiO,” *Phys. Rev. Lett.*, vol. 53, pp. 2339–2342, 1984.

[82] A. J. Varkey and A. F. Fort, “Transparent conducting cadmium oxide thin films prepared by a solution growth technique,” *Thin Solid Films*, vol. 239, pp. 211–213, 1994.

[83] Z. Li, T. Schram, T. Witters, H.-J. Cho, B. O’Sullivan, N. Yamada, T. Takaaki, J. Hooker, S. De Gendt, and K. De Meyer, “Investigation on Molybdenum and Its Conductive Oxides as p-Type Metal Gate Candidates,” *J. Electrochem. Soc.*, vol. 155, pp. H481, 2008.

[84] S. Tiwari, R. Master, R. J. Choudhary, D. M. Phase, and B. L. Ahuja, “Effect of oxygen partial pressure and Fe doping on growth and properties of metallic and insulating molybdenum oxide thin films,” *J. Appl. Phys.*, vol. 111, pp. 083905, 2012.

[85] N. Oka, H. Watanabe, Y. Sato, H. Yamaguchi, N. Ito, H. Tsuji, and Y. Shigesato, “Study on MoO[sub 3−x] films deposited by reactive sputtering for organic light-emitting diodes,” *J. Vac. Sci. Technol. A Vacuum, Surfaces, Film.*, vol. 28, npp. 886, 2010.

[86] H. Simchi, B. E. McCandless, T. Meng, J. H. Boyle, and W. N. Shafarman, “Characterization of reactively sputtered molybdenum oxide films for solar cell application,” *J. Appl. Phys.*, vol. 114, pp. 013503, 2013.

[87] A. Szekeres, T. Ivanova, and K. Gesheva, “Spectroscopic ellipsometry study of CVD molybdenum oxide films: effect of temperature,” *J. Solid State Electrochem.*, vol. 7, pp. 17–20, Dec. 2002.

[88] M. A. Motyka, “Effects of microstructure and oxidation state of multi-valent vanadium oxie thin films for use in infrared microbolometers,” Ph.D. dissertation, The Pennsylvania State University, Pennsylvania, USA, 2012.

[89] R. A. May, L. Kondrachova, B. P. Hahn, and K. J. Stevenson, “Optical Constants of Electrodeposited Mixed Molybdenum - Tungsten Oxide Films Determined by Variable-Angle Spectroscopic Ellipsometry,” *J. Phys. Chem.C*, vol. 111, pp. 18251–18257, 2007.

[90] D. O. Scanlon, G. W. Watson, D. J. Payne, G. R. Atkinson, R. G. Egdell, and D. S. L. Law, “Theoretical and Experimental Study of the Electronic Structures of MoO 3 and MoO 2,” *J. Phys. Chem.C*, vol. 114, pp. 4636–4645, 2010.

[91] D. S. Kim, I. W. Kwon, C. H. Hwang, H. C. Lee, and Y. S. Lee, “Properties of Reactive sputtered nickel oxide films as a microbolometer sensing material,” in *Proc. SPIE 7660 Infrared Technogloy and Applications XXXVI*, 2010, pp. 76601B.

[92] H. U. Li and T. N. Jackson, “Controllability of RF Diode Sputter Vanadium Oxide Thin Films,” Presented at the Electronic Material Conference, State College, Pennsylvania, USA, 2012.

[93] I.-M. Chan, T.-Y. Hsu, and F. C. Hong, “Enhanced hole injections in organic light-emitting devices by depositing nickel oxide on indium tin oxide anode,” *Appl. Phys. Lett.*, vol. 81, pp. 1899, 2002.

[94] S. Tokito, K. Noda, and Y. Taga, “Metal oxides as a hole-injecting layer for an organic electroluminescent device,” *J. Phys. D Appli. Phys*, vol. 29, pp. 2750–2753, 1996.

[95] Q. Fu, J. Chen, and C. Shi, “Room-Temperature Sol − Gel Derived Molybdenum Oxide Thin Films for E ffi cient and Stable Solution-Processed Organic Light-Emitting Diodes,” *Appl. Mater. interfaces*, vol. 5, pp. 6024–6029, 2013.

[96] M. D. Irwin, J. D. Servaites, D. B. Buchholz, B. J. Leever, J. Liu, J. D. Emery, M. Zhang, J.-H. Song, M. F. Durstock, A. J. Freeman, M. J. Bedzyk, M. C. Hersam, R. P. H. Chang, M. a. Ratner, and T. J. Marks, “Structural and Electrical Functionality of NiO Interfacial Films in Bulk Heterojunction Organic Solar Cells,” *Chem. Mater.*, vol. 23, pp. 2218–2226, Apr. 2011.

[97] J. Meyer, S. Hamwi, M. Kröger, W. Kowalsky, T. Riedl, and A. Kahn, “Transition metal oxides for organic electronics: energetics, device physics and applications.,” *Adv. Mater.*, vol. 24, pp. 5408–27, Oct. 2012.

VITA

Yao Jin

Yao was born on October 17th, 1985 in Shanxi, China to Lianbo Jin and Yan Huo. Yao attended Hangzhou Dianzi University from 2003 to 2008. She earned a dual B.S. in Applied Physics and Accounting Science. She began an M.S. program in Southeastern Louisiana University within the department of Physics and Chemistry. Her M.S. research was conducted on purification and photophysical properties study of higher fullerenes isomers. Following the obtaining of her M.S. degree in 2010, she began a Ph.D. research program in Penn State University within the department of Engineering Science and Mechanics. She conducted her research on reactive sputter deposition of VO_x, NiO_x, and MoO_x thin films for uncooled infrared imaging.

The Pennsylvania State University

The Graduate School

Department of Engineering Science and Mechanics

THIN FILM MATERIALS AND DEVICES FOR RESISTIVE TEMPERATURE SENSING APPLICATIONS

A Dissertation in

Engineering Science and Mechanics

by

Hitesh A. Basantani

© 2014 Hitesh A. Basantani

Submitted in Partial Fulfillment
of the Requirements
for the Degree of

Doctor of Philosophy

December 2014

The dissertation of Hitesh A. Basantani was reviewed and approved* by the following:

Mark W. Horn
Professor of Engineering Science and Mechanics
Dissertation Advisor
Chair of Committee

Thomas N. Jackson
Robert E. Kirky Chair Professor of Electrical Engineering

Susan Trolier-McKinstry
Professor of Ceramic Science and Engineering

Michael T. Lanagan
Professor of Engineering Science and Mechanics

S. Ashok
Professor of Engineering Science

Judith A. Todd
P. B. Breneman Department Head
Head of the Department of Engineering Science and Mechanics

*Signatures are on file in the Graduate School

ABSTRACT

Thin films of vanadium oxide (VO_x) and hydrogenated amorphous silicon (a-Si:H) are the two dominant material systems used in resistive infrared radiation detectors (microbolometers) for sensing long wave infrared (LWIR) wavelengths in the 8–14 μm range. Typical thin films of VO_x ($x < 2$) currently used in the bolometer industry have a magnitude of temperature coefficient of resistance (TCR) between 2%/K – 3%/K. In contrast, thin films of hydrogenated germanium (SiGe:H) have |TCR| between 3%/K to 4%/K. Devices made from either of these materials have resulted in similar device performance with NETD ≈ 25 mK. The performance of the microbolometers is limited by the electronic noise, especially 1/*f* noise. Therefore, regardless of the choice of bolometer sensing material and read out circuitry, manufacturers are constantly striving to reduce 1/f noise while simultaneously increasing TCR to give better signal to noise ratios in their bolometers and ultimately, better image quality with more thermal information to the end user.

In this work, thin films of VO_x and hydrogenated germanium (Ge:H), having TCR values > 4 %/K are investigated as potential candidates for higher sensitivity next generation of microbolometers. Thin films of VO_x were deposited by Biased Target Ion Beam Deposition (BTIBD) (~85 nm thick). Electrical characterization of lateral resistor structures showed resistivity ranging from 10^4 Ω–cm to 2.1×10^4 Ω–cm, TCR varying from –4%/K to –5%/K, normalized Hooge parameter (α_H/n) of 5×10^{-21} to 5×10^{-18} cm^3. Thin films of Ge:H were deposited by plasma enhanced chemical vapor deposition (PECVD) by incorporating an increasing amount of crystal fraction in the growing thin films. Thin films of Ge:H having a mixed phase, amorphous + nanocrystalline, having a |TCR| > 6 %/K were deposited with resistivity < 2,300 Ω–cm and a normalized Hooge's parameter 'α_H/n' $< 2 \times 10^{-20}$ cm^3.

Higher TCR materials are desired, however, such materials have higher resistivity and therefore unacceptable large electrical resistance in a lateral resistor configuration. This work looks at an alternate bolometer device design which incorporates higher TCR materials in a vertically integrated configuration.

Thin films of high TCR hydrogenated germanium (Ge:H, |TCR| > 6%/K) and vanadium oxide (VO_x, TCR > 5%/K) were integrated in lateral and through film configuration. The electrical performance of the vertically integrated devices is compared with lateral resistance structures. It was confirmed experimentally that the device impedance was significantly lowered while maintaining the signal to noise ratio of the lateral resistor configuration. The vertically integrated devices allow higher device currents without any increase in self heating. These structures may help reduce integration time and may result in higher frame rate.

Finally, one dimensional arrays were fabricated using both lateral and vertically integrated configurations and their performance was evaluated. It was found that the performance of the lateral devices was limited by noise floor of the measurement setup used. However, due to the lower impedance of the vertically integrated resistors, a higher signal and therefore higher signal to noise ratio could be obtained. These vertically integrated devices exhibited low RMS noise values of 12 mK.

.

TABLE OF CONTENTS

LIST OF FIGURES

LIST OF TABLES

ACKNOWLEDGEMENTS

The proverb, “It takes a village to raise a child” is certainly true of my time in graduate school. This work would not have been possible without the encouragement and support in both professional and personal capacity by numerous people who I would like to acknowledge. Firstly, I would like to thank the U.S. Army Research Office and U.S. Army Research Laboratory for funding this work.

I would like to thank my advisor Dr. Mark Horn for giving me this opportunity, for providing guidance, constant support, and for always encouraging thought-provoking discussions. Secondly, I would like to acknowledge Dr. Thomas Jackson for being an excellent advisor and a tremendous role model. I would like to thank him for treating me as his graduate student and providing me with limitless resources without which this work would not have been possible.

I would like to thank the Penn State Nanofabrication facility, especially William Drawl who mentored me when I was a superuser for the group. Bill is an excellent teacher with a lot of patience. Without his trust, encouragement, and mentorship I would have never been able to develop the hands on skills which will be valuable as I grow in my career.

I would like to thank Dr. David Saint John for introducing me to PECVD hydrogenated germanium and taking the time to assist in the thin film depositions of this work. I would also like to thank Dr. Nikolas Podraza and Dr. Michael Motyka for teaching me valuable skills related to ellipsometry and for helping with data analysis. In addition, I would also like to thank fellow graduate students, Yao Jin, Myung-Yoon Lee, Israel Ramirez and Haoyu Li for many useful discussions and assistance.

I would like to thank my family, Arjun, Meena and Prerna for their unconditional love and support, without which I would have given up a long time ago; and finally my fiancée Jennifer Ober, for her constant love, support and unlimited patience, especially over the last year of this doctorate.

Chapter 1. Introduction and Goals

1.1. Introduction

Temperature sensing is the measure of the heat of a body. There are two types of thermal sensors, contact and non-contact sensors. The contact sensors touch the object being measured, while the noncontact sensors measure the temperature by measuring the infrared radiation emitted by that object. The second chapter provides background on temperature sensing and compares the different types of temperature sensors available in order to put in perspective the work done in this thesis.

Noncontact thermal imaging systems, also known as infrared imaging arrays, have seen a marked increase in the last decade and find applications in both military and civil applications. These systems consist of arrays of micromachined sensors, known as microbolometers, based on an electrical response from resistors, capacitors, etc. Resistive thin films of VO_x and $Si_{1-x}Ge_x$:H are the imaging materials that are the most most dominant types of infrared imaging systems. The second chapter also provides an overview of the state-of-the-art resistive microbolometer technology based on VO_x and $Si_{1-x}Ge_x$:H thin films, and discusses important figures of merit and the read out circuits used in such devices. These discussions will help understand why detectors based on materials with vastly different electrical properties lead to similar detector sensitivity.

Chapter 3 provides an overview of experimental aspects of this thesis including the processing and characterization techniques used in this work. Relevant literature on the thin film deposition techniques is reviewed in this section. Details on thin film lithographic processing, electrical characterization, X−ray diffraction (XRD), atomic force microscopy (AFM), spectroscopic ellipsometry (SE), Rutherford backscatter spectroscopy (RBS) are also discussed in context with this chapter.

1.2. Statement of Problem

The performance of thin films of VO_x and $Si_{1-x}Ge_x$:H has remained relatively unchanged since the first literature appeared detailing their use. For years, much of the effort to improve the detector performance was focused towards improvement of the performance in the underlying read out circuits. However, as the need for higher density pixel arrays increases, the performance of these infrared systems is being limited by the signal to noise ratio of existing thin films. This motivated the study of high TCR materials having reasonably low electrical noise, which has been explored in Chapter 4 of this work. Thin films of VO_x and Ge:H have been explored with a focus on depositing and characterizing thin films having |TCR| values > 3%/K.

Although numerous materials have a high TCR, the accompanying large resistance in a lateral pixel configuration makes integration with existing readout circuits difficult. Chapter 5 investigates an alternate pixel geometry so as to reduce the device resistance and facilitate integration of high TCR materials.

Finally, the high TCR thin films of VO_x were exploited in temperature sensors arrays fabricated on glass substrates. Chapter 6 describes the fabrications of these thin film sensor arrays using both the lateral and the vertically integrated configuration. Two dimensional arrays were also fabricated and were multiplexed using integrated ZnO transistors fabricated on the underlying circuits. The resulting devices were characterized for their performance.

Chapter 2. Introduction to Temperature Sensing

Temperature is a measure of heat of an object. The concept of temperature invokes the physiological experience of touching an object and describing them as cold, cool, warm, hot, etc. Warmer objects transfer heat to colder objects till both their temperatures have reached equilibrium.

Temperature is an important physical parameter which influences all physiological, and thermal processes. Proper functioning of these processes requires accurate measurement of the corresponding temperature. There is a vast and an ever-growing number of methods for temperature sensing, however, the measurement techniques best suited for the application must be chosen in order to obtain readings which are as precise as required by that application.

Temperature sensors (or thermometers) can be classified based on heat transfer mechanisms as either contact or non-contact sensors.

2.1. Contact Temperature Sensors

The most accurate type of contact sensors are the electrical response contact sensors. In these types of sensors, the temperature response is converted into an electrical signal. Some commonly used electric contact sensors are discussed below:

2.1.1. Thermocouples

The thermocouple is based on the phenomenon known as the Seebeck effect. Named after the T. Seebeck who first observed this effect, he noted that there is a current flow in a closed loop of two dissimilar metals if their junctions are kept at two different temperatures. The corresponding voltage associated with this effect is known as the thermal electromotive force. A device which uses the Seebeck effect for the measurement of temperature is known as a thermocouple.

A thermocouple consists of two wires of dissimilar conductors (metals, alloys or semiconductors) connected at one end. The connected end is placed at the point of measurement, while the unconnected

end is the reference junction and can be used to readout the electromotive force developed using a voltmeter. Depending on the material used, these thermocouples can have an operation range of up to 3000 °C [1]. The most sensitive thermocouples are based on two alloys made from Nickel-chromium or Nickel-copper [1]. Thermocouples made from these alloys can achieve a sensitivity of 6.32 mV/ 100°C and have an operating range of 0°C to 1100°C [1]. The accuracy of such thermocouples is ≈ ± 1 °C [1].

2.1.2. Resistance Thermometer Detectors (RTD)

Resistance thermometers consist of thin wires of a metal or an alloy whose resistance changes linearly as a function of temperature. Platinum, Nickel, Copper and alloys of Rhodium-Iron are some commonly used materials in resistance thermometers [1] [2]. Nickel has the largest temperature response that of 0.62 %/K while Platinum has the highest range of operation between −260 K to 1100 K [1]. Due to the low resistivity of these materials, they are usually thin, long wires wound into a small form factor. The typical accuracy of measurement of RTDs in this form factor is ≈ ±0.2 °C. Typical limitations include a relatively large form factor, cost associated with platinum wires and a high response time associated with the large thermal mass of the wires. Thin films have also been fabricated using these materials and thus have the advantage of miniaturization and the ability to fabricate temperature sensing arrays.

2.1.3. Semiconductor Thermometers

Semiconductor thermometers are made from semiconductor materials and can be divided into two main groups: bulk effect and junction effect sensors. In these types of temperature sensors, the conductivity of the semiconductor material changes due to a change in temperature of that material.

2.1.3.1. Thermistors

In these types of materials the resistance of the material changes as a function of temperature. This change in resistance can be readout electrically to give the change in temperature of the body under investigation. The resistance change of a thermistor is non-linear and follows a thermally activated behavior described by the Arrhenius equations such that:

$$R_T = R_0 e^{-E_a/k_B T^2} \quad \text{Equation 1}$$

Where R_T is the temperature of the thermistor at a temperature T. R_0 is the temperature at room temperature, k_B is the Boltzmann's constant, and E_a is the activation energy which is a material property of the thermistor.

The temperature response or the temperature coefficient of resistance (TCR) of the thermistor can then be estimated as:

$$TCR\ (in\ \%/K) = \frac{-E_a}{k_b T^2} \times 100 \quad \text{Equation 2}$$

Thermistors are typically made using ceramic manufacturing techniques from oxides of Mn, Ni, Co and Cu; they are pressed at high pressures and sintered at temperatures up to 1000 °C [1] [3]. Typical TCR values of thermistor lie between −2 %/K to −6 %/K [1]. This temperature response makes these thermistors some of the most sensitive types of temperature detectors with temperature errors as low as ± 0.1 °C [1] [4]. Limitations of thermistors include a lower and a smaller temperature range of operation (typically between -100 °C and 200 °C) and the non-linearity of the electrical response [5].

2.1.3.2. Diode and Transistor Based Thermometers

The output characteristics of a junction are dependent on its temperature of operation such that:

$$I_d\ (T) = I_S \left(e^{\frac{V_D}{nV_T}} - 1 \right) \quad \text{Equation 3}$$

Where I_d is the forward current of the diode, I_S is the reverse saturation current, V_D is the forward bias voltage, n is the ideality factor and V_T is the thermal voltage associated with temperature T (26 mV at 300 K). The change in V_T associated with the change in temperature can be used to calculate the temperature of the object with respect to a reference. Commercial temperature sensors based on junction effect are available and have a sensitivity of −2 mV/°C for silicon based diodes and −1.25 mV/°C for germanium

based diodes [1]. In addition, sensitivity as high as 40 mV/°C has been demonstrated using ZnO based transistors [6].

2.2. Non-contact Thermometers or Pyrometers

Pyrometers or infrared detectors are thermometers which measure the temperature of the object based on the emitted thermal radiation of that object. Pyrometers are commonly used in applications such as infrared imaging [7] [8] [9], temperature sensors for biological applications [10] [6], aerodynamics and space exploration [11], monitoring industrial processes, etc.

According to the Stefan-Boltzmann's law, the total radiant intensity W_0 of a black body depends on its temperature T [1]:

$$\boldsymbol{W_0 = \sigma_0 T^4} \qquad \textbf{Equation 4}$$

σ_0 is the Stefan-Boltzmann's constant and has a value of 5.67×10^{-8} W/m^{2}K^4

The spectral radiant flux distribution is given by [1]:

$$\boldsymbol{W_{0\lambda} = \frac{c_1 \lambda^{-5}}{e^{c_2/\lambda T} - 1}} \qquad \textbf{Equation 5}$$

where $W_{0\lambda}$ is the spectral radiant flux distribution of a black body in W/m^{2}μm, T is the temperature of the black body in K, $c_1 = 3.7415 \times 10^{-16}$ W.m^2 and $c_2 = 14{,}388$ μm.K.

There are numerous detectors that can be used for detection of thermal radiation. Some common detector types are discussed in detail in the following subsections.

2.2.1. Thermopiles

A thermopile is a series connection of numerous thermocouples whose hot junction is in contact with a black body which absorbs the incident radiation. Since a single thermocouple produces a small

electromotive force, a series of such thermocouples can produce thermometers with high sensitivity. Such devices have demonstrated sensitivity of several hundred μV/K. Detailed descriptions of state-of-the-art thermopiles can be found elsewhere in refs. [3] [12].

2.2.2. Pyroelectric Detectors

Pyroelectric detectors are based on the principle that the dipole moments in a pyroelectric material change their orientation as a function of temperature. Materials such as lead zirconium titanate (PZT), triglycine sulphate (TGS) and barium strontium titanate (BST) have a large pyroelectric coefficient response > 2×10^{-8} C–cm^{-2}–K^{-1} [1] [3].Thin film temperature sensing arrays have been fabricated using pyroelectric materials, the details of which can be found in ref. [3] [13] [14].

2.2.3. Photoconductive Detectors

Photoconductive detectors are made from materials whose electrical conductivity changes due to the generation of carriers in the material as a function of incident radiation. Depending on the choice of material, the detector can have a different spectral response. For example, CdS has a spectral response in the visible spectral region while PbS is in the 0.5 μm–4 μm wavelength range.

2.2.4. Photovoltaic Cells

A photovoltaic device generates a voltage depending on the incident infrared radiation. The photovoltaic material absorbs radiation, exciting valence band electrons into its conduction band. Similar to other photoelectric detectors, the spectral response depends on the choice of material. InAs has a spectral response between 1 μm–3.8 μm while InSb has a maximum sensitivity to radiation of wavelength 8 μm.

2.2.5. Thermistor or Metal Bolometers

Bolometers based on thermistors or metal bolometer arrays are thermometers based on the temperature coefficient of resistance of the thermistors or metals. However, in these non-contacting detectors, the heating of the resistor takes place by absorption of the infrared radiation by the material or by an absorber layer for non-absorbing thermistor materials [3]. These types of detectors are by far the

most popular for imaging in the 8 μm–14 μm range [15]. Bolometers, especially microbolometers are the focus of this work and are discussed in greater detail in the subsequent sections.

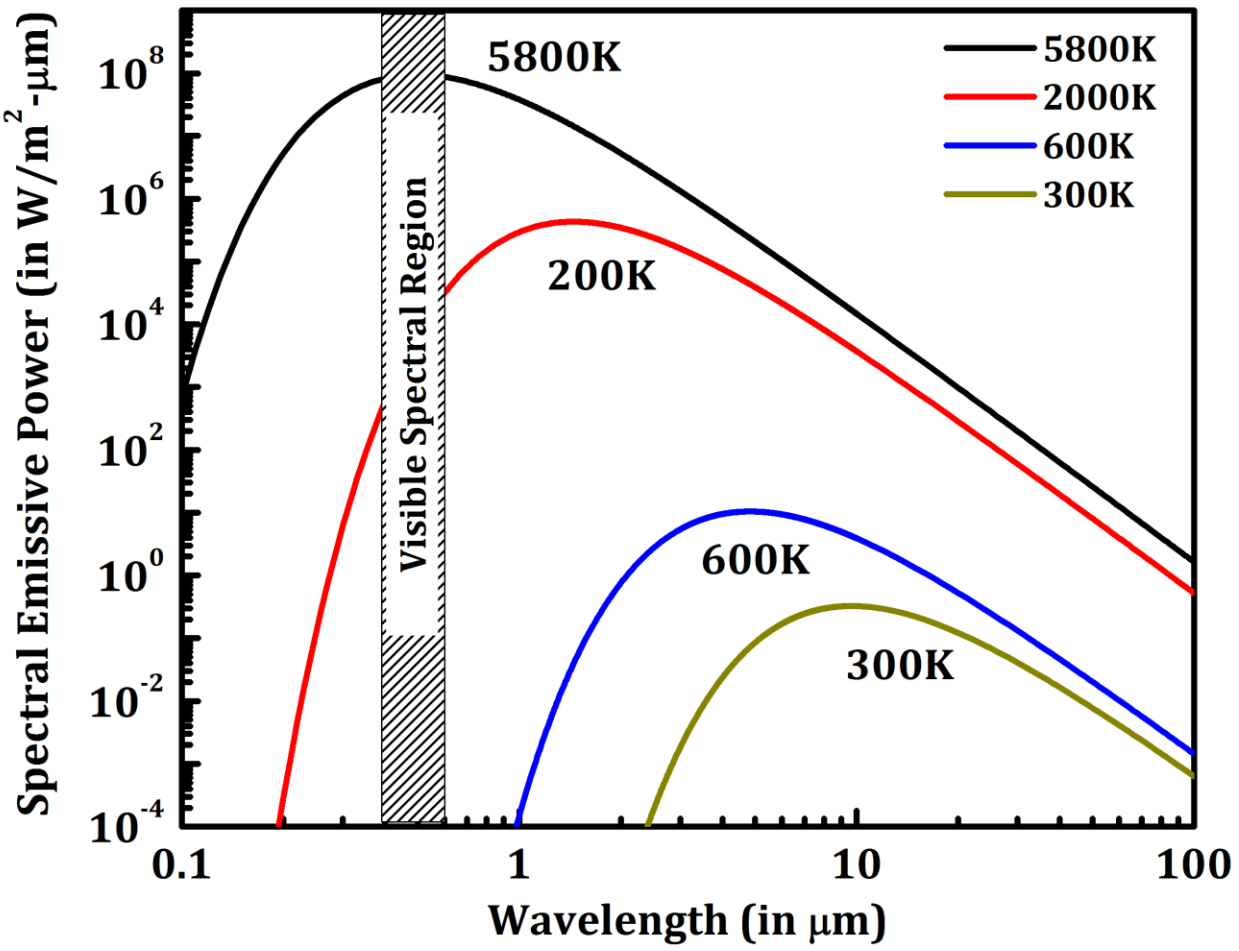

Figure 2-1. Calculated spectral radiant emissive power of a black body (in W/m^2·μm) at different temperatures. The maximum emissive power for objects ≈ 300 K lies between 8 and 14 μm.

Figure 2-1 shows the spectral emissive power of a black body in accordance with Equation 5 at different temperatures of the object. The choice of infrared detector depends on the desired temperature range of measurement. One of the biggest applications for temperature sensing is room temperature imaging of objects at temperatures between –40 °C and 120 °C. Today, the most common type of detector for room temperature infrared imaging is based on thermistor materials whose resistance changes as it heats up due to incident infrared. This imaging technique is described in the subsequent subsections in further detail.

2.3. Resistive Infrared Imaging or Microbolometer

A bolometer is a temperature-sensitive electrical resistor whose resistance changes due to an increase in temperature caused by incident infrared radiation. The magnitude of the resistance change is proportional to the temperature of the black body emitting the incident radiation. Two dimensional arrays of miniaturized resistors (microbolometer) can be used for mapping the thermal field of the scene under investigation.

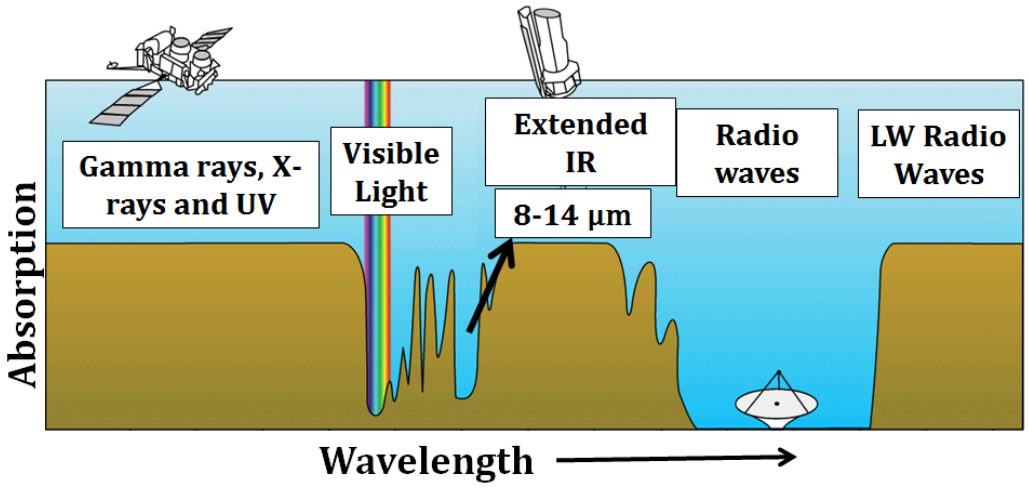

Figure 2-2. The electromagnetic spectrum and the opacity of the atmosphere at different wavelengths, from ref. [16].

Since a microbolometer is a non-contact temperature sensor, the infrared radiation must travel through the atmosphere before it reaches the detector element. H_2O and CO_2 molecules present in the atmosphere absorb certain wavelengths of radiation, as can be seen in Figure 2-2 [16]. Radiation in the 3–5 µm range (Mid-Wavelength IR or MWIR) and 8–14 µm range (Long Wavelength IR or LWIR) is transmitted through the atmosphere and can be used for detecting infrared radiation. Due to the higher intensity of radiation in the 8–14 µm band at 300K (Figure 2-1), LWIR detectors are preferred. However the choice of detector depends on the specific application at hand.

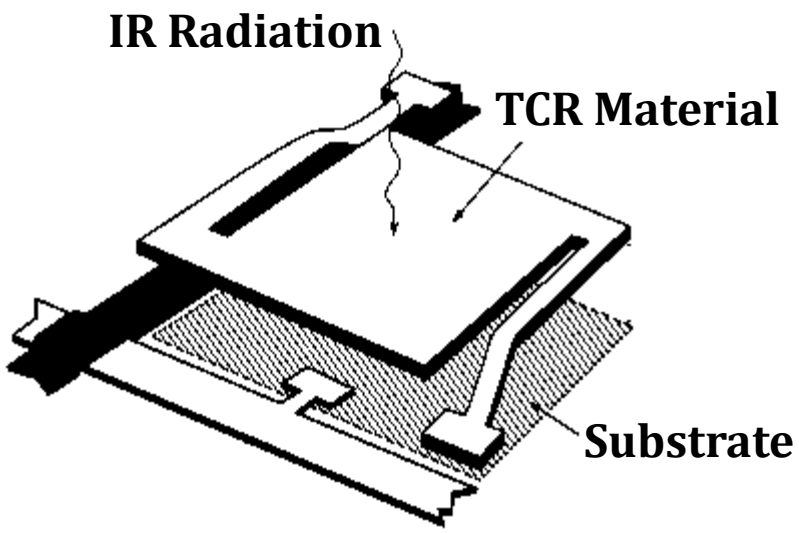

Figure 2-3. A schematic of a single free standing microbolometer with the underlying read out integrated circuit (ROIC), from ref. [17].

The actual sensor used for infrared imaging is a monolithic structure prepared by silicon micromachining, originally developed by Honeywell [8]. A simplified schematic of such a pixel structure is shown in Figure 2-3. The detecting area is a thin film of the temperature sensitive material employed (metal or semiconductor) having a temperature coefficient of resistance (TCR) of α, atop a thin free standing membrane, usually Si_3N_4 [17] [3]. The membrane is supported by legs which have a low thermal conductance to maximize thermal isolation from the environment. The legs also have a thin film of metal which serve as electrical contacts to the resistive thin film. In addition, the underlying substrate has a reflective thin film which causes the unabsorbed radiation to reflect back to the resistive layer [17] [3]. It was found that the reflection is at a maximum when the spacing between the reflective layer and the suspended resistor is one quarter of the wavelength being sensed [3] [17].

2.3.1. Figures of Merit

The performance of a microbolometer depends on two important properties which are discussed in further detail in the following subsections.

2.3.1.1. Temperature Coefficient of Resistance (TCR)

The performance of a microbolometer depends on several factors, one of which is the temperature coefficient of resistance or TCR. The temperature coefficient of resistance is defined as the percentage change in resistivity of the material per degree Kelvin of increase in its temperature. TCR can be negative or positive. While metals have a positive TCR, semiconductors have a TCR which is typically negative. In general, TCR can be defined using Equation 6:

$$\boldsymbol{TCR\ (\alpha) = \frac{1}{\rho}\frac{d\rho}{dT}} \qquad \textbf{Equation 6}$$

where α is the TCR of the material, ρ is the resistivity and dρ is the change in resistivity of the material associated with a change in its temperature dT.

The resistivity of a material is given by Equation 7:

$$\boldsymbol{\rho = \frac{1}{ne\mu}} \qquad \textbf{Equation 7}$$

where n is the free carrier concentration, μ is the mobility of carriers and e is the charge of an electron.

There are two factors which may contribute to a change in the resistivity of the material with temperature as observed in Equation 7, namely, the free carrier concentration (n) and the mobility (μ). Metals show little change in the free carrier concentration as a function of temperature. However, the mobility of the charge carriers decreases with increasing temperature, resulting in a positive TCR, which is constant as a function of temperature. On the other hand, in the case of intrinsic semiconductors, both the free carrier concentration and mobility of the material changes with temperature, this is usually results in a TCR which is negative. The resistivity of semiconductors changes as a result of thermally activated charge carriers across the band gap such that:

$$\boldsymbol{\rho = \rho_o \exp\left(\frac{\Delta E_a}{kT^2}\right)} \qquad \textbf{Equation 8}$$

where, ΔE_a is the activation energy, k is the Boltzmann's constant. Thus it follows that for a semiconductor, the TCR is given by:

$$\alpha = \frac{1}{\rho}\frac{d\rho}{dT} = -\frac{\Delta E_a}{kT^2}$$ **Equation 9**

Since all the work discussed in this thesis is based on uncooled infrared detection, T is taken to be room temperature (300 K) when reporting the TCR of a material.

Given this relationship, it is easy to calculate the theoretical TCR which can be achieved by using some common semiconducting materials such as silicon and germanium. For single c-silicon, the activation energy is roughly half of the band gap ($E_g/2$) and is equal to 0.55 eV, which results in a |TCR| of 7.2%/K. However, in the case of single c-germanium, whose activation energy is 0.335 eV, a |TCR| of 4.3%/K can be achieved. Although, higher TCR materials are desired, increasing activation energy (and therefore increasing bandgap) results in a decrease in the free carrier concentration; this results in high material resistivity (from Equation 7). Undoped crystalline silicon has a resistivity of 3.2×10^5 Ω-cm, whereas crystalline germanium has a resistivity of 50 Ω-cm. Unfortunately high resistivity materials tend to have higher noise [3] [18] [19] [20] [21] [22] [23] [24] [25] [26] [27], which is another figure of merit for a detector, as we will see in the subsequent sections. In addition, single crystal materials such as c-Ge are hard to integrate with standard MEMS fabrication protocol.

2.3.1.2. Electrical Noise

Device performance of microbolometers does not solely depend on TCR of the thin film. For example, although thin films of SiGe:H have |TCR| > 5%/K, they inherently have higher resistivity and higher electrical noise. Electrical noise is an important limiting factor in the sensitivity of a semiconductor-based temperature sensor. An important figure of merit that relates thin film properties directly to the device performance is the Noise Equivalent Temperature Difference or NETD. In terms of the sensing material properties, the NETD can be derived [17]:

$$NETD \propto \frac{I_{noise,\ total}}{I_{bias} \times TCR}$$ **Equation 10**

where I_N is the noise current due to the thin film, I_{bias} is the bias current due to the applied voltage bias ($I_{bias} = \frac{V_{bias}}{R_b}$) and TCR is the temperature coefficient of resistance of the sensing material.

The ratio $\frac{I_{bias}}{I_N}$ is also known as the signal to noise ratio and is given by the ratio:

$$\boldsymbol{SNR = \frac{I_{bias}}{\sqrt{I^2_{noise,\ total}}}} \qquad \textbf{Equation 11}$$

where $I_{noise,\ total}$ is the total noise current due to the detector material and is comprised of mainly two components, the Johnson noise ($I_{noise,\ J}$) and the flicker noise or 1/f noise ($I_{noise,\ 1/f}$).

Johnson noise

Johnson noise is the electrical noise generated as a result of thermal agitation of carriers and is related to the resistance and the temperature of that resistor. Depending on the bias conditions, Johnson noise can manifest itself as either current noise or voltage noise. The current noise is given by [17]:

$$\boldsymbol{I^2_{noise,\ J} = \frac{4k_bT(f_2 - f_1)}{R_d}} \qquad \textbf{Equation 12}$$

where, K_b is the Boltzmann's constant, T is the temperature of the bolometer, R_d is the resistance of the device, while the bandwidth of measurement extends from f_1 to f_2. The voltage Johnson noise is given by [17]:

$$\boldsymbol{V^2_{noise,\ J} = 4k_bTR_d(f_2 - f_1)} \qquad \textbf{Equation 13}$$

From the above two equations it can be seen that the Johnson noise is independent of the frequency but depends on the temperature and the resistance of the device as well as the bandwidth of measurement.

Equation 12 describes the current Johnson noise contribution to the detector signal. Due to the inverse relationship between the current Johnson noise and the detector resistance, the Johnson noise decreases with increasing device resistance. This inverse relationship allows for small Johnson noise contributions in constant bias bolometers even though high resistance thin films are used [18]. It is for this reason that

most bolometer designs use a voltage bias with current as the output signal. Further discussions on electrical noise will focus on current noise.

Flicker noise or 1/f noise

1/f noise is the fluctuation in conductance with a power spectral density proportional to $f^{-\gamma}$ where $\gamma = 1 \pm 0.1$ [28]. The current 1/f noise is given by empirical relationships proposed by F. N. Hooge [28]:

$$I^2_{noise,\ 1/f} = I^2_{bias}\ \frac{\alpha_H}{nVf} \qquad \textbf{Equation 14}$$

Where I_{bias} is the bias current as a result of the applied voltage, V is the volume of the sample; ƒ is the frequency range of measurement; α_H is Hooge's parameter; and n is the carrier concentration.. For a bandwidth of measurement between f_1 and f_2, the corresponding 1/f noise becomes [3]:

$$I^2_{noise,\ 1/f} = I^2_{bias}\ \frac{\alpha_H}{nV}\int_{f_1}^{f_2}\frac{1}{f}\,df = I^2_{bias}\ \frac{\alpha_H}{nV}\ \ln\left(\frac{f_2}{f_1}\right) \qquad \textbf{Equation 15}$$

The two components, Johnson noise and 1/f noise, combine to produce a total mean square microbolometer current noise given by:

$$\overline{I^2_{noise,\ total}} = \overline{I^2_{noise,\ J}} + \overline{I^2_{noise,\ 1/f}} \qquad \textbf{Equation 16}$$

Figure 2-4 shows an equivalent circuit diagram for a resistor which consists of an ideal resistance of value R_B and a current noise source in parallel with the ideal resistor.

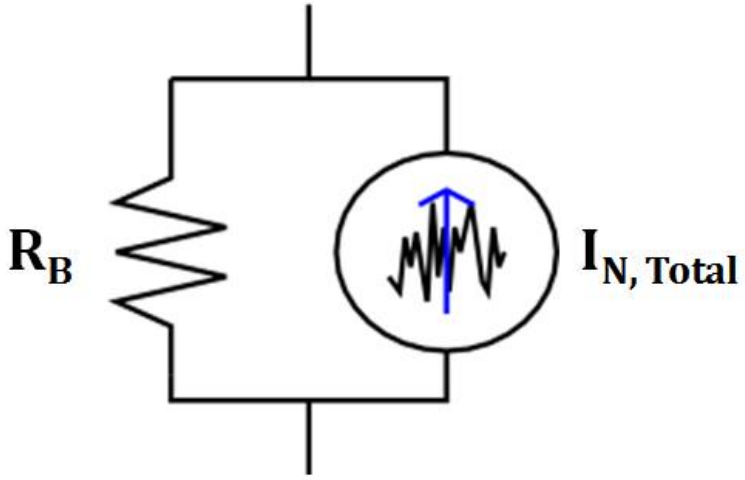

Figure 2-4. Noise equivalent circuit of a resistor for a 1-Hz bandwidth with an ideal resistance of R_B and an RMS current noise source I_N, Total in parallel with the resistor.

2.3.2. Choice of Resistive Material

Figure 2-5 shows a plot of resistivity versus TCR of selected temperature sensitive materials which have been explored for use in infrared imaging [3] [18] [19] [20] [21] [22] [23] [24] [25] [26] [27]. These materials are metals, their alloys, semiconducting materials, and thermistor materials such as spinels of manganese, cobalt and nickel oxides.

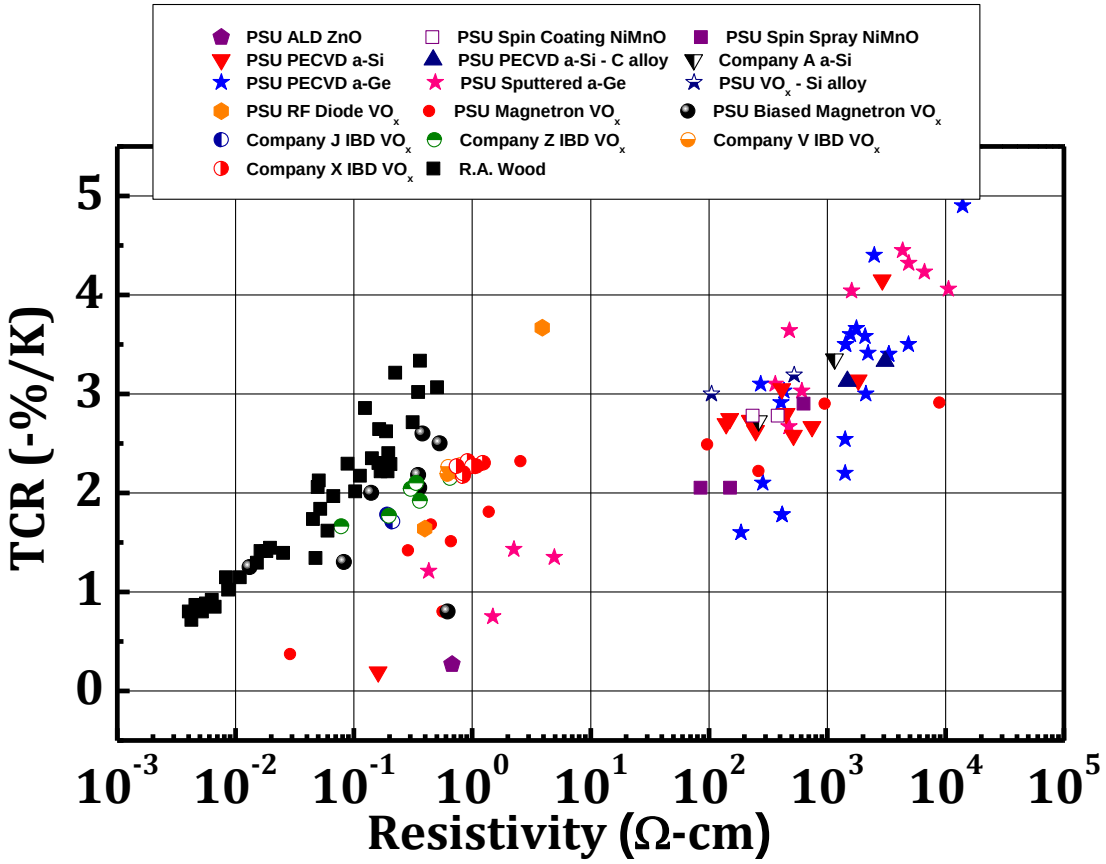

Figure 2-5. TCR vs. resistivity of various materials explored as candidates for temperature sensing [3] [18] [19] [20] [21] [22] [23] [24] [25] [26] [27].

2.3.2.1. Metals

In the low resistivity range of Figure 2-5, metals and alloys such as titanium (0.43%/K), platinum (0.18%/K) and Ni-Fe alloys (0.23 %/K) dominate [17]. Although metals and their alloys have low TCR values, their resistivity and therefore the inherent noise is extremely low, making them potential candidates for infrared imaging. In addition, processes exist for controllable, repeatable deposition of metal thin films. In fact, some of the first microbolometers were made using sputter deposited metals on Si_3N_4 membranes [3]. Because the resistivity of metals is low, very long serpentine resistors were fabricated to form the bolometer resistors [17]. Numerous metals and their alloys were explored as potential candidates; however in the early 1990s, semiconductor materials having five to ten times larger TCR replaced metals as the choice for bolometer materials.

2.3.2.2. Vanadium Oxide (VO_x) Thin Films

Most of the vanadium oxide microbolometer work was classified research and was kept secret until 1991, when Wood et al. at Honeywell Inc. filed a patent on the development of thin films of mixed phase vanadium oxides (VO_x) which had a TCR value of up to five to ten times higher than those of metals [8]. However, because of the United States International Traffic in Arms Regulations (ITAR) restrictions [33], the first public disclosure of the work, including details of materials and bolometer design was not published until 1994 by Wood et al. [8]. The performance of VO_x thin films achieved using the patented method was sufficient and surpassed other candidates for infrared imaging. The resistivity of these films was moderately higher than those of metals, at around 0.01 – 1 Ω–cm [8]. Thin films could be repeatedly deposited by ion beam sputtering at room temperatures on to commonly used substrates such as Si_3N_4 coated Si wafers [8] [30]. For these reasons, VO_x thin films have dominated the microbolometer industry in the 1990s to early 2000s [30]. All VO_x thin films were made either at Honeywell or were made using technology licensed from Honeywell [31] [32]. All literature, including the Honeywell patent, gave little to no description of the microstructure of the thin films obtained [8].

By the early 2000s, the underlying read out circuit technology had matured and the detector sensitivity had reached limits imposed by the electrical noise of VO_x thin films. To facilitate the development of VO_x thin films, the Pennsylvania State University was awarded a grant sponsored by the Army Research Office. One of the goals of the research initiative was to develop an understanding of the relationship between the electrical and microstructural properties of the VO_x thin films. In addition, alternate deposition methods were also explored to improve the throughput limitation imposed by ion beam deposition.

VO_x thin films can be deposited by various sputtering methods including ion-beam sputtering [3] [33] [34], RF sputtering [35], direct current (DC) [36] and pulsed DC sputtering [37] [38] [39]. However, films deposited by ion-beam deposition exhibited better film properties, i.e. higher TCR and lower 1/f noise for comparable resistivity values with other deposition techniques [23]. Most references to

industrially manufactured vanadium oxide thin-films for use in infrared imaging, to date, call for reactive ion-beam sputtering as the primary method of deposition [3] [8] [33] [34] .

Some of the first published work on developing an understanding between the structure–property relationships for VO_x thin films was done by Kerry Wells at the Pennsylvania State University by pulsed DC magnetron deposition of thin films of VOx using a V_2O_3 target. Thin films deposited using this method resulted in films which were voided and mostly amorphous with some nano crystalline grain growth for thicker films [40]. It was also shown that different processing parameters such as, partial pressure of oxygen during sputtering and total sputtering pressure, produced films with different microstructure and electrical properties. In general, the resistivity and TCR of films was found to increase with an increase in the oxygen partial pressure, as well as with an increase in the total sputtering pressure. TCR values between –1 %/K and –3%/K were achieved; however the resistivity was orders of magnitude higher than those of films deposited by ion beam deposition [40].

Dr. Chandrasekaran Venkatasubramanium investigated the use of metallic vanadium target for depositing microbolometer grade vanadium oxide thin films. Dr. Venkatasubramanium characterized the inherent process hysteresis associated with the reactive pulsed Direct Current (DC) magnetron sputtering of the metallic vanadium target. Thus, thin films with resistivity and TCR values comparable to those of films deposited by ion beam deposition were grown [20] [41]. It was found that the room temperature resistivity of films increased with increase in total flow rate as well as with the increase in the oxygen partial pressure during sputtering [20] [42].

Films with good electrical characteristics (high TCR with moderately low resistivity) were deposited at low total flow rates and low oxygen partial pressures [20] [42]. These films showed the presence of nano-crystallites in an amorphous matrix in films, with high levels of porosity, which was confirmed by both transmission electron microscopy (TEM) and grazing incidence x-ray diffraction methods (GIXRD) [20].

Post deposition annealing experiments were also performed in oxygen and nitrogen environments in an attempt to improve the trade-off between TCR and resistivity. Films annealed in oxygen were driven towards higher oxides of vanadium, which have unacceptably high resistivity at room temperature. Annealing the thin films in nitrogen ambient yielded better results; for example, for films annealed at 300° C in nitrogen, the resistivity dropped by an order of magnitude, without significant deterioration of the film TCR. Structural analysis by XRD, Rutherford backscattering spectroscopy (RBS), Raman spectroscopy, scanning electron microscopy (SEM), TEM, and atomic force microscopy (AFM) did not reveal any significant changes between the annealed and the un-annealed films [20]. It was speculated that the improvement in thin film characteristics was due to reordering between the amorphous and nano-crystallite phases or due to grain growth. Nick Fieldhouse investigated the effects of substrate heating during reactive deposition of vanadium oxide thin films using a metallic vanadium target. The thin films obtained were mixed phase with VO and V_2O_3 crystallites in an amorphous matrix with moderate improvement in the film's electrical properties [42].

B. D. Gauntt extensively studied the microstructure-property relationships by altering processing parameters during pulsed DC magnetron deposition of VO_x thin films. It was found that all thin films deposited either by ion beam deposition or by pulsed DC sputtering resulted in one of three microstructures: an amorphous often voided columnar structure, a polycrystalline structure with nanometer-sized grains, or a nano-composite structure composed of columnar or conical nanocrystallites of vanadium oxide in an amorphous matrix. Gauntt concluded that thin films of VO_x exhibiting the best electrical properties were found to contain conical/columnar grains in an amorphous matrix and were deposited by ion beam deposition [43].

H. A. Basantani attributed the superior electrical properties of thin films deposited by ion beam deposition to the energetics associated with the process. To replicate the results with pulsed DC sputtering, substrate bias was applied during deposition. The electrical properties of the thin films deposited were superior (higher TCR with lower electrical noise) to those obtained with ion beam

deposition [37]. The films obtained were mixed phase with V_2O_3 nanocrystallites in an amorphous matrix. The x value in VO_x was between 1.5–2 [37]. In general, the microstructure of the thin films obtained was similar to the ones obtained with ion beam deposition; however these films had a higher density (> 4.2 gm/cm^3 versus 3.8 gm/cm^3 for ion beam deposited thin films.

The best films of that work had a TCR of −2.6%/K with a resistivity of 0.6 Ω−cm [37]. Attempts to increase the TCR further resulted in an abrupt increase in the resistivity which was not of interest for that work [44]. Venkatasubramanium and Gauntt explored the parameter space during deposition by pulsed DC magnetron sputtering and obtained high TCR VO_x thin films having very large resistivities [20] [21]. Figure 2-6 compares the electrical properties of VO_x thin films deposited by pulsed DC magnetron sputtering and ion beam deposition from numerous references [3] [33] [42] [37]. It is interesting to note that although the obtainable range of TCR is between −0.2%/K and −5%/K, there are two ranges of resistivity between 10^{-3} to 1 Ω−cm and 10^3 to 10^5 Ω−cm. At the time of writing this dissertation, thin films having intermediate resistivity between 1 Ω−cm and 10^3 Ω−cm have not been successfully deposited.

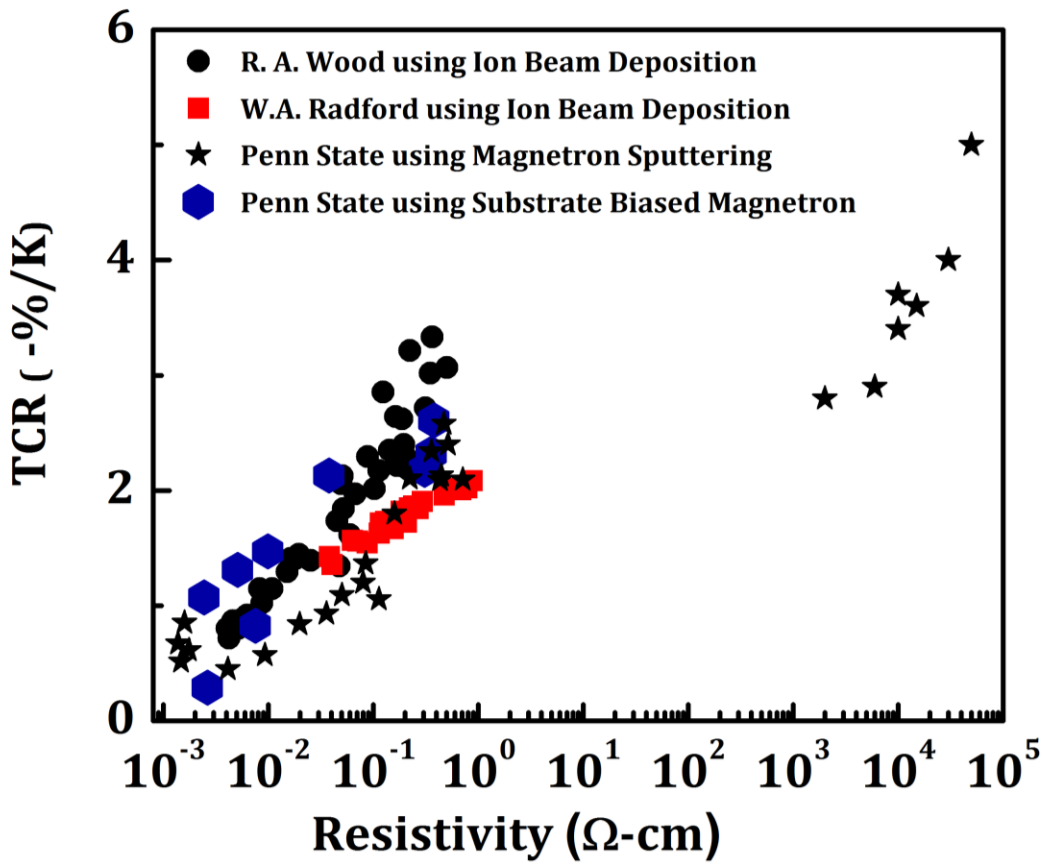

Figure 2-6. Comparison of Resistivity vs. TCR of VO_x thin films deposited by ion beam sputtering [8] [33] and magnetron sputtering [37].

There are fundamental differences between VO_x thin films belonging to the two distinct resistivity ranges. While thin films having resistivity between 10^{-3} Ω–cm and 1 Ω–cm are mixed phase, films with higher resistivity and high TCR are x-ray amorphous [21] [37]. The high resistivity films typically have x-values in VO_x between 2 – 2.5, compared with 0.8 – 2 for films with resistivity < 1 Ω –cm [45]. The resistivity and the inherent 1/f noise of thin films with |TCR| > 4%/K was found to be too high for use in existing read out circuit technology at the time [3].

Both deposition techniques, ion beam deposition and magnetron sputtering, are limited in deposition rates to ~ 1Å/s [44] [46]. Deposition rates in ion beam deposition is limited by ion current density of the ion source, whereas in magnetron sputtering the deposition rate is limited by the process

window associated with reactive deposition and therefore the throw distance associated with the reactive deposition [42].

In order to increase through-put, industry is looking for alternate deposition techniques that would result in higher deposition rates. One such candidate is the biased target ion beam deposition which is capable of achieving deposition rates > 10Å/s. VO_x thin films deposited by this deposition technique were investigated in this work [47].

2.3.2.3. Hydrogenated Silicon Germanium Alloys ($Si_{1-x}Ge_x$:H)

A considerable research effort has been made in the development of thin films of amorphous hydrogenated silicon (a-Si:H) and hydrogenated silicon germanium alloys ($Si_{1-x}Ge_x$:H) for use in large area devices such as solar cells, liquid crystal displays and most recently as sensing material for infrared detection [48] [49] [50]. In particular, alloys of Si and Ge have been heavily investigated because the optical band gap of the deposited material can be tailored between 1.1 eV and 1.7 eV depending on the composition of the alloy. However, the success in developing SiGe alloys for microbolometer applications having superior electrical properties has been rather limited.

Although VO_x thin films have been demonstrated to be useful microbolometer TCR materials, their maximum TCR is limited to about −5%/K. Mark Unewisse and Jean Tissot in 1996 demonstrated amorphous hydrogenated silicon−germanium (SiGe:H) thin films having TCR values larger than those of VO_x, around −2.5%/K to −8%/K [50] [50]. Although TCR values as high as −8%/K were attainable, Liddiard et al. concluded that the electrical properties were accompanied by unacceptably high 1/f noise [17].

An analogous material system lying on the other extreme of the spectrum, consisting of amorphous hydrogenated germanium (a-Ge:H), has also been investigated [51] [52] [53] [54] [55]. However, these thin films could not compete with the performance of Si:H/SiGe:H systems for photovoltaic or thin film transistor applications. While Si:H and SiGe:H have dark resistivity between

$10^{11} - 10^{13}$ Ω–cm with light resistivity as low as 10^4 Ω–cm, Ge:H thin films show smaller dark resistivity of 10^7 Ω-cm with smaller thermal activation [49] [52] [53] [54] [55]. However, the lower resistivities of Ge:H thin films make them good candidates for further investigation as infrared imaging materials.

Electrical properties of hydrogenated germanium have been investigates for over three decades. Numerous research groups have demonstrated thin films of amorphous Ge:H having |TCR| as large as 5%/K and having resistivity of the order of 10^5 Ω-cm [51] [52] [53] [54] [55] 4]. Campinas et al. studied the effect of deposition conditions on the electronic quality of a-Ge:H and a-Ge thin films deposited by RF sputtering [53]. Plasma enhanced chemical vapor deposition (PECVD) technique which had proved to be very effective in producing a-Si:H thin films, was also used to deposit Ge:H. The highest |TCR| obtained was 4.6 %/K with a resistivity of 10^5 Ω–cm [55].

Ambrosio et al. demonstrated thin films of a-Ge:H and a-SiGe:H, deposited using GeF_4 diluted in H_2 having |TCR| as high as 5%/K with moderately low resistivity of 20,000 Ω–cm [56]. These publications contained no information on the underlying microstructure or the inherent 1/f noise properties of the films obtained. Further improvements on the electrical properties came in 2012, when Moreno et al. published information on polymorphous thin films of Ge:H [57].

In the work by Moreno et al., growth of nanocrystallites was encouraged by varying the total pressure of deposition from 600 mTorr to 2500 mTorr [57]. Cross sectional TEM of the thin films revealed that the films contained nanocrystals of size 2–4 nm in an amorphous matrix [57]. As a function of pressure, Moreno claimed that the grain size grew and its value reached a maximum at around 2,000 Torr before decreasing for 2.5 Torr [57].

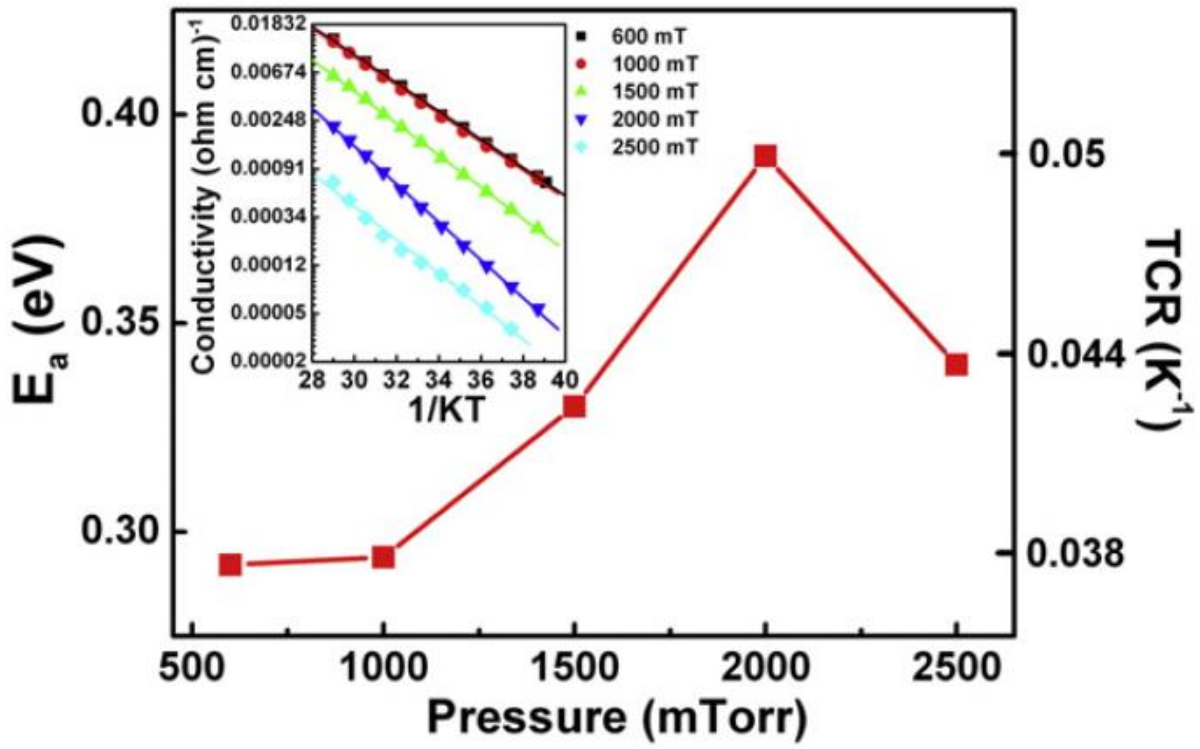

Figure 2-7. Graph showing the effect of total deposition pressure on TCR and resistivity of deposited pm-Ge:H thin films from ref [57].

Figure 2-7 shows the resistivity and TCR data of deposited thin films as a function of deposition pressure from reference [57]. Thin films deposited in this work showed |TCR| between 3.8 %/K and 5 %/K with resistivity between 1,100 Ω–cm and 20,000 Ω–cm [57]. This resistivity – TCR tradeoff was amongst the best reported in the literature for thin films of hydrogenated germanium [57]. No 1/f noise properties were reported for these thin films.

Around the same time Saint-John et al. also investigated if the electrical properties of the Ge:H thin films can be improved by introducing small amounts of nanocrystalline Ge:H material during the natural growth evolution [51] [19]. It was hypothesized that addition of nanocrystalline germanium, which has a resistivity of 50 Ω–cm, would help reduce the resistivity and the electronic noise while keeping the high TCR associated with the amorphous Ge:H material [57].

The dilution ratio (given by R = $[H_2]/([GeH_4] + [H_2])$) used during PECVD is an important parameter in the nucleation of crystallites [19] [51]. Similar to PECVD deposition of Si:H and SiGe:H

thin films, thin films of Ge:H also show a decrease in the thickness of amorphous bulk layer prior to the nucleation of crystallites [51] [58]. Figure 2-8 shows the skeletal growth evolution diagram which was developed by Saint-John for Ge:H, similar to the microstructural evolution associated with PECVD deposited Si:H, to confirm the location of the transition regions between amorphous, amorphous and nanocrystalline, and nanocrystalline microstructures [19].

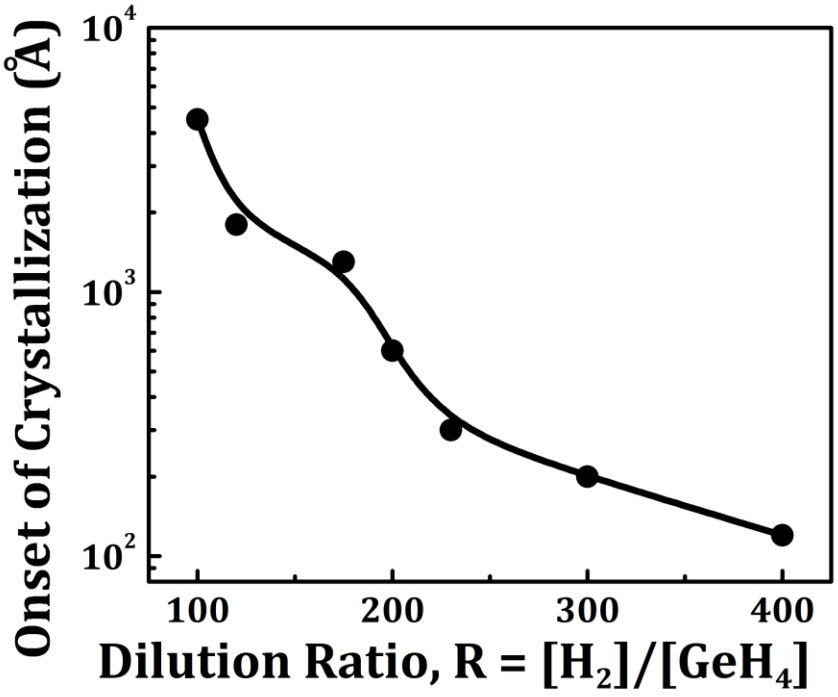

Figure 2-8. Growth evolution diagram for Ge:H thin films grown on native oxide on c-Si showing the thickness values at which crystallization becomes evident (re-plotted from ref [19]).

By depositing thin films at different dilution ratios of the growth evolution diagram, Saint-John's work aimed to assess the electrical property of the thin films as a function of microstructure. Figure 2-9 summarizes the electrical properties of thin films obtained in that work [19].

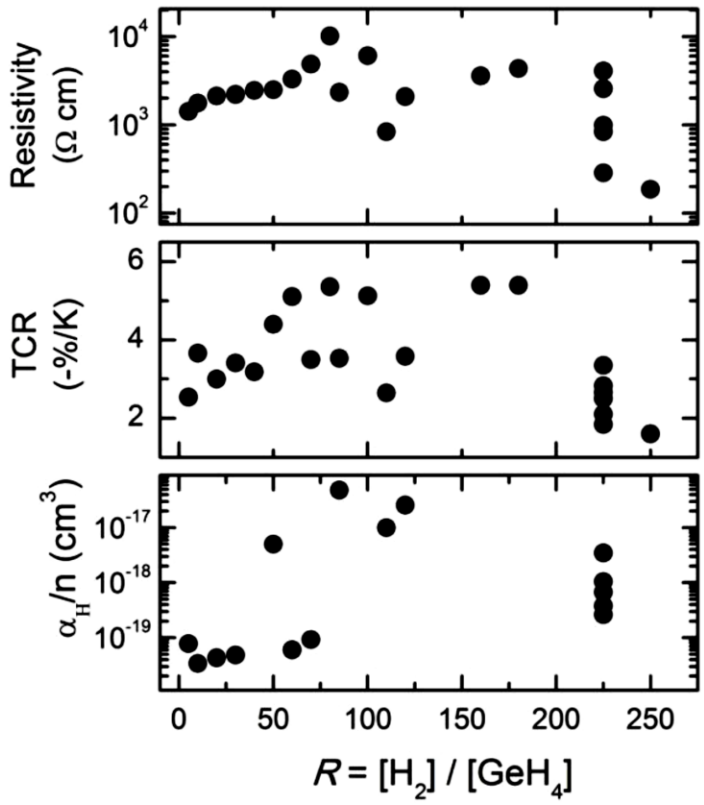

Figure 2-9. Summary of electrical properties (resistivity, TCR and normalized Hooge's parameter) for thin films of Ge:H thin films deposited at different dilution ratios [19].

TCR values between –2 %/K and –5 %/K were obtained with resistivity between 10^3 Ω–cm and 10^4 Ω–cm and α_H/n values between 10^{-20} and 10^{-17} cm^3 [19]. However, no obvious trend in the electrical properties could be inferred as a function of R. Part of the reason could be that there are several factors involved. For example, the plot compares electrical properties of films having different thicknesses and therefore different microstructures. Thus it is hard to get a true sense for a relationship between the microstructure and electrical properties.

Figure 2-10 shows the electrical properties of thin films as a function of crystal fraction obtained by growing thin films of increasing thicknesses at a dilution ratio of R = 225. Saint-John noticed a decrease in the resistivity for small crystal fractions following which both the resistivity and TCR increased while α_H/n values remained around 10^{-18} cm^3 [19]. The largest TCR value of –3.5 %/K was obtained for the thin film with a crystal fraction of 55 % for a film thickness of 200 nm [19]. Thin films

with larger crystal fractions were not deposited in this work, and so it is unclear if larger TCR values could be obtained for films with higher crystal fractions.

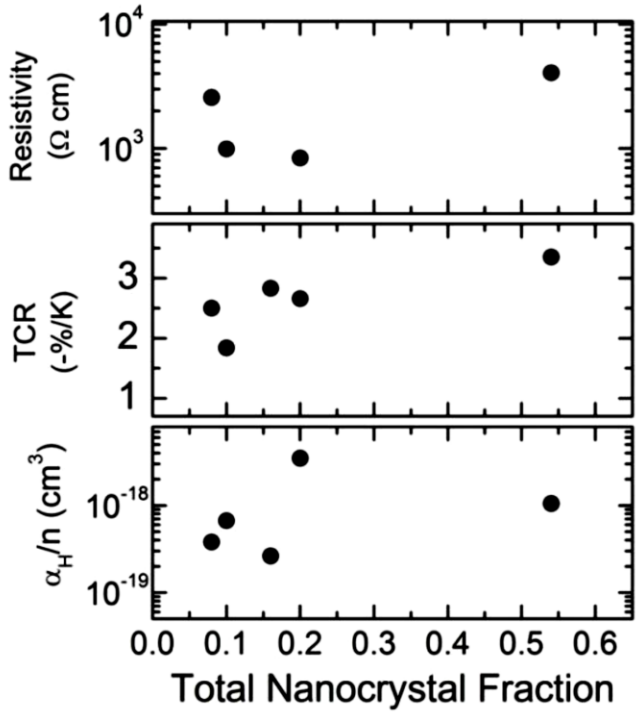

Figure 2-10. Electrical properties of (a+nc)-Ge:H thin films grown at R = 225 for increasing thicknesses. The x-axis plots the total nanocrystalline fraction as it relates to the thickness [19].

Saint John noted that to obtain thin films with a larger crystal fraction for a dilution of R = 225, thin films must be thicker than 200 nm [19]. However, for bolometric applications, these thicker films have an unacceptably high thermal mass, thereby limiting the bolometer's performance.

To induce grain growth at small thicknesses, Saint-John observed the microstructural evolution in thin films deposited at a much higher dilution of R = 400. Figure 2-11 shows the microstructure of a 200 nm thick thin film deposited on to native oxide on c-Si [19]. Saint-John observed that thin films deposited at this dilution were dense and the microstructure was nanocrystalline with planar twining defects on the order of ~ 1nm [19]. Despite the unique microstructure, the films were not characterized for their electrical properties because they were not deposited on insulating substrates.

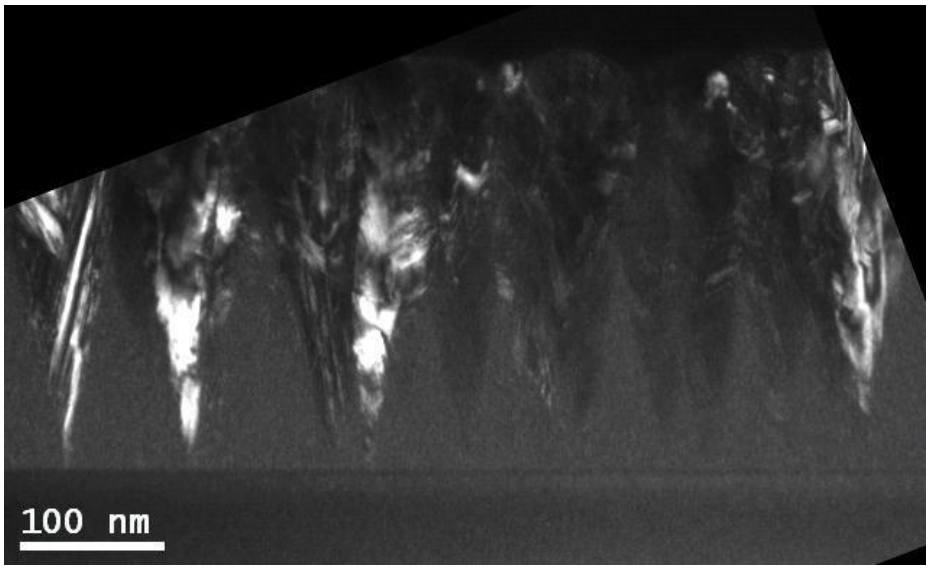

Figure 2-11. Cross-sectional TEM dark field image of an R = 400 (a+nc)-Ge:H thin. The amorphous regions are uniformly illuminated, while the crystalline regions appear light or dark depending on their orientation. Two of the approximately ten discernible cones are oriented such that twinning can be seen [19].

Saint John also observed the surface roughness evolution of thin films deposited at various dilutions and related it to the microstructural evolution of a growing thin film. He observed that for thin films deposited at higher dilutions, the surface roughness increased rapidly and at lower thicknesses, indicating a faster transition from an amorphous to an amorphous + nanocrystalline material [19]. He also observed that the roughness peaked at smaller thicknesses and then decreased. The peak in roughness was attributed the value of film thickness at which the grains coalesced and the film became predominantly nanocrystalline [19].

Saint John also observed that further acceleration of the microstructural evolution is made possible by lowering the substrate temperature used during deposition [19]. Figure 2-12 shows the surface roughness evolution of Ge:H thin films deposited at substrate temperatures of 140 °C, 200 °C and 260 °C [19]. The thin film deposited at 140 °C showed a prompt coalescence at a thickness of 85 nm [19].

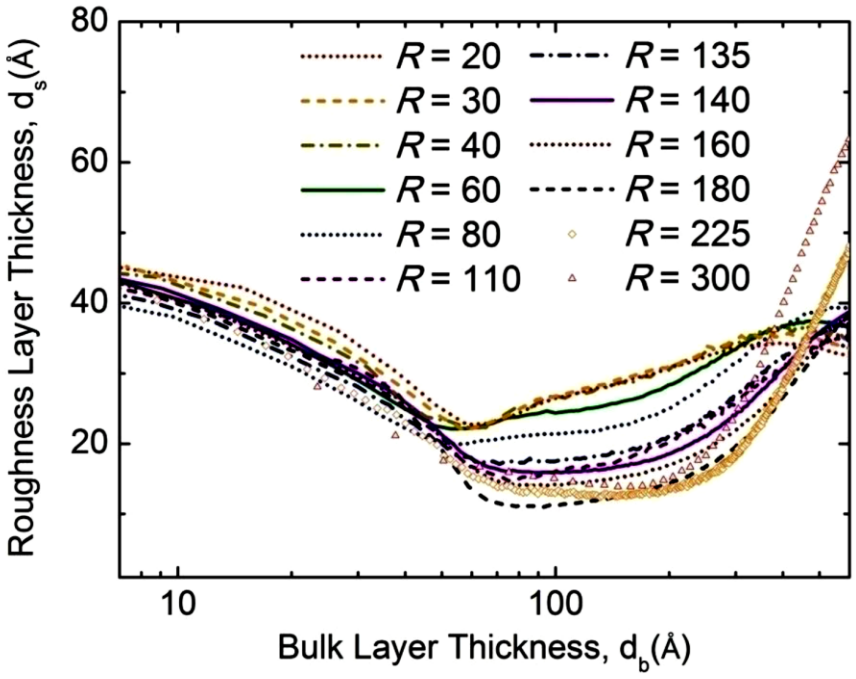

Figure 2-12. Surface roughness evolution for Ge:H films deposited at different dilution ratios, R. Higher dilution ratios show an increase in surface roughness at smaller thicknesses, indicating film transformation from amorphous to a mixed phase thin film ref. [19].

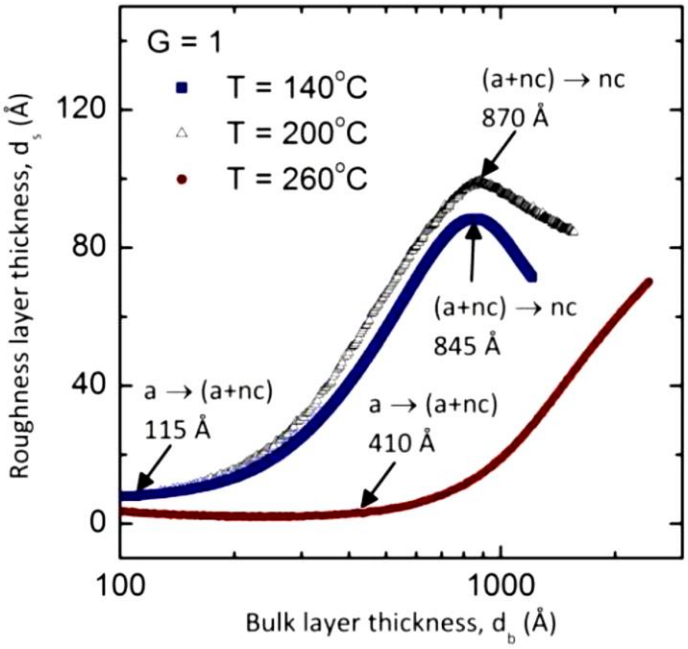

Figure 2-13. Surface roughness evolution for films deposited at increasing substrate temperatures on to SiN_x substrates on c-Si. Lower substrate temperatures result in a quicker decrease in roughness, indicating a more a more prompt coalescence [19].

2.3.3. Comparison of Material Performance

The total noise due to the sensing thin film depends on the bias current, but can be calculated based on values known from the industry [18] [19]. Due to their lower resistance, thin films of VO_x are pulsed biased with a current of ~ 10 μA. SiGe:H thin films, which have a much higher resistance in comparison, are biased using a constant current of ~ 40 nA. The noise contribution of the two material systems can then be calculated from the above equations and have been summarized in Table I below.

Table 1 lists relevant thin film parameters and the calculated noise current in VO_x and SiGe:H thin films.

Table 1. Parameters for commonly used IR imaging layers [17] [18].

Parameter	Value (VO_x Thin Film)	Value (SiGe:H Thin Film)
Resistance (T_{room})	100 KΩ	> 100 MΩ
Bias Current (I_{bias})	10 μA	40 nA
Bandwidth (B)	15 KHz – 0.0001 Hz	7.8 KHz – 0.0001 Hz
TCR (α)	–2.4 %/K	–3.9 %/K
Normalized Hooge' Parameter (α_H/n)	10^{-21} to 10^{-23} cm^3	10^{-18} to 10^{-20} cm^3
Thickness	50 nm	50 nm
Cell Area	17 μm × 17 μm	17 μm × 17 μm
Johnson Noise	**50 pA**	**1 pA**
1/f Noise	**0.072 nA to 7.2 nA**	**21 nA**
Total Noise	**75 pA to 7.2 nA**	**21 nA**

It can be seen that SiGe:H thin films can have lower Johnson noise values, yet much higher 1/*f* noise in comparison with VO_x thin films. Recent advances in the underlying read out integrated circuits (ROIC) have made a-SiGe based thin films competitive for use in microbolometer devices, as shown in the following section.

2.3.4. Readout Circuits used in Infrared Imaging Focal Plane Arrays

As it can be seen from Table 1 above and Figure 2-3, there are many deposition techniques and numerous materials that can yield thin films that can be used as sensing materials in infrared imaging. Thin films of VO_x, and SiGe:H have all been used for infrared imaging, yielding similar device performances [9] [18]. This begs the question, how can materials having orders of magnitude difference in resistivity and five to ten times difference in TCR result in similar sensitivity of the fabricated microbolometer array? The answer lies in the resistivity of the material and the underlying readout circuitry associated with that resistivity.

2.3.4.1. Low Resistivity Materials and Pulse Biasing

In the case of materials with resistivity < 1 Ω–cm, the device resistance is typically < 10^5 Ω. When a bias is applied to the thin film resistor on a substrate membrane of SiN_x, the film undergoes Joule heating which leads to a rise in temperature at a rate of [3]:

$$\boldsymbol{\Delta T = \frac{V_{bias} I_{bias}}{c}} \qquad \textbf{Equation 17}$$

where c is the thermal capacity of the detector. For a bias of 1 Volt this results in the rate of rise of temperature of 50,000 °C/second. To avoid a large rise in temperature, the bias time is limited to about 100 μsec, which limits the temperature rise to about 5 °C [3]. Following the pulse duration, the detector is left unbiased for 29.8 msec such that the thin film cools and reaches the substrate temperature and is ready for the next bias pulse [3]. The total pixel readout time is 30 msec which results in a frame rate of ≈ 30 Hz [9] [3].

Figure 2-14 shows the schematic of the Readout Integrated Circuit (ROIC) developed at FLIR Inc. to multiplex a VO_x based bolometer array [59]. The entire array is read in batches of 20 × 128 devices at a time with 8 channels to read out the entire array of 160 × 128 [59]. Each channel contains an on-chip bias compensation to provide a uniform output over a wide range of operating temperatures. This allows the operation of the bolometer without the need for thermoelectric cooler stabilization [59].

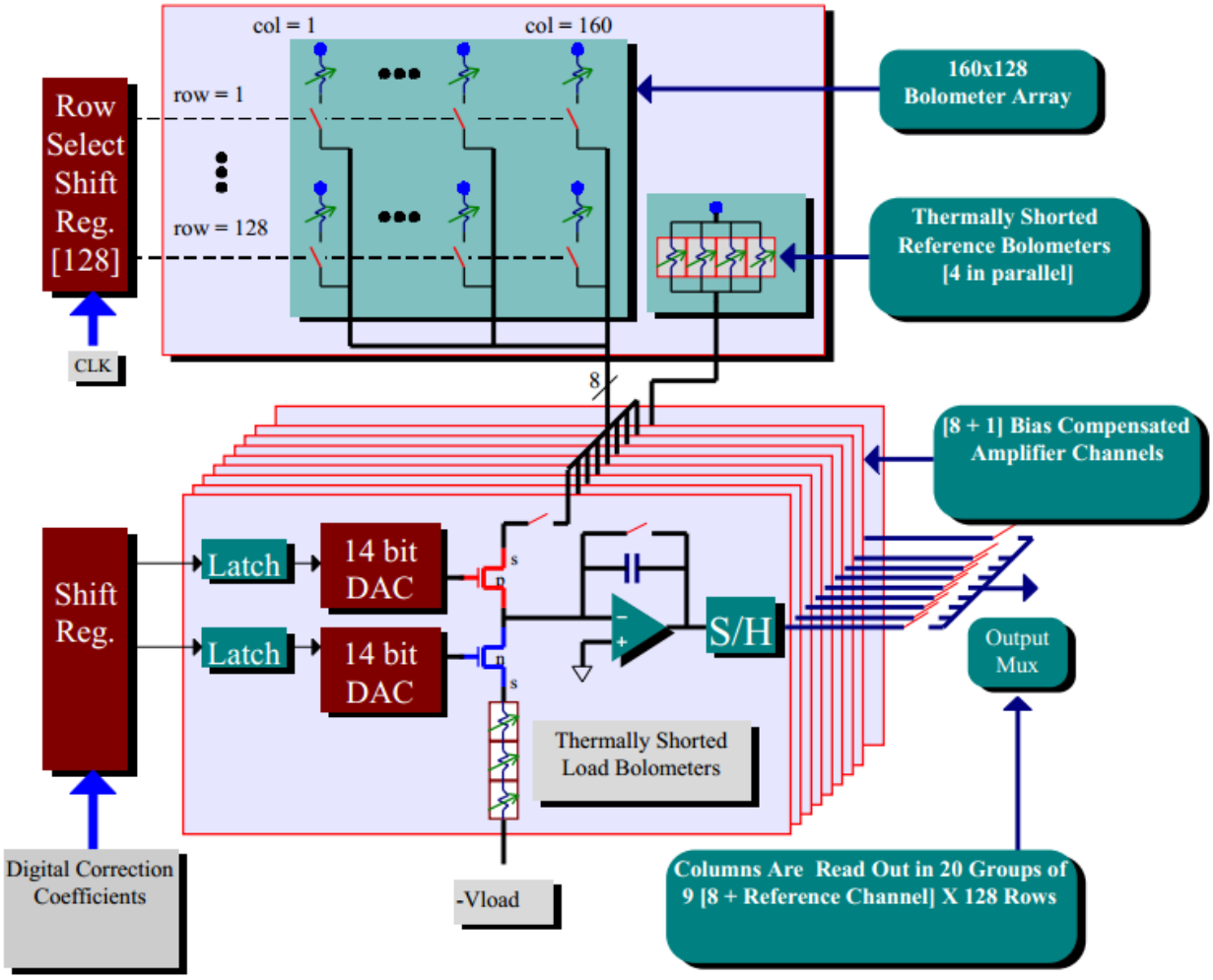

Figure 2-14.The readout circuit for a pulse biased VO_x based 160×128 bolometer array developed at FLIR [59].

The pulsed bias readout circuit employed by FLIR inc. is as follows [59]: The bolometers are sequentially biased and multiplexed to amplifiers in groups of eight. The detector is interfaced with the amplifier by a common gate p-channel MOSFET. The MOSFET biases the detector to a programmable voltage using on-chip DACs to vary the MOSFET gate voltage. A programmable load current is generated by thermally shunted bolometers connected to the source of an n-channel MOSFET. The drain current of the n-channel MOSFET is used to offset the detector current such that only temperature difference induced currents are integrated. The temperature induced currents is integrated over a sample period by an integrator and subsequently sampled and held for output multiplexing. The integrator can be reset using a shunt which allows amplification in addition to limiting the bandwidth of the output signal.

The pulse biasing scheme described above has been used for low resistivity materials such as VO_x and metallic thin films such as permalloy (Ni-Fe) and titanium.

2.3.4.2. High Resistivity Materials and Constant Biasing

For materials with high resistivity (> 1,000 Ω–cm), the pulse bias method is not necessary and in fact limits the sensitivity of the bolometer array. As discussed in the previous sub-section, these high resistivity materials have a high TCR but also high 1/f noise. For thin films belonging to the SiGe:H material system, the 'α_H/n' value is around 10^{-20} cm^3; as seen in Table 1 this leads to a 1/f noise value of 20 nA, a value roughly half that of the current signal. At these noise levels, it would be impossible to manufacture bolometer arrays with sensitivities anywhere close to those achieved by low resistivity material.

In the early 2000s, Level−3 Communications designed a unique ROIC which allowed for a dramatic reduction in noise by averaging the continuously biased signal [60]. The ROIC technology contains an in-pixel bias subtraction as well as an in-pixel switched capacitor filter/integrating amplifier to maximize signal integration and signal gain and enables simultaneous signal integration on every pixel [60]. Hanson et al. claim that the novel ROIC design enables the possibility of increasing the array size by adding rows, does not impact the array performance and theoretically allows for multi-megapixel sized FPAs with high performance [60]. A simplified version of the unit cell switched capacitor filter integrating amplifier design is shown in Figure 2-15 [60].

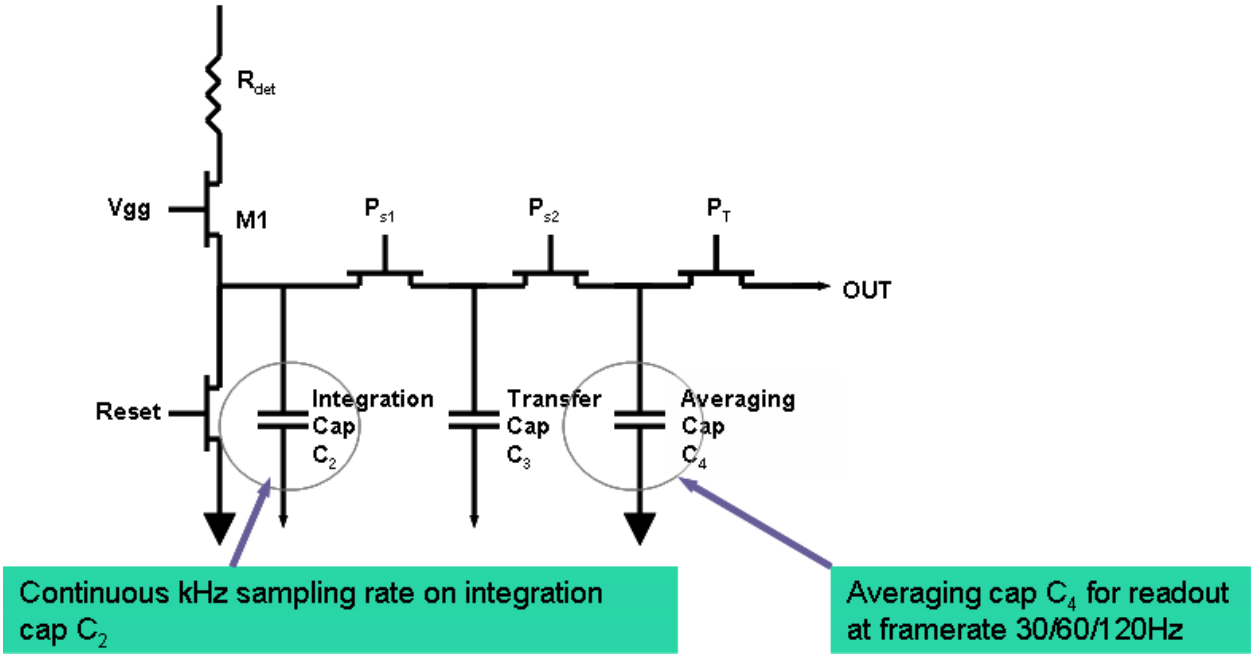

Figure 2-15. Schematic of the L-3 EOS switched capacitor filter/integrating amplifier integrated in the unit-cell of each pixel as in ref [60].

The operation of the readout circuit has been described in ref [60]: in Figure 2-15, the detector pixel is represented by a resistor (R_{det}). Detector signal current is injected through the input field effect transistor (FET M1) by biasing its gate V_{gg}. The detector current is sampled continuously on the integrating capacitor C_2 at a rate of ~7.8KHz. The continuously sampled current signal is filtered by the switched capacitor filter network through a transfer capacitor C_3 and averaged on capacitor C_4. It is at this capacitor, C_4, where the signal is averaged and the 1/f noise reduced. For example, for a desired frame rate of 60 Hz, the sample can be averaged over 130 times resulting in 1/ƒ noise reduction by a factor > 11. The processed signal on capacitor C_4 is sampled and read out at the desired frame rate. Hanson points out that the FPA sensitivity is not dependent on frame rate but rather on the KHz rate at which signal is integrated on C_2. Although a high integration frequency would help further reduce 1/f noise, the Johnson noise value would then increase. The sweeping frequency is chosen in a way that 1/f noise and the Johnson noise contribution is minimized. The filter network is chosen such that the noise bandwidth is significantly lower than the Nyquist frequency. The noise bandwidth is substantially lower than the filter Nyquist frequency.

Hanson claims that for the above mentioned reasons, L-3 ROIC's performance is independent of frame rate making frame rates of 60Hz, 120Hz, and beyond achievable without performance loss [60].

Chapter 3. Experimental Methods

3.1. Deposition of VO_x Thin Films: The LANS Biased Target Deposition System

Thin films of VO_x were deposited by a novel sputtering technique known as Biased Target Ion Beam Deposition (BTIBD) or simply Biased Target Deposition (BTD) (manufactured by 4Wave Inc. based in Sterling, VA).

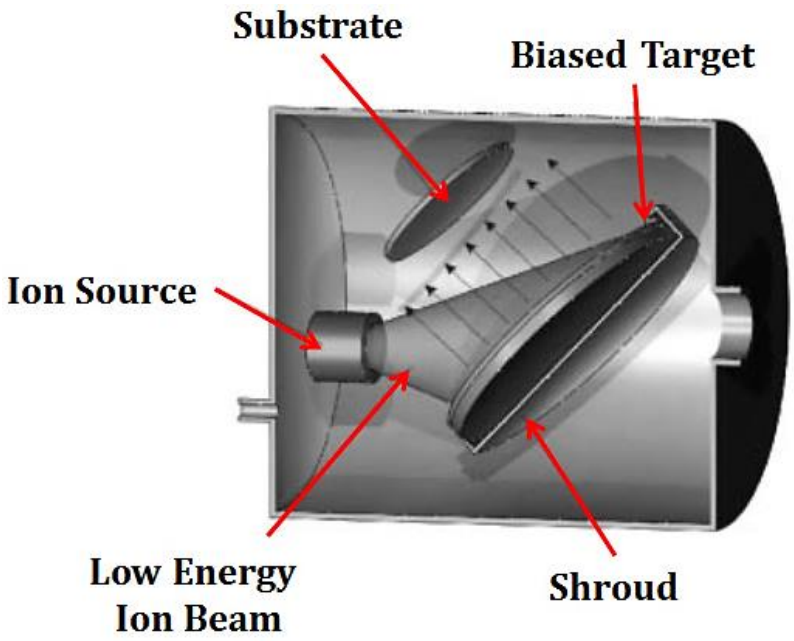

Figure 3-1. Concept sketch of Biased Target Ion Beam Deposition system [61].

A concept sketch of this technique can be seen in Figure 3-1 [61]. The operation principle of the technique has been discussed elsewhere and is summarized [47]: In this deposition technique, a low energy, broad beam ion source (Energy of ions < 25 eV) is used to illuminate the target. No attempt is made to focus the ion beam on to the target material. The ion energy of the beam is low compared (<40 eV) and so the sputter yield of materials in the chamber from this beam is minimal.. Once a stable ion beam has been established, a negative bias is applied to the target. This negative bias establishes a sheath in front of the target which accelerates the positively charged ions from the ion beam to cause sputtering.

The deposition system used in this work is detailed in Figure 3-2. This system is sold as the LANS BTIBD tool. In this geometry, the low energy ion-beam producing ion gun is facing the substrate and illuminating three targets. Targets are biased using a single programmable pulsed DC power supply source. The pulsed DC power source is connected to the three targets in parallel configuration to allow for simultaneous sputtering of up to three targets. Therefore the control of adatom arrival rate and the adatom energies is accomplished threefold by:

1. Sputter yield is controlled by the ion current established by the ion source.
2. Sputtering rate is additionally controlled at each target by controlling the pulse frequency and the duty cycle.
3. The adatom energy is decided by the operating pressure. .

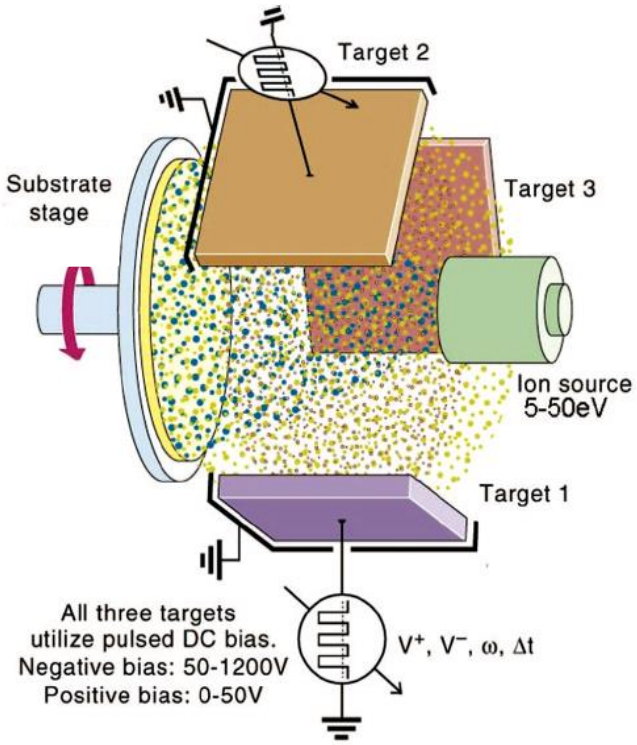

Figure 3-2. Schematic of the Laboratory for Alloying and Nano layer Sputtering by the 4Wave Inc. used in this work [62].

3.1.1. Ion Source used in BTD: Broad Beam, Gridless Ion Sources

A broad-beam ion source is defined as a beam of ions whose diameter (length of transverse direction) is much larger than the physical dimensions of its optics or the Debye length of the accelerating voltage [63]. These sources are much more interesting as ion sources for thin film processing applications than other types such as Von Ardenne type ion source (mainly used for high energy thin beam of ions carrying high energy and multiple charges), Electron Cyclotron Resonance Type (ECR) ion sources, electron beam ion sources, laser ion sources and vacuum arc ion sources. Broadly speaking, there are two types of ion sources commercially used in thin film processing, gridded and gridless type [63]. The fundamental difference between the two types of sources is that while gridded ion sources produce ions with a narrow energy distribution, gridless ion sources produce ion beams that are unfocussed and have a broad energy distribution [63] [64]. This section is aimed at discussing the fundamental theory of operation of the ion source in the context of this work.

The Hall-current ion sources operate on the principle of significantly increasing the plasma's electrical resistance and the electron lifetime in the plasma using a magnetic field [63] [64] [65]. The increased electron lifetime allows for an increase in the interaction time of the electrons with the neutral atoms/working gas which is being expelled from within the ion source.

In the ion source discharge channel, the electrons are magnetized. If ω_e is the electron cyclotron frequency and τ is the average time between collisions with other particles and the chamber walls, then $\omega_e \tau \gg 1$ [61] [63] [64]. These magnetized electrons move from their source of origin (cathode/electron source) to the anode (ion source discharge channel) in a helical path prescribed by the electrical and magnetic fields. Under optimum conditions, the ions are usually not magnetized, i.e. $\omega_i \tau \ll 1$ (where ω_i is the ion cyclotron frequency in the magnetic field and τ is the average time between the ion collisions with other particles and the chamber walls) [61] [63] [64]. The ions move between their source of origin (anode discharge channel) and the cathode along the electrical field. During this path, the plasma picks up

the necessary number of electrons for neutralization, resulting in a quasi-neutral beam of ions and electrons known as the ion beam [61] [63] [64].

Unlike in gridded ion sources where the ion beam experiences space charge limitations due to limitations imposed by Child's law, the Hall-current sources do not have any limitation for the ion beam current that can extracted [63].

Schematics of the geometry and the electrical circuit of the most popular type of ion source are shown Figure 3-3a and Figure 3-3b. A detailed description of the operation of the ion source can be found in reference [61] but is briefly discussed here: Figure 3-3b shows the electron emission from the cathode is controlled by the use of an AC power supply connected to the electron source. The anode potential is determined by the anode current, the magnetic field strength and the gas flow. The power supply to an electromagnet impresses a variable magnetic field on the electrons being emitted from the cathode. For a known regime of operation, a permanent magnet can replace the electromagnet, thereby eliminating the use of an extra power supply. A mass flow controller is used to control the amount of gas being introduced into the system, and thereby control the conductivity of the plasma. This gas flow dictates the discharge voltage of a particular ion beam discharge current. The cathode used in normal operation is either a filament type or a hollow cathode type.

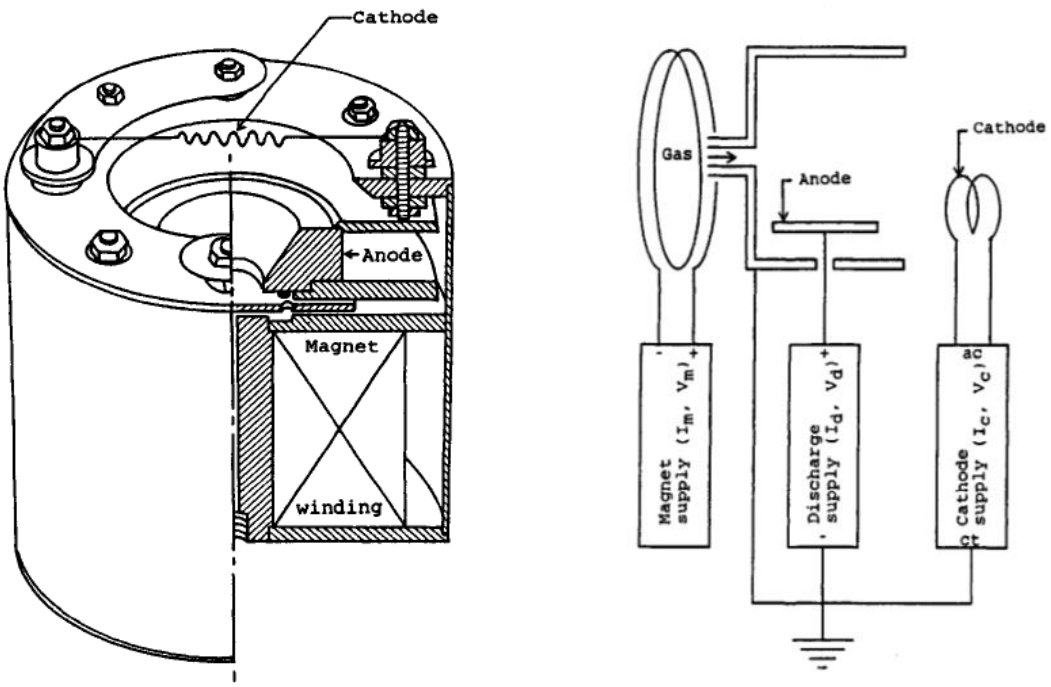

Figure 3-3. Schematic of a) Cross-section of one of the first ion sources, b) Electrical diagram of a basic ion source as it appears in ref. [64].

3.1.1.1. Ion Generation Mechanisms

The operating principle and various processes of the anode are discussed as follows and are pictured in Figure 3-4. The neutral atoms/gas molecules are introduced using a mass flow controller (1). Electrons (2) generated at the cathode, crossed between electric field and magnetic field lines follow the path given by (3) in a helical manner towards the discharge chamber of the anode. These electrons strike the neutral atoms/molecules (4) and ionize them (5). A combination of electrons (2) and ions (5) forms the plasma which is directed downstream by the radial and axial components of the electric field as well as a gas distributor/reflector.

Due to the conical axisymmetric shape of the discharge chamber and the positive charge enforced on the anode, the ions that are created near the discharge chamber are accelerated away from the anode in the axial direction. The velocity acquired by these ions and the positive potential on the other side of the axis forces the ions to crisscross the axis multiple times and undergo several collisions [66]. The positive space-charge and the current due to the ions are neutralized by electrons generated from the electron gun

(7). These processes result in a divergent, neutral beam comprised of ions (6) and electrons (7) of ions being generated and directed downstream from the discharge chamber.

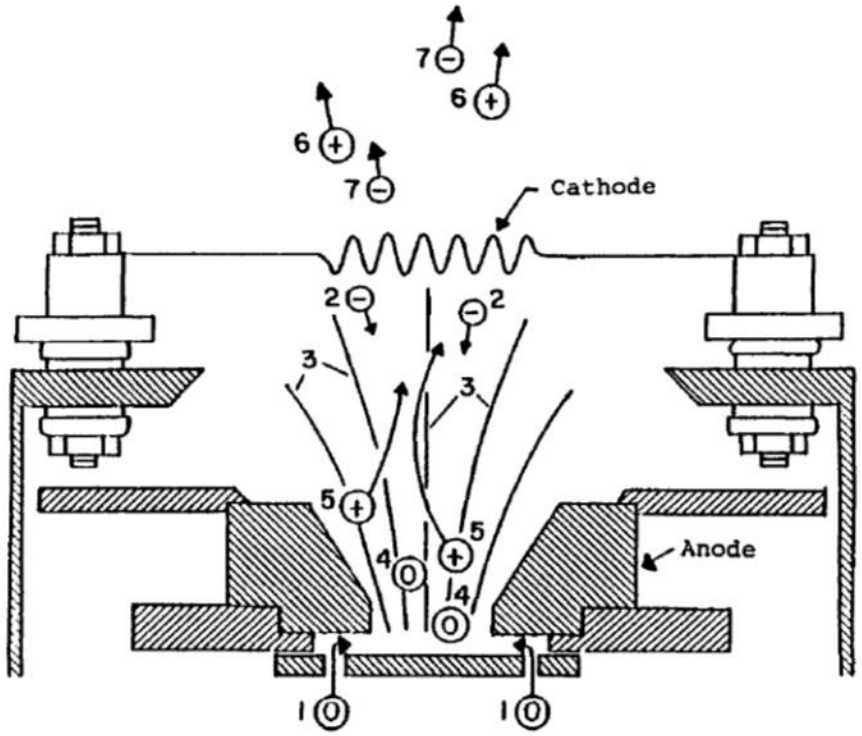

Figure 3-4. Various processes in an end-Hall ion source [66].

It should be noted that discharge current of the anode and the cathode does not equal the electron and ion currents in the quasi-neutral beam. In fact, the current to the anode is almost entirely composed of electrons – both the electrons from the electron source, and secondary electrons generated during ionization. The excess electron generation from the cathode is usually sufficient to current-neutralize the ion beam with electron emission from the anode when the cathode current is set to the anode current [66]. However, the cathode current is usually set in excess of this current.

3.1.1.3. Electric Discharge and Voltage-Current Characteristics

Since, typical thin film processing/modification pressure ranges from 10^{-5} Torr and 5×10^{-3} Torr (Figure 3-5), ion sources must be operated in this region for ion assist modifications. Ion beam operation

in this pressure range exists in primarily two modes of operation, a) a self-sustained discharge and b) a non-self-sustained discharge.

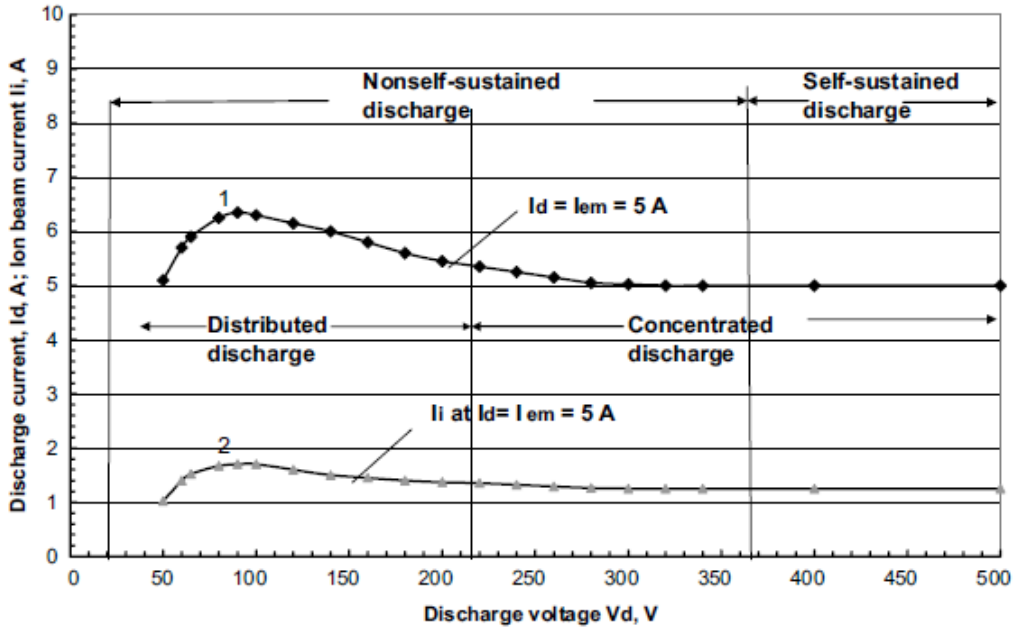

Figure 3-5.Voltage-current characteristics (between 5 x 10^{-5} Torr and 1 x 10^{-3} Torr) of an end-Hall ion source showing the various regimes of operation of its plasma discharge. The two curves show the voltage-current characteristics for a discharge current of I_d = 5A and corresponding ion beam current of I_i [61].

In the self-sustained discharge region, the plasma is comprised of ions generated by the ion source and a number of electrons equaling the total positive charge in the plasma [61]. These electrons are generated when a plasma discharge voltage of $V_d \geq 300$ - 350V is applied between the anode (ion source) and any surface that can act as a conductor in the vacuum chamber (chamber walls, flanges, bellows, etc.). These surfaces can potentially serve as the cathode materials from which a sufficient number of electrons can be generated from the ion bombardment. Because no external source of electrons is needed, this discharge is known as a self-sustained discharge [61].

However, at discharge voltages between 50 V and 300 V, the discharge voltage by itself does not produce enough secondary electrons to sustain the discharge [61] [64]. This region of operation is called a non-self-sustained discharge. In this type of discharge, an external source of electrons is needed to

generate and maintain stable plasma. The source of electrons is either a hot filament (HF) or a hollow cathode (HC), and will be discussed in the next section.

The voltage-current characteristics of a Hall current ion source depend on several factors such as [61]:

1. Pressure at the discharge channel. Higher the pressure, the lower the discharge voltage.
2. Magnetic field value atop the gas reflector at the anode. In general, the lower the magnetic field, the lower the ignition voltage (However, this leads to a lower ion beam current)
3. System geometry, anode dimensions and the relative placement of the electron source.

3.1.1.4. The Ion Source for the LANS BTD System

For this thesis, an ion source is required which produces ions with energy less than the sputter threshold of all material in the deposition chamber. In addition, the ion source required must be rugged for operation in a reactive environment. The EH-1000 compares well to the required specifications (Figure 3-6). Some key features are as follows [63] [67]:

1. A hollow cathode was used to as the source of electrons to prevent cathode oxidation during reactive sputtering.
2. The anode was grooved (Figure 3-7) to prevent the oxidation/deposition of dielectric materials that prevents operation at a low discharge voltage.
3. The discharge voltage was reduced to < 30 V by reducing the strength of the magnetic field in the discharge chamber. The ion source was custom designed for this sputter system by Kauffman and Robinson Inc. The magnetic field was established using an Alnico magnet whose field intensity was reduced to 400 G (versus the original 550 G) atop the gas reflector. This reduced magnetic field strength was measured using a F.W. Bell Gaussmeter, Model 410 and compared with quoted values from the product technical specifications.

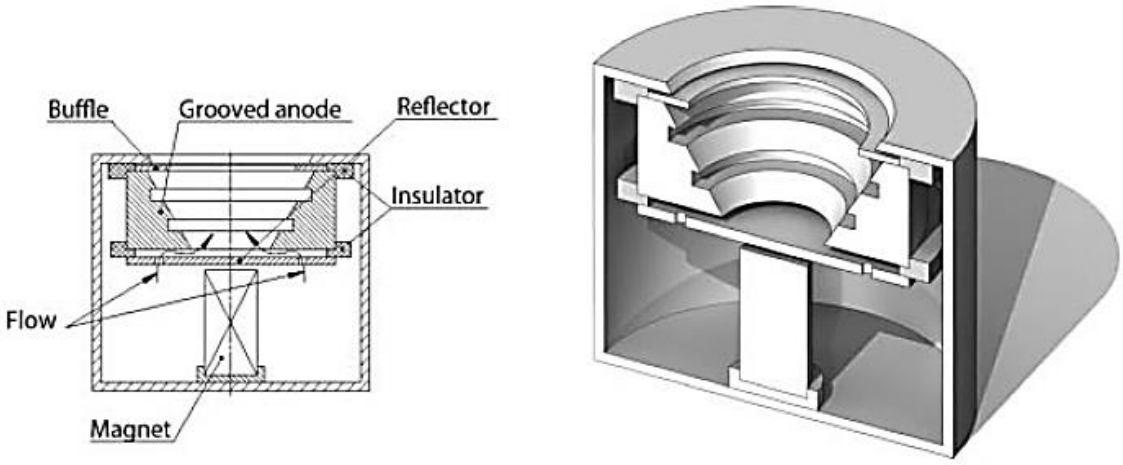

Figure 3-6. An End-Hall ion source with a grooved anode and baffle to reduce anode "poisoning"/oxidation [61].

A retarding potential analysis (Figure 3-7) at different angles at a distance of 30 cm from the center of the ion source shows that > 90% of the ions have energies < 30 eV, which is less than the sputter threshold of most materials in the deposition chamber [61] [68].

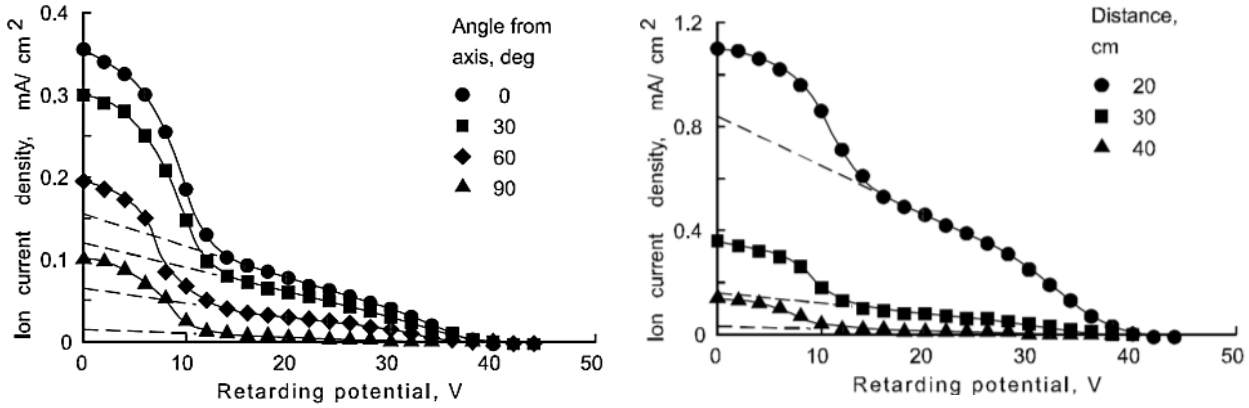

Figure 3-7. a) Angular retarding potential analysis of a modified KRI EH1000 ion source indicating most ions having energy < 30 eV. The measurements were made at a distance of 30 cm. b) Angular retarding potential analysis of a modified KRI End-Hall 1000 ion source as a function of distance from the ion source. The operating gas is Ar at a pressure of 1 mTorr. The discharge characteristics were 10 Amperes at 42 V with a gas flow of 70 sccm [68].

Because End-Hall ion sources are unfocussed ion generators, it is important to understand the angular distribution of ion current produced by the ion sources. Figure 3-8 shows the angular distribution of ion current density at a distance of 30 cm from the ion source, as is the case in the 4Wave's LANS System [68].

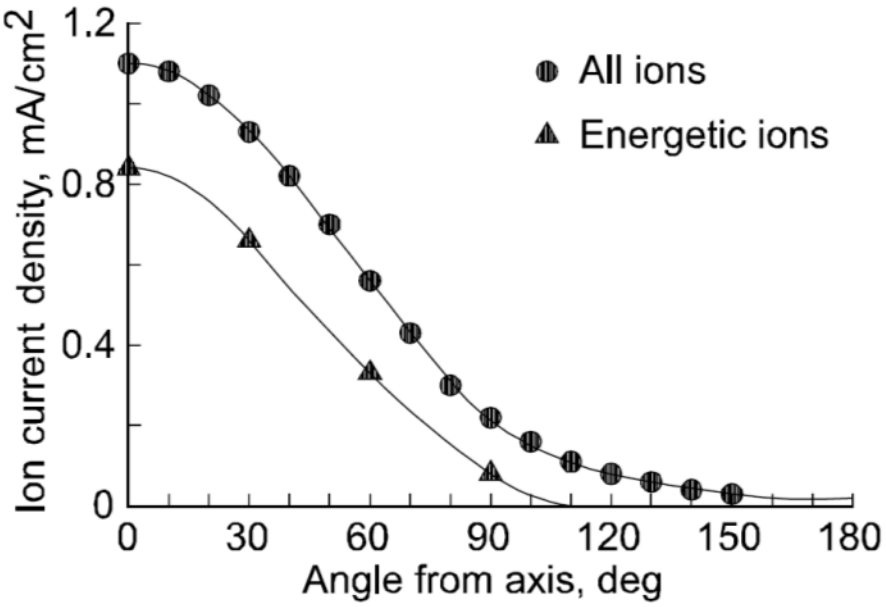

Figure 3-8. Spherical ion current density profiles for the KRI End-Hall 1000 ion source with the source at the center of the sphere. Source to target distance is 30 cm (12 in.). The working gas was 70 sccm of argon and the discharge characteristics were 10 A and 45 V [68].

3.1.2. Hollow Cathode Electron Source

As discussed in the previous sections, the ion source's mode of operation of interest lies in the non-self-sustained discharge region: an external source of electrons is required for ionization and neutralization of the space charge region of the ion beam. Without an external source of neutralization the plasma is under neutralized and extracts electrons from any object in the deposition chamber [61] [64]. This extraction manifests itself in the form of an undesirable arc that could last for a several microseconds and whose frequency of occurrence may depend on the degree of under neutralization of the ion beam.

In an ion source, the discharge current is given by the sum of the ion current and electron current produced by the discharge:

$$\boldsymbol{I_d = I_{i,d} + I_{e,d}}$$

In the case of a non-self-sustained discharge $I_{i,\,d} > I_{e,\,d}$, the neutralizer should provide the difference between the ion and electron current such that the net neutralization electron current is equal to the ion current. This can be expressed as:

$$I_d = I_n = I_{e,n} + I_{e,d}$$

Therefore the ion source discharge current is the sum of ion current and the current from an electron neutralizer as:

$$I_d = I_{i,d} + I_{e,n}$$

Typically the electron current from the neutralizer is set to a value higher than the ion source discharge current. The effect of under neutralization can be seen in Figure 3-9. The additional electron current not only facilitates the ionization of the working gas in the ion source discharge chamber but also to produce an ion beam with low energy spread as shown in Figure 3-9.

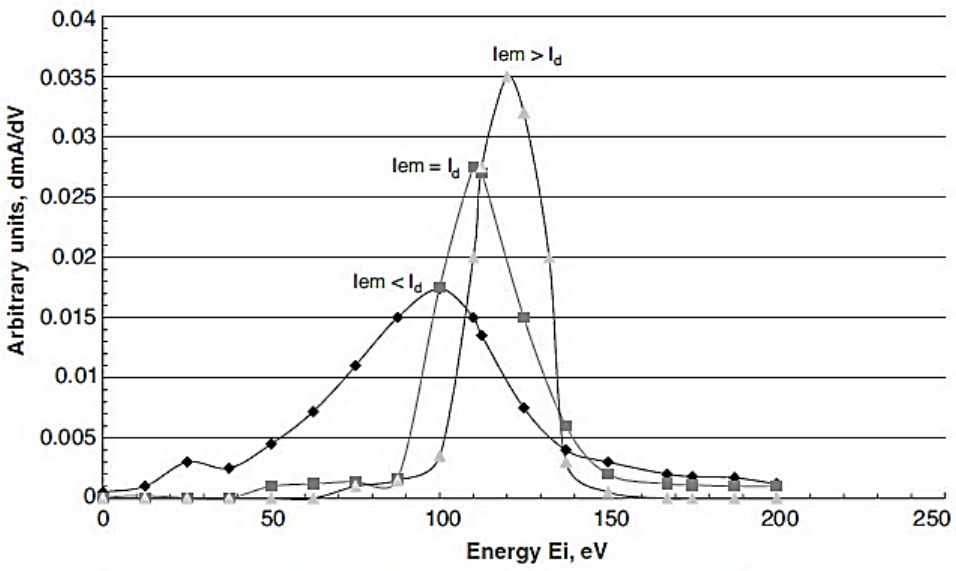

Figure 3-9. Typical ion beam energy distribution for different neutralization ratios: I_{em} (3.8 A) < I_d (4 A), I_m = I_d = 4 A and I_{em} (6 A) > I_d (4 A) [61].

There are two main types of electron sources: the Hot Filament type (HF) or the Hollow Cathode type (HC). Due to the limited lifetime of HF type source in thin film deposition, HC type electron sources are commonly used.

Hollow cathode electron sources are an alternative source of electrons that overcome the shortcomings of the hot filament type electron sources as described in the previous section. In these types

of sources, a refractory metal tube is negatively biased to create argon ion bombardment. This ion bombardment causes significant heating, leading to thermionic emission from the refractory metal (tungsten) [61] [66] [69]. Because of the low pressure regime of operation of these electron sources (< 0.01 Torr), these electron sources are operated by maintaining a constant flow of ionizable gas through them [61] [66] [69].

Thermoelectron emission current of a material with a square potential barrier is governed by the Richardson-Dushman equation [70]. For a conductor at temperature T and a work function φ, the emission current density is given by:

$$\boldsymbol{j = A_0 T^2 e^{-\varphi/kT}} \qquad \textbf{Equation 18 [70]}$$

W here $A_0 = 4\pi mek^2/h^3 = 120.4$ A/cm^{2}K^2 is the Richardson constant for a tungsten filament, T is the temperature of operation (≈2500K) for the tungsten filament and *k* is the Boltzmann's constant, k = 1.38 × 10^{-23} J/K. This gives a typical current density of ≈ 0.65A/cm^2 [61].

One of the first hollow cathode assemblies was described by [69]. Since its invention, there have been numerous performance improvements. One such iteration of the hollow cathode is manufactured by the Kaufman & Robinson Inc. and is shown in Figure 3-10 [71].

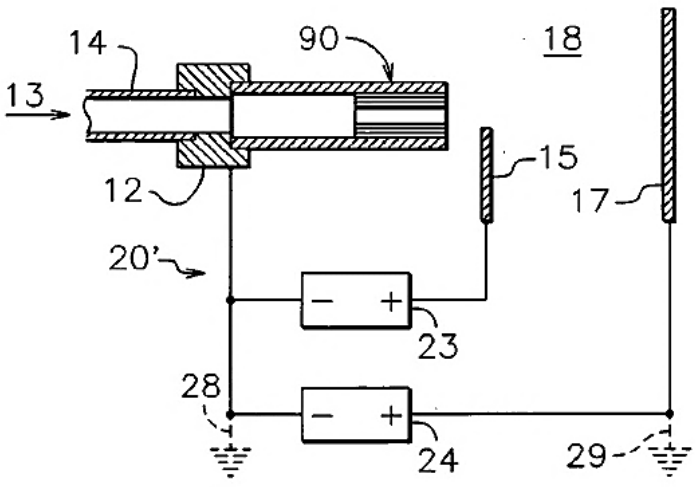

Figure 3-10. Schematic and electrical circuit diagram of a hollow cathode assembly [71].

The operation of this Hollow Cathode is described in reference [68] and is summarized here: Prior to operation of the hollow cathode, a flow > 75 sccm is maintained to purge contamination physisorbed in the hollow cathode assembly. This high flow rate also produces a large number of electrons which facilitates to strike the plasma. To start the hollow cathode electron source (HCES), a voltage of several hundred volts is applied between the keeper 17 and the cathode body 90. Once a plasma is established between the keeper and the cathode, the keeper current should rise to ≈ 1.5 A (for LHC-1000). At this point sufficient argon ions are generated in the gas 13, flowing out of the cathode tip to start thermionic emission of the cathode. A current controlled power supply can be used to supply a positive to the assembly body with respect to the tip 90, thereby causing ion bombardment of the tip.

Figure 3-11. An end-Hall ion source showing the typical placement of a filament [68].

The hollow cathode design adopted in the biased target deposition of this work is one of such iterations detailed in a 2010 patent filing (Figure 3-11) and realized as LHC-1000 electron source by Kaufman & Robinson Inc. [71]. Figure 3-11 shows the ion and electron source assembly. The electron source is physically mounted on the ion source in the direction of the ion beam propagation.

3.1.3. Summary of Operation of 4Wave LANS system

The key points that are to be kept in mind when setting parameters for deposition in this tool are:

1. The ultimate requirement for deposition with this technique is obtaining a large flux of ions in the deposition chamber
2. A large amount of electrons must be generated for igniting and sustaining ion generation of low energies
3. The gridless type ion source produces ions with different energies whose distribution is angular. The ions along the axis carry the highest energy and can be used for secondary conditioning of the growing thin film with minimal contamination from the sputtering of the chamber walls.

Table 2 gives the parameters used for deposition in this work. The only variable in this work is the partial pressure of oxygen whose values will be given in subsequent chapters in which VO_x thin films were deposited.

Table 2. Parameters used for deposition of VO_x thin films in this work

<table>
<tr><td colspan="2">Hollow cathode (HC) Ar flow rate: 10 sccm</td><td colspan="2">Ion Source Ar flow rate: 60 sccm</td><td colspan="2">O_2 flow: Varies based on oxygen partial pressure</td></tr>
<tr><td colspan="2">Keeper V/I: 20 V/1.5 A</td><td colspan="2">Bias V/I: 23 V/8 A</td><td colspan="2">Source V/I: 38 V/8 A</td></tr>
<tr><td colspan="2" rowspan="2">Target Material(s)/Gun(s):
3 Vanadium Targets</td><td rowspan="2">Spin: 20 rpm
Time: 30 min.</td><td>V/I (Gun 1):
–800 V
+5 V</td><td>V/I (Gun 3):
–800 V
+5 V</td><td>V/I (Gun 5):
–800 V
+5 V</td></tr>
<tr><td>Pulse Width #1:
1 μsec</td><td>Period #1:
100 μsec</td><td>Pulse Width # 3:
1 μsec</td><td>Pulse # 3:
100 μsec</td><td>Pulse Width # 5:
1 μsec</td><td>Pulse # 5:
100 μsec</td></tr>
<tr><td colspan="2">P_{Total}: 5.8 × 10^{-4} Torr</td><td colspan="2">P_{H20}: < 2 × 10^{-7} Torr</td><td>P_{O2}: Varies</td><td>P_{H2}: < 1×10^{-7} Torr</td></tr>
</table>

3.2. Deposition of Hydrogenated Ge:H Thin Films

Thin films of Hydrogenated Germanium (Ge:H) were deposited using a research scale Plasma Enhanced Chemical Vapor Deposition (PECVD) with 13.56 MHz RF power capacitively coupled to the two electrodes of the system as can be seen in Figure 3-12. The thin films of Ge:H were deposited using

the carrier gas germane (GeH_4) gas diluted with hydrogen before entering the deposition chamber by a variable dilution ratio. The dilution ratio {$R = [H_2]/([H_2]+[GeH_4])$} is programmable by means of varying the gas flow using a mass flow controller. The dilution can be increased or decreased by increasing the amount of GeH_4 to H_2.

The deposition of thin films of hydrogenated SiGe alloys using PECVD is well known with numerous reports detailing the process. In CVD, a source gas is used in the fluid-flow regime (High pressure). Briefly, during the PECVD deposition of Ge:H, the carrier gas for germanium (GeH_4) is mixed with hydrogen gas (H_2) and introduced into the chamber through a mass flow controller (MFC) which is programmable for a certain dilution ratio. Figure 3-12 shows a schematic of the chamber used in this work. A low power plasma is struck with a power density of 0.08 W/cm^2, using an inductively coupled plasma at a radio frequency of ƒ=13.56 MHz. By electron impact ionization, the gas disassociates to produce a variety of ions, radical species and primary and secondary electrons. These species may adsorb onto the surface of the substrate to form a thin film.

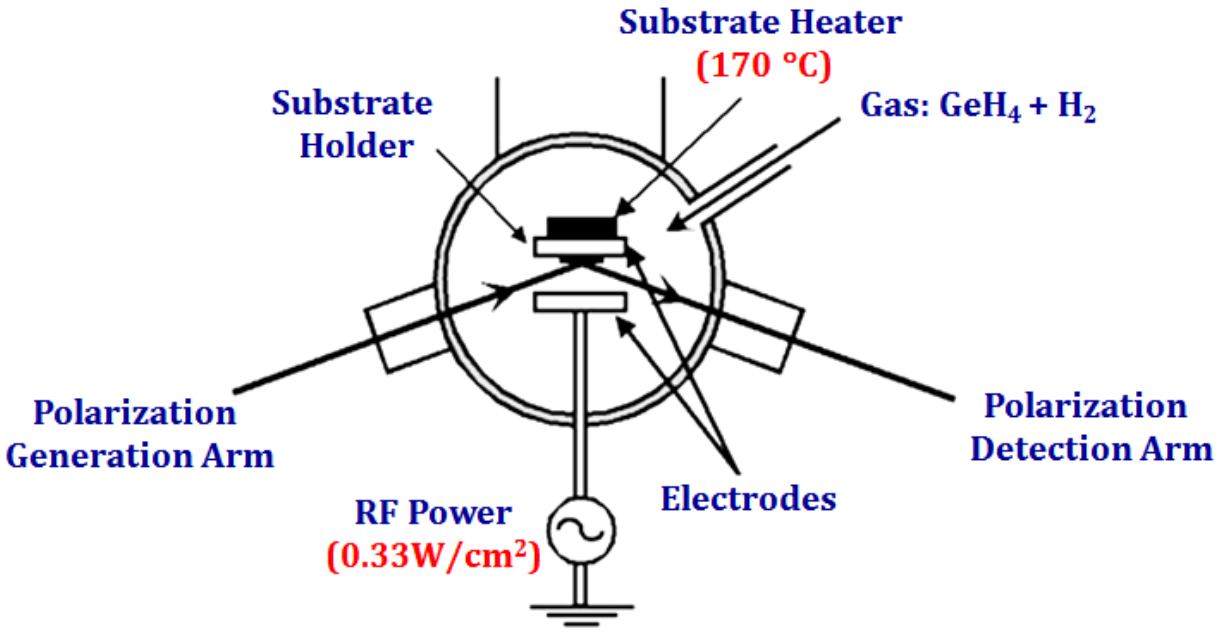

Figure 3-12. Schematic of the plasma enhanced CVD deposition chamber used to deposit the Ge:H of this work as it appears in ref. [72].

The spacing between the electrodes and the plasma power density are used to control the plasma kinetics and therefore the ion bombardment experienced by the growing thin film. The substrate temperature on the other hand influences the surface reactions on the substrate. Low substrate temperatures may lead to a low density, disordered thin film because the impinging species may not have enough adatom mobility. On the other hand a high substrate temperature may lead to reduced hydrogen incorporation, which may leave the growing thin film unpassivated.

The total flow rates and the pressure for deposition, as with any vapor deposition, decides the residence time of the disassociated species created during the RF plasma. Large deposition pressures may lead to significantly reduced mean free paths. This in turn leads to an increase in gas phase reactions and produces an undesirable number of particles.

In the case of Si:H deposition, the process parameters have been optimized for infrared imaging applications over many years of active investigation [53] [73]. The substrate temperature is usually kept at 200 °C, the total pressure is around 0.5 Torr and a low plasma is applied (plasma density ~0.08 W/cm^2) [74]. These deposition conditions optimized for Si:H were found to be non-optimal for thin films of Ge:H [53].

3.3. Characterization Techniques

3.3.1. Grazing Incidence X-Ray Diffraction (GIXRD)

Grazing-incidence diffraction is a scattering geometry that combines the Bragg condition with the conditions for x-ray total external reflection from crystal planes to identify the crystalline phase of the sample under investigation. This configuration uses small angle of incidence and reduces the penetration depth of the x-ray by up to three orders of magnitude (typically from 1-10μm to 10-100°A).

Grazing incidence x-ray diffraction was done using a PANAnalytical PRO X'Pert MPD with Cu Kα1 (λ = 1.54 Å) radiation, to analyze the structure of the deposited thin film. Diffraction patterns were

collected for 2θ values between 10° and 85°, and a scan rate of 1.2°/min. The crystalline phase and the lattice parameter were determined by comparing the peak positions and intensities and their corresponding 2θ values to that of standards using MDI Jade V9.0 software.

3.3.2. Atomic Force Microscopy (AFM)

Atomic force microscopy is a form of surface probe microscopy technique in which a sharp tip is scanned across the surface and the surface-tip interaction force is used to infer the surface morphology of the surface under investigation. For measurements in this work, measurements were made using the peak force tapping method using instrumentation developed by Bruker Icon.

3.3.3. Rutherford Backscattering Spectroscopy (RBS)

Rutherford Backscattering Spectroscopy (RBS) was used in this work to determine the stoichiometry of the VO_x thin films. RBS operates on a phenomenon that occurs when a high-energy primary ion (typically He^{++} ions with energies in the order of MeV) is elastically scattered. The energy and angle of the scattered ion yields information about the mass of the scattering atom in the sample. This information then can be used for composition analysis of thin films.

All RBS data described herein was collected at the Tandem Accelerator at the Department of Physics and Astronomy, Rutgers University. Figure 3-1 describes the schematic used for RBS experiments. All measurements were performed in a standard RBS chamber under a vacuum of 10^{-6} Torr using two Si surface barrier detectors: one at 155° and other at 100° scattering angle. A 2 MeV He++ ions from a 1.7MV tandem accelerator was used with an ion current of 2-3nA and a beam spot of 2mm.

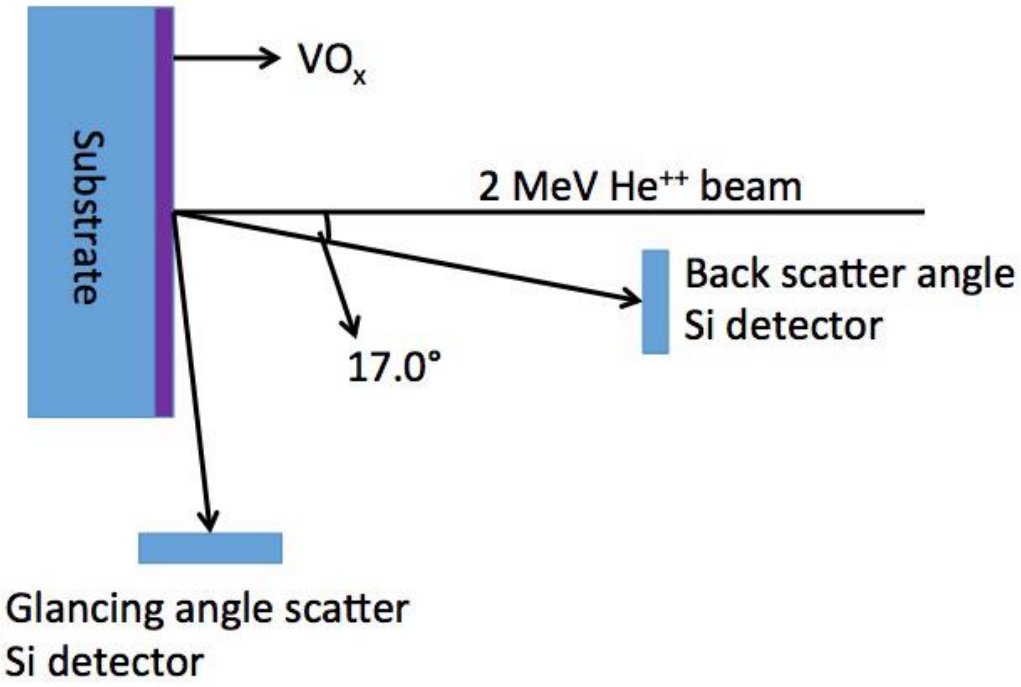

Figure 3-13. Schematic of a typical RBS experimental setup.

This ion beam is deflected into the RBS chamber, where it is incident on the sample under investigation. The He^{++} ions that are deflected are backscattered and their intensity is measured at a Si surface barrier detector which is placed at a 17° angle with respect to the incoming incident radiation. Data was collected till 10μC of charge was accumulated (typically 15 minutes).

3.3.4. Ellipsometry

Ellipsometry is a non-destructive technique which measures the change in polarization of a reflected beam of light from the sample's surface with a known polarization state. The change in the polarization of light depends on the structural and the optical properties of the sample under investigation. Unlike x-ray diffraction, ellipsometry is a portable and versatile tool that can be used to monitor in-situ the growth of thin films. Ellipsometric measurements in this work were conducted by using a J.A. Woollam Co. M2000-DUV variable angle rotating-compensator multichannel spectroscopic ellipsometer. This instrument uses two light sources, a Xe lamp and a Quartz Tungsten Halogen (QTH) lamp. By combining both light sources, the attainable ellipsometric spectra from the RC2 instrument spans over the

0.73 – 5.15 eV (1700 – 240 nm) spectral range. Figure 3-14 shows the schematic of an ellipsometry configuration. The measured response is a function of optical properties and the thickness of the thin film.

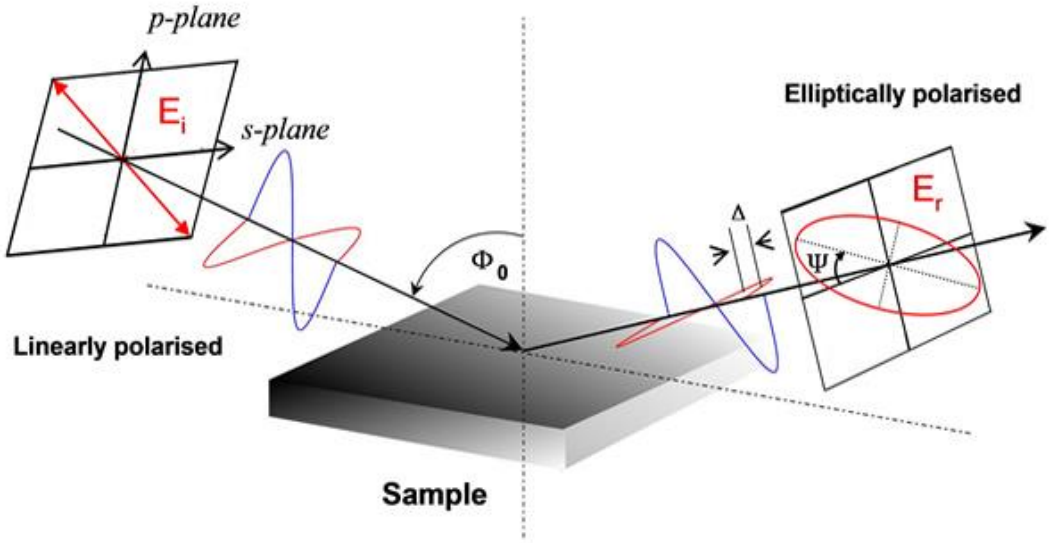

Figure 3-14. Typical configuration for ellipsometry measurement [75].

3.3.5. Resistivity Measurements

The resistivity of the thin film deposited was measured by using the Transmission Line Method (TLM). The TLM method gives a complete characterization of the contact by providing the sheet resistance, the contact resistance, and the specific contact resistivity. For top contacts to VO_x thin films, 100 nm of titanium was deposited using the Perkin Elmer sputtering system. Bottom contacts to VO_x thin films were obtained using only Vanadium as the bottom metal. The mask set used to extract resistivity values is shown in Figure 3-15. It consists of two layers, the first of which is used to isolated the TCR material so as obtain an accurate value of resistivity; the second layer consists of a series of five electrodes for metal contacts with spacings of 10µm, 30µm, 70µm, 150µm and 310µm respectively.

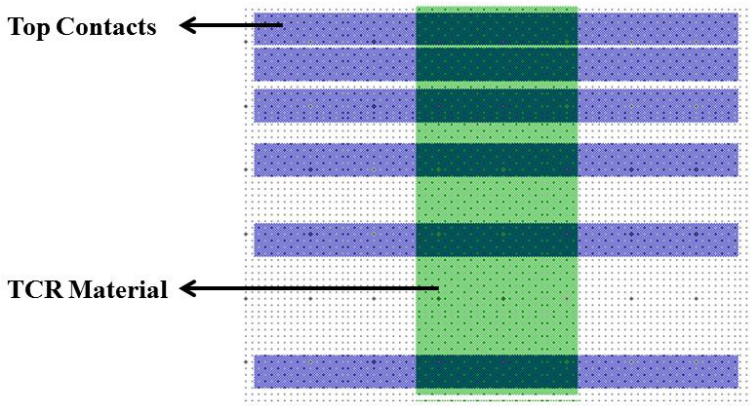

Figure 3-15. Transmission Line Method test structures showing features used in isolation of the TCR material and to deposit the metal contacts.

Current–Voltage (I-V) characteristics were measured by sweeping voltage using a Hewlett Packard 4140B pA meter/ DC Voltage source and the resistance was recorded. A LabVIEW program was used to collect the data. The I–V curves were examined to ensure ohmic behavior of the resistance structures. The resistance of each resistor with different spacing is plotted as in Figure 3-16. The Y–intercept gives the contact resistance. Apart from ensuring ohmic contacts, another important parameter used to assess the quality of the contacts is the transfer length [76]. Half the value of the x–intercept gives a value known as the transfer length. Transfer length is defined as the distance at which '1/e' of the current is transferred from the semiconductor to the electrode or vice-versa. Thus an accurate measurement of the transfer length helps to determine the minimum spacing of electrodes (therefore the size of the active region) that can be used to extract electrical properties from the sample with minimal contribution from the contact resistance itself.

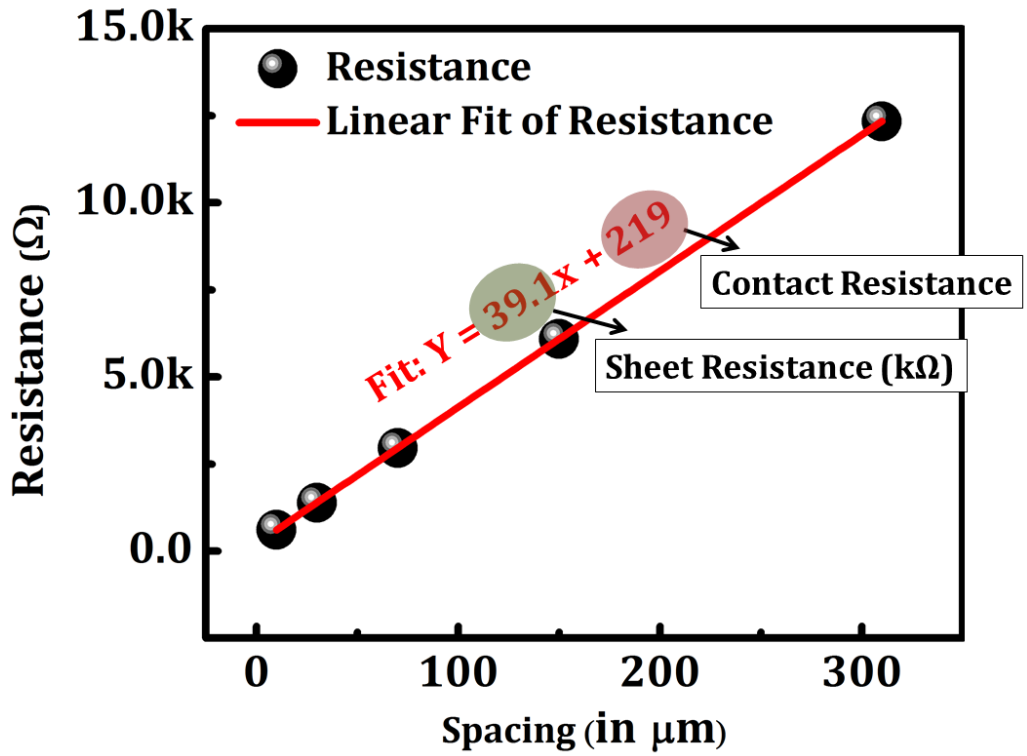

Figure 3-16. Plot of total resistance as a function of electrode spacing.

3.3.6. Temperature Coefficient of Resistance Measurements

As a prerequisite to measurements, electrical contacts must be made to the thin films. Metal contacts were deposited onto the thin film whose electrical properties need to be measured. Prior to the measurement, the contact quality is evaluated to ensure that Ohmic contacts were obtained. An HP4141B picoammeter was set up to source voltage and bias the thin film resistors, the resultant current was recorded. These I-V measurements were performed as a function of temperature from 30°C to 65°C at 5 °C increments. The data was exported into excel and the resistance was calculated at each temperature step. The resistivity is a function of temperature and can be described by:

$$\rho = \rho_0 e^{\frac{-E_a}{k_B T^2}} \qquad \text{Equation 19}$$

$$\text{Or,} \quad \text{Ln}(\rho) = \frac{-E_a}{k_B T^2} + \text{Ln}(\rho_0) \qquad \text{Equation 20}$$

A Ln resistance versus '$1/k_BT^2$' plot was used to extract the activation energy of the thin film. The TCR can be calculated using the formula:

$$TCR = \frac{-E_a}{k_B T^2} \quad \text{Equation 21}$$

3.3.7. Measurement of Electrical Noise in Thin Films

As discussed in the previous chapter, the electrical noise in a thin film is comprised of two components, the Johnson noise and the 1/f noise. While the Johnson noise is a function of device resistance and the bandwidth of the measurement, the origin of 1/f noise, on the other hand, depends on the value of Hooge's parameter and the carrier concentration. Therefore in order to compare the inherent noise of a thin film the parameter 'α_H/n' or the normalized Hooge's parameter must be extracted.

If the parameters V, f, I_{bias} and the measured I_{noise} are known, 'α_H/n' (units: cm^3) can be extracted from Equation 14 such that:

$$\frac{\alpha_H}{n} = \frac{I_{N,1/f}^2}{I_{bias}^2} Vf \quad \text{Equation 22}$$

Thin film samples were patterned using lithographic processing to define a known volume of the sample area. Figure 3-17 shows the patterns used to extract the normalized Hooge's parameter.

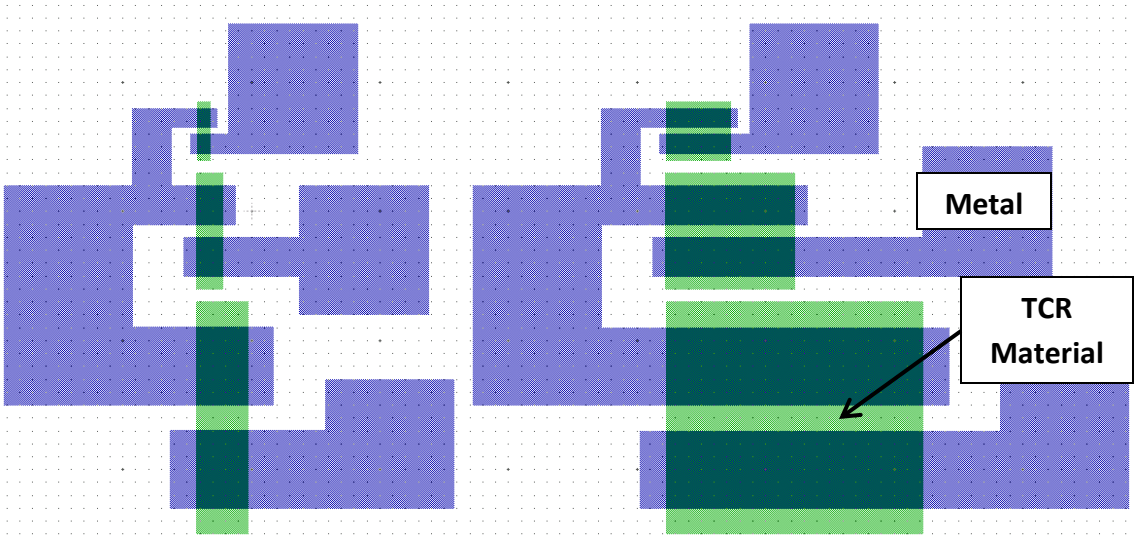

Figure 3-17. Schematic images from the mask set used to extract the normalized Hooge's parameter. Each pattern has a different volume but the same resistor width to length ratio.

Each pattern in Figure 3-17 contains three distinct volumes; however for each volume the aspect ratio (width to length ratio) is maintained the same. The similar aspect ratios allows for interrogation of different volumes while the thin film resistance remains the same. The lithographic patterning was done as shown in Figure 3-18 using Shipley Microposit 1800 series photoresist and Poly(methyl methacrylate) or PMMA C4. The active material was patterned using either dry or wet etching techniques. Thin films of Ge:H were etched in 30% hydrogen peroxide (H_2O_2). Since VO_x thin films are etched in the developer we used (Microposit 351), a double layer lithography technique was used with PMMA C4, as the underlying layer since PMMA can be developed in toluene (non-aqueous) post-exposure. A dry etch recipe was developed which utilized CF_4/O_2 plasma (100 mTorr, 25 sccm CF_4: 100 sccm O_2, -100V self-bias at a power of 100W). For high resistivity VO_x the etch rate was found to be ≈ 40 nm/min.

It was observed that for vertically integrated (through film) devices of VO_x, dry etching caused the thin film of VO_x to break down, and so, a wet etch recipe was also developed. High resistivity thin films of VO_x were found to be etched in dilute solutions of H_2O_2 (1:2,000) at an etch rate of 200 nm/min.

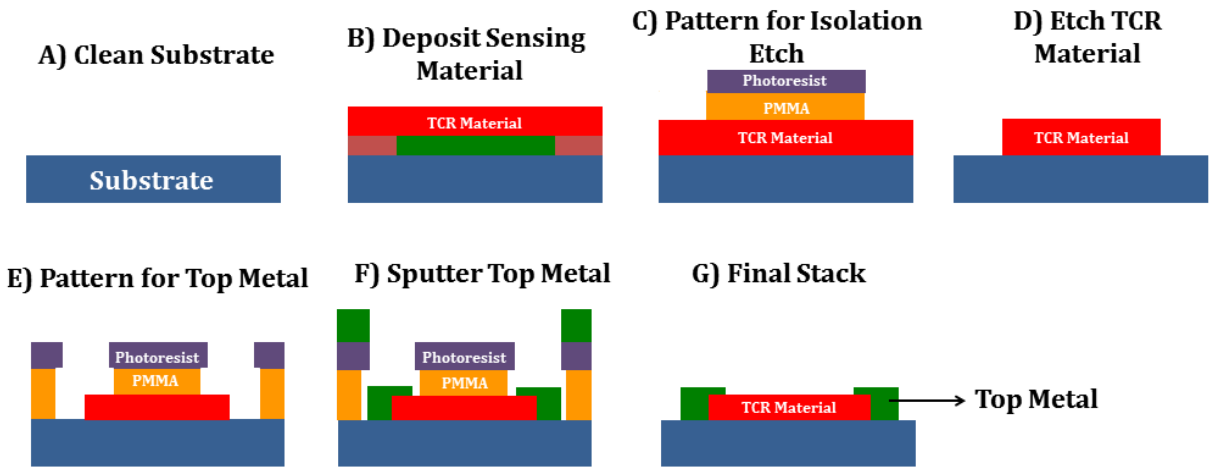

Figure 3-18. Schematic of lithographic processing of TCR material to extract resistivity, TCR and the normalized Hooge's parameter.

Once the sensing material was patterned, top electrodes were deposited using double layer lithography using PMMA as the liftoff resist. 100 nm of chromium was sputtered for making ohmic contacts to Ge:H, while 100 nm of sputtered titanium was used for thin films of VO_x.

Since the 1/f noise of a device also depends on the electrical contacts to the semiconductor [77], it is necessary to evaluate the contact quality and choose a device geometry from which the contribution from the contact resistance in minimized. Transmission line measurements were made and the contact resistance was evaluated. Electrical noise measurements were made on patterns such that the total contact resistance was significantly less than the total device resistance under consideration.

Previous attempts to measure 1/f noise of thin films have been through the measurement of a current power spectral density (PSD) at a specific volume and a reference frequency using a known electrical bias. Such spot measurements are performed using a dynamic signal analyzer (DSA) and are limited to one data point per measurement and could include unwanted contributions from the system noise, Joule heating, temperature fluctuation of ambient air, etc.

In this work, a custom-built 1/f noise measurement system and the technique to extract the 1/f noise of thin films is described which isolates the material 1/f noise from other noise sources. Some advantages to this noise measurement system over previous methods include: a large frequency range of

data acquisition obtained in a single measurement, a user controlled bandwidth of measurement, digitization of the output signal for post-measurement processing of the data, and low frequency drift correction for accurate measurement of the thin film's 1/f noise. The construction of the automated 1/ƒ noise measurement system was mostly developed by Myung-Yoon Lee from the department of Electrical Engineering at the Penn State University.

3.3.7.1. Effect of Low Frequency Drift for the Measurement of Noise in Thin Film Resistors

Some devices consist of materials sensitive to temperature fluctuations while others may contain materials whose electrical property drifts due to physical changes associated with aging of the thin film in ambient. In such devices, the electrical output of the film drifts over time [77]. During their regular operation, these thin films are isolated from the ambient by vacuum packaging and temperature stabilization. However, these provisions are not feasible in laboratory desktop style measurement system in which numerous samples deposited using various deposition conditions need to be analyzed. Figure 3-19 shows the drift in resistance of a thin film of vanadium oxide measured over more than 45 hours. The resistance change manifests itself in the measured current as a sinusoidal variation with a long, non-constant time period (low frequency) which we refer to herein as 'drift'.

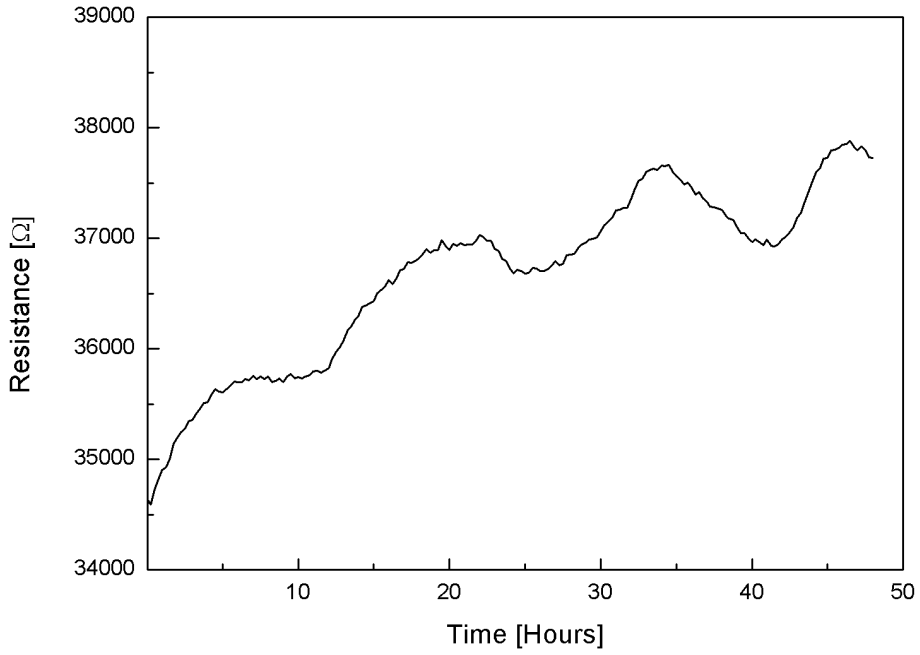

Figure 3-19. Resistance fluctuation (drift) of a thin film resistor of vanadium oxide capped with SiO_2

This drift causes variations in the measurement which makes both data acquisition and data analysis difficult. When the acquired time−signal data is converted into the frequency domain, this low frequency drift causes a shift in the acquired spectra and makes the $1/f$ noise of the thin film appear larger than its true intrinsic value.

In the measurement system developed for this work; the low frequency drift has been subtracted using post-measurement data processing. A voltage offset correction has been applied whose value as calculated as follows. Let us assume that the measured voltage output can be modeled by a sinusoidal signal using the following equation:

$$\boldsymbol{V = X\sin(2\pi f t) + Y + Zt} \qquad \textbf{Equation 23}$$

Where V is the voltage noise modeled, X is the amplitude of $1/f$ noise, Y is a constant voltage offset required to subtract the bias voltage, Z is the magnitude of the drift effect, f is the frequency and t is the discrete time which has a range of 0 sec to 10 sec for our measurement, so that the lower limit of frequency is 0.1Hz. When the acquired time domain signal is converted into frequency domain, the

obtained result is shown in Figure 3-20. The noise PSD displays a sharp peak given by the $1/f$ noise at a frequency f of 10Hz.

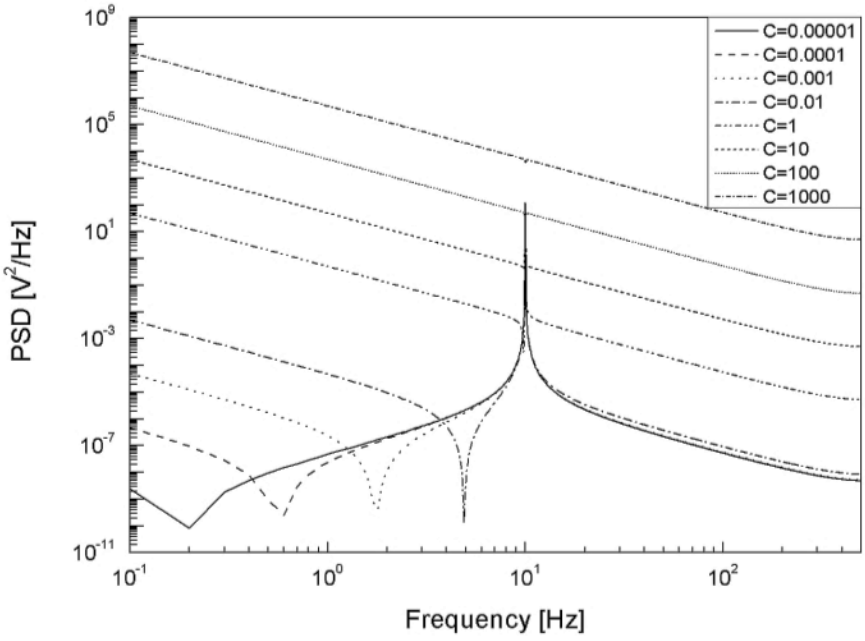

Figure 3-20. The recorded PSD for varying magnitudes of drift, C. The peak represents the 1/ƒ noise (in this case at 10 Hz).

We observed no change in the spectra with the magnitude of the offset value used; which implies that the $1/f$ noise is not affected by the offset of the amplifier at least when offset value is within the input range of filter or the measurement instrument. On the other hand, the plotted $1/f$ noise spectrum of Figure 3-20 is strongly affected by the drift of resistance of the thin film which appears as a linear function of f^{-2}. As the drift effect gets larger, the Z value increases and can even surpasses the $1/f$ noise of the material seen here for large values of C and for smaller frequencies. However, due to the difference in their frequency dependence, (Drift has a $1/f^2$ dependence, while flicker noise has a $1/f$ dependence), they can be separated from each other. The noise measurement system developed in this work consists of drift filtering to obtain a noise spectral density that follows Hooge's empirical relationship and has a slope of negative unity. It must be noted that since we attribute this drift to self-heating of the resistor, we find this drift particularly large when a large power is dissipated across the resistor.

A schematic flow chart of the noise measurement setup is shown in **Error! Not a valid bookmark self-reference.**. The setup consists of three instruments: A low noise current amplifier (A Stanford Research SR-570), a dual channel filter and a data acquisition hardware (DAQ) card which is controlled by a personal computer. The SR570 contains an RS-232 interface which allows for remote control of each operation eliminating the need for a manual operation. The SR570 has internal batteries capable of providing up to 5V. To avoid the need for microscope and a probe station, and hence make the setup simpler, a 16 pin ceramic dip package is used along with Al or Au wires. The dip package is placed in a faraday's cage (a small Al box) to isolate the sample from the environment. A second shielding box is used to isolate the entire shielding assembly and the measurement setup from the environment. In addition, all assemblies and instruments are grounded using a heavy copper wire. A floating table is used to isolate the measurement assembly from all sources of vibration.

Using a LabVIEW program, the wire bonded samples were biased using the internal battery of the SR−570. Prior to data acquisition at the DAQ, proper filtering of the acquired data is necessary. A low pass filter of 1 KHz is used as an anti-aliasing filter to remove the high frequency signal, which may affect the lower frequency noise. In addition a high pass filter of frequency 0.1 Hz is necessary to remove any low frequency drift which leads to erroneous values of the thin film's inherent 1/f noise. To avoid aliasing, sampling rate of DAQ should exceed Nyquist rate. We have used a sampling rate of 20 KHz, much higher than the Nyquist rate which is set to be ≈ 2 KHz (2 × (1 KHz – 0.1 Hz)). The acquisition time is set to 20 seconds, and the data collected is averaged over 20 samples. At the end of the measurement, the sample is connected to a pico ammeter (HP 4140B DC SMU) and the current bias is recorded.

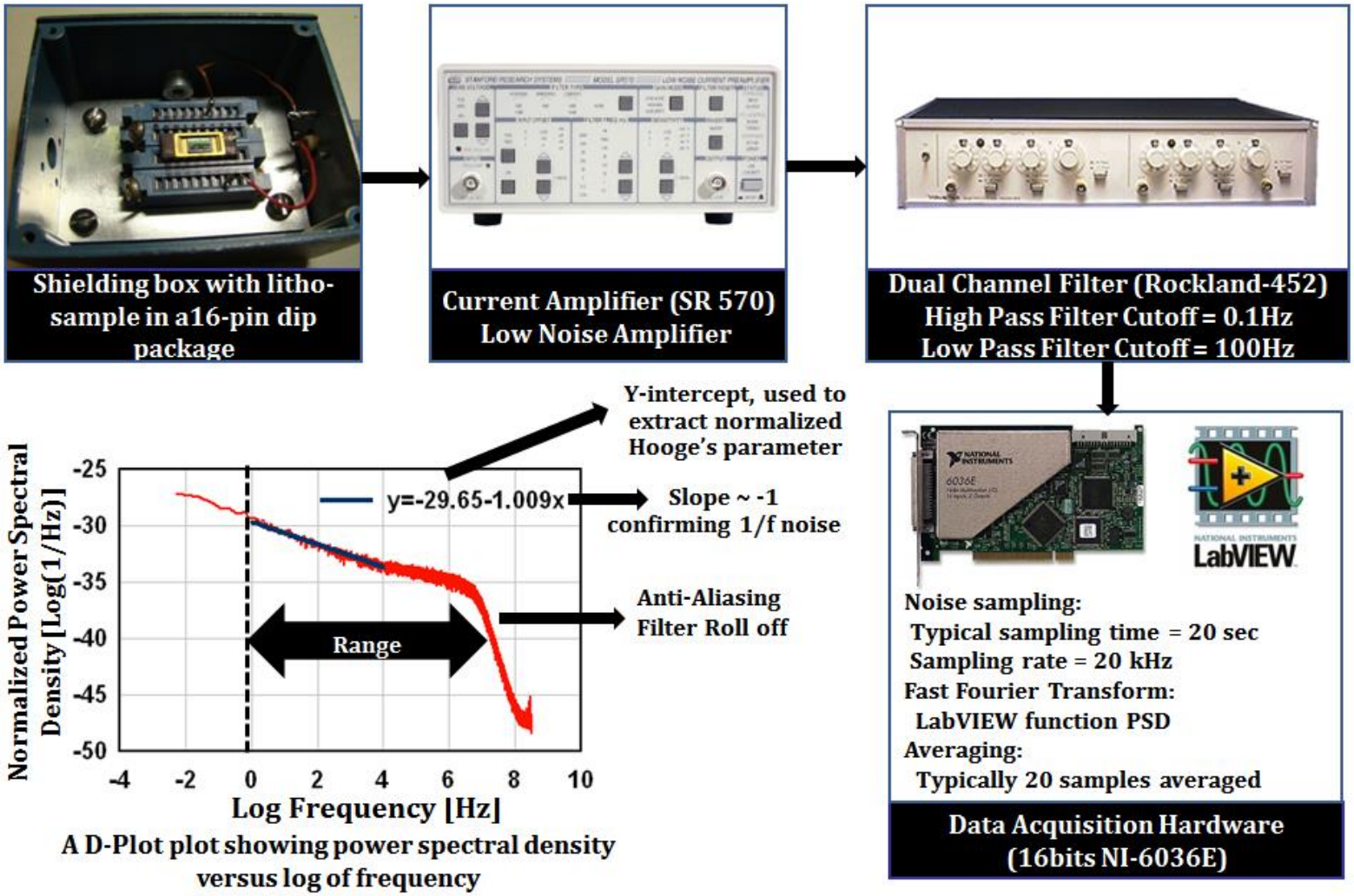

Figure 3-21. A schematic showing the process flow used in this work for the measurement of 1/f noise in thin films.

The averaged time varying signal is converted into the frequency domain using the LabVIEW's Fast Fourier transform function. This power spectral density (PSD) is plotted as a function of frequency such that the resultant graph resembles the schematic representation of Figure 3-22.

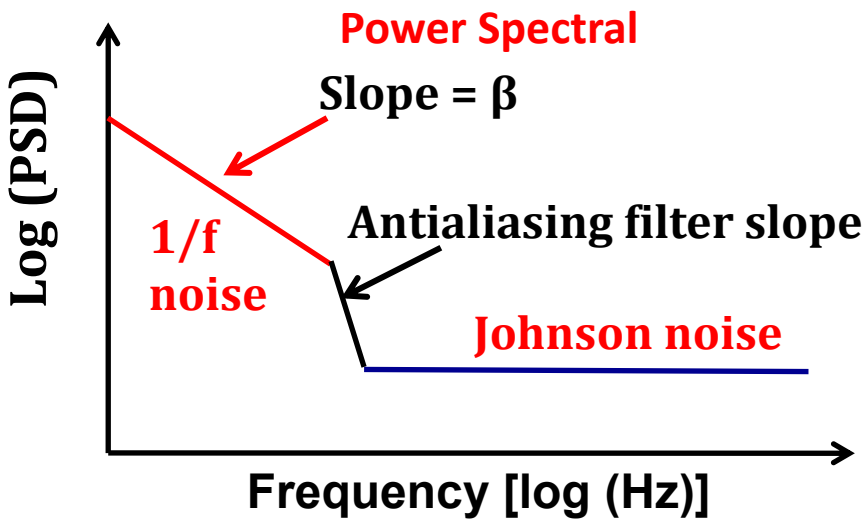

Figure 3-22. Frequency spectra representation of collected spectra showing two distinct regions: a) Region with 1/f noise and, b) Region with Johnson noise

If the magnitude of the 1/f noise is higher than the Johnson noise, the lower frequency of the spectra is a line with a slope of '–1' in a log-log scale. An anti-aliasing filter roll off appears at 1 KHz which is associated with the low pass filter; whereas the Johnson noise appears as 'white' because it is independent of the frequency. Depending on which noise contributor is larger the recorded power spectral density (PSD) may differ from Figure 3-22. If the device resistance is high, the total noise may be dominated by Johnson noise and the 1/f noise may be suppressed in the spectra. In such a case, an alternate aspect ratio of the same thin film must be measured such that the device resistance and therefore the Johnson noise is lower than the thin film's 1/f noise.

In summary, In order to successfully extract the normalized Hooge's parameter it is necessary to ensure that the Hooge–Vandamme relationship is satisfied. As Equation 22 suggests, the intensity of the recorded PSD depends on:

1. f^{-1} (1/frequency) of measurement,
2. The volume of the device interrogated,
3. The bias applied to the device and
4. The normalized Hooge's parameter or 'α_H/n'.

Thus if everything but normalized Hooge's parameter is knows, it can be estimated by using Equation 22. Figure 3-23 shows the acquired PSD of the data with decreasing volume of the sample and with increasing bias applied to the sample. If the sample bias is kept constant and the volume is halved, the magnitude of PSD is doubled. Similarly if the volume is kept constant and the applied bias is doubled, the magnitude of PSD is also doubled.

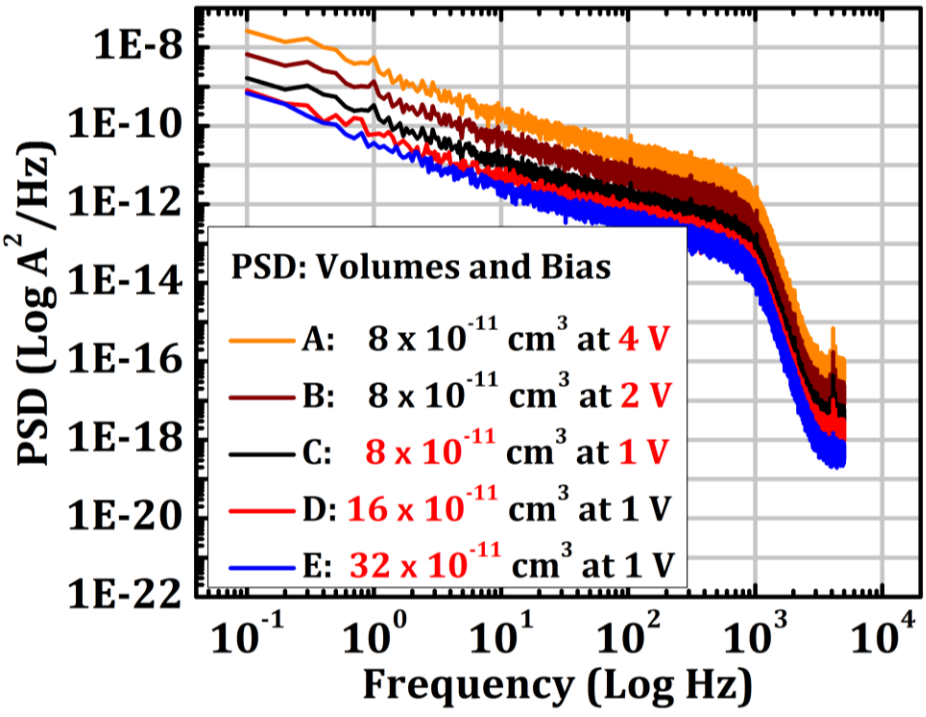

Figure 3-23. Acquired Power Spectral Densities of a thin film for different volumes and different biases to confirm the Hooge–Vandamme relation and extract the materials normalized Hooge's parameter.

Chapter 3 has provided an overview of the experimental methods used in this work. Detailed specifics are added in the following chapters as necessary. Having discussed all the tools required for characterization of thin films, the next chapter looks at high TCR thin films of VO_x and Ge:H for use as infrared imaging materials.

Chapter 4. High TCR Thin Films of Vanadium Oxide (VO_x) and Hydrogenated Germanium (Ge:H)

4.1. Introduction

Thin films of vanadium oxide (VO_x) and hydrogenated amorphous silicon (a-Si:H) are the two dominant material systems used in resistive infrared radiation detectors for sensing wavelengths in the 8–14 μm range. While thin films of VO_x ($x < 2$) currently used in the bolometer industry have a magnitude of temperature coefficient of resistance (TCR) between 2%/K – 3%/K, the magnitude of TCR of a-Si:H thin films lies between 3%/K to 4%/K [8] [30] [78] [18]. Although high TCR materials are desired, increasing the activation energy (and therefore the effective band gap) results in a decrease in the mobile carrier concentration and therefore resistivity [30]. This is evident from the fact that while VO_x thin films have a resistivity between 0.1 – 1 Ω–cm, a-Si:H used in microbolometers have a resistivity between 200 and 2,500 Ω–cm [8] [30] [78] [18].

Unfortunately high resistivity materials are also associated with high Johnson and 1/f noise. The fundamental differences in resistivity and electrical noise of VO_x and a-Si:H thin films used in the microbolometer industry requires two distinctly different read out circuits [18] [60] [59]. To overcome the higher noise in a-Si:H thin films, the devices are constantly biased and averaged numerous times at the pixel level so that the noise contribution can be reduced dramatically [18] [60]. Such a constant bias readout circuit cannot be used for thin films of VO_x due to the self-heating associated with their lower resistivity [30] [59]. In 2013, Jin et al. demonstrated thin films of VO_x having the lowest resistivity of all previously deposited VO_x thin films with $|TCR| > 5$ %/K (Figure 4-1) [79]. In this work, thin films with |TCR| as high as –5%/K were deposited having resistivity as low as 10,000 Ω–cm [79]. The obtained TCR and resistivity values made these films potential candidates for use in constant bias bolometer systems. However, this work did not contain any information on the inherent 1/f noise properties of these thin films.

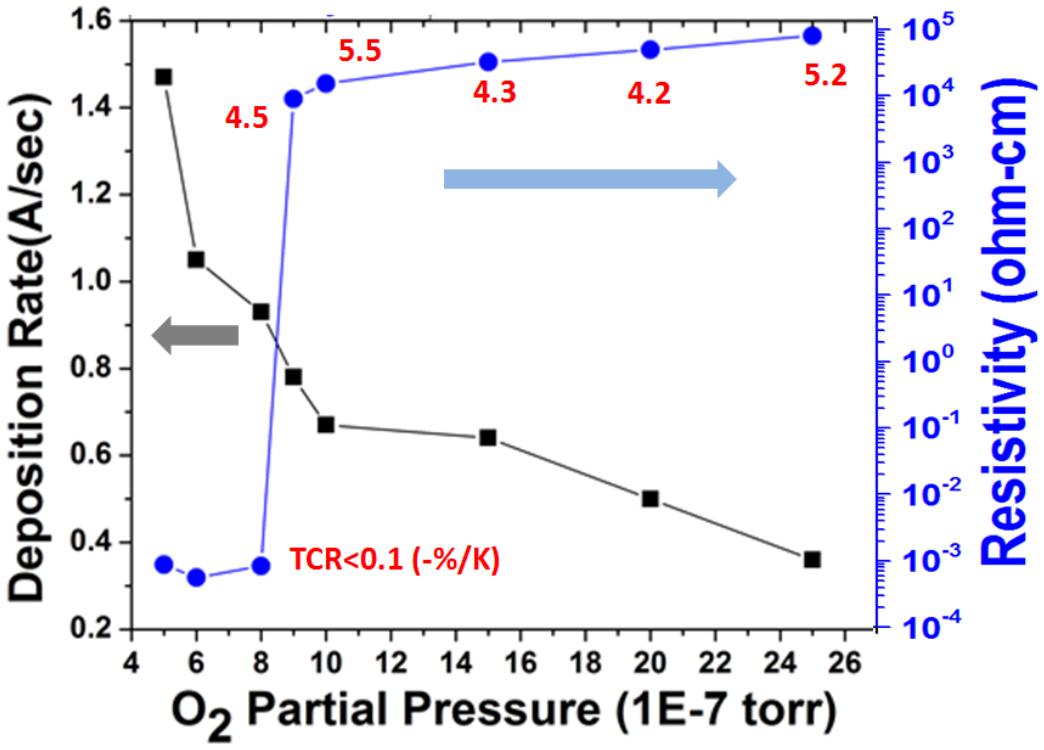

Figure 4-1. Deposition rate, resistivity and TCR of thin films of VO_x deposited by Biased Target Ion Beam Deposition as a function of partial pressure of O_2 as it appears in ref. [79].

Another material system, consisting of amorphous silicon germanium alloys ($Si_{1-x}Ge_x$:H) has also been investigated for use in constant bias bolometer systems. The motivation for its use stems from a considerable research effort in the development of thin films of amorphous hydrogenated silicon (a-Si:H) for use in large area devices such as solar cells and as transistors in liquid crystal displays and for use as sensing material for infrared detection [73] [80] [50]. An analogous material system consisting of amorphous hydrogenated germanium (a-Ge:H) was also investigated for use in those applications [51] [52] [53] [54] [55], however, these thin films could not compete with the performance of Si:H/SiGe:H systems for the stated applications. While Si:H and SiGe:H have a dark resistivity between 10^{11} – 10^{13} Ω–cm with light resistivities as low as 10^4 Ω–cm, Ge:H thin films show smaller dark resistivity of 10^7 Ω-cm with smaller thermal activation [80] [52] [53] [54] [55]. However, the lower resistivity of Ge:H thin films make them good candidates for further investigation as infrared imaging materials.

Further improvement in the resistivity – TCR tradeoff was necessary, even at these levels. In addition to the high Johnson noise imposed by high resistivity, these films have fairly high 1/f noise with the 'α/n' values around 10^{-18} cm^3 [51].

It was hypothesized that in the case of Ge:H thin films a reduction in the resistivity was possible by incorporation of nanocrystallites. Saint-John found that for PECVD deposited Ge:H, nanocrystallites can nucleate as early as 10–15 nm for a dilution ration ($[H_2]/GeH_4$]) of 400 [74]. Furthermore, it was suggested that the nucleation density of germanium crystallites can be increased by lowering the substrate temperature from the previously investigated value of 200 °C to 170 °C [74]. Indeed it was seen that by incorporating a small fraction of nanocrystallites, thin films with resistivity of around 1,500 Ω–cm were deposited having a |TCR| value of 3.7 %/K [57].

To further the development of high TCR materials, this work investigates high TCR VO_x and Ge:H thin films for use in constant bias systems. For thin films of VO_x, normalized Hooge's parameter values are measured. To improve the electrical properties of Ge:H, in this work thin films of Ge:H have been deposited at a very high dilution ratio of GeH_4 in H_2 to incorporate germanium nanocrystallites. Electrical properties of mixed phase amorphous + nanocrystalline thin films are investigated by varying the crystal fraction of germanium; this was achieved by changing the total thicknesses of the deposited thin films.

4.2. High TCR VO_x Thin Films

4.2.1. Experimental Details

High resistivity VO_x thin films were deposited using a Biased Target Ion Beam Deposition System (BTIBD), the details of which were described in the previous chapter. Thin films ~ 85 nm thick were deposited having a thickness uniformity >±3% for a 4" wafer. A three-target configuration was used to deposit the thin films. A series of films was deposited as a function of oxygen partial pressure, pO_2, ranging from 1×10^{-6} Torr to 2.1×10^{-6} Torr, corresponding to oxygen flow 5 % – 8.5% of argon. Detailed

values for the parameters used can be found in Table 2. The total flow was kept at 70 sccm, corresponding to a deposition pressure of $\approx 5.8 \times 10^{-4}$ Torr. A pulsed waveform was used to increase the sputter yield and prevent arcing of the target. The sputtering voltage was kept at −800 V while the duty cycle was set to 99%, for all three targets yielding a film growth rate of ≈ 0.5 Å/second.

Thin films were patterned using lithographic processing steps described in Section 3.3.7. The thickness of the deposited VO_x and Ge:H thin films was measured using an AFM, Dimension Icon made by (Bruker Corporation) on a lithographically patterned step in the thin films. The roughness of the thin films was evaluated using the same AFM. The crystal structure of the thin films was evaluated by grazing incidence XRD using a PANalytical's X'Pert Pro MPD. The composition of the VO_x films was evaluated by Rutherford back scattering (RBS) using a 2.275 MeV He^{2+} ion beam with the detector set at a backscattering angle of 160° [81].

4.2.2. Results and Discussion

Thin films of VO_x were deposited by BTIBD as a function of pO_2, from 1×10^{-6} Torr to 2.1×10^{-6} Torr. The films were found to be 85 nm thick. All the thin films deposited were found to be amorphous and a characteristic plot of the grazing incidence x-ray data is shown in Figure 4-2. The angle of incidence for the measurement was 0.8°. The x-value in 'VO_x' (obtained from the RBS analysis) increased linearly from 2.2 to 2.4 as the partial pressure was increased from 1×10^{-6} Torr to 2.1×10^{-6} Torr.

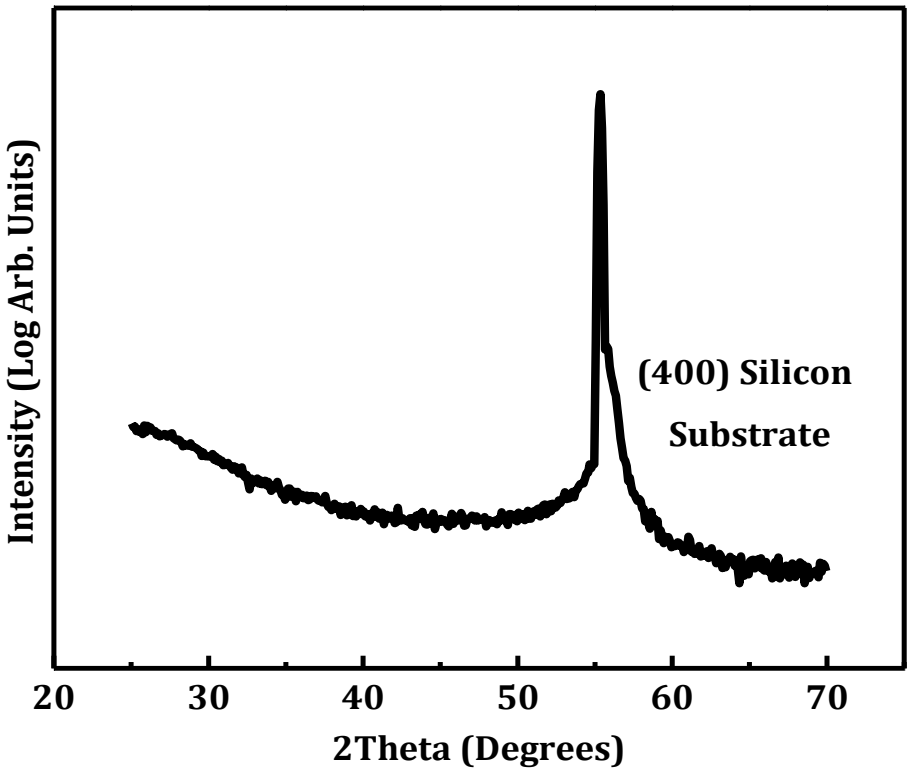

Figure 4-2. Grazing incidence X–ray diffraction spectra associated with high resistivity VO_x thin films deposited at high partial pressure of oxygen using Biased Target Ion Beam Deposition showing amorphous thin film structure.

The samples show a temperature dependent resistivity which is dominated by thermal activation at least in the range of 300 K – 350 K. The magnitude of TCR was calculated by extracting the thermal activation energy (E_a) from material's resistivity-temperature plots.

The room temperature TCR is given by:

$$TCR = -\frac{E_a}{k_b T^2} \qquad \text{Equation 24}$$

Where E_a is the extracted activation energy, κ_b is the Boltzmann's constant in eV and T is room temperature or 300 K.

The 1/f noise of the thin film samples was evaluated using Hooge-Vandamme relation given by [28] [82]:

$$\frac{S_I(f)}{I_{bias}^2} = \frac{\alpha_H}{nVf}$$ **Equation 25**

where $S_I(f)$ is the spectral current density, I_{bias} is the sample current, V is the volume of the sample, f is frequency range of measurement, α_H is Hooge's parameter and n is the carrier concentration. Since the volume and the bandwidth of measurement are chosen on a system level, the parameter 'α_H/n' (normalized Hooge's parameter) was used as a measure of evaluating the 1/f noise of the samples.

To extract the normalized Hooge's parameter, samples having different volumes were lithographically patterned and biased using a voltage source in a shielded iron box. A low noise current amplifier (Stanford Research Model –570) was used to amplify the measured current power spectral density (PSD) which was recorded using a National Instruments data acquisition card (NI-6036E). The recorded PSD was converted into the frequency domain by using the Fast Fourier Transform function in LabVIEW. When normalized for volume, the three curves overlap as predicted by the Hooge-Vandamme relation. Similarly, the bias dependence of noise was also confirmed by applying three distinct biases. The measured power spectral density at 1 Hz (also referred to as the k–value) was multiplied by the sample volume to determine the normalized Hooge's parameter, or 'α/n' value of our thin film.

Figure 4-3 shows the resistivity, TCR and α_H/n (1/f noise) of the deposited films as a function of pO_2. As expected, the resistivity of the deposited films increases as a function of pO_2, reaching 20,000 Ω-cm at an oxygen partial pressure of 2.1×10^{-6} Torr. The TCR and the characteristic 1/f noise of the films followed no particular trend. The |TCR| was a maximum of 5%/K for the film deposited with a pO_2 of 1×10^{-6} Torr while the α_H/n was found to be the lowest for the film deposited at 1.79×10^{-6} Torr with a value of 1×10^{-20} cm^3. In other material systems, the inherent noise of the amorphous semiconductor has been associated with the short-range order in the amorphous material [83].

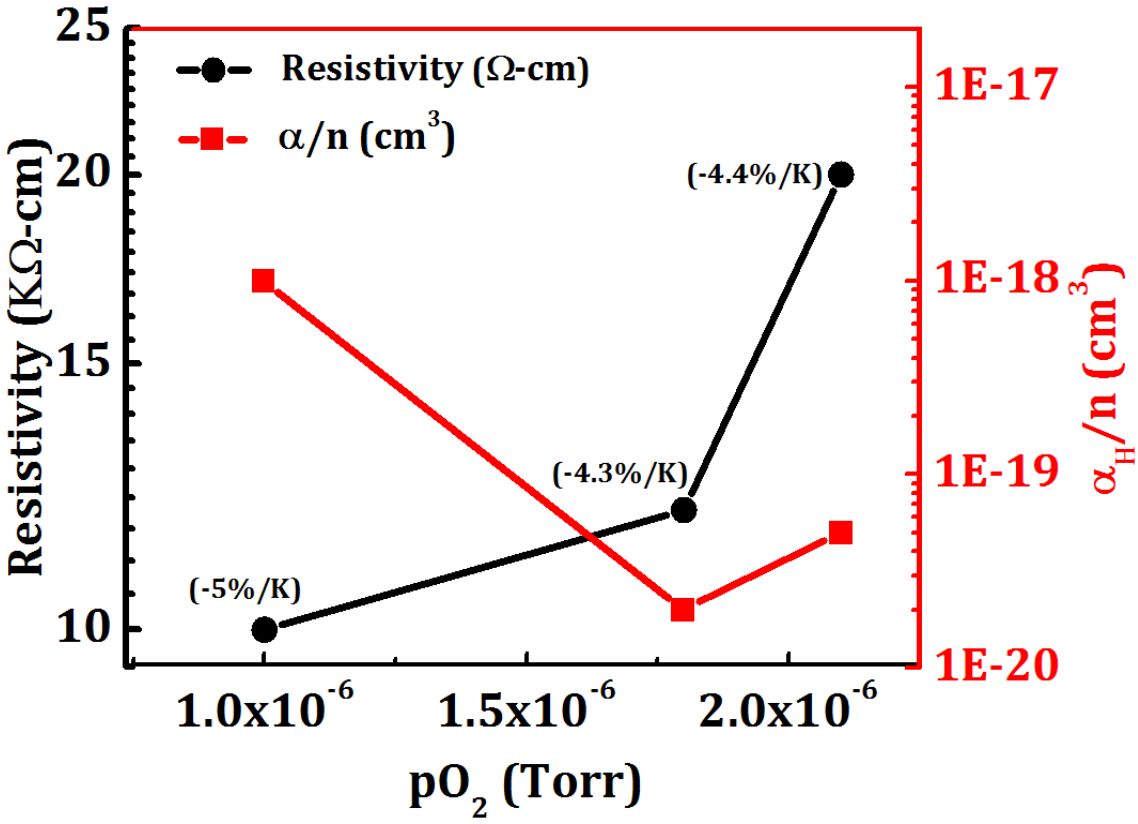

Figure 4-3. Resistivity, temperature coefficient of resistance (TCR) and the normalized Hooge's parameter (α_H/n) of VO_x thin films deposited by BTIBD as a function of partial pressure of oxygen (pO_2).

Regardless of the deposition conditions, the lowest resistivity deposited for the high TCR material was > 10,000 Ω–cm. This limitation put the high resistivity VO_x material system at a disadvantage when compared with Si:H thin films even for use in constant bias readout integrated circuit bolometer cameras. Although this resistivity is higher than the currently used a–Si:H thin films for constant bias bolometer devices, their α_H/n values are on the order of those of Si:H thin films. A reduction in the total device resistance might make these thin films competitive for use in constant bias bolometer devices.

None the less, the magnitude of TCR, noise and resistivity observed for some of the thin films of VO_x of this work are better than other materials with high TCR such as spinels based on transition metal oxides and hydrogenated silicon as manufactured by L–3 communications [18] and ULIS [84].

4.3. High TCR Mixed Phase Thin Films of Ge:H

4.3.1. Experimental Details

A series of mixed phase amorphous + nanocrystalline hydrogenated germanium ((a+nc)-Ge:H) thin films having different thicknesses (thickness = 7 nm – 200 nm) were deposited onto c-Si wafers coated with 20 nm of silicon nitride by RF (f= 13.56 MHz) plasma enhanced chemical vapor deposition (PECVD) using ultra-high purity germane (GeH_4) gas diluted with H_2. A number of deposition parameters were fixed along the lines of previous work including: a total pressure of ~ 93 Pa and a low plasma power density of 0.08 W/cm^2.The background pressure was typically < 5×10^{-5} Pa. To facilitate an earlier nucleation of crystallites, the substrate was held at a temperature of 170°C and the hydrogen-to-reactive gas dilution ratio was maintained at R = $[H_2]/[GeH_4]$ = [160 sccm]/[0.4 sccm] = 400.

To extract the electrical properties such as resistivity and TCR, the deposited thin films of Ge:H were patterned by photolithography and wet etching in a 30% H_2O_2 solution. Top contacts were made to the patterned thin films by photolithography and lift-off of sputter deposited chromium. The thickness of deposited Ge:H thin films were measured using an AFM, Dimension Icon made by (Bruker Corporation) on lithographically patterned steps in the thin films. The contact quality and thin film resistivity was evaluated using transmission line measurements on these lithographically patterned samples. As expected, the samples show a temperature dependent resistivity which is dominated by thermal activation at least in the range of 300 K – 350 K. The magnitude of TCR was calculated by extracting the thermal activation energy (E_a) as described in the previous sub-section.

4.3.2. Results and Discussion

Figure 4-4 shows the measured resistivity and TCR of the samples as a function of thickness. Starting with the 7 nm thin film, the magnitude of TCR increased from 1.8%/K to a value of about 6.5%/K for the 100 nm thick film. The 200 nm film showed a decrease in |TCR| from the 100 nm film to about 3.6%/K. The resistivity of these films was between 750 Ω–cm and 4,500 Ω-cm. Of particular interest are the films of thicknesses 50 nm and 100 nm which show a |TCR| of 5%/K and 6.5 %/K for a

resistivity of about 1,500 Ω-cm and 2,250 Ω–cm respectively. To verify reproducibility of results, the 100 nm thin film was re-deposited with similar results, as can be seen in the graph.

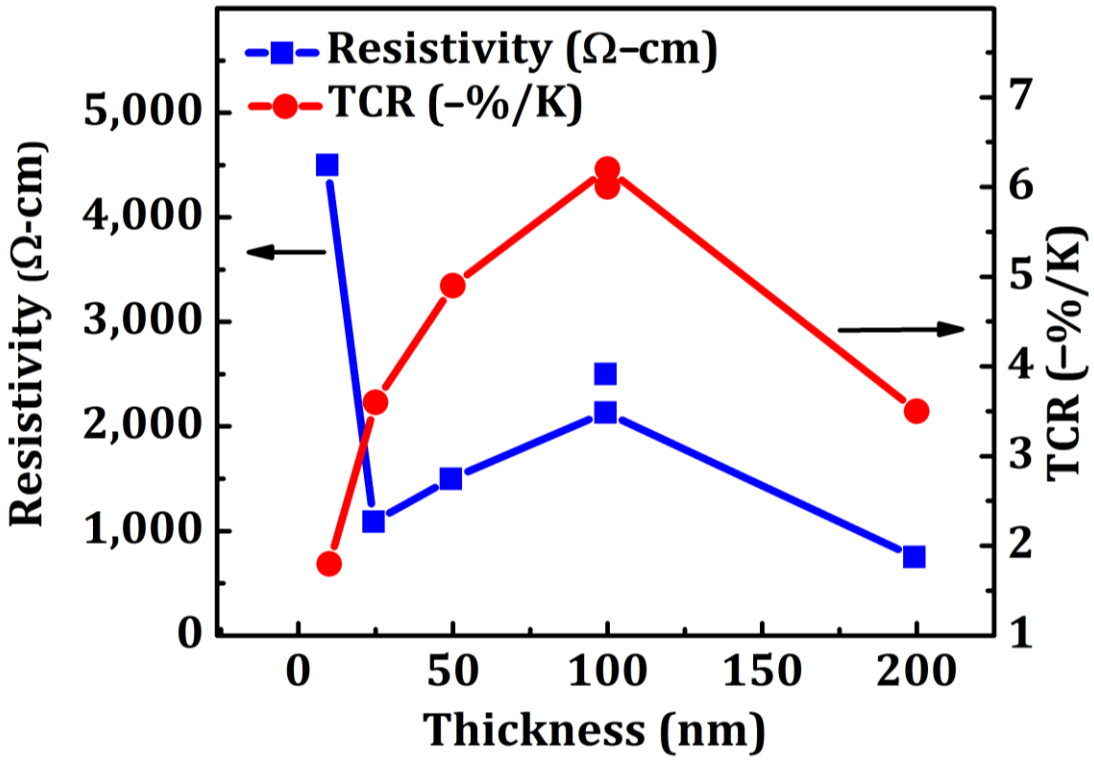

Figure 4-4. Resistivity and TCR of lithographically patterned samples of Ge:H as a function of thickness. The electrodes used for electrical measurements were evaluated to ensure ohmic contacts were obtained for all measurements.

The 1/f noise of the thin film samples was evaluated using the Hooge-Vandamme relation as described in the previous sub-section. Figure 4-5 shows the measured power spectral density (PSD) of a 100 nm film of Ge:H deposited in this work, confirming the volume dependence in these thin films. The y–intercept at a frequency of 1 Hz can then be used to extract α_H/n value of that thin film.

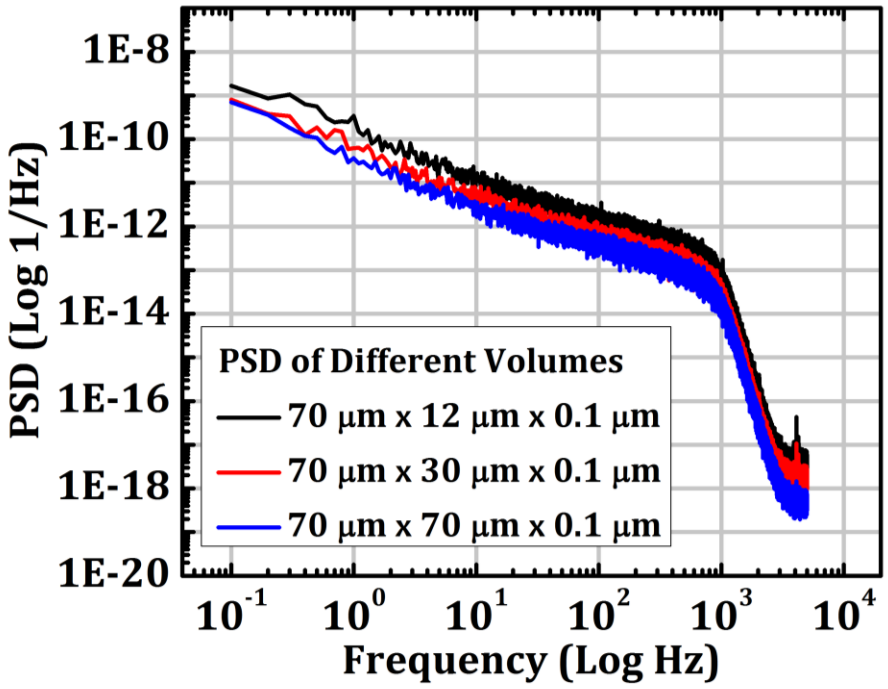

Figure 4-5. The measured Power Spectral Density (PSD), S_I^2/I_{bias}^2, for the 100 nm sample of Ge:H showing volume dependence as predicted by the Hooge-Vandamme relation.

Figure 4-6 shows the extracted α_H/n values for the thin films of this work as a function of thickness. The 1/f noise for the 7 nm thick film could not be measured accurately. One possible reason for this high drift might be a resistance variation due to Joule heating of the thin film having a small cross-section for current flow (due to extremely small thickness). These values were found to be between 10^{-18} cm^3 (25 nm) and 10^{-20} cm^3 (100 nm) for the films. Interestingly, the film having the largest TCR value was also found to have the lowest α_H/n value, while the film with the lowest TCR was also found to have the highest α_H/n value.

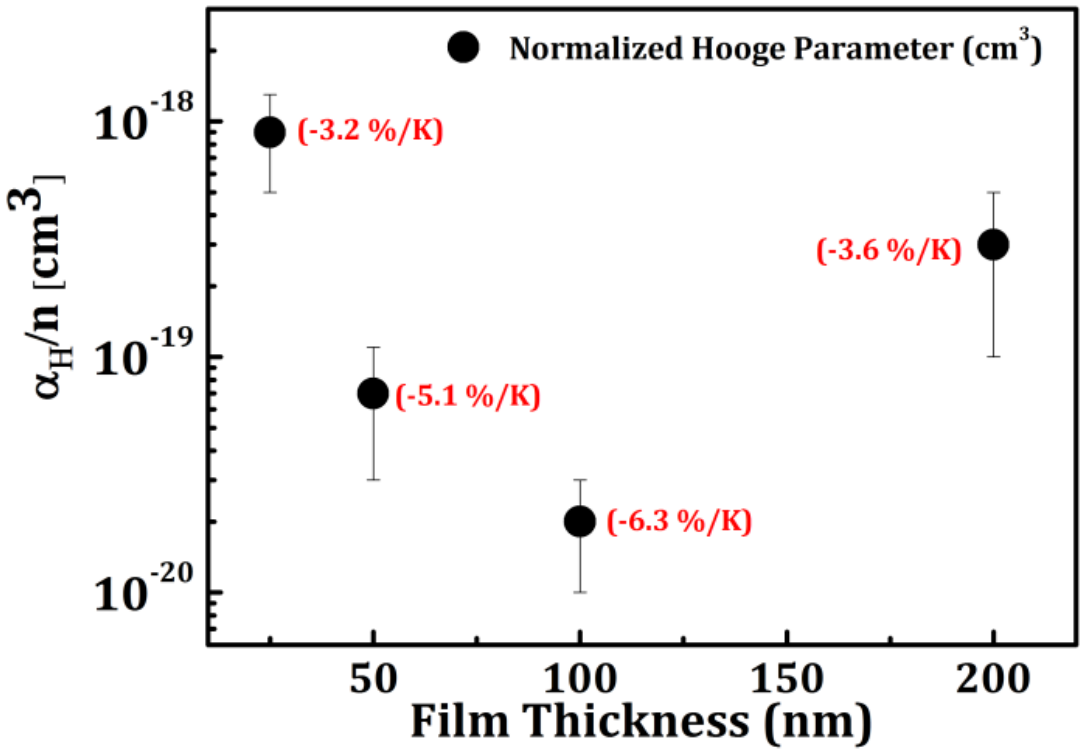

Figure 4-6. Extracted normalized Hooge's parameter 'α_H/n' as a function of thickness for thin films of Ge:H each annotated with their corresponding value of TCR. Note that the 100 nm thin film had the lowest α/n value while having the highest TCR.

In an effort to explain the combination of high TCR and low 1/f noise in thin films of PECVD deposited Ge:H, the thin film microstructure was characterized. The crystal structure of the thin films was evaluated by grazing incidence X–ray diffraction using PANalytical's X'Pert Pro MPD with a step size of 0.026 degrees at a rate of 1.2 degrees/minute. Figure 4-7 shows the x-ray diffraction spectra for the 200 nm thin film grown on thermally oxidized silicon wafers. The data shows the presence of diamond cubic structure as expected from high dilution ratio during PECVD.

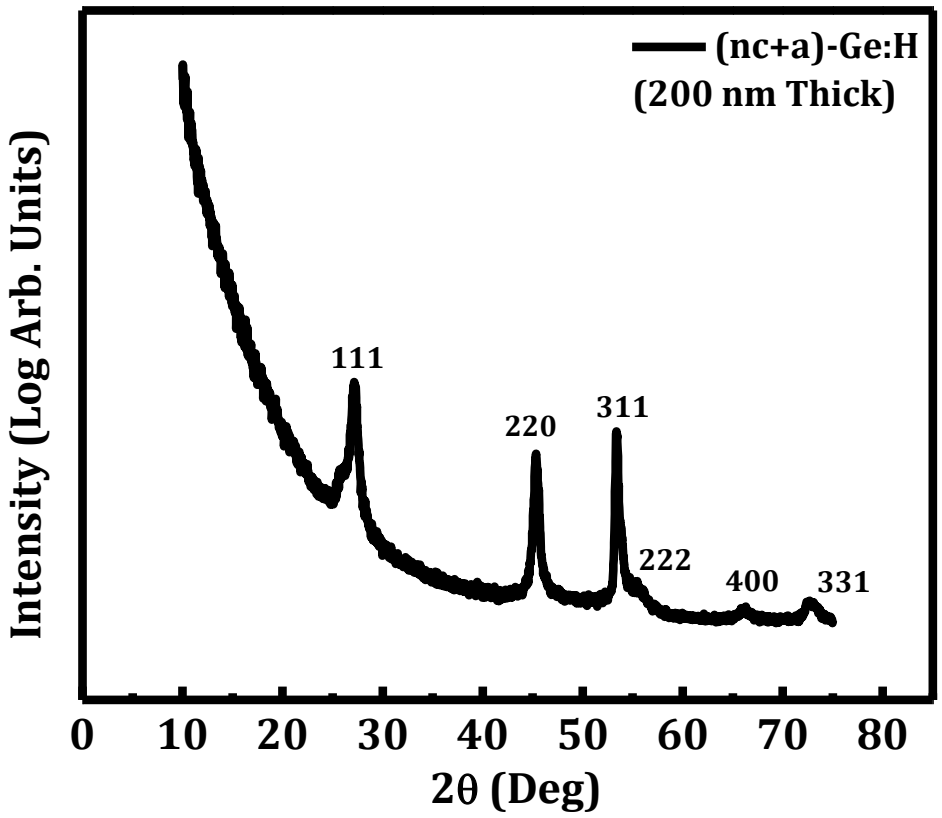

Figure 4-7. Grazing incidence x-ray diffraction pattern of a 200 nm thin film of Ge:H confirming the presence of diamond cubic crystal phase (as indexed).

To extract a first order estimate of the crystal size of the grains, the diffraction pattern for the 200 nm thick film was also collected in the Bragg-Brentano geometry, as shown in Figure 4-8. The first order grain size of the crystallites present in the films can be obtained using Scherrer's formula [85]:

$$D_p = \frac{0.94\lambda}{\beta_{1/2} Cos\,\theta} \qquad \text{Equation 26}$$

where D_P is the calculated grain size, $\lambda$is the wavelength of radiation used for diffraction (1.54 Å); $\beta_{1/2}$ is the angle at full width half maximum. Using the Scherrer's formula, the grain size for this film was calculated to be about 140 nm.

An even thicker sample (250 nm) was deposited on a native oxide coated c-Si wafer for TEM analyses (albeit at a slightly higher temperature of 200 °C as opposed to 170 °C). Figure 4-9 shows a dark field TEM micrograph collected by Dr. David Saint John from the sample which shows that initial layers of the Ge:H are amorphous [19].

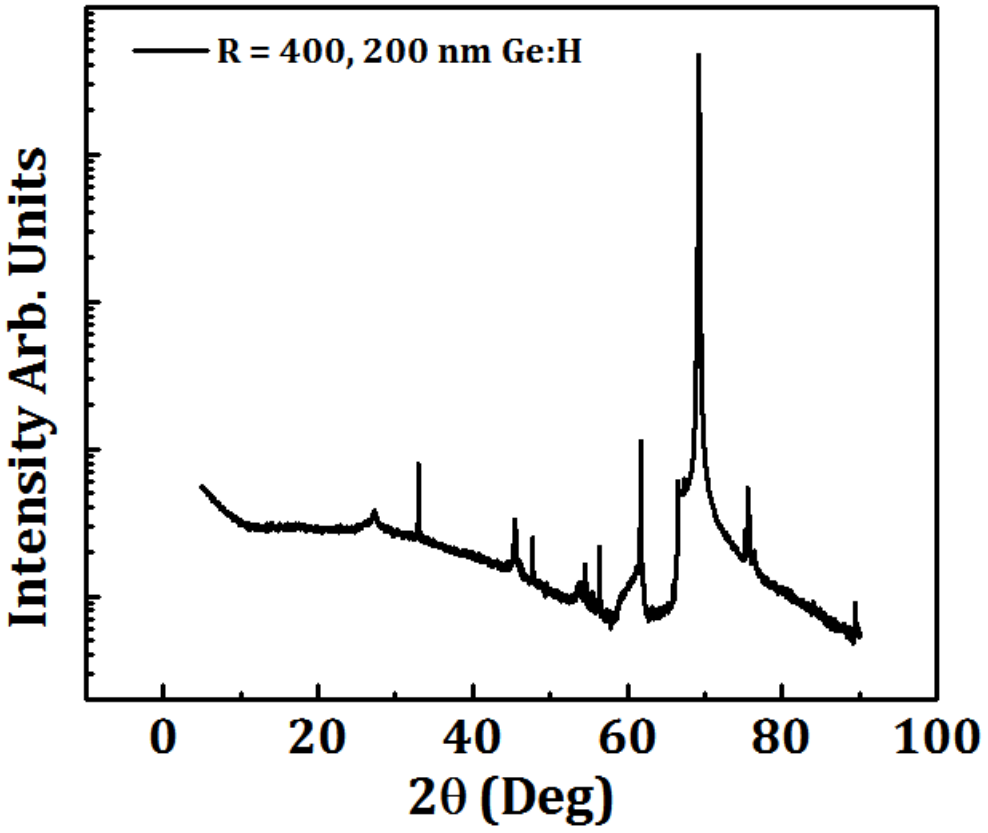

Figure 4-8. Bragg-Brentano x–ray diffraction pattern of the 200 nm thin film of Ge:H used to extract the size of crystals to the first order using the Scherrer's formula.

Around a bulk thickness of 10–15 nm, nanocrystallites start to nucleate and continue to grow segregated in an amorphous matrix until a thickness of around 100 –120 nm when these grains coalesce. In addition, the planar twinning defects with a regular periodicity of ~ 1nm were also observed in this thin film.

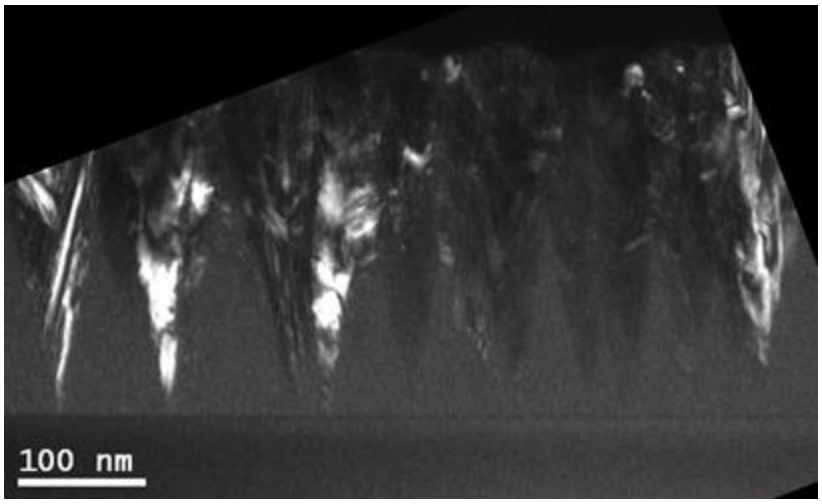

Figure 4-9. Dark field TEM micrograph of a 250 nm thin film of Ge:H showing the presence of nanocrystallites in an amorphous matrix [published previously in ref. [19].

The roughness of the thin films as a function of thickness was evaluated using an AFM. Figure 4-10 shows AFM micrographs of thin film of Ge:H with a thickness of 7 nm and 200 nm. Figure 4-10a shows the 7 nm thin film having a peak-to-valley height of 7nm having small island sizes. In contrast Figure 4-10b shows the 200 nm film has a much larger grains (> 50 nm).

Figure 4-12 illustrates the surface roughness evolution (both RMS and peak-to-valley) of the thin films of varying thicknesses deposited in this work. The RMS roughness of the films < 25 nm thick is around 8 Å – 9 Å. The 100 nm thin film shows the highest roughness with an RMS value of 2.7 nm and a peak-to-valley height of 15 nm. Such a texture evolution is typical of growing crystallites and has been noted in Ge:H and Si:H/SiGe:H material system by numerous authors [15] [86] [72] [87]. For a film thickness of 200 nm, the RMS roughness decreases to about 2nm (peak-to-valley height of 12 nm).

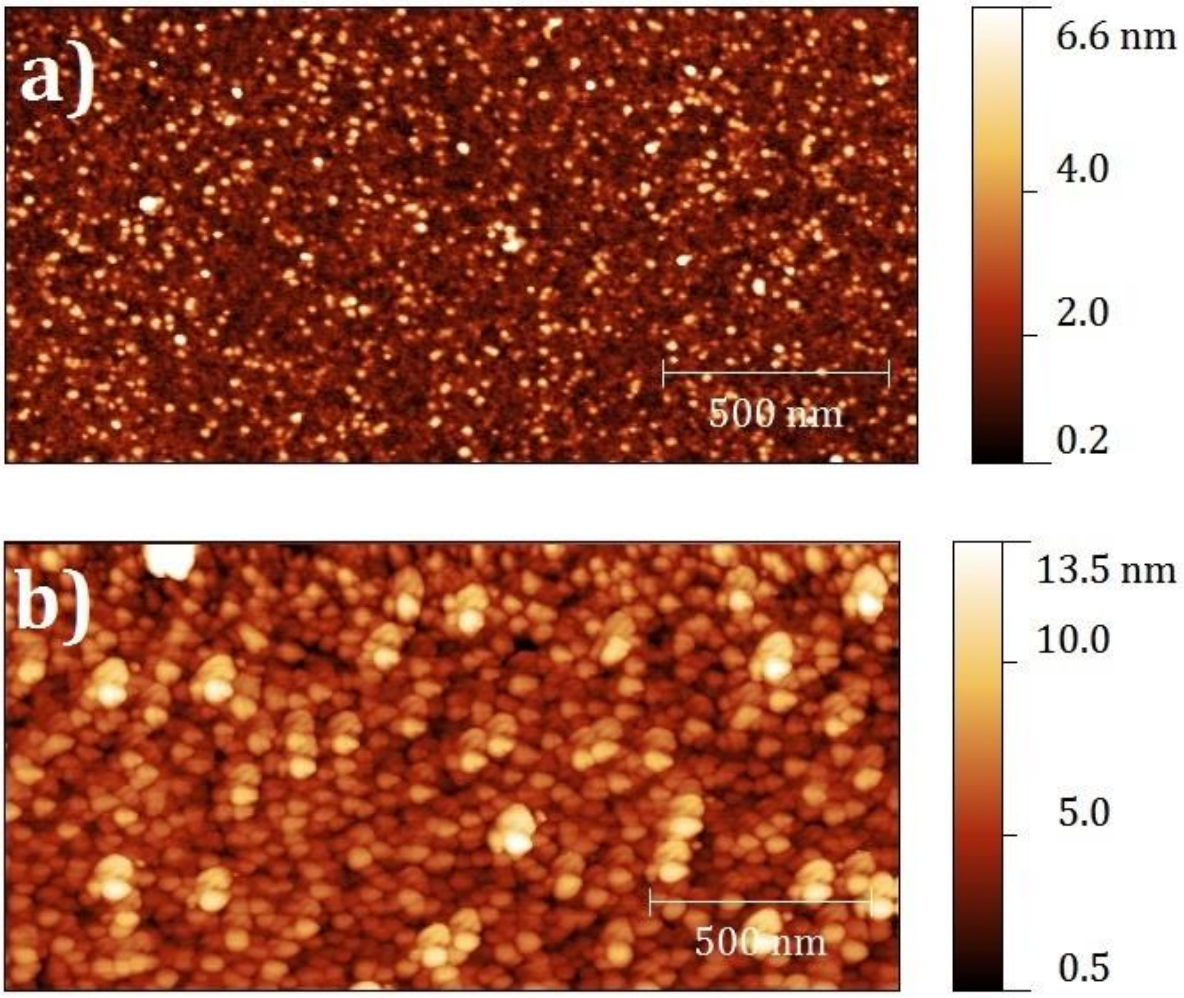

Figure 4-10. AFM micrographs of Ge:H thin films with thicknesses a) 7 nm and b) 200 nm presenting differences in surface morphology. The 200 nm thin film shows larger grains and larger peak-to-valley heights than the 7 nm thin film

Figure 4-11 shows a detailed three–dimensional image obtained for the 100 nm thin film of Ge:H. Clusters of Ge:H can be seen protruding from the surface of the film which results in the larger peak-to-valley height of 15 nm as measured for this thin film.

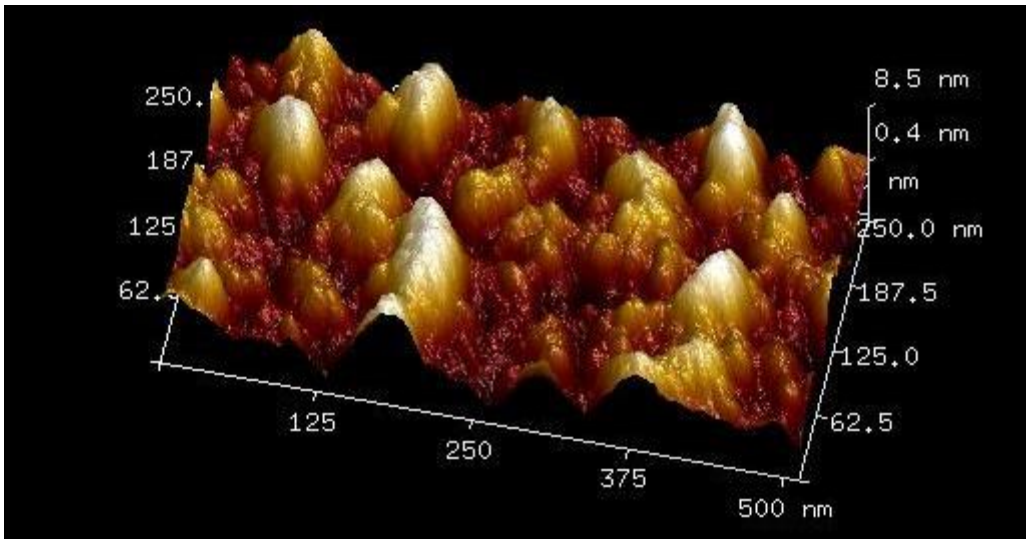

Figure 4-11. A three dimensional AFM micrograph showing the peak-to-valley roughness associated with the large grain sizes for the 100 nm thin film of Ge:H deposited in this work.

The presence of nanocrystallites in films thicker than 20 nm is confirmed in the electrical resistivity data. While amorphous germanium has been observed to have a resistivity as high as 10^7 Ω–cm, crystalline germanium has a resistivity of about 50 Ω–cm. The incorporation of these nanocrystallites lowers the resistivity of the films to about 750 Ω–cm for the films in which the crystalline grains have coalesced. The increase in the resistivity and TCR for increasing film thicknesses is unexpected especially because the fraction of nanocrystallites is increasing with increasing thickness. To shed light on this behavior, the thin films were characterized using Real Time Spectroscopic Ellipsometry or RTSE.

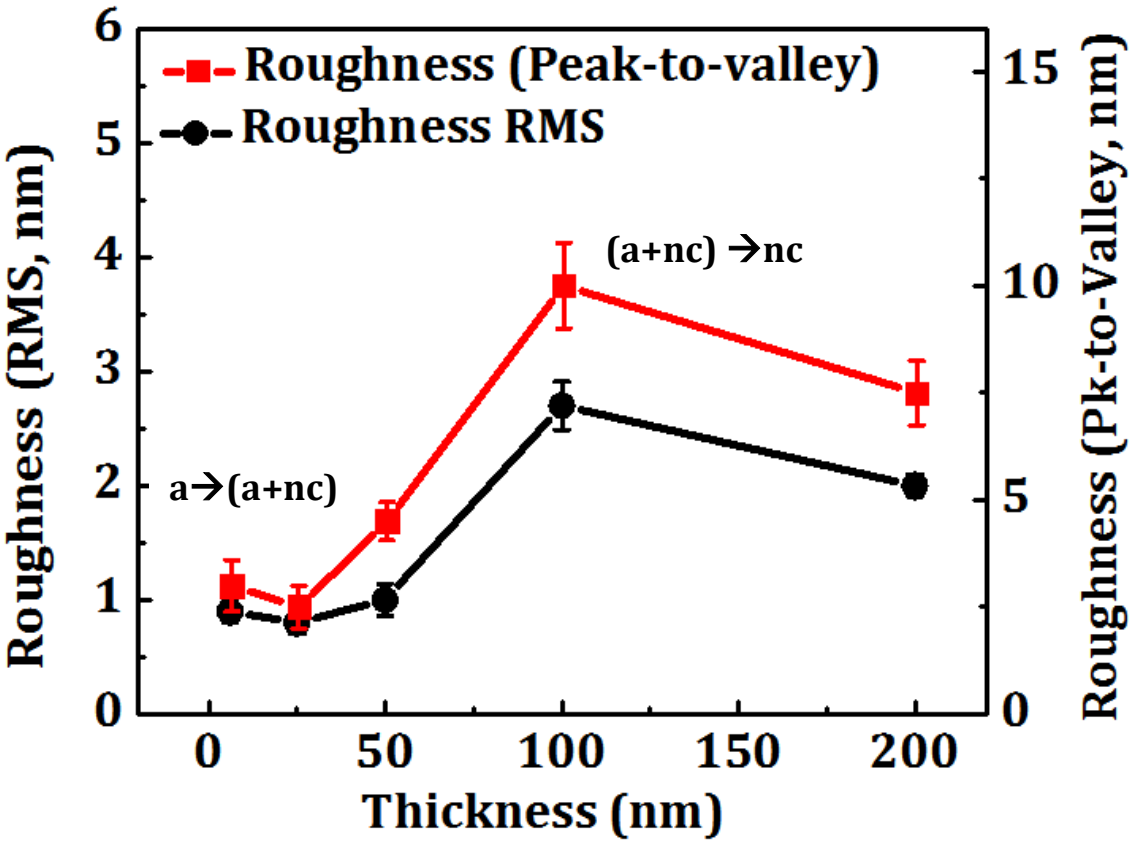

Figure 4-12. Peak to valley height (red) and RMS roughness (black) of thin films of Ge:H deposited in this work.

RTSE data was analyzed by a global Σσ-minimization procedure to obtain optical properties, in the form of the complex dielectric function spectra $\varepsilon = \varepsilon_1 + i\varepsilon_2$, and the time dependence of the bulk layer (d_b) and surface roughness (d_s) thicknesses while the film remains in the amorphous growth regime [88]. After crystallite nucleation occurs, virtual interface analysis (VIA) is used to obtain ε for the nanocrystalline phase and the time dependence of d_s and the nanocrystallite fraction (f_{nc}) [89] [90] [91]. In the mixed-phase amorphous + nanocrystalline (a + nc) regime, VIA uses a Bruggeman effective medium approximation [92] consisting of variable fractions of ε for a-Ge:H and nc-Ge:H to represent the optical response of the outermost 1.5 nm of the growing film. From this information, a depth profile in crystallinity can be determined.

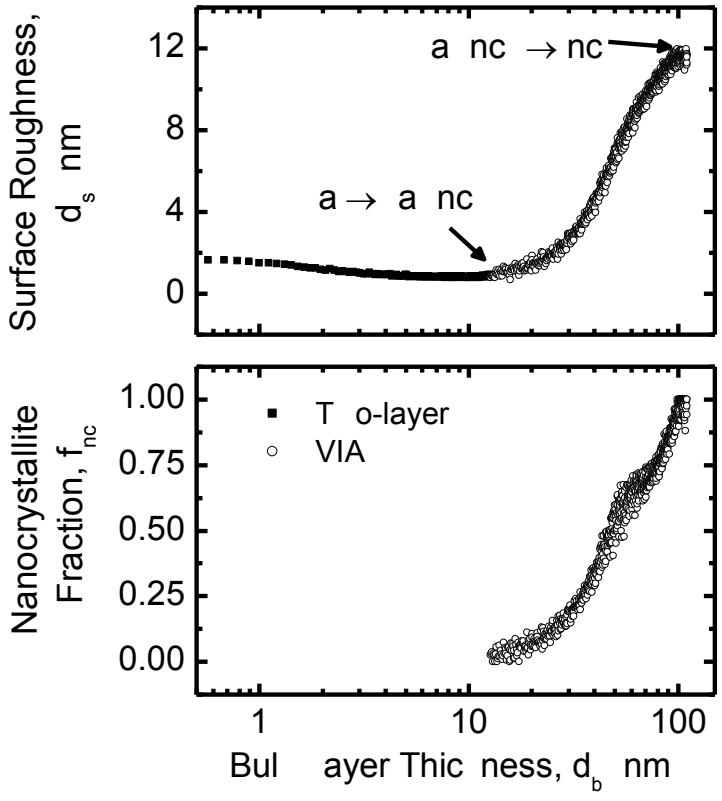

Figure 4-13. Surface roughness and nanocrystallite fraction for Ge:H on native oxide coated crystalline silicon (c-Si) obtained from two layer modeling and virtual interface analysis (VIA) of real time spectroscopic ellipsometry (RTSE) measurements. The nanocrystallite fraction profile used in the analysis of the single final set of spectra is also shown.

The RTSE data analysis was led by Dr. Nikolas Podraza from The University of Toledo, Toledo, Ohio. The results of RTSE data analysis are provided in Figure 4-13. The film remains amorphous with d_s initially decreasing and reaching a minimum value prior to the amorphous-to-mixed-phase transition [$a \rightarrow (a + nc)$] at d_b = 13 nm. Afterward, f_{nc} and d_s begin to increase as nanocrystallites grow preferentially over the surrounding amorphous phase. Coalescence of nanocrystalline clusters occurs when f_{nc} = 1, d_s reaches a maximum, and is called the mixed-phase-to-single-phase nanocrystalline transition [$(a + nc) \rightarrow nc$] at d_b = 100 nm. After the (a + nc) → nc transition, d_s deceases slightly as a single phase nanocrystalline layer is formed and protruding clusters coalesce.

The initial decrease in resistivity could be due to the initial nucleation of crystallites or enhanced ordering of protocrystalline Ge:H prior to the onset of crystallinity. Resistivity, however, subsequently

increase with f_{nc}, reaches a maximum near the $(a + nc) \rightarrow nc$ transition, then decreases. An explanation for this behavior is that while the initial appearance of more conductive crystallites reduces film resistivity, subsequent evolution introduces a significant amount of grain boundary material into the film. Poorly passivated grain boundaries can act as oxidation pathways post-deposition as the films are exposed to atmosphere, thereby increasing resistivity.

Figure 4-14 shows variations in ε for the nanocrystalline component of the nominally 100 nm film deposited on native oxide coated c-Si, monitored by RTSE, and characterized by ex situ spectroscopic ellipsometry post-deposition. RTSE VIA analysis yielded $a \rightarrow (a + nc)$ and $(a + nc) \rightarrow nc$ transition thicknesses as well as ε for a-Ge:H and nc-Ge:H in vacuum at the deposition temperature. The final RTSE data point was analyzed using these reference ε and a structural model incorporating a 13 nm continuous amorphous layer, a 93 nm mixed-phase layer with nanocrystallite fraction incorporating an exponential gradient shown in Figure 4-13, a 15 nm continuous nanocrystalline layer, and a 12 nm surface roughness layer in accord with VIA results. These structural parameters were fixed and used to fit ex situ ellipsometric spectra collected from the same sample after exposure to atmosphere at room temperature. The temperature dependence of ε for c-Si is known [93] and that for a-Ge:H was obtained from in situ spectroscopic ellipsometric monitoring of a 60 nm thick film prepared at T = 200 ^{o}C and R = 120 which remains amorphous.

Spectra in ε for a-Ge:H can be described using the Cody-Lorentz oscillator model [94] in terms of energy independent parameters including an amplitude (A), broadening (Γ), resonance energy (E_0), band gap (E_g), partition energy (E_p), and constant additive term to ε_1 (ε_∞ = 1). The temperature dependence of E_g, E_p, and A were identified as dE_g/dT = –0.000411 eV/K, dE_p/dT = –0.000617 eV/K, and dA/dT = –0.02 eV/K, respectively, which are in reasonable agreement with previous results for hydrogenated amorphous silicon germanium alloys [95]. Variations in Γ and E_0 were not greater than the error limits within this temperature range and were fixed. Spectra in ε obtained from RTSE for R = 400 a-Ge:H prior to

nanocrystallite nucleation was parameterized using the Cody-Lorentz model at the deposition temperature, and room temperature ε was simulated using these temperature dependencies to assist in fitting ex situ ellipsometric measurements of nominally 100 and 200 nm thick films. Spectra in ε for nc-Ge:H were parameterized using three Tauc-Lorentz oscillators [96] [97].

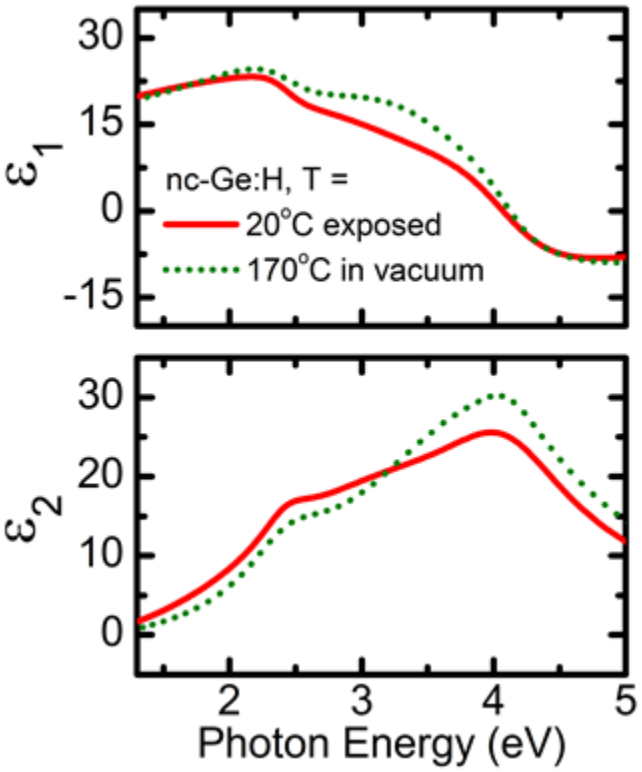

Figure 4-14. Complex dielectric function, $\varepsilon = \varepsilon_1 + \iota\varepsilon_2$, spectra for nanocrystalline Ge:H (nc–Ge:H) obtained in situ, in vacuum from virtual interface analysis of RTSE data and obtained ex situ, after atmospheric exposure.

Differences in ε for nc-Ge:H are expected with differences in temperature, although typically critical point broadening decreases and amplitude increases at lower temperatures for crystalline materials [93]. The data shown in Figure 4-14 shows an increase in broadening and decrease in amplitude, particularly for the higher energy critical point feature. This variation is consistent with partial oxidation of a material. When ε obtained at room temperature after atmospheric exposure is treated as a pseudodielectric function and fit to a structural model consisting of un-oxidized nc-Ge:H, in this case ε obtained in vacuum, and an overlayer of germanium oxide [98], the overlayer thickness is 1.5 nm thick.

This model is a gross simplification, but it also seems to indicate that some fraction of the nc-Ge:H has oxidized.

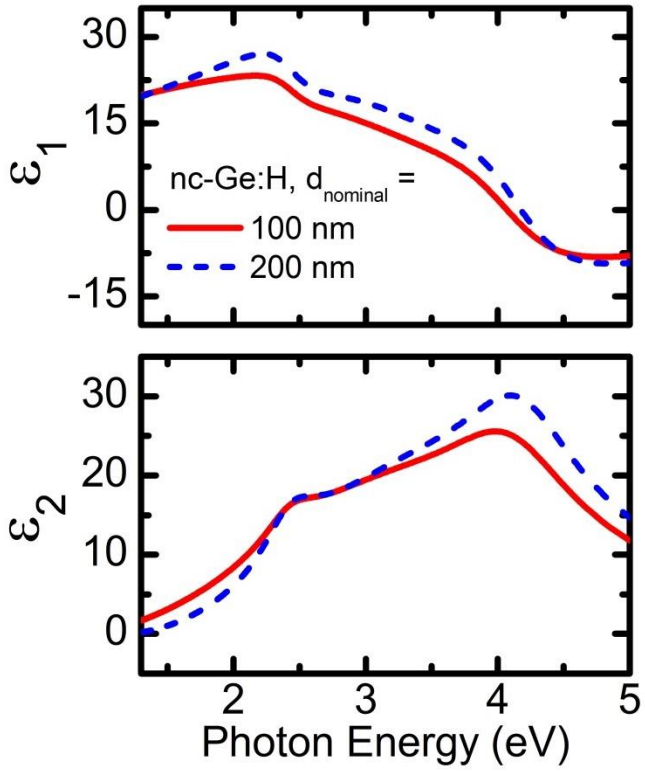

Figure 4-15. Spectra in ε for nc-Ge:H obtained ex situ, after atmospheric exposure for nominally 100 and 200 nm thick films.

Figure 4-15 shows a comparison of ε obtained at room temperature, after atmospheric exposure for the nominally 100 nm film on native oxide coated c-Si and nominally 200 nm film on SiN_x coated c-Si. Although the substrate is different, previous studies indicate that the $a \rightarrow (a + nc)$ transition occurs as at similar thicknesses for Ge:H, as given in Figure 4-15. The features in ε for the thicker film are sharper and have a larger magnitude, indicating that grain size has increased, the amount of grain boundary material has been reduced, and/or a smaller fraction of the film has oxidized.

A proposed model describing the variations in resistivity and TCR relies on nanocrystalline grain boundaries acting as oxidation pathways. At low crystalline content as in the nominally 25 nm thick film, improved ordering in the amorphous phase may lower film resistivity. When crystallites begin to occupy a significant fraction of the surface, as in the 50 and 100 nm films, resistivity increases as the grain

boundaries enable the internal crystallite surfaces to oxidize. At greater thickness, the increase in grain size and reduction in grain boundaries again reduce resistivity since more interconnecting pathways between un-oxidized grains exist. The highest *TCR* is observed for the highest resistivity, which potentially consists of crystallites encompassed by higher resistivity germanium oxide material. This structure is similar to that of microbolometer device grade vanadium oxide, where low resistivity, small defective face centered cubic vanadium monoxide nanocrystallites are surrounded by higher oxygen content, higher resistivity material [43]. Similar vanadium oxide thin films also exhibit significant post-deposition oxidation as monitored by RTSE [99].

4.4. Conclusion

Thin films of VO_x and Ge:H having TCR values larger than 4%/K have been deposited in this work. Thin films of VO_x were found to be amorphous, with resistivity around 10,000 Ω–cm to 21,000 Ω–cm with α_H/n values between ~ 10^{-18} and 10^{-20} cm^3. Ge:H thin films were found to be amorphous or amorphous + nanocrystalline depending on thickness and dilution ratio of the film deposited. When deposited by PECVD using high dilutions of GeH_4 in H_2, these films show nanocrystalline grain growth in an amorphous matrix. At thicknesses optimized for a dilution ratio, R of $[H_2]/[GeH_4]$, films 50 – 100 nm thick exhibit large TCR (5%/K – 6.4%/K) with reasonable values of α/n (~ 10^{-19} and 10^{-20} cm^3) having low resistivity (1,500 Ω–cm and 2,250 Ω–cm). This superior combination of electrical properties was attributed to the incorporation of an optimal value of grain size and the crystal fraction of the germanium nanocrystallites.

Figure 4-16 shows a comparison of TCR versus resistivity of various thin films reported in the literature in comparison with thin films deposited in this work. Both Ge:H and VO_x thin films show the highest reported TCR for the resistivity < 10,000 Ω–cm. However, thin films of (nc+a)-Ge:H show a superior resistivity to TCR tradeoff in comparison with thin films of VO_x deposited in this work.

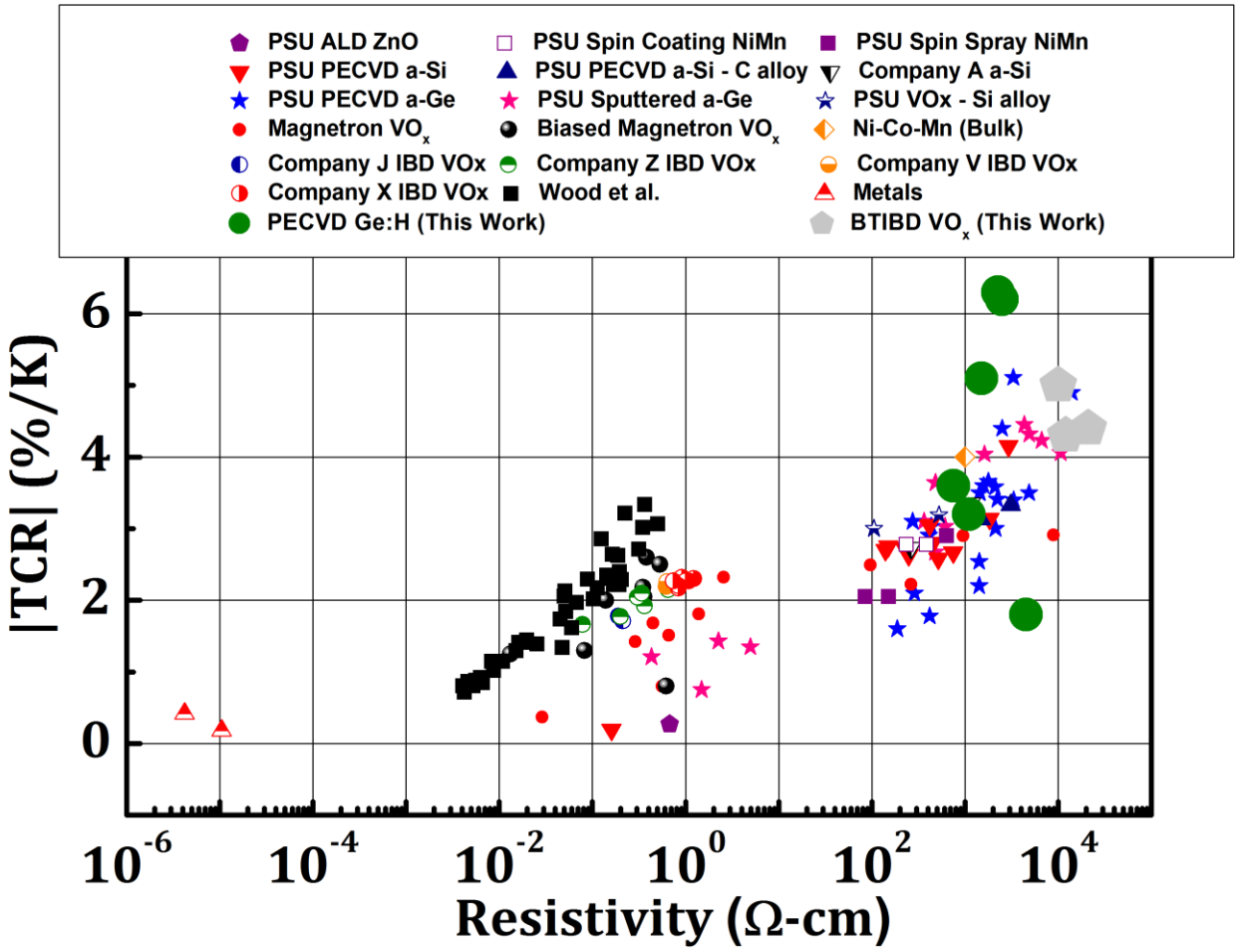

Figure 4-16. A comparison of Resistivity vs. TCR of thin films reported in literature to the thin films of Ge:H and VO_x deposited in this work.

However a more comprehensive figure of merit is the NETD which was discussed in Chapter 2. For a given material, the theoretical NETD is given by:

$$NETD \propto \frac{I_{noise,\ total}}{I_{bias} \times TCR} \qquad \text{Equation 27}$$

Or,

$$NETD \propto \sqrt{\left(\frac{\alpha_H}{nVf}\right)} \times \frac{1}{TCR} \qquad \text{Equation 28}$$

From equation 2 it is evident that a metric of comparison between different materials is the ratio of (α_H/n) to TCR^2. Figure 4-17 gives a comparison of the normalized Hooge's parameter 'α_H/n' versus TCR for different materials reported in the literature with the materials deposited in this work.

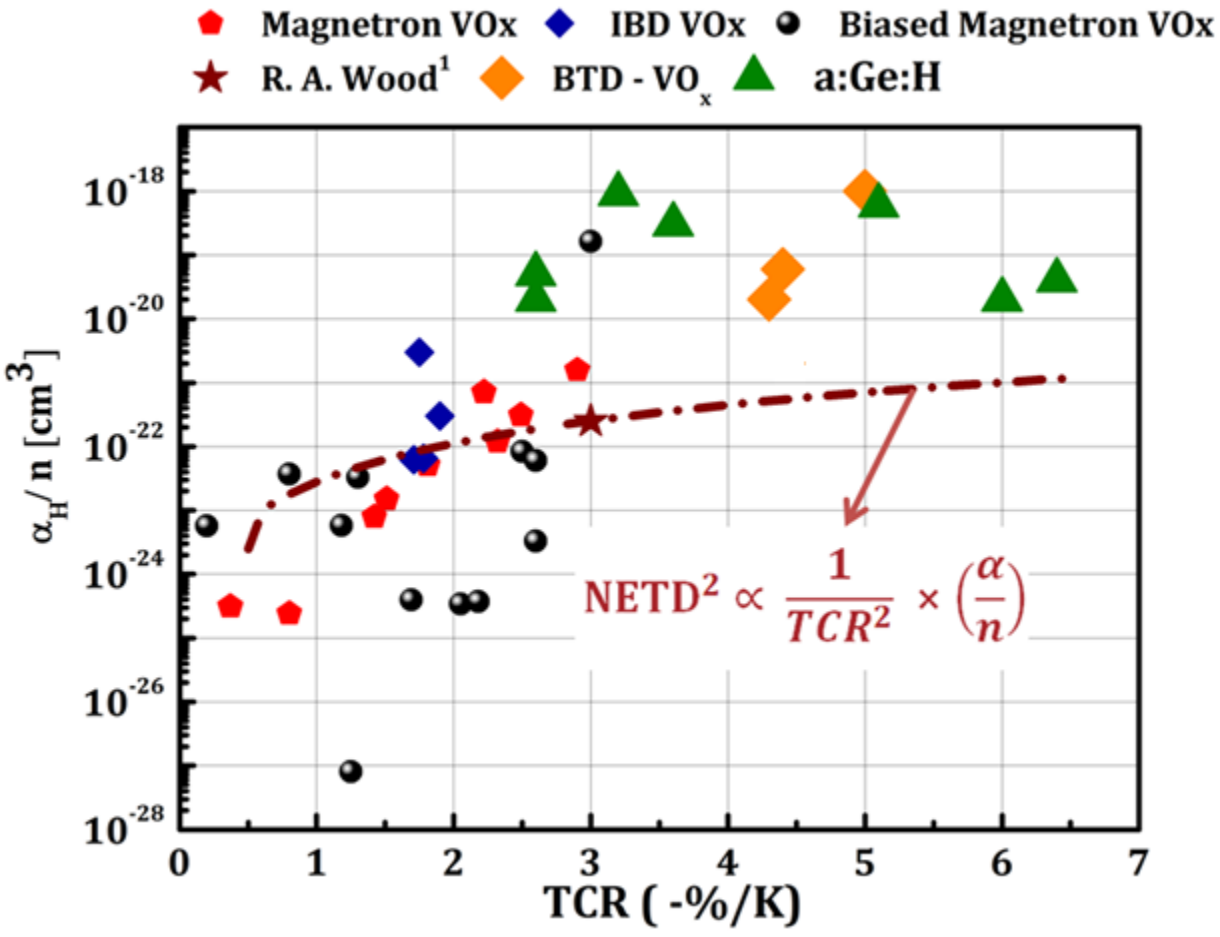

Figure 4-17. A comparison of the Normalized Hooge's parameter of some common materials reported in literature vs. thin films deposited in this work. The dotted line represents a constant ratio of α_H/n : TCR^2.

The dotted line is a curve of an equipotential NETD^2. This curve shows the values which would give the same NETD regardless of the fact that the TCR and noise values are changing between the thin films. This line shows that although films with higher TCR are deposited is this work, the tradeoff of TCR and noise is not sufficient for use of these high TCR materials in a pulsed bias geometry as with the VO_x microbolometer system. The real advantage in using these thin films can be obtained by advanced circuits such as those used in constant bias bolometer devices existing at L-3 communications. Both the

hydrogenated nanocrystalline + amorphous (nc+a)–Ge:H thin films and possibly VO_x thin films are potential candidates for high TCR materials used in constant bias microbolometers.

Chapter 5. High TCR Bolometers Using Vertically Integrated Thin Film Resistors

5.1. Introduction

Vanadium oxide (VO_x) and hydrogenated silicon germanium (SiGe:H) having a magnitude of TCR between 2%/K and 4%/K form an integral part of a majority of infrared imaging systems manufactured today [8] [30] [78] [100] [18]. The material properties of these thin films used in making uncooled infrared focal plane arrays has remained largely unchanged since some of the first investigations detailing their properties [8] [100] [18]. Most of the performance improvement in these devices has come from the evolution of the underlying read out circuits [101] [59] [102] [103] [104].

The current pixel structure in infrared imaging sensors employs a lateral resistor configuration with a square geometry in which the length and width of the sensing material is 17 μm × 17 μm. To minimize thermal mass and optimize performance, the thickness is kept to ≈ 50nm to 100 nm. Though high TCR materials are preferred, these materials typically have higher resistivities and therefore higher device resistance and noise associated with them. Existing materials with large values of TCR (~ 4%/K) typically have a resistivity larger than 2,000 Ω–cm with higher TCR materials having even larger resistivities. Although higher TCR materials exist, they have not been incorporated into infrared focal plane arrays due to their higher resistivity (> 100 MΩ) and higher noise in the lateral resistor configuration [50] [42] [51] [105] [106] [84].

To overcome this limitation, in this work, an alternate pixel design is investigated in which a high TCR material is incorporated into a structure having low device resistance. In the literature, only a few other device configurations have been explored which use the out of plane conductivity (or through film) as opposed to the lateral conductivity currently used in resistive bolometers. Figure 5-1 shows the three bolometer pixel designs explored by Unewisse et al. which are detailed in ref. [107]. These through film devices can have resistance values up to 10^5 smaller for the sandwich–gap type structures [107] [108].

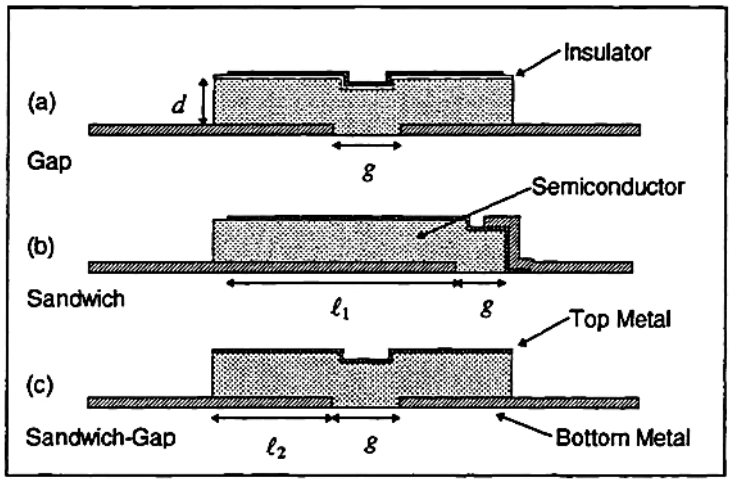

$$R = \frac{\rho g}{wd} \qquad \text{gap}$$

$$R = \rho \frac{dg}{w(d^2 + g\ell_1)} \qquad \text{sandwich}$$

$$R = \rho \frac{2dg}{w(2d^2 + \ell_2 g)} \qquad \text{sandwich-gap}$$

Figure 5-1. The three bolometer design structures explored by Unewisse et al. in ref. [107].

where ρ is the resistivity of the semiconductor material, g is the gap length, d is the thickness of the detector, w is the width of the detector, and l_1 and l_2 are the lengths of the bottom contact in the sandwich and the sandwich–gap type detectors, respectively.

Figure 5-1(a) shows the standard device structure used by the resistive microbolometer industry, whereas the detector of Figure 5-1(b) shows the sandwich type configuration in which the current flows in the transverse direction [107]. This greatly reduces the length to area ratio of the detector and hence the resistance. Due to the change in the length over area ratio associated with the through–film configuration, the resistance of a bolometer can be lowered ($R_{in\text{-}pane}/R_{out\text{-}of\text{-}plane}$) by up to a factor of 10^4 for 10 μm × 10 μm pixel dimensions in a sandwich type configuration [107]. Another type of detector was named the Sandwich-gap type detector, as shown in Fig. 2(c), which essentially consists of two sandwich type elements in series, separated by a small gap [107]. In this configuration, the resistance could be reduced up to a factor of 10^5 [107]. Although these alternate designs were investigated at the Defense Science and Technology Organisation, in Australia from 1995 through 2003, there is a limited body of literature detailing the performance of microbolometers in this configuration [107].

In 2010, Moreno et al. investigated the electrical performance of the sandwich type structure and detailed it in ref. [108]. It was found that the sandwich structures had a higher level of electrical noise (5

orders of magnitude higher, 10^{-11} A/√Hz vs. 10^{-16} A/√Hz) [108]. However, no reason was attributed to this higher level of noise. One possibility for the higher level of noise could be the higher electric field to which the sensing thin films were subjected. Indeed the 'I–V' curves of the biased sandwich structures was found to be nonlinear [108].

This work looks to fabricate sandwich type detector elements (referred to here as the through film device structures) with high TCR and high resistivity materials. The resultant through films structures are characterized for their electrical properties, especially their electrical noise. Thin films of high TCR hydrogenated germanium (Ge:H, |TCR| > 6%/K) and vanadium oxide (VO_x, TCR > 5%/K) were integrated in lateral and through film configuration. The Johnson noise of the devices was reduced significantly while maintaining the same contribution of 1/f noise.

5.2. Theoretical Performance of Through Film Structures

An important figure of merit is the Noise Equivalent Temperature Difference or NETD, which can be used to compare the theoretical performance of the through film structures. The NETD is the measure of the sensitivity of an IR imaging system. It is defined as, "….the change in the temperature of a black body of infinite lateral extent which, when viewed by the thermal imaging system, causes a change in the signal-to-noise ratio of unity in the electrical output of the pixels of a focal plane array…." [17]. The NETD of a detector is given by [30] [17]:

$$NETD \propto \frac{I_{noise,\ total}}{I_{bias} \times TCR} \qquad \text{Equation 29}$$

Where $I_{noise,\ total}$ is the resultant total electrical noise from an electrical bias I_{bias}. The ratio of $I_{bias}/I_{noise,\ total}$ is also known as the Signal to Noise Ratio or 'SNR'.

When a microbolometer, dominated by the material noise, is biased using a voltage source, V_{bias}, producing a current I_{bias} the obtained SNR is given by [30]:

$$SNR = \frac{I_{bias}}{\sqrt{\frac{4\kappa T(f_2 - f_1)}{R_b} + I_{bias}^2 \frac{\alpha_H}{nV} \ln\left(\frac{f_2}{f_1}\right)}}$$ **Equation 30**

where κ is the Boltzmann's constant, T is the temperature of operation, f_1 and f_2 is the range of frequency for the bandwidth of operation, R_b is the electrical resistance of the bolometer, α_H is Hooge's parameter, n is the carrier concentration and V is the volume of the sample.

From Equation 29 and Equation 30, the NETD can be written as:

$$NETD \propto \frac{1}{SNR \times TCR}$$ **Equation 31**

To compare the electrical performance of the lateral and through film configurations, their TCR and the SNR must be evaluated. While the TCR of a device is an inherent property of the particular device and depends on the activation energy of the material used, the SNR depends on the electrical bias, applied to the device.

From Equation 30, the SNR increases for increasing bias values and reach a maximum when the device is operated at a bias level such that the 1/f noise dominates the total noise contribution. On the other hand the power dissipated across the thin film ($V_{bias}I_{bias}$) increases with increasing bias which may cause Joule heating of the thin film.

Due to these conflicting factors, a new set of bias conditions must be considered for this new configuration. Figure 5-2 shows calculated values of the power dissipated and the theoretical maximum values of SNR which can be achieved for the through film configuration with the following values:

Table 3. Parameters and their values used for estimating the SNR ratio and the power dissipated as a function of applied bias.

Parameter	Value
κ_b	1.38×10^{-23} $m^2.kg.s^{-2}.K^{-1}$
T	300 K
f_1	0.001 Hz
f_2	1 KHz
ρ	20,000 Ω–cm
α_H/nV (k)	1×10^{-11}
Dimensions	17 μm ×17 μm

A large voltage bias, similar to the one in the lateral configuration produces a bias current value 10^4 times larger than in the lateral configuration, causing a significant heating of the bolometer material leading to low frequency drift of the signal current [77].

The increase in the temperature of the bolometer due to the bias current is given by ΔT [30]:

$$\boldsymbol{\Delta T = \frac{V_{bias} I_{bias}}{c}} \qquad \textbf{Equation 32}$$

where ΔT is the rise in temperature of the bolometer per second of applied bias, and c is the heat capacitance of the bolometer material [30].

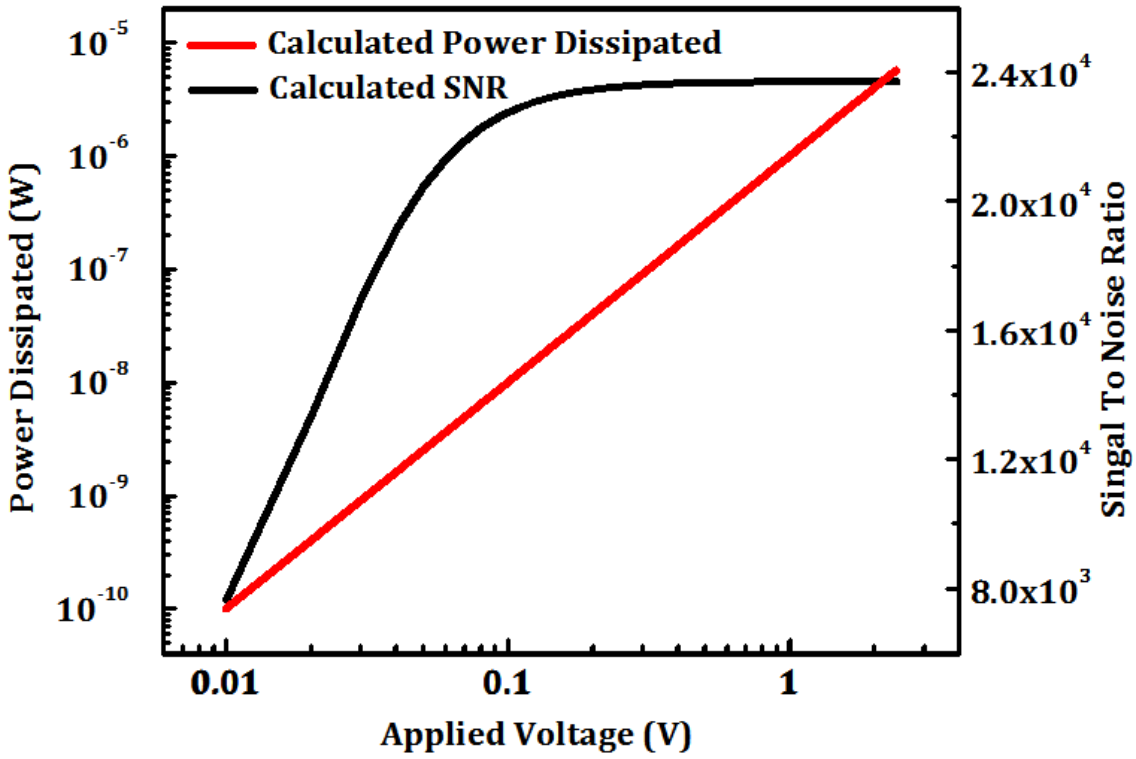

Figure 5-2. Graph showing theoretically calculated values of the power dissipated (red) and the maximum attainable signal to noise ratio (black) for a thin film device with a resistivity of 20,000 Ω–cm and dimensions of 17 μm × 17μm.

While a large bias voltage may cause bias–induced heating, a low voltage bias may result in a low SNR (from Equation 30). Figure 5-2 shows that the SNR increases dramatically for low bias vales; which is also when the total noise is dominated by the Johnson noise of the bolometer. The SNR reached a maximum when the 1/f noise contribution in equation 1 dominates**. Thus it can be concluded that for the vertically integrated thin films the optimal bias level is the lowest voltage value for which the SNR has reached a maximum OR the bias value should be high enough so that the device performance is dominated by the 1/f noise and not by Johnson noise.**

5.3. Experimental Details

To compare the electrical performance of the through film structures to the conventional lateral configuration, both the lateral and through film configurations have been fabricated using thin films of

high resistivity and high TCR VO_x and Ge:H. The process steps for fabricating the devices are described in the following subsections.

5.3.1. Lithographic Fabrication of Device Structures

Figure 5-3 shows a schematic for the two device structures whose electrical properties were compared. The lateral resistors devices were processed as described in Section 3.3.7. Briefly: thin films having a high TCR were first deposited onto an electrically insulating substrates (100 nm thermally grown SiO_2 on c-Si for VO_x thin films and 20 nm LPCVD SiN_x for Ge:H). The TCR material is then isolated in a 1:2,000 H_2O_2:H_2O solution, following which top electrodes are deposited by liftoff (titanium for VO_x and chromium for Ge:H).

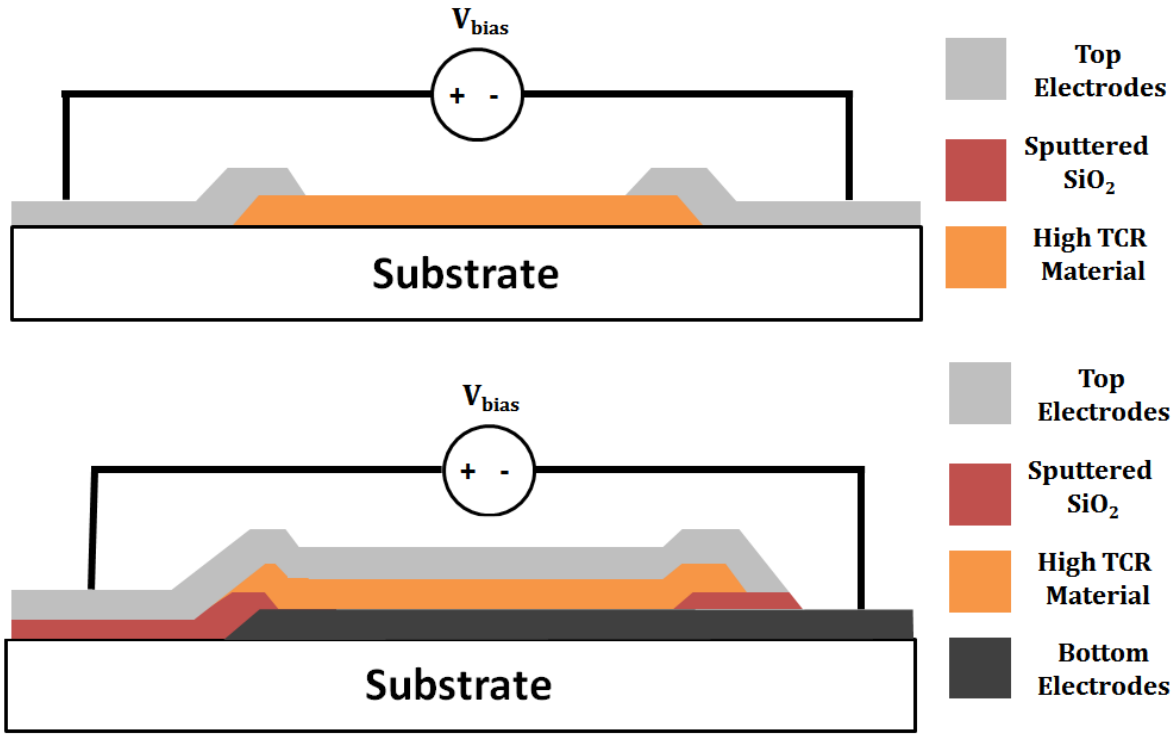

Figure 5-3. Cross-sectional schematic of bolometer configurations explored: a) In-plane conductivity (top); b) Out-of-plane conductivity (bottom).

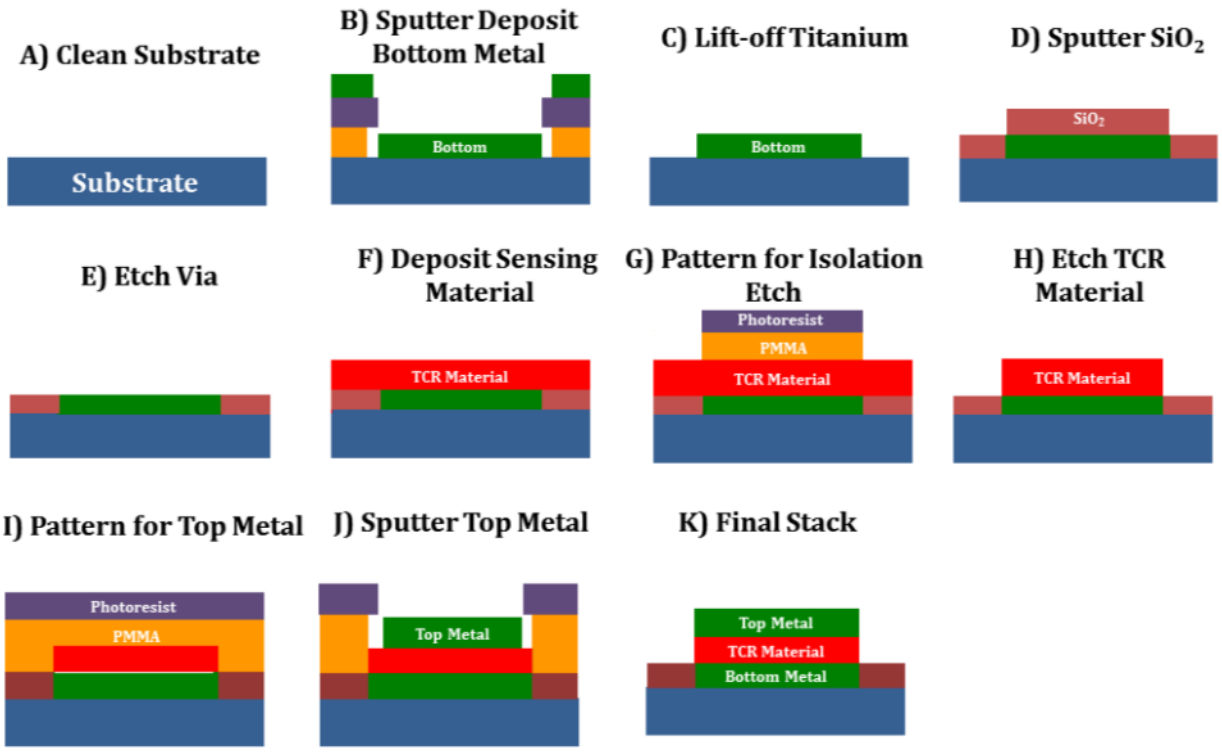

Figure 5-4. Lithographic processing for through film resistance structures.

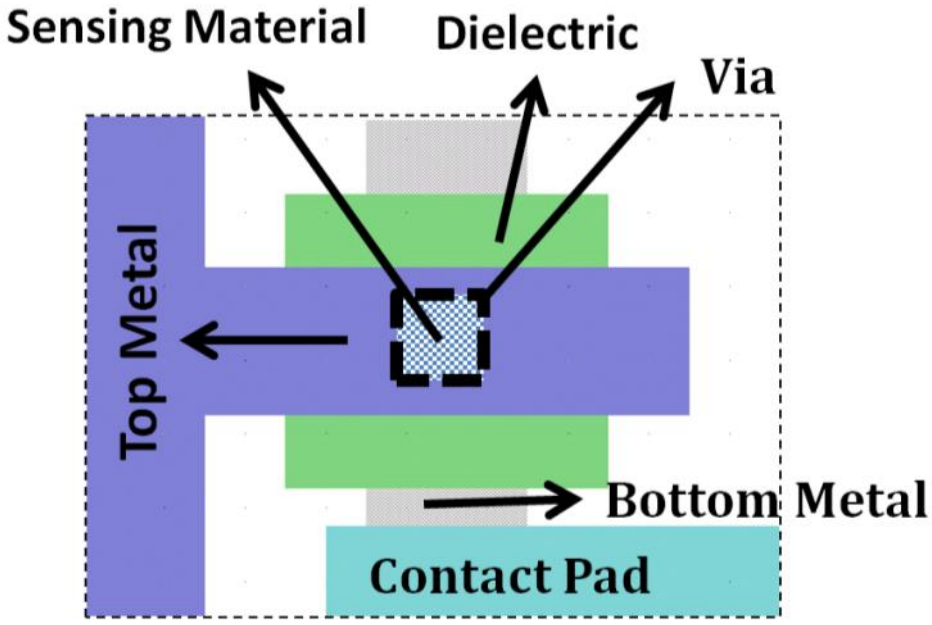

Figure 5-5. Top view of a mask set showing the different layers used for fabricating the out of plane resistance structure.

The processing of through-film structures was performed by using a mask set as shown in Figure 5-5. The processing was done following the process flow diagram of Figure 5-4 as follows: Bottom

contacts were deposited onto insulating substrates by a liftoff method. 100 nm of chromium was used for bottom contacts to Ge:H, whereas bottom contacts to high TCR VO_x thin films were obtained using either 100 nm of Titanium or Vanadium. Following the patterning of bottom contacts, 100 nm of SiO_2 was sputtered using magnetron sputtering of a 3–inch silicon target (99.999% pure) with 20% of O_2 flow in argon. A bias of −120 Volts was applied to improve the leakage current density through the sputtered SiO_2. Following this step, vias were etched using (6:1) BOE solution down to the bottom metal. High TCR VO_x deposited using Biased Target Ion Beam Sputtering (BTIBD) while Ge:H was deposited using Plasma Enhanced Chemical Vapor Deposition (PECVD) whose deposition will be described in the following subsection.

5.3.2. Deposition of High TCR, High Resistivity VO_x Thin Films

Previously, it has been shown that high TCR VO_x thin films can be deposited using a novel deposition technique of Biased Target Ion Beam Deposition (BTIBD) that incorporates precise control of the oxygen content of the thin film using a residual gas analyzer (RGA). The details of this deposition technique have been discussed in a previous chapter. Detailed values for the parameters used can be found in Table 2.

Briefly, a three-target configuration was used to deposit the thin films. A series of films was made with increasing partial pressure of oxygen, pO_2, ranging from 1×10^{-6} to 3×10^{-6} Torr, corresponding to an oxygen flow of 3 sccm–5 sccm. Total flow was kept at 70sccm, corresponding to a deposition pressure of $\approx 5.8\times10^{-4}$ Torr. A pulsed waveform was used to increase the sputter yield of the target in the oxidized regime. The target voltage was pulsed between –800V and +5 V to help minimize arcing during reactive sputtering. The voltage was pulsed at 10 KHz with a pulse width of 1 μsec. Thin films were deposited to a thickness of ≈ 100 nm (at a deposition rate of 0.17 Å/sec) and were found to be highly uniform in thickness and its electrical properties (better than ± 3%).

5.3.3. Deposition of High TCR, High Resistivity Ge:H Thin Films

Thin films of Ge:H having thicknesses of 25 nm to 100 nm were deposited by RF (f= 13.56 MHz) plasma enhanced chemical vapor deposition (PECVD) using ultra-high purity germane (GeH_4) gas diluted with H_2. The deposition conditions were similar to the experiment described in Section 3.2. A number of deposition parameters were fixed along the lines of previous work including: a total pressure of ~ 0.7 Torr and a low plasma power density of 0.08 W/cm^2. The substrate was held at a temperature of 170°C and the hydrogen-to-reactive gas dilution ratio was maintained at $R = [H_2]/[GeH_4] = [160\ sccm]/[0.4\ sccm] = 400$.

5.3.4. Electrical Characterization of Device Performance

The three most important electrical properties for thin film microbolometer materials are: room temperature resistivity, temperature coefficient of resistivity (TCR) and the electrical noise given by the normalized Hooge parameter (α_H/n). The lateral resistivity of the thin films was extracted using the Transmission Length Method (TLM) patterns. Figure 5-6 shows a graph of resistance versus spacing of electrodes for a thin film of VO_x deposited using the BTIBD system at a partial pressure pO_2 of 3×10^{-6} Torr. The other deposition conditions are described in section 5.3.2. The contact resistance is given by the y–intercept (here $2\times10^7\ \Omega$), the transfer length is given by half the value of the x–intercept (here 2 μm) and the resistivity is given by multiplying the slope of the graph with the cross-sectional area of the thin film (here ρ = 21,000 Ω–cm). The transfer length is used to decide on the minimum feature size which can be used to extract accurate thin film properties.

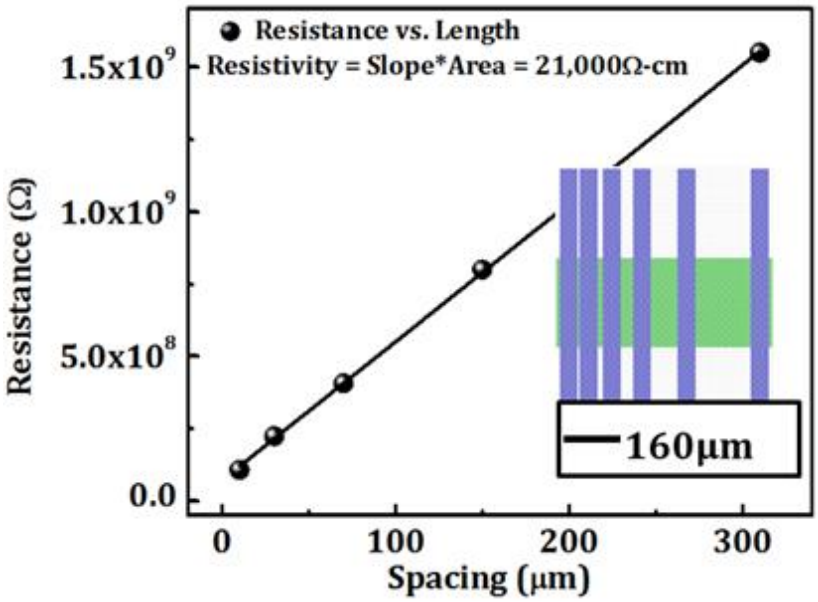

Figure 5-6. Resistance vs. electrode spacing measurements used to extract the sensing material's resistivity and the contact resistance.

Since the thickness of thin film is constant, the resistivity of the through film structures could not be measured using the TLM method. Instead, the effective through film resistivity was determined by patterning through film structures having different areas as can be seen in Figure 5-7.

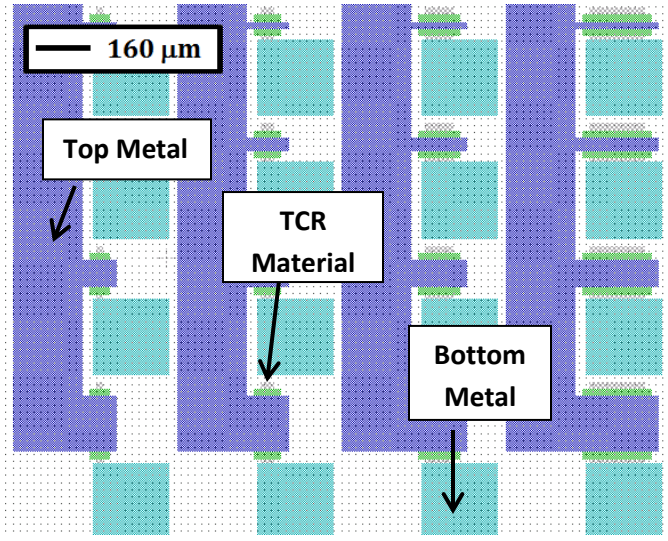

Figure 5-7. Top view of the mask set used for the measurement of resistivity of the sensing material.

I–V measurements were made on each through film resistor VO_x thin film and is evaluated in Figure 5-6. The resulting resistance values are plotted as a function of '1/contact area' and are shown in

Figure 5-8. The slope of the graph can be used to obtain the 'effective resistivity' of the thin film such that:

$$\rho = \frac{1}{thickness} \times \frac{R_B}{1/Area} = \frac{Slope}{Thickness} \qquad \textbf{Equation 33}$$

Similarly, the contact resistance can be calculated using the x–intercept of the curve. The x–intercept gives a point in which the area of the device interrogated is infinitely large. Such a point would contain only the contact resistance and have a relatively insignificant contribution from the thin film itself.

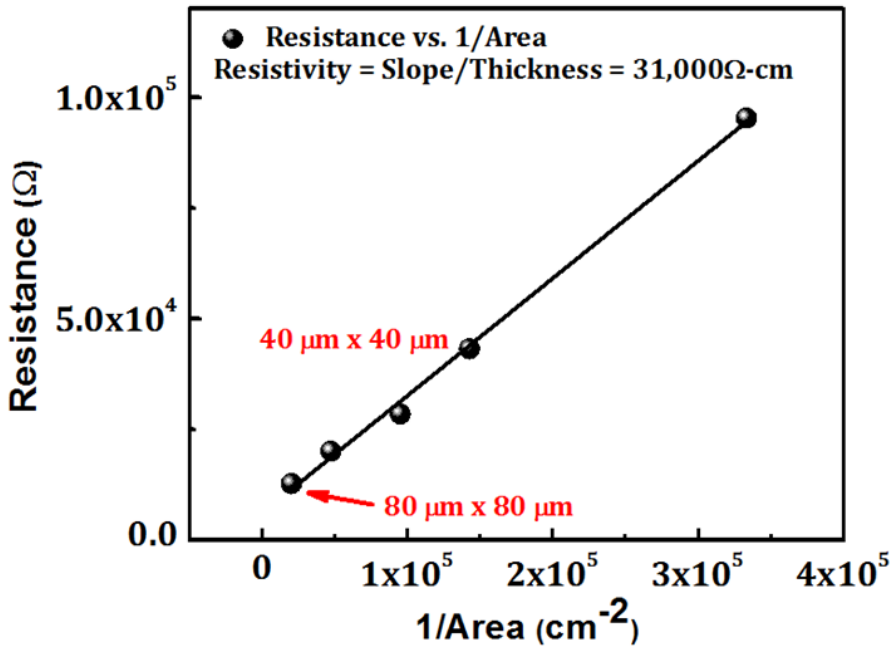

Figure 5-8. A plot of resistance vs. 1/Area used to extract the resistivity of the sensing material as measured from the structures in Figure 5-7. By dividing the slope of the line and the thickness of the film, the material's resistivity can be extracted.

The TCR measurements were made using a heated stage and a computer controlled HP4140B pA /DC voltage source. The TCR value was extracted from the activation energy after measuring the temperature dependence of resistance at incremental temperatures between 20-60°C using the relation given by:

$$TCR = -\frac{E_a}{k_b T^2} \qquad \text{Equation 34}$$

where E_a is the activation energy of the thin film material, κ_b is the Boltzmann's constant and T is the temperature at which the TCR value is to be calculated.

The 1/f noise of the material is evaluated by the Hooge-Vandamme relation given by:

$$Log\left(\frac{S_I(f)}{I_{bias}^2}\right) = Log\left(\frac{\alpha_n}{n \times V}\right) - \beta Log(f) \qquad \text{Equation 35}$$

where, $S_I(f)$ is the spectral current density, I_{bias} is the sample current, V is the volume of the sample, f is the frequency of measurement, α_n is the Hooge's parameter, β is the slope of 1/f noise measurement and n is the carrier concentration in the samples. To evaluate the properties of the films, 'α_H/n' was treated as the property of interest as described previously. The instrumentation for this measurement has also been described in a previous chapter.

5.4. Experimental Results

Since in the through film configuration, the thickness of the thin film is used as the length of the resistor, small electrical biases can result in large electric fields across the thin film. These large electric fields can result in nonlinear I–V characteristics of the through film resistors. The result of which can be seen in Figure 5-9.

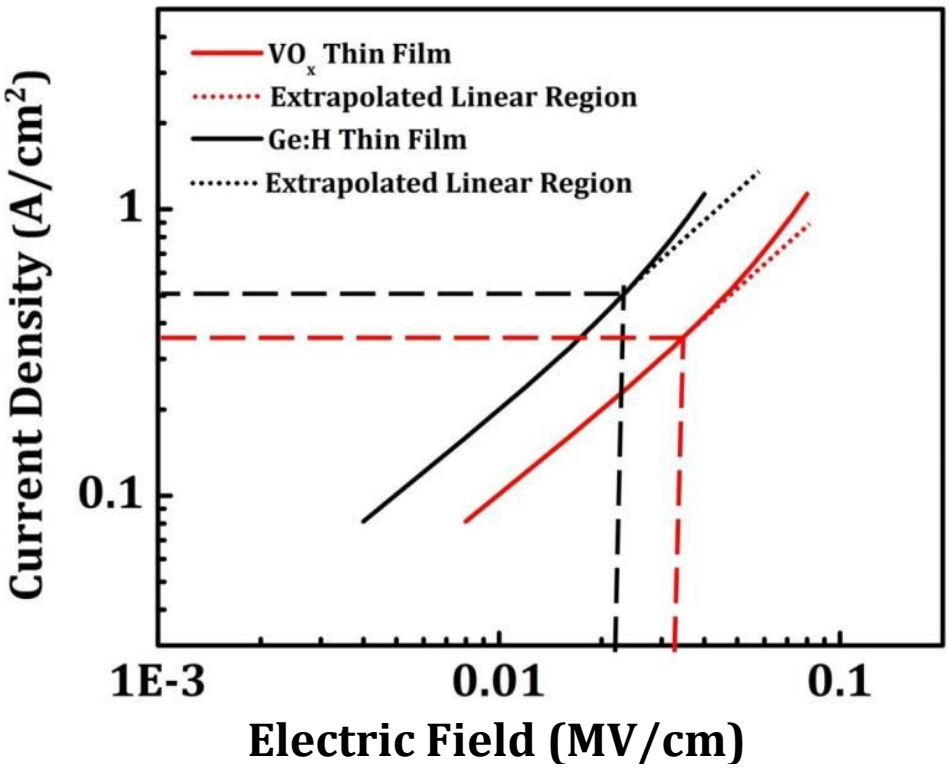

Figure 5-9. Current density as a function of electric field applied across the thin film resistor.

To ensure accurate measurements, the through film sensors were biased in the linear region of Figure 5-9. Figure 5-10 shows the lateral and through film resistivities of thin films of Ge:H deposited in this work. The lateral resistors of Ge:H have been investigated in Chapter 4. The lateral resistivity depends on the thickness of the thin film investigated. The through film resistivity varies significantly from its lateral resistivity: from 1,000 Ω–cm for the 200 nm (750 Ω–cm for the lateral configuration) to 28.6 MΩ–cm for the 25 nm thin film (1,250 Ω–cm for the lateral configuration). The disparity in the resistivity between the lateral and the through film configuration suggests that there exists an insulating layer at the interface of the bottom metal and the resistive thin film, or the initial layers of the resistive thin film have an extremely high resistivity.

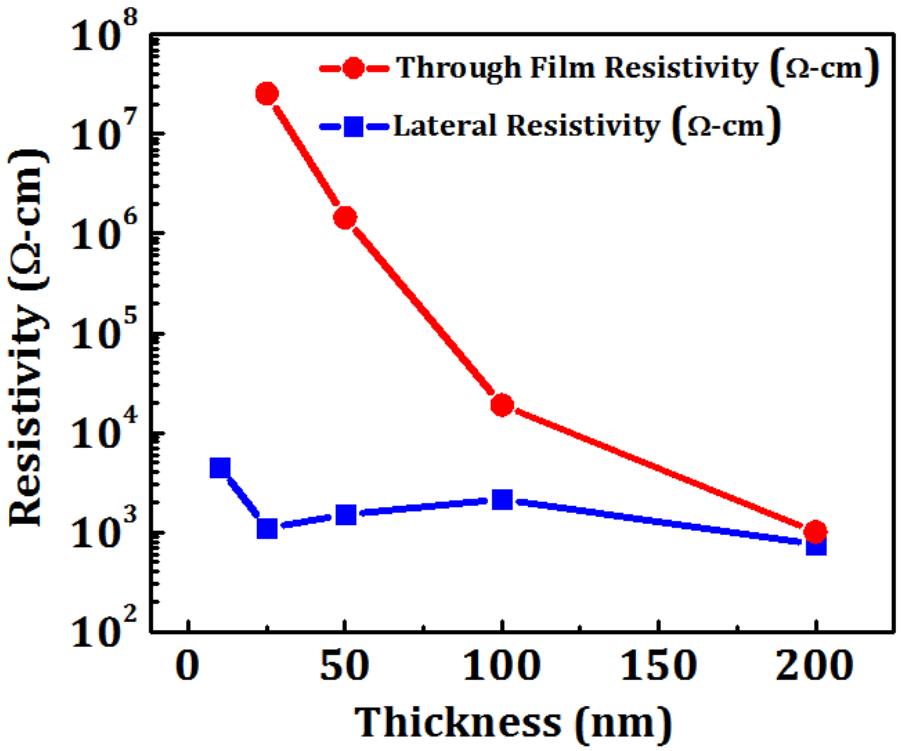

Figure 5-10. Lateral and through film resistivity of thin films of Ge:H thin films as a function of thickness. The through film resistivity increases dramatically for smaller thicknesses, indicating an insulating interfacial layer between the bottom metal and the resistive thin film.

Figure 5-11 shows a plot of natural log of resistance versus temperature of thin films of VO_x and Ge:H in the lateral and through−film configurations. For the through film measurements, the resistors were biased by using small electric fields such that the 'I–V' data collected were linear. It was found that though the lateral and through film resistance values are orders of magnitude different, the TCR values remained the same. These results are a strong proof of concept for the proposed through film resistor design.

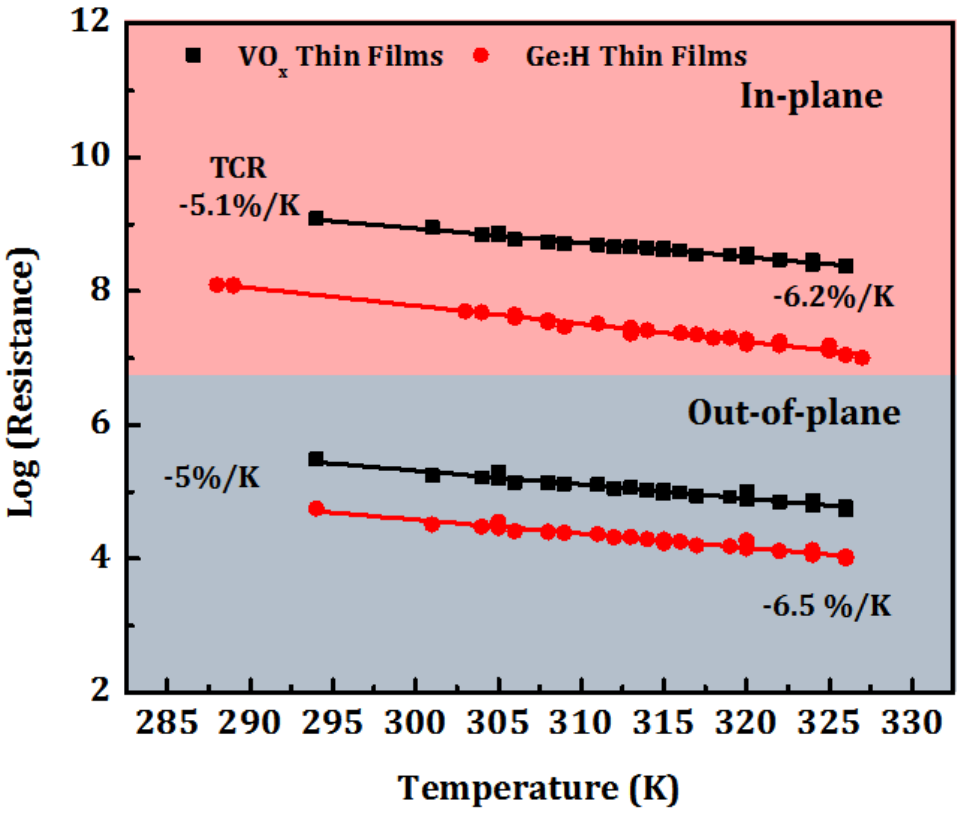

Figure 5-11. Resistance vs. temperature plots for thin films of VO_x and Ge:H fabricated in lateral and through film configuration showing orders of magnitude difference in resistance but similar TCR.

Having measured the resistance and the TCR values of the through film resistors, the 1/ƒ noise of the thin films was evaluated using methods described in Chapter 3. Figure 5-12 shows the acquired Power Spectral Density of thin films of Ge:H, 50-nm-thick with different volumes of the thin film resistors in both lateral and through film configurations. As expected, the 1/ƒ noise increases with decreasing device volume. When normalized for volumes, the magnitude of the 1/ƒ noise was found to be the same as can be seen from the inset of Figure 5-12.

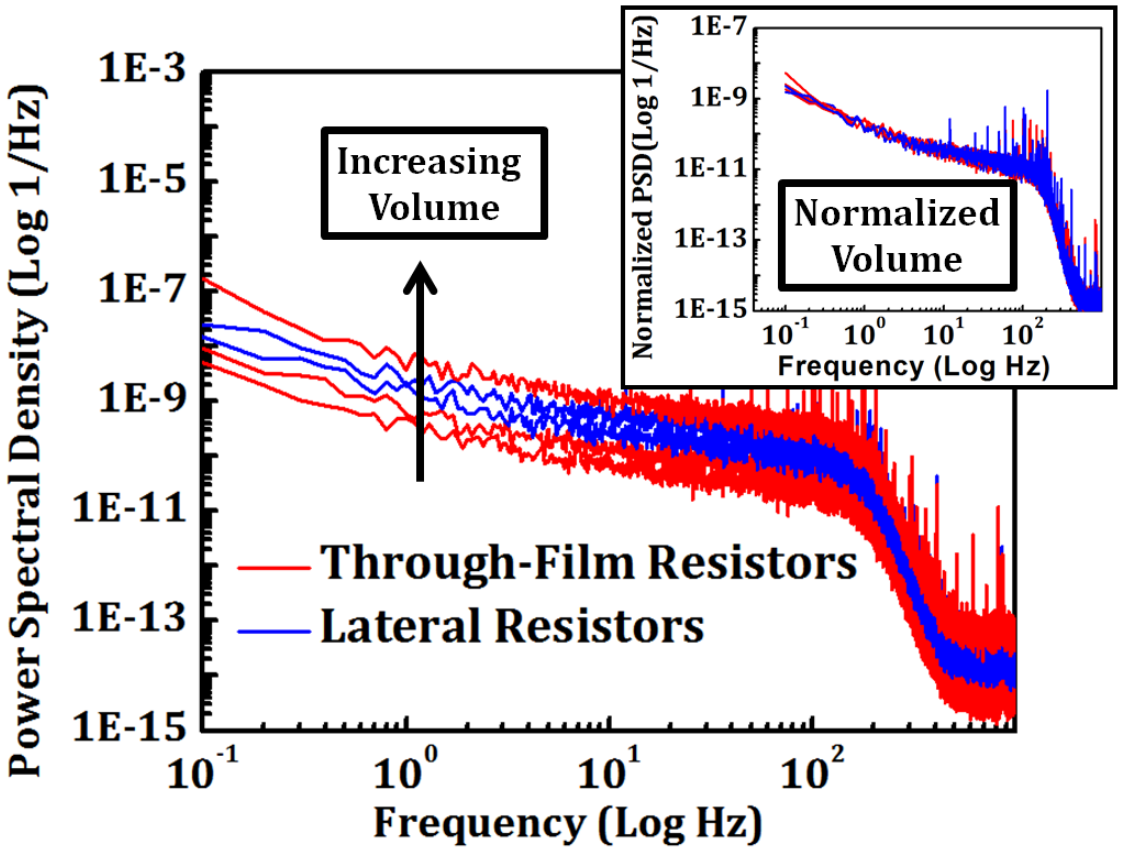

Figure 5-12. The measured Power Spectral Density (PSD), S_I^2/I_{bias}^2 for a 50 nm thin film of Ge:H showing good agreement with the Hooge's relationship, independent of device structure used (lateral or through film). Inset shows the PSD normalized for volume.

Table 4 compares the TCR and 'α_H/n' of thin films in lateral and through film configuration deposited in this work. Within the margin of error of measurement, the TCR and the 'α_H/n' of thin films was found to be the same.

Table 4. Summary of TCR and'α_H/n' values in lateral and through film configuration deposited in this work.

Sample	TCR Lateral (%/K)	TCR Through Film (%/K)	'α_H/n' Lateral (cm^3)	'α_H/n' Through Film (cm^3)
VO_x	–4.1	–4	1.4×10^{-19}	1×10^{-19}
VO_x	–4.5	–4.6	1.5×10^{-18}	1×10^{-18}
VO_x	–4.7	–5	4×10^{-18}	1×10^{-18}
VO_x	–5	–5.3	3×10^{-18}	1×10^{-18}
Ge:H	–3.4	–3.6	7×10^{-19}	5×10^{-19}
Ge:H	–5	–5.1	1.7×10^{-19}	1×10^{-19}
Ge:H	–6.2	–6.5	8×10^{-20}	1.2×10^{-20}

Similar values of TCR and α_H/n shows that in going from the lateral device configuration to a through film configuration there is no change in the signal to noise ratio (SNR). However, as it was noted in section 5.2, the vertically integrated devices can sustain larger signal currents due to their lower device resistance without any change in self heating. This means that although the SNR has not changed with device configuration, the magnitude of the signal is larger. As was seen in Section 2.3.4.2, a higher signal current implies reduced integration time on the readout capacitor, thereby increasing the available frame rate of the sensing array.

5.5. Conclusion

Vertically integrated VO_x thin films structures have been demonstrated as potentially viable alternative to the conventional lateral-pixel configuration used in uncooled imaging bolometers, for next generation IR FPAs that employ higher TCR and higher resistivity material. In this work, high VO_x thin films were obtained using BTIBD and high TCR Ge:H thin films were obtained by PECVD of GeH_4 at high dilution ratios.

Using lithographically patterned structures it has been shown that through film conductivity measurements make it possible to reduce the device resistance of high TCR materials. The SNR for the through film structures equal to those obtained using lateral conductivity.

Chapter 6. Resistive Temperature Sensing Arrays

6.1. Introduction

Microbolometer arrays have been at the forefront non-contact thermometry. These devices have high sensitivity (NETD < 30 mK) and high frame rates (> 30 Hz) [15] [18]. However, these systems are based on the principle of differential temperature and are not designed for use in the contact mode or for mapping the absolute temperature of the object under investigation. In addition, these sensors are based on materials with |TCR| < 4 %/K in the lateral configurations where the device impedance is relatively high (>100 MΩ). In this work, thin films of VO_x with TCR ≈ 4.4 %/K were used to fabricated one dimensional arrays of vertically integrated temperature sensors on glass substrates. The performance of these arrays is compared with those of the lateral resistors. In addition, discrete devices are fabricated with integrated ZnO based transistors to allow multiplexing of two dimensional arrays.

6.2. Array Design and Fabrication

6.2.1. Design and Processing of 1-D VO_x Sensor Array

Figure 6-2 shows the schematic of the 1×8 1-D temperature sensing array fabricated in this work. The total length of the sensor was kept at 2 cm, while the head of the sensor was fabricated to be 500 μm wide. The narrow width of the top of the sensor was designed to reduce the thermal mass, and facilitate implant for in-vivo testing. The base of the sensor was kept wide to facilitate bonding to the pads. The bonding pads had a width of 250 μm with a pitch of 500 μm.

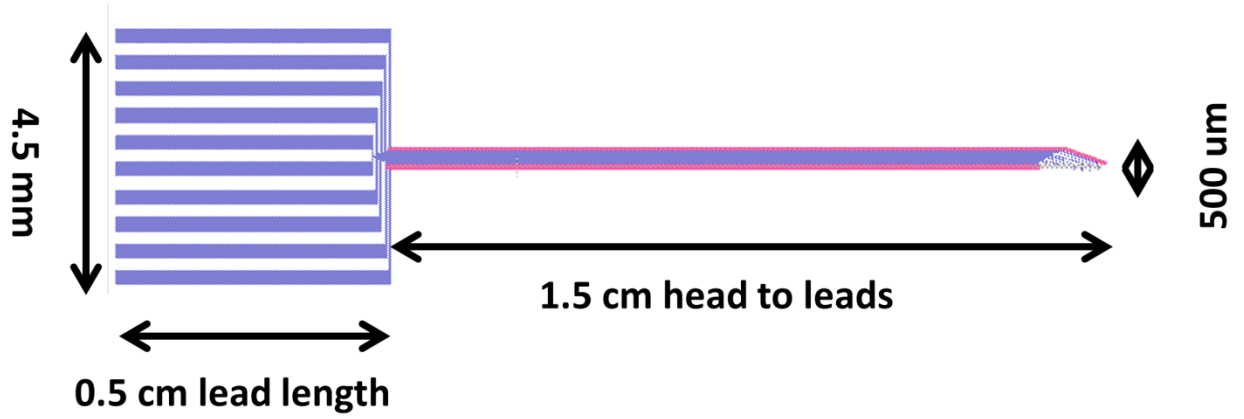

Figure 6-1. Schematic showing the 1x8 temperature sensing array fabricated in this work. The top of the sensor is kept narrow while the leads are spread out to facilitate wire bonding.

Figure 6-2 shows a close up view of the top of the sensor array. Although the array shown in this figure consists of vertically integrated thin films of VO_x, lateral configurations were also investigated in this work. Vertically integrated resistors had dimensions of 10 μm × 10 μm, while the lateral configuration had a W/L ratio of 10 μm/50μm, both with a film thickness of 85 nm. To avoid catastrophic failure of the vertically integrated sensors due to electrostatic discharge during handling, all leads were connected using a shunt. Once the array was ready for measurement, the shunt connection could be cut by using micromanipulators on a probe station.

To improve the sensitivity of the fabricated array, glass substrates (≈ 2 mm thick) were used due to their low thermal conductivity and therefore a lower ability to transport heat away from the sensors. The fabrication of the vertically integrated resistor array was done using a procedure described in section 5.3 and Figure 5-4, while the lateral configuration resistors were fabricated using the procedure detailed in Figure 3-18. The thin films of VO_x were deposited using the BTIBD system using a three target configuration. The deposition parameters can be found in Table 5. The obtained resistivity of the thin films was ≈ 12,000 Ω–cm.

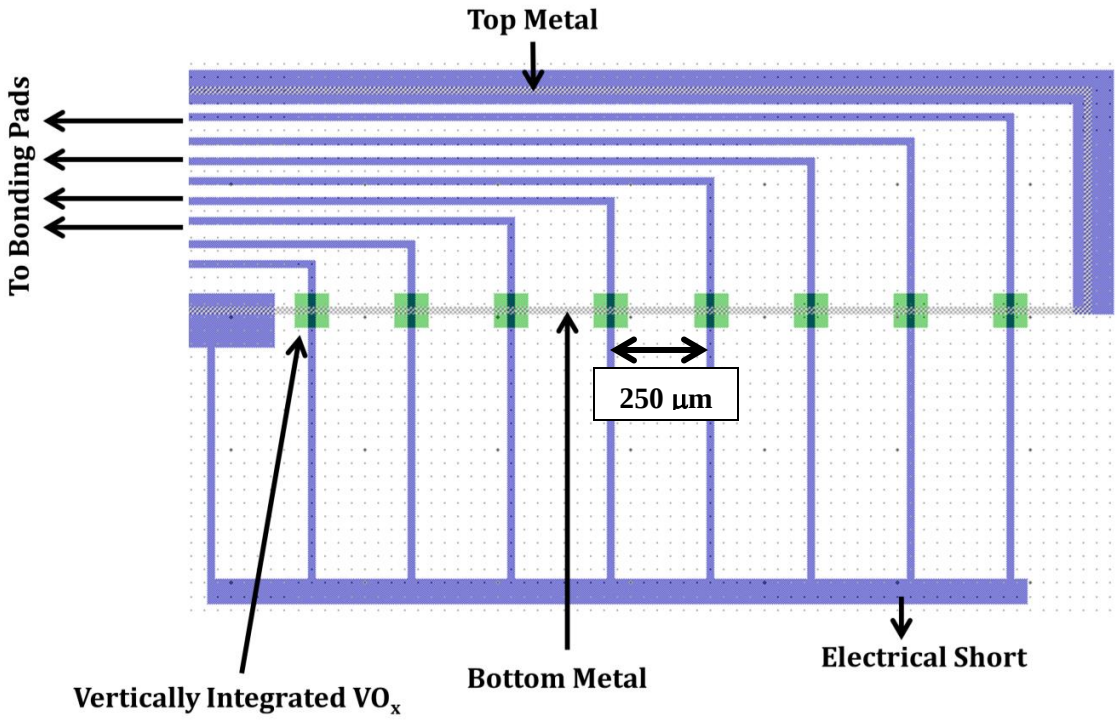

Figure 6-2. Schematic of the top of the 1×8 vertically integrated VO_x sensor array fabricated in this work. All through film sensors were electrically shorted during fabrication, dicing and wire bonding. Prior to measurement they were cut using a micromanipulator.

Table 5. Typical parameters used for the deposition of VO_x thin films for this chapter

Deposition Conditions	Value
Base Pressure	$< 1 \times 10^{-7}$ Torr
Targets	3, Vanadium (99.99% pure)
Total pressure	5.8×10^{-4} Torr
O_2 Partial pressure	3×10^{-6} Torr (4–5 sccm)
H_2O partial pressure	$< 2 \times 10^{-7}$ Torr
Voltage pulse	99 μsec/1 μsec (–800V/+5 V) = 100 μsec
Target current	285 mA
HC parameters	10 sccm Ar flow, 1.5 A, 20 V
Ion source parameters	60 sccm Ar flow, 7.5 A, 38 V
Pre-sputter time	10 minutes
Stage spin	20 rpm
Time	30 minutes (85 nm thick)

An equivalent circuit diagram of a second design consisting of a ZnO based transistor/switch is shown in Figure 6-3. The VO_x sensor/resistor is placed on the drain of the transistor. The current (and therefore impedance) is read between the drain and the source terminals when the transistor is turned on

and a bias is applied using a voltage source. Devices were fabricated using both the vertically integrated and the lateral resistance structures.

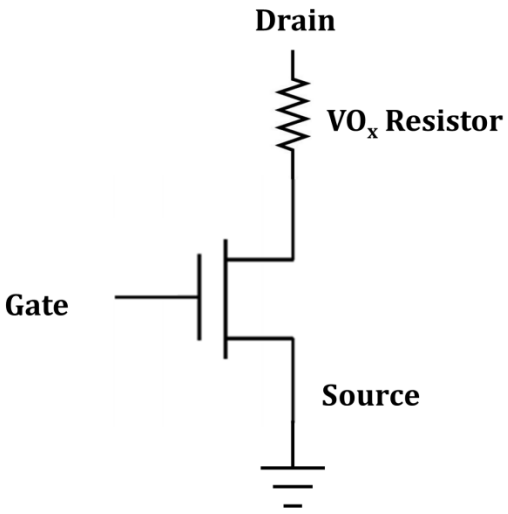

Figure 6-3. Equivalent circuit diagram showing VO_x resistors integrated with ZnO transistors as fabricated in this work.

To reduce the resistance of the lateral VOx structures, interdigitated electrodes were fabricated as can be seen in Figure 6-4. The resistor's W/L ratio was designed to be 160 μm/5 μm. For high TCR VO_x thin films (85 nm thick) having resistivity of ≈10,000 Ω–cm, this implied a resistance value of ≈ 35 MΩ for the lateral devices and ≈ 1.5 MΩ for the vertically integrated devices Figure 6-5. The W/L ratio of the transistor was chosen so that the TFT's contribution to the total impedance is minimal. This ratio is especially critical for the vertically integrated transistors where the resistance of the VO_x structure is of the order of 1 MΩ. For these TFTs, interdigitated source drain contacts were deposited having a W/L ratio of 470 μm/5 μm for TFT on resistance of ≈ 1,500 Ω.

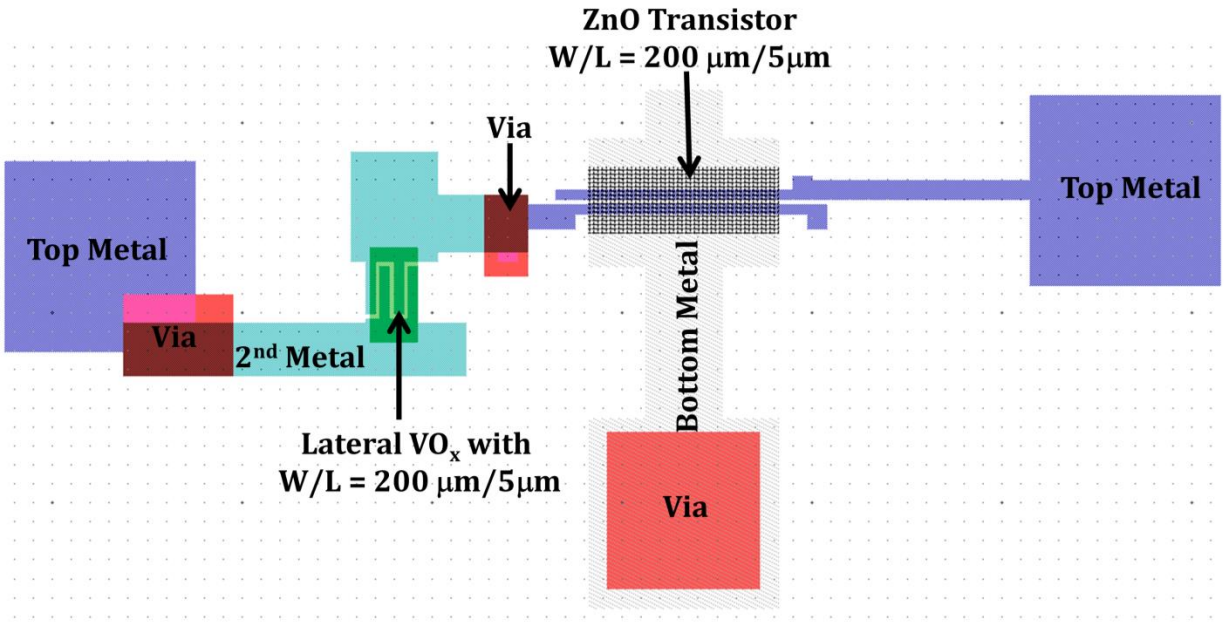

Figure 6-4. Schematic of lateral VO_x sensors integrated with ZnO based transistors. To allow for low impedance, the width to length ratio of 200μm/5μm was designed for both the VO_x resistors (100 MΩ) and the ZnO transistors (4,000 Ω).

Processing of these TFT integrated VO_x thin films was done using a 6 layer mask set as follows. Bottom gate metal (100 nm of Ti) was patterned by using sputter deposition and liftoff techniques. The thin film of VO_x was deposited using parameters shown in Table 5. Following this the VO_x thin films were patterned and etched using double layer lithography in a 1:2,000 solution of H_2O_2 and H_2O. A second layer of Ti metal was sputter deposited onto the VO_x thin films to serve as electrodes for the thin film.

The gate oxide and ZnO layers were deposited using plasma enhanced atomic layer deposition (PEALD) with help from Yiyang Gong from the department of Electrical Engineering. A 32 nm of Al_2O_3 was deposited from trimethylaluminum (TMA) and CO_2, and a 10 nm ZnO film was deposited from diethylzinc and N_2O, both at 200 °C. After the PEALD step the ZnO was patterned by wet etching in diluted HCl (1:4000), and vias were etched in the Al_2O_3 down to the bottom metal and the second metal contacts, by wet etching in hot (80 °C) phosphoric acid. Finally the source drain contacts were sputter deposited and patterned by liftoff.

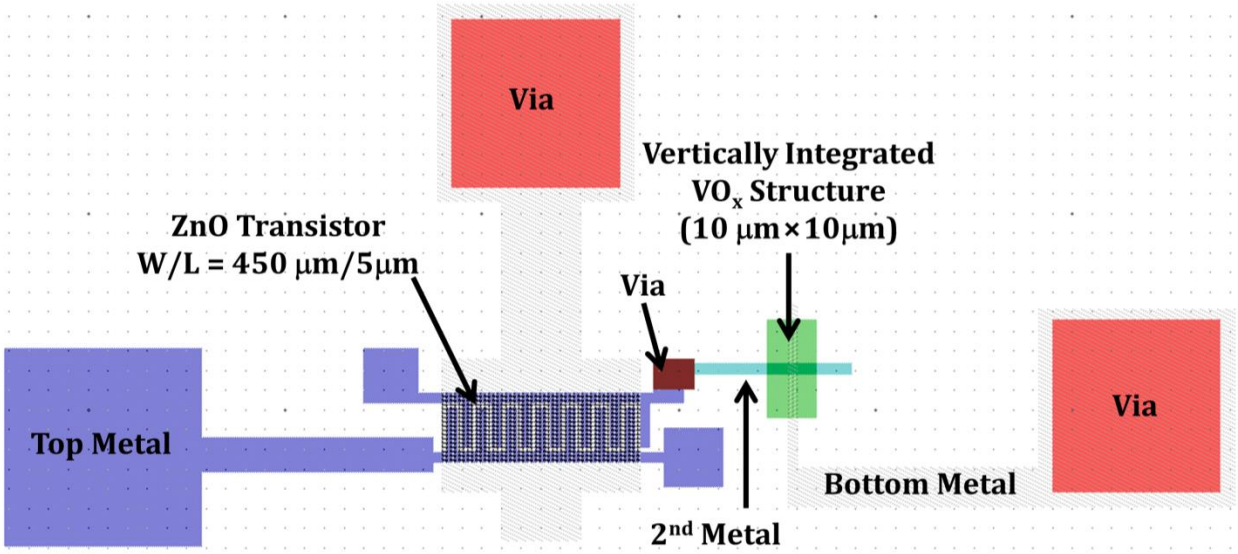

Figure 6-5. Schematic of vertically integrated VO_x sensors with ZnO based transistors. The through film resistors had dimensions of 10 μm × 10μm × 100 nm (1.3 MΩ), while the ZnO transistors were fabricated with a width to length ratio of 450 μm/ 5μm (1,500 Ω).

Figure 6-5 shows the schematic of vertically integrated VO_x resistors. For these structures, the bottom metal used as the gate metal for the ZnO TFT, was used as the bottom electrode for VO_x thin films.

6.2.2. One Dimensional Testing Setup

One dimensional arrays were fabricated using both lateral and through film configurations using high TCR VO_x thin films. Figure 6-6 shows the equivalent circuit diagram of the design used for the fabrication of the array. Resistors R_1 through R_8 are resistors of VO_x thin films which could be fabricated using either lateral or vertically integrated configurations. Switches S_1 through S_8 are relays of the Keithley 7075 general purpose multiplex card which can be used to select the resistor to be interrogated. Each switch of the Keithley 7075 general purpose multiplex card is connected to an HP 414B DC source/monitor unit (SMU) which sources voltage and measures current through each resistor. Since 4 SMUs are available on an HP 4141B, up to four resistors could be read simultaneously to achieve a higher array refresh rate. The 1-D array was measured by bonding the array to a PC Board using anisotropic conductive film (ACF) bonding. Leads from the board were connected to individual relays of

the Keithley 7075 multiplex card. Figure 6-7 shows an array bonded to a PC Board and the setup used for measurement of the 1-D array.

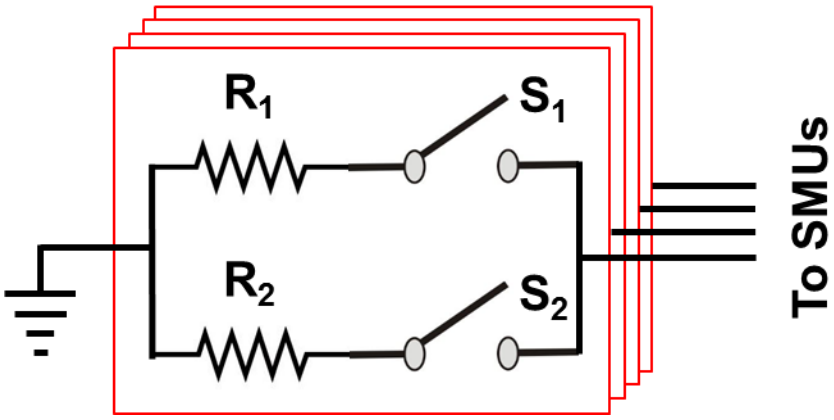

Figure 6-6. Equivalent circuit diagram of the 1x8 array fabricated in this work. The resistors can be lateral or vertically integrated, a Keithley 7075 general purpose multiplex card is used as the switch matrix while an HP4141B DC SMU is used for measuring the output current.

For temperature stabilization, the entire array was placed on a VWR heater block which had a temperature stability of ± 0.1 °C and a surface temperature variability of ± 0.1 °C. The entire setup was insulated from the environment using a foam construction as seen in Figure 6-7.

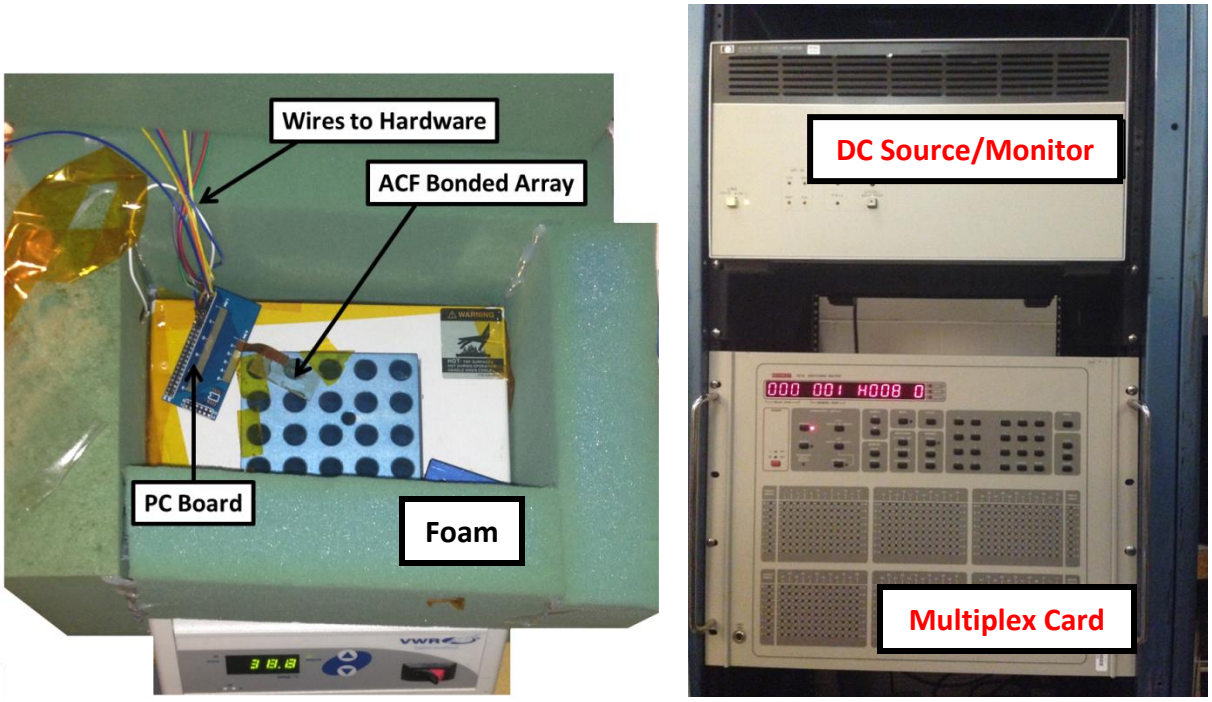

Figure 6-7. Test setup for the measurement of the 1-D arrays. ACF bonded samples on a VWR heater block (left) and the sensor biasing hardware including the HP4141B DC SMU and the Keithley 707A mainframe consisting of the Keithley 7075 general purpose multiplex card (right).

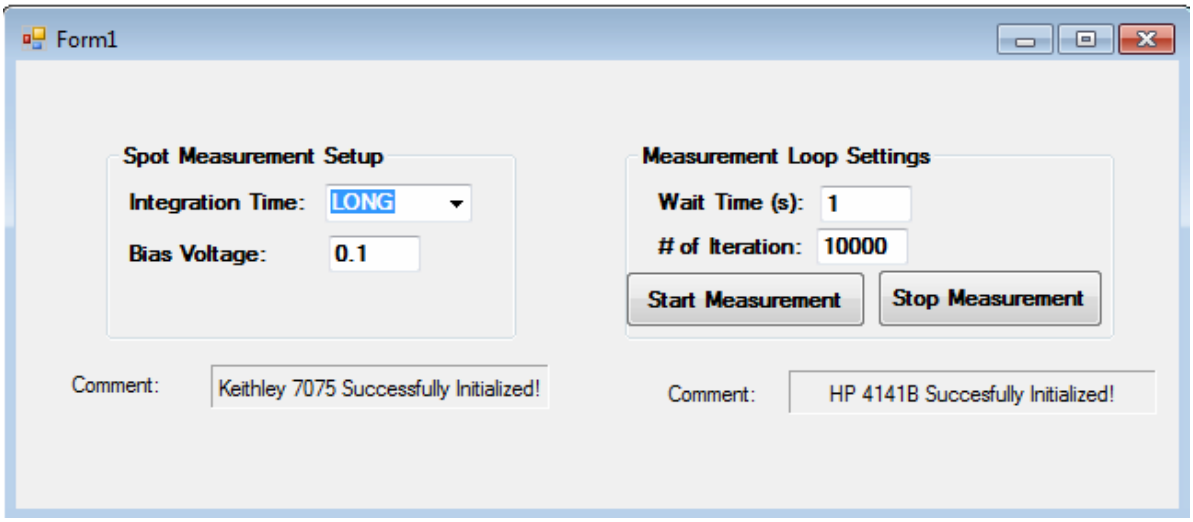

Figure 6-8. Screenshot of the C++ based program written to readout the 1D array by remote operation of the HP4141B DC SMU and the Keithley 7075 general purpose multiplex card. The program sets parameters for the array voltage bias, current measurement, the number of spot measurements to be performed and the wait time between each measurement.

The testing of the array was performed using a C++ program (screenshot in Figure 6-8) which provided computerized control and automation of the measurement. Appropriate bias, the integration time

for the HP 4141B DC SMU as well as the number of iterations the array needed to be measured can be remotely selected. The program triggered a spot measurement of the HP4141B after the selected bias was applied. Since two sensors are needed to be measured by one SMU, each device was left unbiased while the other device was being measured. Using a long integration time, the array had a refresh time of 3.5 seconds.

6.3. Results and Discussion

The 1-D array consisting of lateral VO_x resistors was biased using a voltage of 1 V. The output current for all the 1×8 sensors was recorded over a 24 hour time period at a temperature of 35 °C. The current of one of the sensors is shown in Figure 6-9. The output current has an RMS noise of ≈ 160 mK and is found to drift by ≈ 0.25 °C over the 24 hour time period. In addition, the output current shows periodic oscillations with a frequency of 4×10^{-4} Hz.

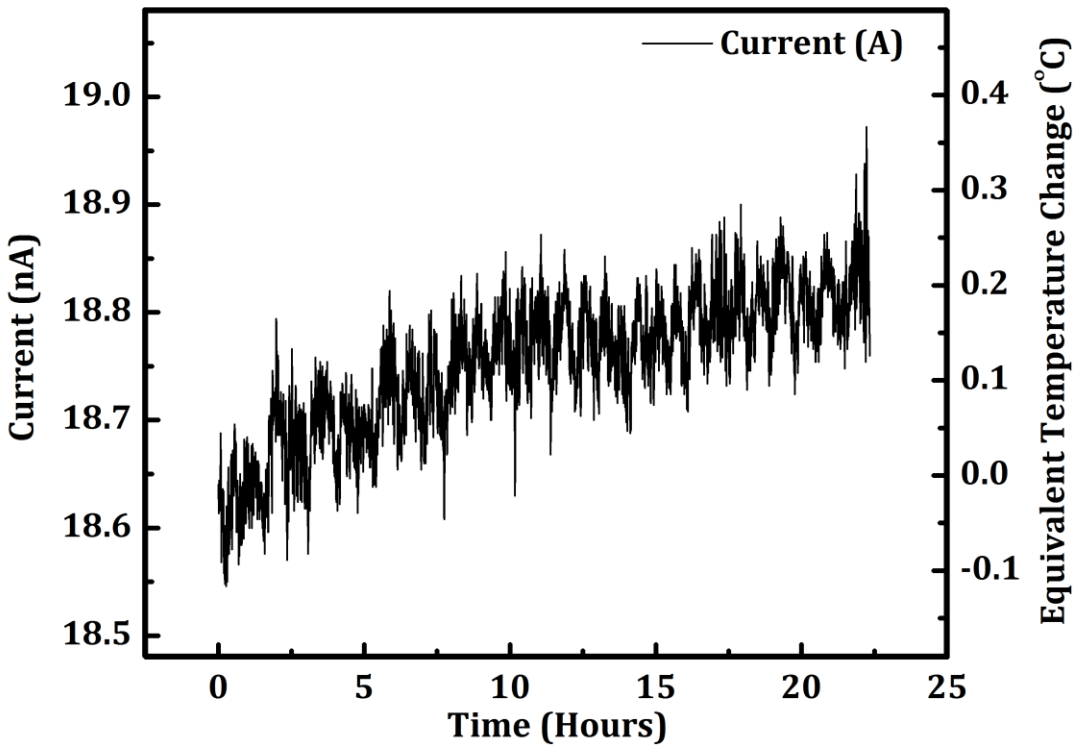

Figure 6-9. Current output for a lateral VO_x sensor with a resistance of ≈ 50 MΩ at 35 °C measured over 24 hours. The periodicity arises from the attempts of the heater block to stabilize to a set point of 35 °C. The measured RMS noise was found to be 160 mK.

Figure 6-10 shows the output current from all 8 sensors of the lateral 1×8 sensor array. It can be seen that all sensors have similar values of resistance (≈ 1 %). All sensors have similar drift in the long term performance of 0.2 °C. The low frequency oscillations observed appears at the same time for all senors. This implies that the observed periodic fluctuation in the output current at a frequency of 4×10^{-4} Hz is due to oscillations in the temperature of the heater block.

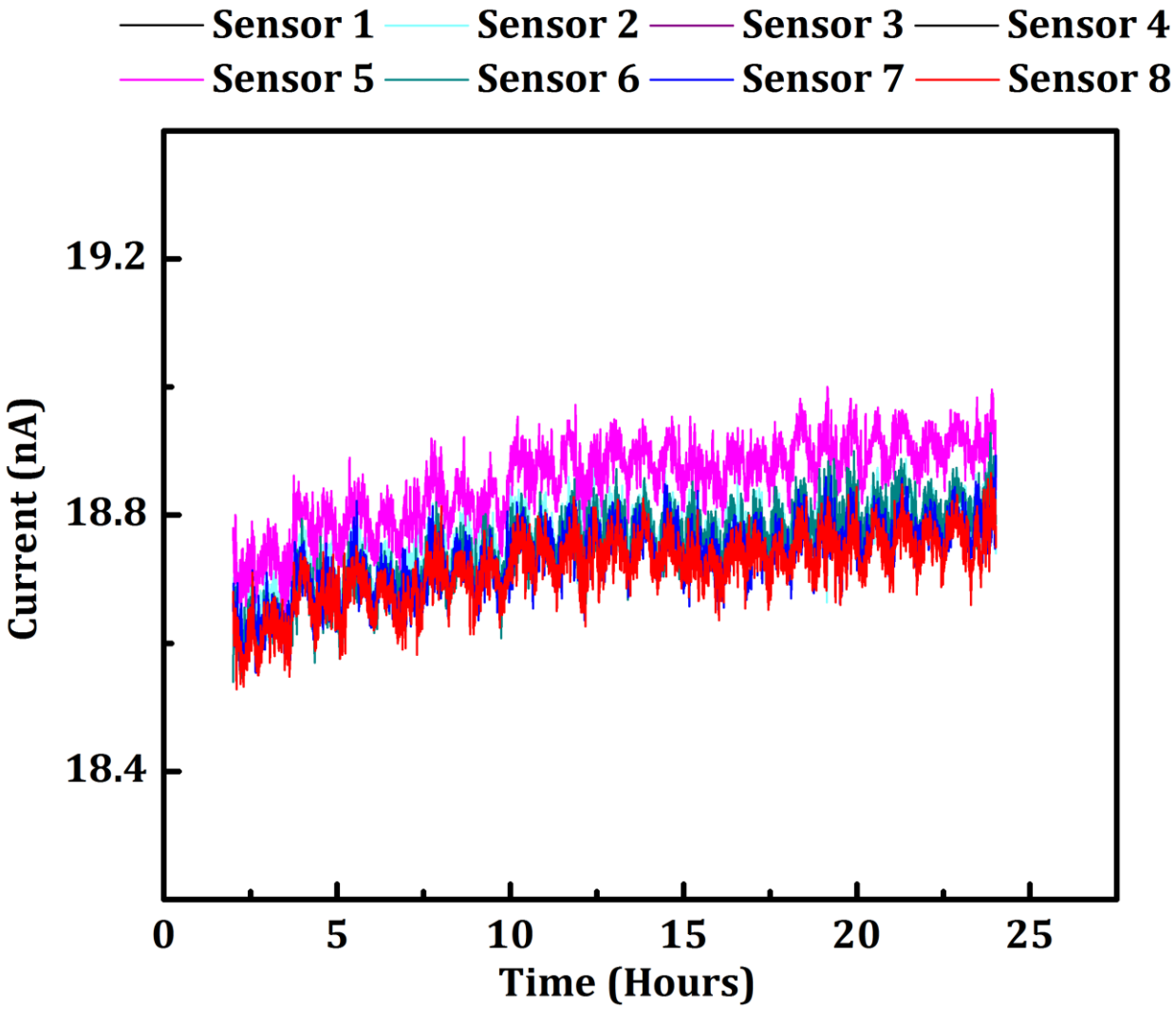

Figure 6-10. Current output of the 8 VO_x temperature sensor array measured at 35 °C on a VWR heater block at bias voltage of 1 V for 24 hours.

The RMS noise observed in all 8 sensors is ≈ 160 mK. Table 6 gives the parameters used as well as the calculated and observed signal to noise ratio (SNR) of thin film sensors using lateral resistance structures. The experimentally observed noise is ≈ 40 times higher than the theoretical calculations

estimated using Equation 30. The higher noise can be attributed to the cables used in the setup and leakage through the Keithley switch matrix card. When open circuit measurements were performed with the setup, current leakage of ± 40 pA was observed.

Table 6. Assumed parameters for SNR calculation

Parameter	Lateral	Vertically Integrated
Resistance	50 MΩ	1.5 MΩ
V_{bias}	1 V	0.1 V
N. Hooge's parameter (α_H/n)	10^{-18} cm^3	10^{-18} cm^3
f_2	714 Hz (1.4 ms measurement)	714 Hz (1.4 ms measurement)
f_1	1 Hz	1 Hz
Samples averaged (based on integration time)	256	256
TCR	−4.4 %/K	−4.4 %/K
T	308 K	308 K
Volume	10 μm × 50 μm × 85 nm	10 μm × 10μm × 85 nm
Calculated SNR from Equation 30	**10,000**	**7,200**
Observed SNR	**≈ 280**	**≈1,500**

Figure 6-11 shows the current response of a vertically integrated sensor from a 1×8 temperature sensing array. These devices were biased with 0.1 V with other relevant measurement parameters as shown in Table 1. The observed SNR ratio was 1,500 compared with 280 for the lateral resistance structures as calculated from Equation 30. The recorded RMS noise for these sensors was ≈ 35 mK compared with 160 mK for the lateral devices. The periodic fluctuation in the temperature of the heater block can be seen much clearly for these vertically integrated sensors.

Figure 6-12 shows a plot of log resistance versus temperature for a lateral device. The TCR from the measurement was found to be −4.4 %/K which was similar to that of vertically integrated thin films.

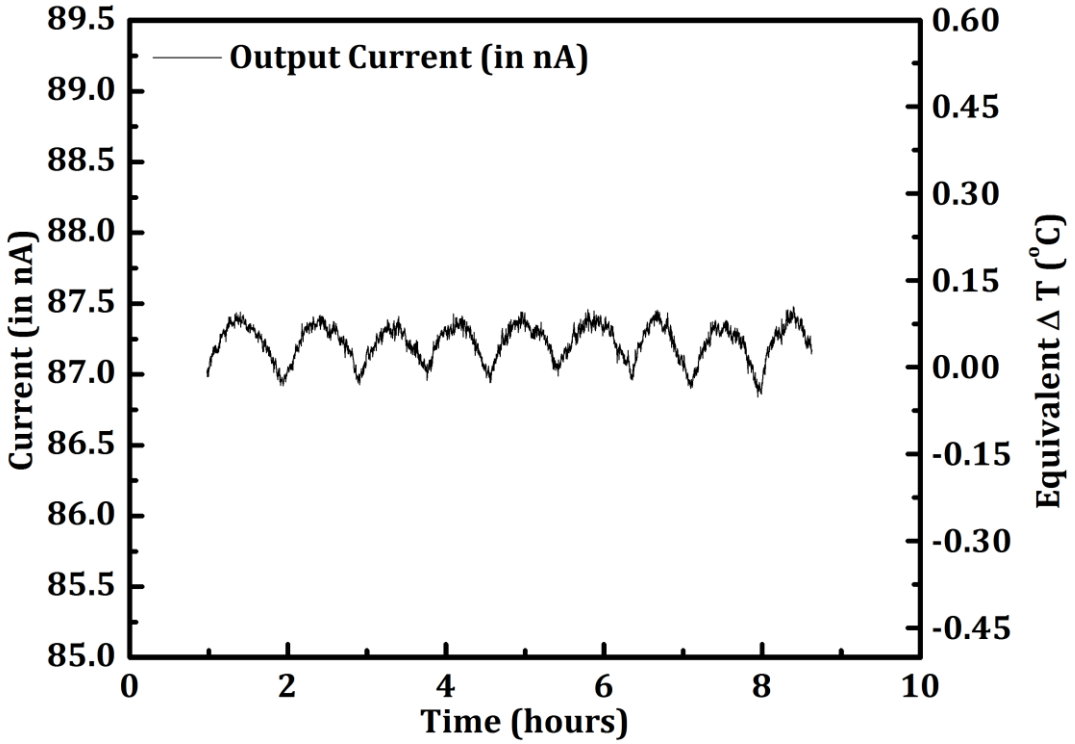

Figure 6-11. Output current of vertically integrated VO_x sensors 10 μm × 10 μm × 85 nm having a resistance of 1.3 MΩ at a temperature of 35 °C. The resistor was biased with a voltage of 100 mV. The measured RMS noise was found to be ≈ 35 mK.

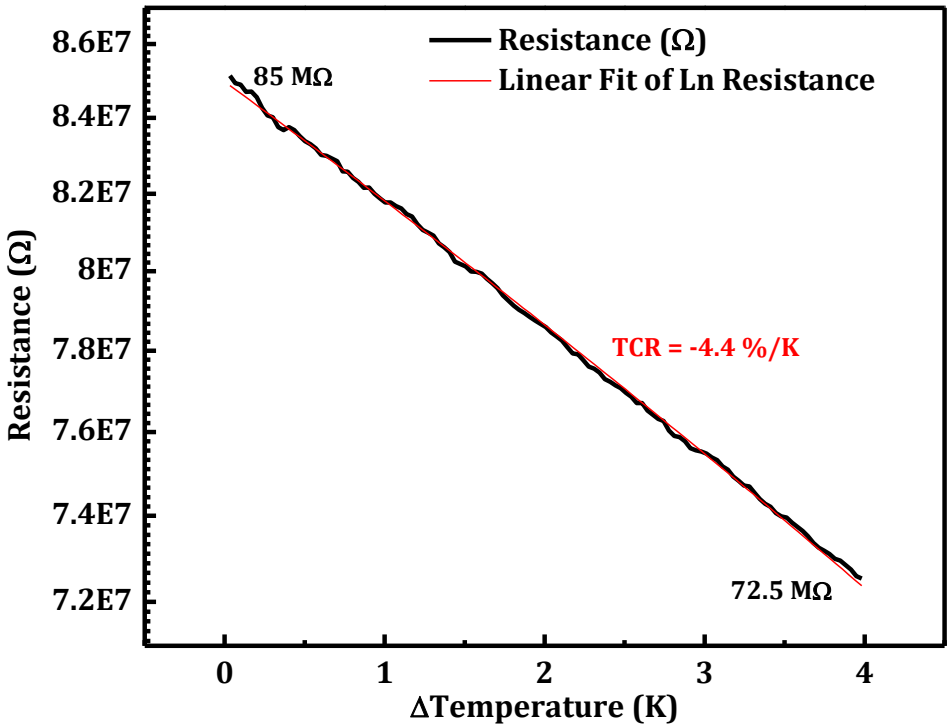

Figure 6-12. A plot of natural log of resistance as a function of temperature for lateral thin film resistors of VO_x having dimensions of 10 μm × 50 μm × 85 nm. The TCR extracted using activation energy was found to be –4.4 %/K.

Although there is a significant decrease in the electrical noise for the vertically integrated devices in comparison with the lateral devices (from 160 mK to 35 mK), the noise is significantly higher than the theoretical calculation of electrical noise of 8 mK. One such reason for the disparity in the electrical noise could be elevated levels of electrical noise due to the ribbon cables used in the test setup. Figure 6-13 shows the measured current noise of the measurement system over duration of 8 hours with the VO_x sensors disconnected. This open circuit measurement gives the lower limit of the current signal current which can be measured and hence sets a lower limit on the achievable sensitivity. This current noise was found to be of the order of 40 pA.

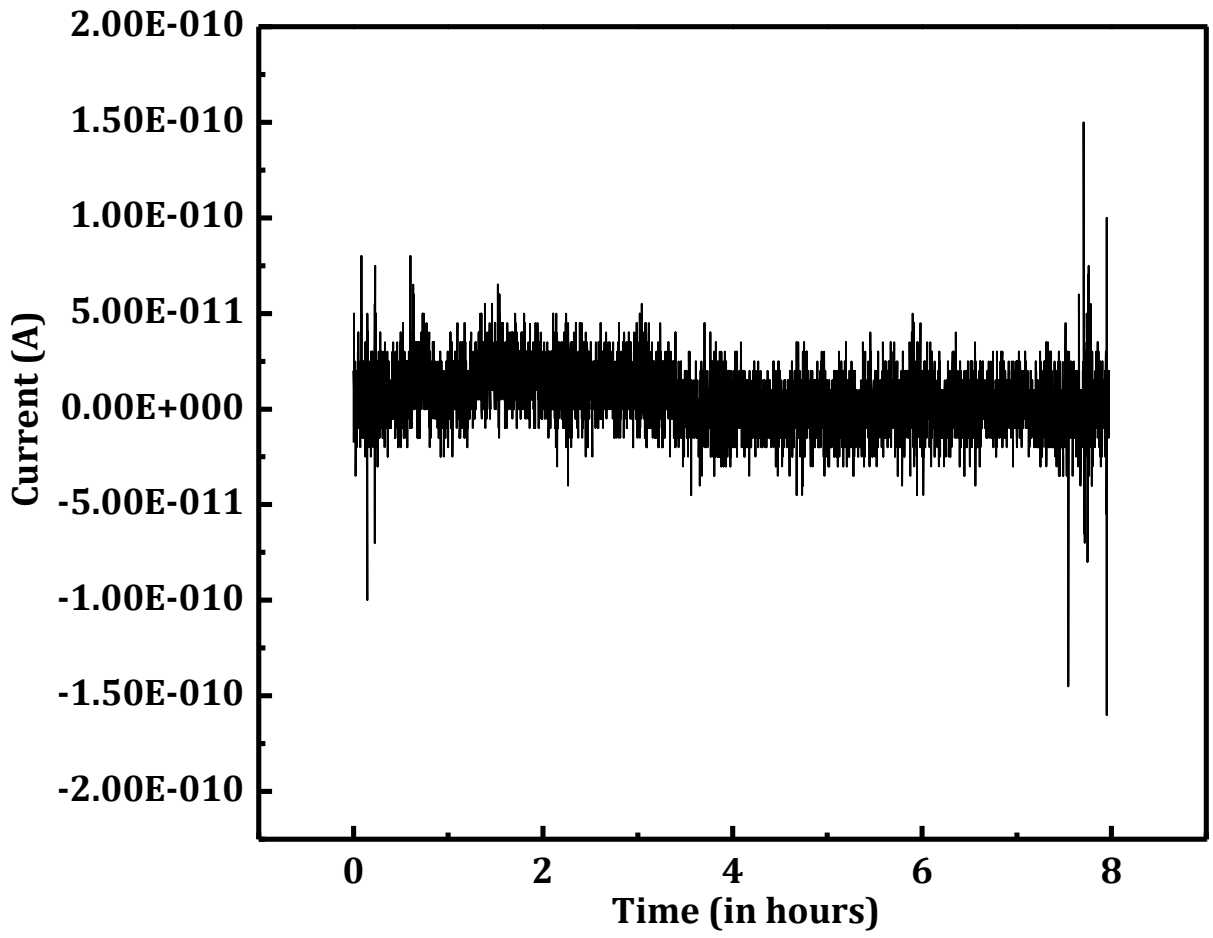

Figure 6-13. A plot of leakage current through the ribbon cables used during measurement.

In order to measure the sensitivity of the sensor, a lower noise test setup was used. The sensors were measured without the use of the ribbon cables on a probe station using the HP 4141B DC SMU. Figure 6-14 shows the electrical output of the temperature sensors measured on the probe station without the ribbon cables. These sensors have sensitivity of 12 mK, a significant improvement from 35 mK measured using ribbon cables.

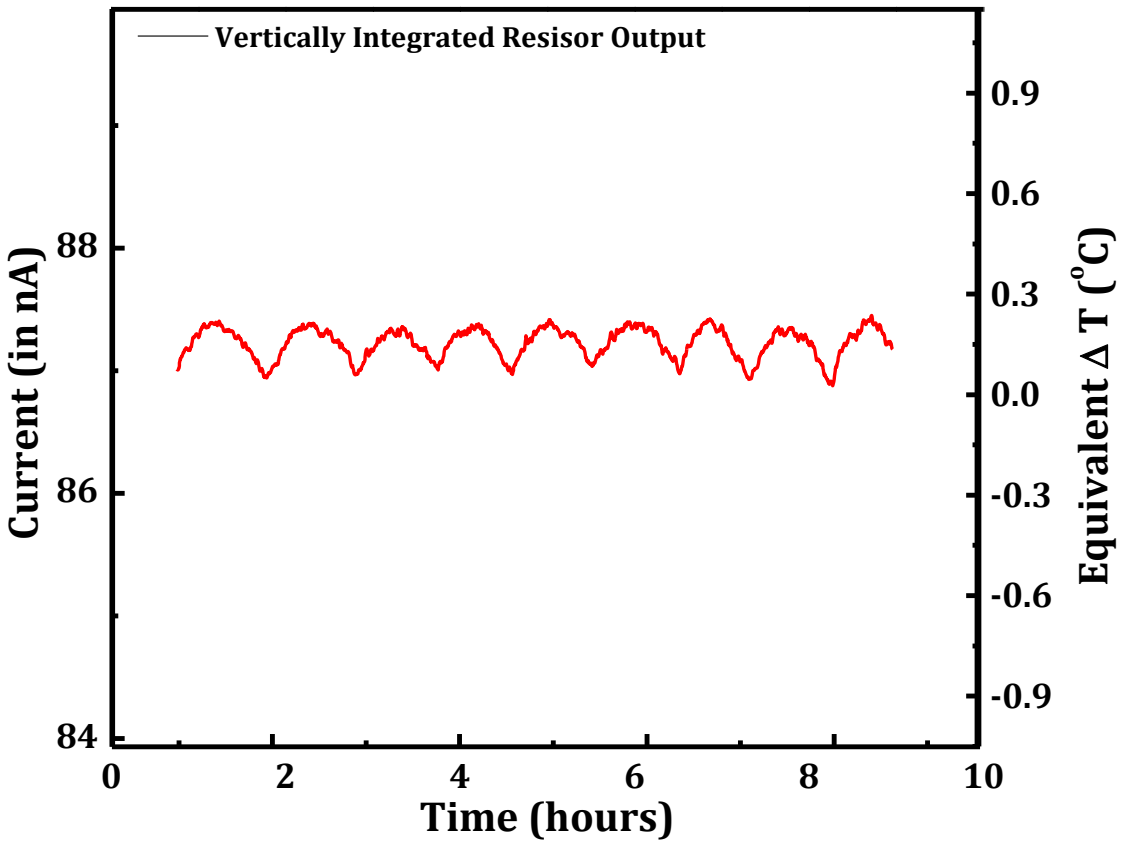

Figure 6-14. Output current of vertically integrated VO_x sensors 10 μm × 10 μm × 85 nm having a resistance of 1.3 MΩ at a temperature of 35 °C measured without a switch matrix using the HP4141B DC SMU. The resistor was biased with a voltage of 100 mV. The measured RMS noise was found to be ≈ 12 mK.

To evaluate the performance of the TFT integrated temperature sensors, the TFT performance was characterized to extract the threshold voltage (V_T), the resistance of the TFT when turned on (R_{on}) and its mobility. Figure 6-15 (black curve) shows a plot of the Log (I_D) versus gate voltage (V_G) for a transistor with a width to length ratio (W/L) of 400 μm/15μm. The extracted differential mobility (red

curve) was found to be ≈ 10 cm^2/V–s at a V_{DS} of 1 V at a V_{GS} of 12 V. R_{on} of ≈ 4,000 Ω was achieved for this W/L.

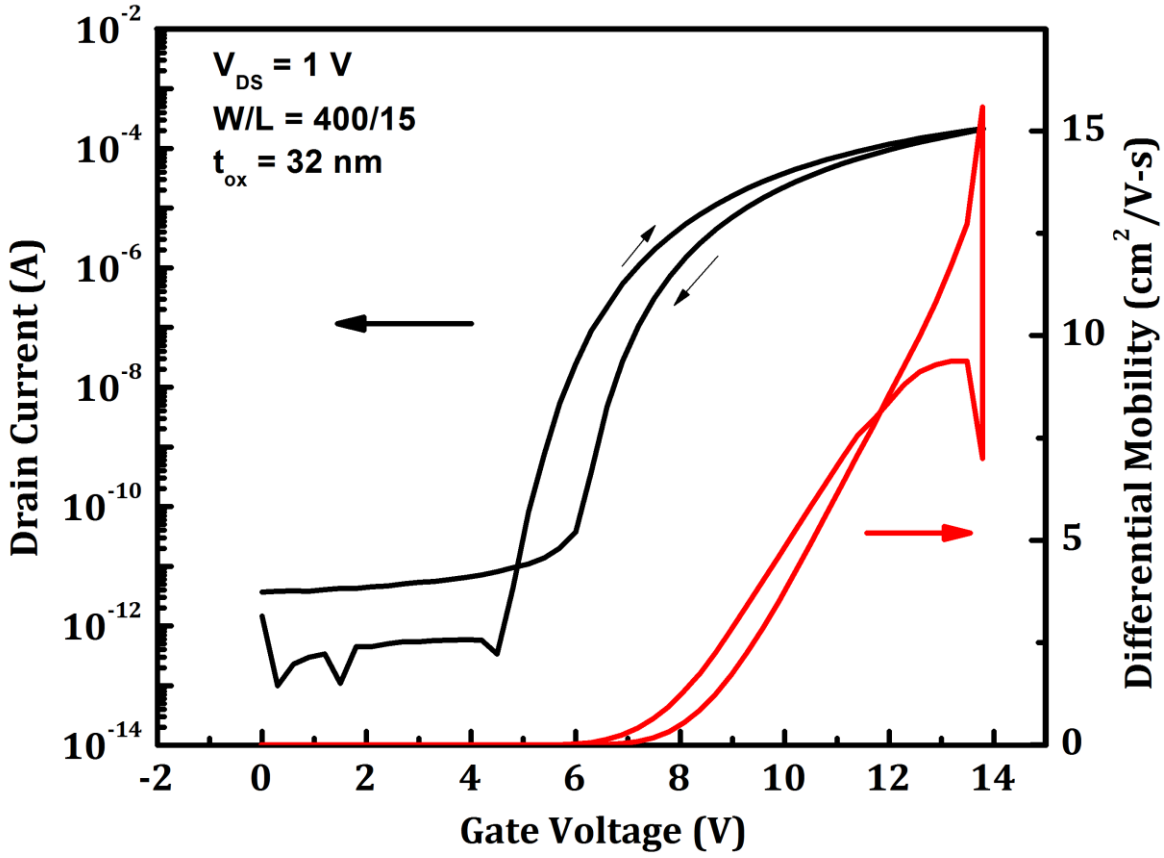

Figure 6-15. Linear region log (I_D) versus V_{GS} of a ZnO based TFT with a linear region differential mobility of 10 cm^2/V–s for a V_{DS} of 1 V. The TFT dimensions are W/L = 400 μm/15 μm and t_{ox} = 32 nm. The R_{on} for this W/L ratio was ≈ 4,000 Ω for a V_{GS} of 10 V.

Figure 6-16 shows the I_D versus V_G for a ZnO TFT (W/L = 400 μm/5μm) integrated with vertical VO_x resistors (≈1.5 MΩ) for a V_{DS} of 75 mV. The expected R_{on} for these TFTs I is ≈ 1,500 Ω. It can be seen that the transistor is off at –1 V and is on at 4 V.

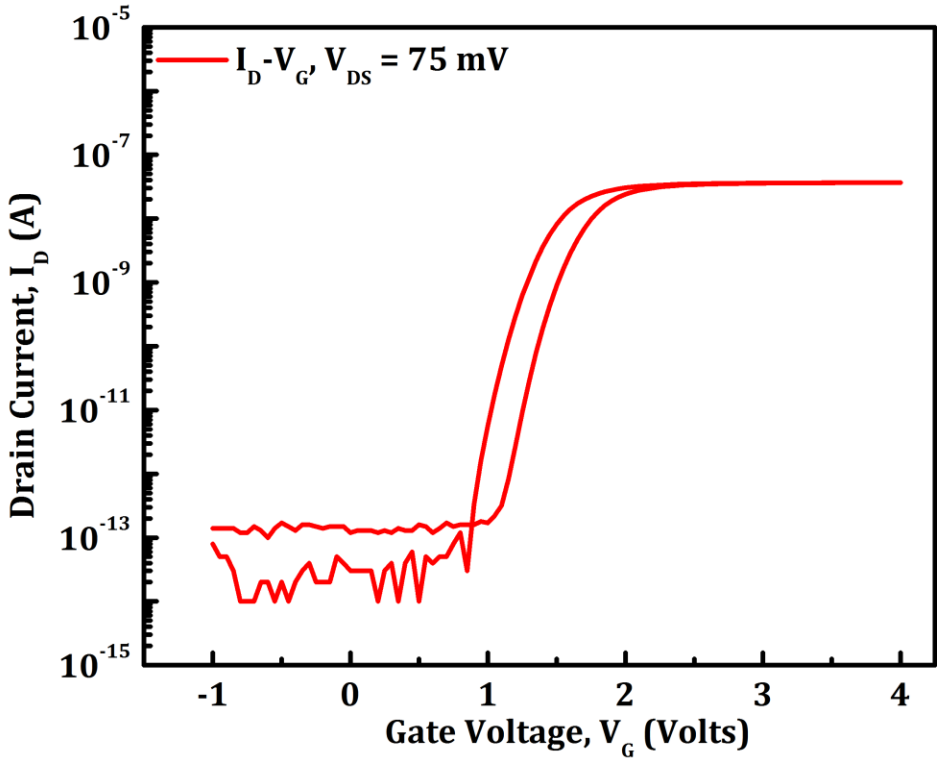

Figure 6-16. Log (I_D) versus V_G for a ZnO based TFT with a vertically integrated with vertically integrated VO_x resistor (1.6 MΩ at room temperature) on the transistor drain for a V_{DS} of 75 mV (W/L = 450 μm/5 μm, t_{ox} = 32 nm).

Figure 6-17 shows the drain current of the TFT integrated with vertical VO_x thin films structures. As the gate voltage is increased from a V_G of −1 V to +5 V, the resistor is swept from a bias of −0.1 V to 0.1 V (V_{DS}) and the current is recorded. When the transistor is off, the impedance of the integrated sensor is 10^{11} Ω, when the transistor is turned on the resistance is 1.3 MΩ (~ the resistance of the VO_x resistor) for V_{GS} higher than 4 V.

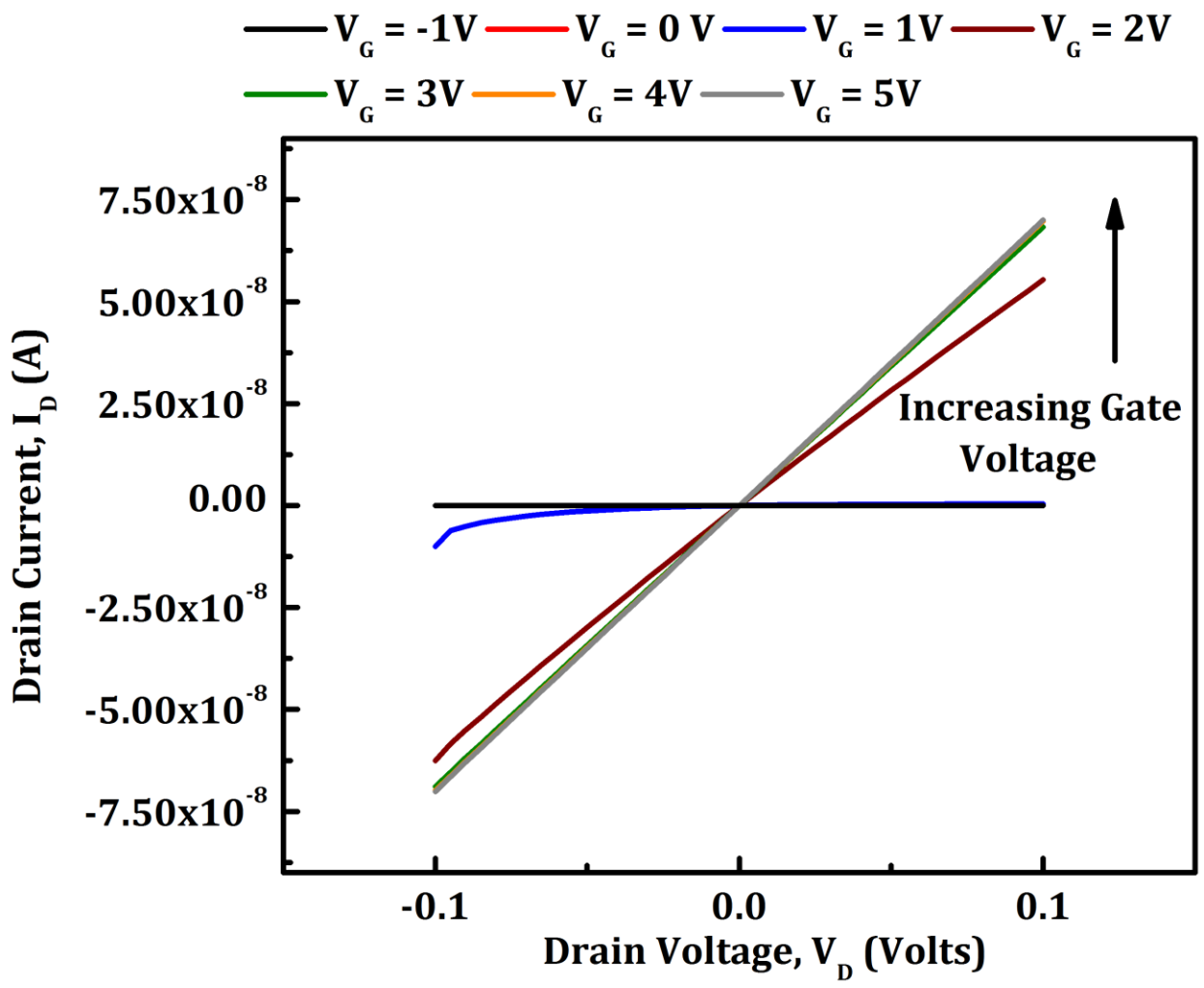

Figure 6-17. I_D versus V_{DS} of a ZnO based TFT with a vertically integrated with vertically integrated VO_x resistor (1.6 MΩ at room temperature) on the transistor drain as a function of V_{GS} from -1 V to 5 V (W/L = 450 μm/5 μm, t_{ox} = 32 nm). I_D–V_D at V_{GS} of 4 V and 5 V are similar indicating a small impedance contribution from the ZnO TFT.

Figure 6-18 shows the I_D-V_D curve of a vertically integrated VO_x sensor incorporated with a ZnO TFT as a function of temperature. The drain voltage is swept from –0.1 V to +0.1 V and the resultant current is recorded. During this measurement, the V_{GS} of the TFT is held at +4 V so that the transistor is turned on. After each measurement the temperature was increased and the I_D–V_D sweep was collected at this new elevated temperature. The resistance of this vertical device along with the TFT was plotted at various temperatures in a Ln (resistance) versus temperature plot and can be seen in Figure 6-19. The extracted TCR from the activation energy was found to be –4.4 %/K.

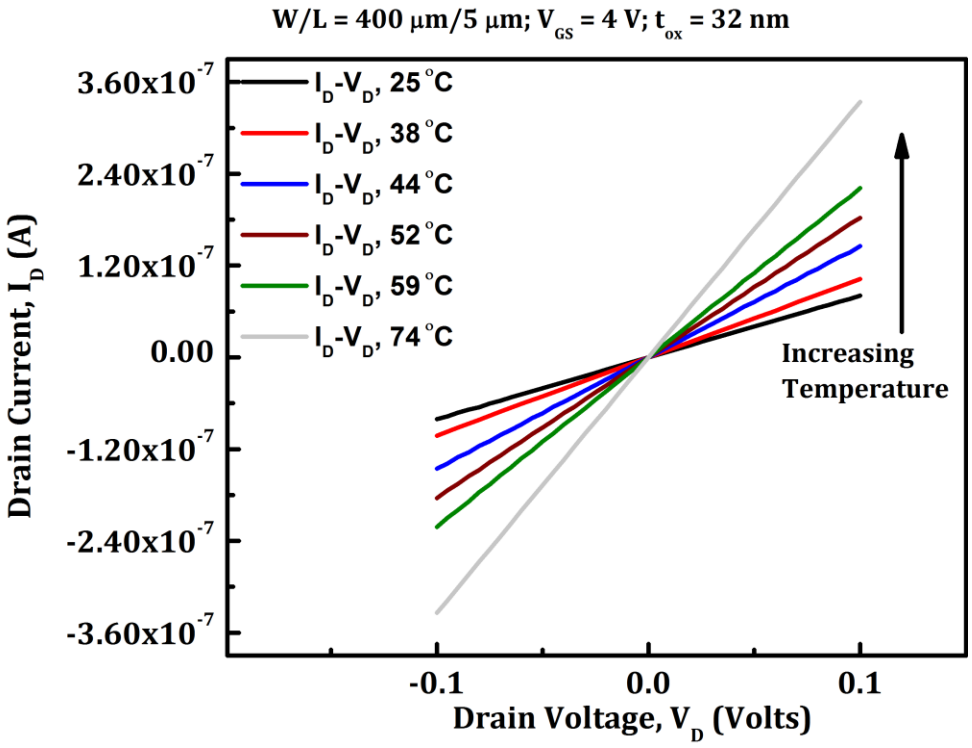

Figure 6-18. I_D versus V_{DS} of a ZnO based TFT with a vertically integrated VO_x resistor (1.6 MΩ at room temperature) on the TFT drain as a function of temperature for a V_{GS} of 5 V (W/L = 450 μm/5 μm, t_{ox} = 32 nm). Increasing temperature of the device leads to lower resistance of the VO_x thin film at higher temperatures which is evident from the increasing slopes of the I_D–V_D characteristics.

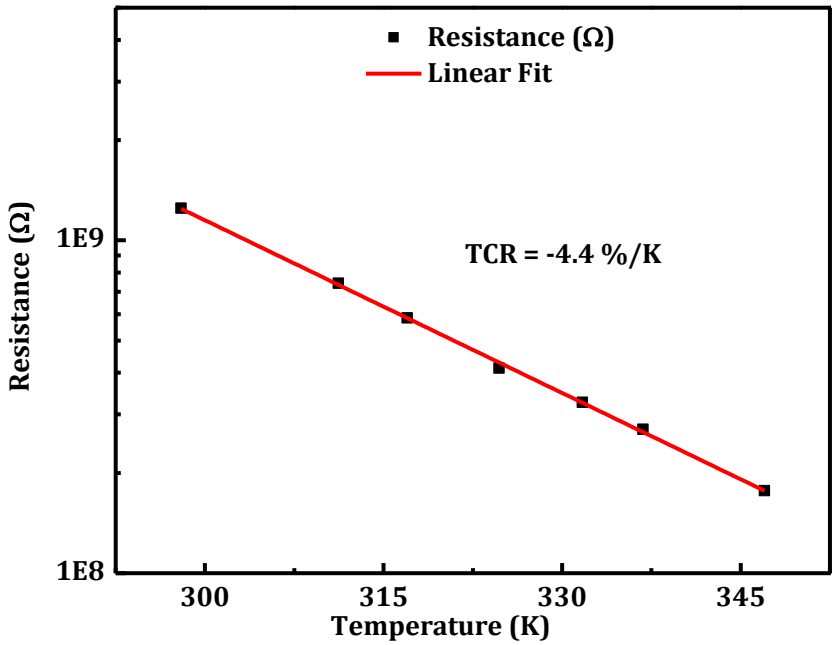

Figure 6-19. Ln (Resistance) versus temperature of vertically integrated VO_x thin film resistors (1.6 MΩ at room temperature) integrated with ZnO TFT at a V_{GS} of 5 V (W/L = 450 μm/5 μm, t_{ox} = 32 nm). The TCR extracted from the activation energy was found to be –4.4 %/K.

6.4. Conclusion

1 × 8 temperature sensing arrays are fabricated using lateral and vertically integrated thin films of high TCR VO_x thin films. Custom hardware and software was built using a DC SMU and a switch matrix to perform the measurements. Thin film TCR of −4.4 %K was maintained in both lateral and vertically integrated structures. The hardware setup allowed for the arrays to have a refresh time of 3.5 seconds. While the arrays using lateral resistance structures have an RMS noise of 160 mK, due to limitations imposed by the hardware setup. The vertically integrated resistors have higher sensitivity due to increased magnitude of the signal. The RMS noise of the vertically integrated structures was found to be 35 mK .

Both the lateral and vertically integrated resistance structures were incorporated along with a ZnO based TFT for device level multiplexing of the sensor arrays. The bias and therefore the current from the resistor could be turned on or off depending on the gate voltage applied to the transistor. Temperature dependent measurements confirmed that the TCR of the thin film material was maintained in these TFT integrated resistance temperature sensors.

Chapter 7. Summary and Future Work

7.1. Summary

High TCR Thin films of VO_x and Ge:H

Resistance based microbolometers are based on two distinct types of materials: materials with |TCR| of 2–2.5 %/K, resistivity between 0.1–1 Ω–cm and those with |TCR| between 3–4 %/K with resistivity between 200–2,000 Ω–cm. This work investigates thin films of Ge:H and VO_x having |TCR| > 4 %/K.

For thin films of undoped Ge:H deposited by PECVD, it was found that significant improvement in the resistivity, TCR and electrical noise could be achieved for a thickness of ≈ 100 nm by increasing the dilution ratio of [GeH_4] in [H_2] to extremely large values (R = 400). Thin films having TCR of ≈6.5 %/K were repeatedly deposited having a resistivity of 2,250 Ω–cm and a normalized Hooge's parameter of $\approx 10^{-20}$ cm^{-3}. In combination with prior work it is concluded that the thickness of thin film showing superior TCR-noise-resistivity tradeoffs could be achieved by could be changed by changing the dilution ratio used during deposition. The combination of electrical properties for thin films of Ge:H deposited in this work are the best in comparison with other materials reported in the literature to date.

Electrical noise in thin films of VO_x with x > 2 and |TCR| > 3%/K was largely uninvestigated prior to this work. Thin films having high TCR (|TCR| of 4–5 %/K) were deposited by Biased Target Ion Beam Deposition. These thin films had very high resistivities (between 10,000 to 20,000 Ω–cm), much higher than those of Ge:H. Their normalized Hooge's parameter values were around 10^{-18} to 10^{-20} cm^3.

Vertically Integrated High TCR Thin Films

The use of large TCR values in microbolometer applications has been limited by large values of normalized Hooge's parameter and the enormous resistivities (10,000 Ω–cm) associated with these materials. High resistivity leads to high pixel resistance in a lateral resistor configuration. In this work, an alternate pixel structure using vertically integrated high TCR films was demonstrated and its electrical performance was characterized.

This configuration resulted in much lower pixel resistance than the lateral configuration with no change in the signal to noise ratio. In addition, TCR and the normalized Hooge's parameter of the vertically integrated configuration were found to be similar to resistors fabricated in the lateral configuration. The reduced pixel resistance allows for sustaining higher bias currents without an increase in Joule heating and therefore operation in a constant bias mode. In addition, the constant SNR and larger signal current might allow for reduced current integration times and therefore higher imaging frame rates.

Temperature Sensor Arrays

Combination of large TCR materials and low impedance devices developed in this work positions the thermistor based contact based temperature sensor at a distinct advantage over existing micro fabricated temperature sensors. 1-D temperature sensing arrays using thin films having large values of TCR lateral and vertically integrated configurations were fabricated on to glass substrates. 1×8 sensor array using the lateral configuration was demonstrated have an RMS noise value of 160 mK, while vertically integrated resistors showed a much lower RMS noise of 35 mK. To allow for measurement of 2-D arrays, sensors were integrated with ZnO based transistors to turn the current through the resistor on or off depending on the gate voltage applied to the bias with no degradation in the sensor performance.

7.2. Future Work

This dissertation investigated several areas of temperature sensing materials and devices. As a result many questions arose which may be answered by future work. One main area of future work would

be to publish the results on the high TCR materials, the through film structure, the noise measurement system and results, and the temperature sensing array.

High TCR thin films of VO_x:

Thin films of VO_x deposited by BTIBD were grown having high resistivity (>10,000 Ω–cm) and moderate values of Hooge's parameter (10^{-20} to 10^{-18} cm^3). These electrical properties are too large for thin films of high TCR VO_x to be incorporated in existing pulse bias, lateral resistor, read out circuits. There appears to be a large gap in terms of resistivity (from 1 Ω–cm to 10,000 Ω–cm), and Hooge's parameter (from 10^{-24} to 10^{-20} cm^3) where thin films of VO_x have not been successfully deposited. It is worth attempting to deposit films in this region to see if the electrical properties of these films are superior films of SiGe:H which are currently used in the constant bias bolometer market.

VO_x thin films with |TCR| > 2.5 %/K and reasonably low resistivity (< 0.1 Ω–cm) have been deposited by reactive pulsed DC magnetron sputtering of a vanadium target with oxygen [37]. Basantani et al. showed that when thin films of VO_x were deposited using pulsed DC magnetron sputtering, an increase in the oxygen content during sputtering led to an increase in the thin film |TCR|. The |TCR| increased from 1.2 %/K at 4 % of O_2/Ar mixture to 2.1 %/K at 11 % O_2/Ar at a substrate bias of –250 V and a sputtering pressure of 2.5 mTorr [44]. In that work, a further increase in the oxygen content led to an abrupt increase in the TCR and resistivity of the thin films. At an O_2/Ar ratio of 12 %, the resistivity increased to 10 Ω–cm and the TCR was 3 %/K [44].

In that work, a further increase in the oxygen content was not investigated because thin films having large resistivity were not of interest for that work. However, high TCR and high resistivity thin films are of interest for the constant bias bolometers. Further investigation of the parameter space not covered in ref. [44] could be performed with the deposition of thin films with oxygen percentage in argon from 12 % to 20 %. Some other deposition parameters that were held constant: the total pressure was maintained at 5 mTorr, the substrate bias was kept at –250 V and the total gas flow was held at 18 sccm.

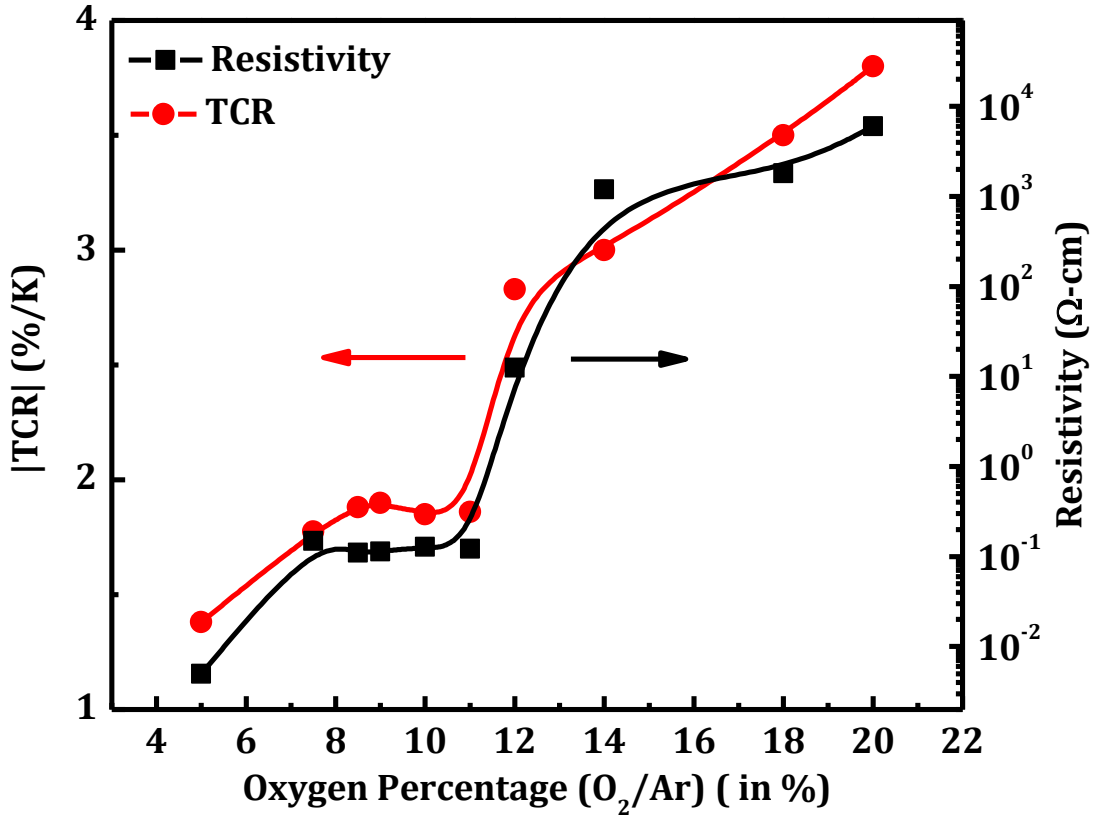

Figure 7-1. Resistivity and TCR of thin films of VO_x deposited by pulsed DC magnetron sputtering using a pure vanadium target with a substrate bias of -250 V. The graph is a compilation of thin films deposited in previous work [44], and films deposited in this work.

Figure 7-1 shows that a further increase in the percentage of oxygen used during deposition led to an increase in the resistivity and the magnitude of TCR for the deposited thin films of VO_x. For the thin film deposited with an oxygen content of 20 %, the resistivity was found to be ≈ 6,000 Ω–cm and the |TCR| was found to be ≈ 3.8 %/K. The resistivity and TCR of these thin films are similar to the thin films of VO_x deposited using BTIBD.

Future work for thin films deposited using pulsed DC magnetron sputtering of VO_x thin films should involve investigation of thin films having even higher TCR values. An increase in the oxygen percentage during deposition beyond the 20 % investigated in this work may result in thin films with even

higher TCR values. In addition, the normalized Hooge's parameter must be investigated for thin films of VO_x deposited using pulsed DC magnetron sputtering.

Hydrogenated Germanium Thin Films:

Thin films of Ge:H were deposited with superior electrical properties of TCR (> 6 %/K), resistivity (2,250 $\Omega-$cm), and normalized Hooge's parameter (10^{-20} cm^3). In combination with prior work it is concluded that the thickness of thin films showing superior TCR-noise-resistivity tradeoffs can be adjusted by changing the dilution ratio used during deposition. Through years of investigation, F. N. Hooge concluded that 1/f noise of thin films is strongly inversely proportional to the number of carriers available for transport [29]. Therefore, similar to the work done for SiGe:H systems, it is worth investigating if the material properties can be improved by doping of the thin films to increase the available carriers for transport. In the case of SiGe:H thin films, Ajmera et al. and Saint John et al. have demonstrated a decrease in the normalized Hooge's parameter 'α_H/n' with little change in the TCR of the thin films [18] [19].

Vertically Integrated Thin Films of VO_x:

Vertically integrated thin films of VO_x were demonstrated as an alternate to lateral resistor configurations. A few key questions arose as a result of this work:

1. It was observed that there exists a barrier layer at the interface of the sensing material for both VO_x and Ge:H based devices. Further investigation must be done to identify this barrier layer which may involve the use of a noble metal.
2. Pin hole defect density for large area out of plane devices is a concern which must be addressed to prove manufacturability of vertically integrated bolometer structures.
3. The performance of the vertically integrated sensor has been evaluated by measuring the electrical response as a function of change in temperature. However, the spot temperature

measurements may require additional information on heat transfer between the substrate, the active thin film material as well as the top and bottom electrodes. This information can be obtained by means of Finite Element Analysis (FEA).

4. The true test of this architecture would be to evaluate a pixel incorporated into a free-standing MEMs structure including a full evaluation of the optical and thermal properties of the device.

Temperature Sensor Array:

One dimensional temperature sensing arrays were demonstrated in this work by means of a Keithley 707A general purpose multiplex card. The ability to switch each sensor ON/OFF was also demonstrated by means of integrated ZnO TFTs.

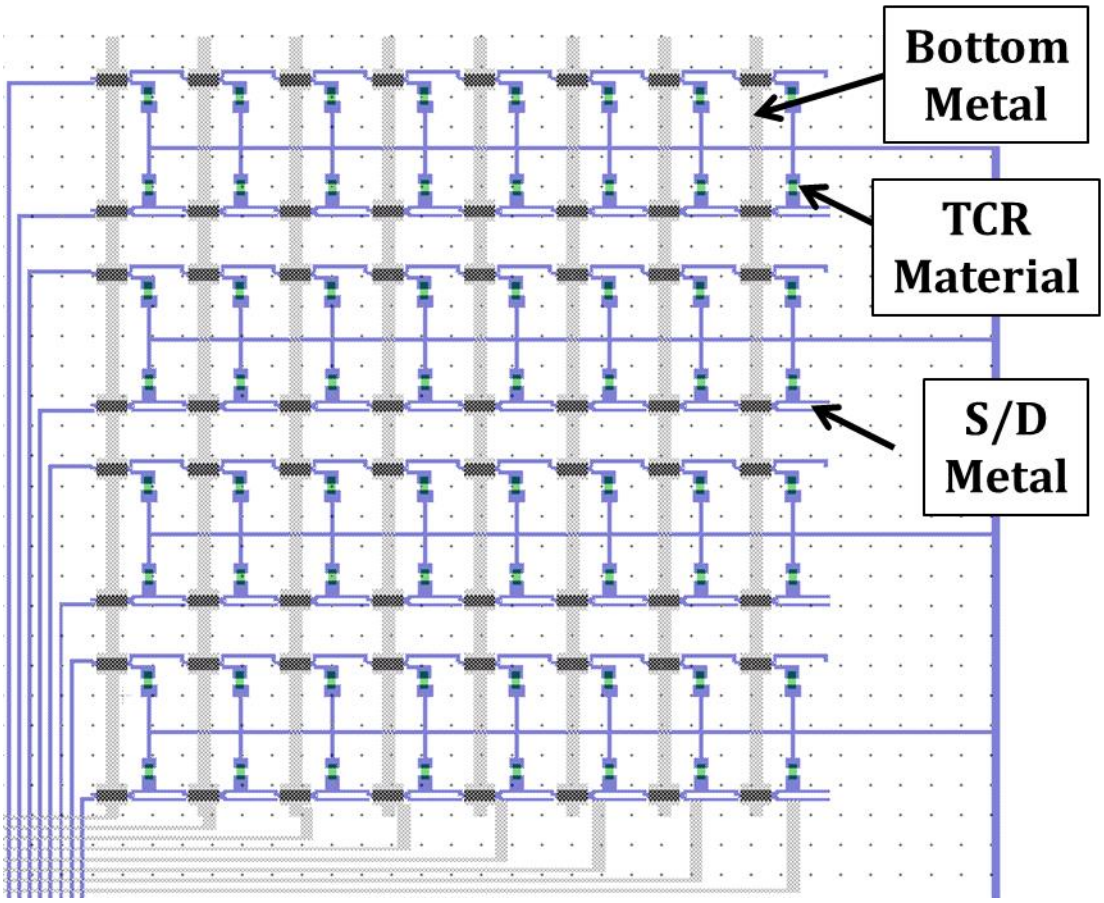

Figure 7-2. A schematic showing the layout of an 8 × 8 temperature sensor array with integrated TFTs for two dimensional temperature sensing applications.

Future work for the one-dimensional sensor array would be to fabricate them on a flexible, biocompatible substrate for insertion into the body, particularly the brain. This would require temporary attachment of the device on a stiff but small cross-sectional area probe that would allow insertion, dissolution of the adhesive and removal of the probe.

Future work for the temperature sensor array includes measurement of two dimensional temperature sensor arrays with integrated TFTs. Figure 7-2 shows a layout of two dimensional temperature sensor arrays with integrated TFTs for in pixel switching. Hardware test setup must be developed for appropriate biasing of these temperature sensor arrays.

Bibliography

[1] L. Michalski, K. Eckersdorf, J. Kucharski and J. McGhee, Temperature Measurement, Chicester: John Wiley and Sons, Ltd., 2001.

[2] E. C. Guyer, Handbook of Applied Thermal Design, Taylor and Francis, 1999.

[3] P. W. Kruse and D. Skatrud, Uncooled Infrared Imaging Array and Systems, Academic Press, 1997.

[4] Amphenol Advanced Sensors, "NTC Interchangeable Type 95 Series," 2014.

[5] Omega, "Introduction to Thermistors," Omega, 2014. [Online]. Available: http://www.omega.com/prodinfo/thermistor.html.

[6] I. Kim, H. Fok, Y. Li, T. N. Jackson and B. J. Gluckman, "Polymer substrate temperature sensor array for brain interfaces," *Engineering in Medicine and Biological Society, Annual International Conference of the IEEE,* pp. 3286-3289, 2011.

[7] B. E. Cole, "Microstructure design for higher IR sensitivity". Patent US Patent No. 5,286,976, 1994.

[8] R. Wood, "Use of vanadium oxide in microbolometer sensors". Patent US5450053 A, 29 June 1993.

[9] FLIR, *FLIR Technical Note.*

[10] C. P. Cain and A. J. Welch, "Thin-film temperature sensors for biological measurements," *IEEE transactions on Biomedical Engineering,* Vols. BME-21, no. 5, pp. 421-423, 1974.

[11] D. C. Murphy, S. E. Persson, M. A. Pahre, A. Sivaramakrishnan and S. G. Djorgovski, "An infrared camera for the Palomar Observatory 60-inch telescope," *Publications Astronomical Soc. of the Pacific,* vol. 107, p. 1234–1242, 1995.

[12] P. W. Kruse, "Thermal Detectors," in *Handbook of Optics*, McGraw-Hill, Inc., 1995, pp. 19.1-19.14.

[13] C. Hanson and H. Beratan, "Uncooled Pyroelectric Thermal Imaging," in *Proceedings of the Ninth IEEE International Symposium on Applications of Ferroelectrics*, University Park, PA, 1991.

[14] C. Ye, T. Tamagawa, R. Schiller and D. L. Polla, "Pyroelectric PbTiO3 Thin Film for Microsensor Applications," *Sensors and Actuators A,* vol. 35, pp. 770-83, 1992.

[15] FLIR INC., "Uncooled detectors for thermal imaging cameras," [Online]. Available: http://www.flir.com/uploadedFiles/Eurasia/Cores_and_Components/Technical_Notes/uncooled%20detectors%20BST.pdf.

[16] E. Hayes and M. Rau, "More than meets the eye: the electromagnetic spectrum," *Science in School,* no. 20, 2011.

[17] P. W. Kruse, Uncooled thermal imaging-arrays, systems and applications, Bellingham: SPIE PRess, 2002.

[18] S. Ajmera, J. Brady, C. Hanson, T. Schimert, A. J. Syllaios and M. Taylor, "Performance improvement in amorphous silicon based uncooled microbolometers through pixel design and materials development.," in *Proc. SPIE 8012, Infrared Technology and Applications XXXVII, 80121L*, 2011.

[19] D. B. Saint John, *Optical and Electrical Characterization of High Resistivity Semiconductors for Constant-Bias Microbolometer Devices,* PhD Thesis. The Pennsylvania State University, 2012.

[20] C. Venkatasubramanian, *Preparation, characterization and post deposition modification of pulsed-DC magnetron sputtered vanadium oxide thin films for microbolometer applications,* PhD Thesis. The Pennsylvania State University, 2010.

[21] B. D. Gauntt, *The nano-composite nature of vanadium oxide thin films for use in infrared microbolometers,* PhD Thesis. The Pennsylvania State University, 2011.

[22] N. Fieldhouse, S. M. Pursel, R. Carey, M. W. Horn and S. Bharadwaja, "Vanadium oxide thin films for bolometric applications deposited by reactive pulsed DC sputtering," *J. Vac. Sci. Technol. A,* vol. 27, p. 951, 2009.

[23] B. D. Gauntt, J. Li, O. M. Cabarcos, H. A. Basantani, C. Venkatasubramanium, Bharadwaja, N. J. Podraza, T. N. Jackson, D. L. Allara, S. Antrazi, M. W. Horn and E. C. Dickey, "Microstructure of Vanadium Oxide Used in Microbolometers," *SPIE Proceedings 8012,* 2011.

[24] S. Baliga, M. Rost and A. Doctor, "Sputtered film thermistor IR detectors," in *SPIE Proc. 2225*, 1994.

[25] W. Zhou, C. Ouyang, J. Wu, Y. Gao and Z. Huang, "Structural, Morphological and infrared detection properties of Mn-Co-Ni-O spinel oxide films," in *Eighth International Conference on Thin Film Physics and Applications, Proc. of SPIE Vol. 9068*, 2013.

[26] D. Zhao, Plasma-enhanced Atomic Layer Deposition Zinc Oxide Flexible Thin Film Electronics, The Pennsylvania State University.

[27] S. W. Ko, J. Li, N. J. Podraza, E. C. Dickey and S. Trolier-McKinstry, "Spin Spray-Deposited Nickel Manganite Thermistor Films For Microbolometer Applications," *Journal of the American Ceramic Society,* vol. 94, no. 2, pp. 516-523, 2010.

[28] F. N. Hooge and L. J. Vandamme, "Lattice Scattering Causes 1/ƒ Noise," *Physics Letters A,* vol. 66, no. 4, pp. 315-316, 1978.

[29] F. N. Hooge, "1/f Noise Sources," *IEEE Transactions of Electron Devices,* vol. 41, no. 11, p. 1926, 1994.

[30] R. A. Wood, "Monolithic Silicon Microbolometer Arrays," in *Uncooled Infrared Imgaging Arrays and Systems*, vol. 47, P. W. Kruse and D. D. Skatrud, Eds., San Diego, CA, Academic Press, 1997, pp. 45-119.

[31] P. E. Howard, C. J. Han, J. E. Clarke, J. C. Stevens, P. Ely and E. T. Fitzgibbons, "Advances in Microbolometer Focal Plane Technology at Boeing," in *SPIE Conference on Infrared Detectors and Focal Plane Arrays V*, Orlando Florida, 1998.

[32] D. Murphy, M. Ray, R. Wyles, J. Asbrock, N. Lum, J. Wyles, A. C. Hewitt, Kennedy, D. V. Lue, J. Anderson, D. Bradley, R. Chin and T. Kostrzewa, "High sensitivity 25 µm microbolometer FPAs," in *Proceedings of SPIE. 4721*, 2002.

[33] W. A. Radford, D. F. Murphy, M. Ray, S. H. Propst, A. Kennedy, J. K. Kojiro, J. T. Woolaway, K. L. Soch, R. Coda, G. Lung, E. A. Moody, D. Gleichman and S. T. Baur, "320x240 silicon microbolometer uncooled IR FPAs with on-chip offset correction," in *Proc. SPIE 2746, Infrared Detectors and Focal Plane Arrays IV*, Orlando, FL, 1996.

[34] K. G. West, J. Lu, J. Yu, D. Kirkwood, W. Chen, Y. Pei, J. Claassen and S. A. Wolf, "Growth and characterization of vanadium dioxide thin films prepared by," *Journal of Vacuum Science & Technology A,* vol. 26, no. 1, pp. 133-139, 2008.

[35] Y.-H. Hana, I.-H. Choia, H.-K. Kang, J.-Y. Park, K.-T. Kim, H.-J. Shin and S. Moon, "Fabrication of vanadium oxide thin film with high-temperature coefficient of resistance using V2O5 / V / V2O5 multi-layers for uncooled microbolometers," *Thin Solid Films,* vol. 205, pp. 260-264, 2003.

[36] C. Batista, J. Mendes, V. Teixeira and J. Carneiro, "Reactive DC Magnetron Sputtering of Vanadium Oxide Thin Films," *Materials Science Forum,* Vols. 587-588, pp. 343-347, 2008.

[37] H. A. Basantani, S. Kozlowski, M.-Y. Lee, J. Li, E. C. Dickey, T. N. Jackson, S. S. N. Bharadwaja and M. W. Horn, "Enhanced Electrical and Noise Properties of nanocomposite Vanadium Oxide Thin Films by Reactive Puulsed-DC Magnetron Souttering," *Applied Physics Letters,* vol. 100, 2012.

[38] N. Fateh, G. A. Fontalvo and C. Mitterer, "Structural and mechanical properties of dc and pulsed dc reactive magnetron sputtered V2O5 films," *Journal of Physics D: Applied Physics,* vol. 40, p. 7716–7719, 2007.

[39] N. Fieldhouse, S. M. Pursel, R. Carey, M. W. Horn and S. S. N. Bharadwaja, "Vanadium Oxide Thin Films for Bolometric Applications Deposited by Reactive Pulsed DC Sputtering," *Journal of Vacuum Science & Technology A ,* vol. 27, p. 951, 2009.

[40] K. Wells, Properties of Pulsed DC Sputtered Vanadium Oxide Thin Films Using a V2O3 Target for Uncooled Microbolometers, The Pennsylvania State University, 2008.

[41] C. Venkatasubramanian, M. O. Cabarcos, R. W. Drawl, L. D. Allara, R. W. Drawl, S. Ashok, M. W. Horn and S. S. N. Bharadwaja, "Process-structure-property correlations in pulsed dc reactive magnetron sputtered vanadium oxide thin films," *Journal of Vacuum Science & Technology A,* vol. 29, no. 6, 2011.

[42] C. O. M. C. W. R. D. D. L. A. S. A. M. W. H. a. S. S. N. B. Venkatasubramanian, "Process-structure-property Correlations in Pulsed Dc Reactive Magnetron Sputtered Vanadium Oxide Thin Films," *Journal of Vacuum Science & Technology A: Vacuum, Surfaces, and Films ,* vol. 29, no. 6, p. 061504, 2011.

[43] B. D. Gauntt, O. M. C. J. Li, H. A. Basantani, C. Venkatasubramanian, S. S. N. Bharadwaja, N. J. Podraza, T. N. Jackson, D. L. Allara, S. Antrazi, M. W. Horn and E. C. Dickey, "Microstructure of vanadium oxide used in microbolometers," in *SPIE Proceedings: Infrared Technology and Applications 8012*, 2011, 2011.

[44] H. A. Basantani, Effect of RF Substrate Bias on Vanadium Oxide Thin Films During Reactive Pulsed DC Magnetron Sputter Deposition, The Pennsylvania State University, 2011.

[45] B. D. Gauntt, M. W. Horn and E. C. Dickey, "Stoichiometry and microstructural effects on electrical conduction in pulsed dc sputtered vanadium oxide thin films," *Journal of Material Research,* vol. 24, no. 4, 2009.

[46] H. Wang, X. Yi, S. Chen and S. He, "Reactive Ion Beams Sputtering of Vanadium Oxides Films for Uncooled Microbolometer," *International Journal of Infrared and Millimeter Waves,* vol. 26, no. 3, pp. 421-431, 2005.

[47] T. L. Hylton, B. Ciorneiu, D. A. Baldwin and O. Escorcia, "Thin Film processing by biased target ion beam deposition," *IEEE Transactions of Magnetics,* pp. 2966-2971, 2000.

[48] R. Street, Technology and Applications of Amorphous Silicon, New york, 2000.

[49] H. Klauk, S. L. Wright, L. F. Palmateer, S. E. Mohney and T. N. Jackson, "Hydrogenated Amorphous Silicon Germanium Black-matrix Material for Active-matrix Liquid-crystal Displays," *Jpournal of the Society for Information Display 5,* vol. 4, p. 393, 1997.

[50] J. -L. Tissot, F. Rotham, C. Vedel, M. Vilain and J.-J. Yon, "LETI/LIR's Amorphous Silicon Uncooled Microbolometer Development," in *Proc. SPIE 3379, Infrared Detectors and Focal Plane Arrays V*, 1998.

[51] D. B. Saint John, H.-B. Shin, M.-Y. Lee, E. C. Dickey, N. J. Podraza and T. N. Jackson, "Thin film silicon and germanium for uncooled microbolometer applications," in *Proc. SPIE 8012, Infrared Technology and Applications XXXVII, 80123U*, 2011.

[52] C. Godet, I. E. Zawawi, M. Théye, M. Gauthier and J. Stoquert, "Improvement of Plasma-deposited a-Ge : H Thin Films by Hydrogen Dilution of Germane," *Solid State Communications,* vol. 74, pp. 721-725, 1990.

[53] I. Chambouleyron, C. F. Graeff, A. R. Zanatta, F. Fajardo, M. Mulato, R. Campomanes, D. Comedi and F. C. Marques, "The Perspectives of Hydrogenated Amorphous Germanium as an Electronic Material," *Physica Status Solidi (b),* vol. 192, no. 2, pp. 241-251, 1995.

[54] W. Palz, G. T. Wrixon and P. Helm, in *Ninth E.C. Photovoltaic Solar Energy Conference: Proceedings of the International Conference*, Freiburg, Fed. Rep. of Germany, 1989.

[55] M. Stutzmann, J. Stuke and H. Dersch, "Electron Spin Resonance of Doped Glow-discharge Amorphous Germanium," *Physica Status Solidi (b),* vol. 115, no. 1, pp. 141-151, 1983.

[56] F. C. Marques and I. Chambouleyron, "Optoelectronic Properties of High Quality Hydrogenated Amorphous Germanium Thin Films," in *Proceedings of the Ninth E. C. Photovoltaic Solar Energy Conference*, Freiburg, Germany, 1989.

[57] M. Moreno, A. Torres, R. Ambrosio, P. Rosales, A. Heredia, A. Kosarev, E. Torres, C. Zuñiga, C. Reyes-Betanzo and M. Domínguez, "Deposition and characterization of polymorphous germanium films prepared by low frequency PECVD," *Journal of Non-Crystalline Solids,* vol. 358, no. 17, pp. 2099-2102, 2012.

[58] N. J. Podraza, D. B. S. John, J. Li, C. R. Wronski, E. C. Dickey and R. W. Collins, "Microstructural Evolution in Si(1-x)Gex:H Thin Films for Photovoltaic Applications," in *Proceedings of the 35th Photovoltaic Specialists Conference*, 2010.

[59] W. J. Parrish, J. T. W. II, G. T. Kincaid, J. L. Heath and J. D. Frank, "Low-cost 160 x 128 uncooled infrared sensor array," in *Proc. SPIE 3360, Infrared Readout Electronics IV, 111*, 1998.

[60] C. M. Hanson, S. K. Ajmera, J. Brady, T. Fagan, W. McCardel, D. Morgan, T. Schimert, A. J. Syllaios and M. F. Taylor, "Small pixel a-Si/a-SiGe bolometer focal plane array technology at L-3 Communications," *Proc. SPIE 7660, Infrared Technology and Applications XXXVI,* p. 76600R, 2010.

[61] V. V. Zhurin, Industrial Ion Sources: Broadbeam Gridless Ion Sources Technology., Weinheim: Wiley-VCH, 2012.

[62] 4Wave Inc., "LABORATORY ALLOY and NANOLAYER SPUTTERING," [Online]. Available:

http://www.4waveinc.com/dslans.html.

[63] Kaufman & Robinson Inc., "Broad Beam Sources," [Online]. Available: http://www.ionsources.com/eh1000.htm.

[64] H. R. Kaufman, R. S. Robinson and R. I. Seddon, "End-Hall Ion Sources," *J. Vac. Sci. Technol.,* pp. 2081-2084, 1987.

[65] H. R. Kaufman, "Explanation of Bohm diffusion," *J. Vac. Sci. Technol. B,* vol. 8, p. 107, 1990.

[66] J. J. Cuomo, S. M. Rossnagel and H. R. C. W. S. Kaufman, Handbook of Ion Beam Processing Technology - Principles, Deposition, Film Modification and Synthesis, Westwood, New Jersey: Noyes Publications, 1989.

[67] J. R. H. R. K. R. E. N. R. S. R. a. C. M. S. Kahn, "Low Energy End-Hall Ion Source Characterization at Millitorr Pressures," *Society of Vacuum Coaters Technical Conference Proceedings,* 2005.

[68] Kaufman & Robinson Inc., *EH1000 Ion Source Manual Filament Cathode Version,* Fort Collins, Colarado, 2003.

[69] J.-L. Delcroix and A. R. Trinidade, "Hollow Cathode Arcs," *Advances in Electronics and Electron Physics,* vol. 35, pp. 87-190, 1974.

[70] D. Faircloth, "Ion sources for high-power hadron accelerators," in *CERN Accelerator School CAS 2011: High Power Hadron Machines*, Bilbao, 2011.

[71] M. C. Shonka, R. J. Kahn and R. H. Kaufman.Patent US 7,728,498, 2010.

[72] N. J. Podraza, *Real Time Spectroscopic Ellipsometry of the Growth and Phase Evolution of Thin Film Si1–xGex:H,* The Pennsylvania State University, 2008.

[73] R. Street, Technology and Applications of Amorphous Silicon, New York, 2000.

[74] D. Saint John, *Optical and Electrical Characterization of High Resistivity Semiconductors for Constant-Bias Microbolometers,* 2012.

[75] T. C. o. D. School of Physics, "Ellipsometry - Surface and Interface Physics," Dublin, 2012.

[76] D. K. Schroder, Semiconductor Material and Device Characterization, Wiley-IEEE Press, 2006.

[77] W. A. Lentz, Characterization of noise in Uncooled IR Bolometer Arrays, Massachussetts Institute of Technology, 1998.

[78] T. Schimert, J. Brady, T. Fagan, M. Taylor, W. McCardel, R. Gooch, S. Ajmera, C. Hanson and A. J. Syllaios, "Amorphous silicon based large format uncooled FPA microbolometer technology," *Infrared Technology and Applications XXXIV,* p. 694023, 17 April 2008.

[79] Y. Jin, H. A. Basantani, A. O. Ozcelik, T. N. Jackson and M. W. Horn, "High-resistivity and high-TCR vanadium oxide thin films for infrared imaging prepared by bias target ion-beam deposition," in *SPIE Conference Proceedings Vol. 8704*, Baltimore, 2013.

[80] H. Klauk, S. L. Wright, L. F. Palmateer, S. E. Mohney and T. N. Jackson, "Hydrogenated Amorphous Silicon Germanium Black-matrix Mateiral for Active--matrix Liiquid-crystal Displays," *Journal of the Society for Information Display 5,* vol. 4, p. 393, 1997.

[81] *SIMNRA software from max-Planck Institute for Physics was used to fit the RBS for compositional analysis.*

[82] F. N. Hooge, T. G. M. Kleinpenning and L. K. J. Vandamme, "Experimental studies on 1/f noise," *Reports on Progress in Physics,* vol. 44, no. 5, 1981.

[83] N. Podraza, B. Gauntt, M. Motyka, E. Dickey and M. Horn, "Electrical and optical properties of sputtered amorphous vanadium oxide thin films," *Journal of Applied Physics,* vol. 111, no. 7, 2012.

[84] J. L. C. T. B. F. A. C. a. O. L. Tissot, "Uncooled Microbolometer Detector: Recent Developments at ULIS," *Opto-Electronics Review,* vol. 14, no. 1, pp. 25-32, 2006.

[85] B. D. Cullity, Elements of X-ray Diffraction, Addison-Wesley Publishing Company, Inc., 1978.

[86] R. W. Collins, A. S. Ferlauto, G. M. Ferreira, J. K. C. Chen, R. J. Koval, Y. Lee, J. M. Pearce and C. R. Wronski, "Evolution of microstructure and phase in amorphous, protocrystalline, and microcrystalline silicon studied by real time spectroscopic ellipsometry," *Solar Energy Materials and Solar Cells,* vol. 78, pp. 143-180, 2003.

[87] N. J. Podraza, J. Li, C. R. Wronski, E. C. Dickey and R. W. Collins, "Analysis of controlled mixed-phase (amorphous + microcrystalline) silicon thin films by real time spectroscopic ellipsometry," *Journal of Vacuum Science & Technology A: Vacuum, Surfaces & Technology,* vol. 27, no. 6, pp. 1255-1259, 2009.

[88] Y. Cong, I. An, K. Vedam and R. W. Collins, "Optical characterization of a four-medium thin film structure by real time spectroscopic ellipsometry: amorphous carbon on tantalum," *Applied Optics,* vol. 30, pp. 2692-2703, 1991.

[89] D. E. Aspnes, "Minimal-data approaches for determining outer-layer dielectric responses of films from kinetic reflect o metric and ellipsometric measurements," *Journal of the Optical Society of*

America A, vol. 10, pp. 974-983, 1993.

[90] A. S. Ferlauto, G. M. Ferreira, R. J. Koval, J. M. Pearce, C. R. Wronski, R. W. Collins, M. M. Al-Jassim and K. M. Jones, "Evaluation of compositional depth profiles in mixed-phase (amorphous+crystalline) silicon films from real time spectroscopic ellipsometry," *Thin Solid Films,* Vols. 455-456, pp. 665-669, 2004.

[91] N. J. Podraza, J. Li, C. R. Wronski, E. C. Dickey, M. W. Horn and R. W. Collins, "Analysis of Si1-xGex:H thin films with graded composition and structure by real time spectroscopic ellipsometry," *Physica Status Solidi A,* vol. 205, pp. 892-895, 2008.

[92] H. Fujiwara, J. Koh, P. I. Rovira and R. W. Collins, "Assessment of effective-medium theories in the analysis of nucleation and microscopic surface roughness evolution in semiconductor thin films," *Physical Review B,* vol. 61, pp. 10832-10844, 2000.

[93] P. Lautenschlage, M. Garriga, L. Vina and M. Cardona, "Temperature dependence of the dielectric function and interband critical points in silicon," *Physical Review B,* Vols. 4821-4830, p. 36, 1987.

[94] A. S. Ferlauto, G. M. Ferreira, J. M. Pearce, C. R. Wronski and R. W. Collins, "Analytical model for the optical functions of amorphous semiconductors from the near-infrared to ultraviolet: applications in thin film photovoltaics," *Journal of Applied Physics,* vol. 92, pp. 2424-2436, 2002.

[95] N. J. Podraza, C. R. Wronski, M. W. Horn and R. W. Collins, "Dielectric functions of a-Si1-xGex:H vs. Ge content, temperature, and processing: advances in optical function parameterization," in *Materials Research Society Symposia Proceedings*, 2006.

[96] G. E. Jellison Jr. and F. A. Modine, "Parameterization of the Optical Functions of Amorphous Materials in the Interbrand Region," *Applied Physics Letters,* vol. 69, p. 371, 1996.

[97] G. E. J. Jr. and F. A. Modine, "Erratum: Parameterization of the Optical Functions of Amorphous Materials in the Inerband Region," *Applied Physics Letters,* vol. 69, p. 371, 1996.

[98] Y. Z. Hu, J.-T. Zettler, Y. S. Chongsawangvirod, Q. Wang and E. A. Irene, "Spectroscopic ellipsometric measurements of the dielectric function of germanium dioxide films on crystal germanium," *Applied Physics Letters,* vol. 61, pp. 1098-1100, 1992.

[99] M. A. Motyka, B. D. Gauntt, M. W. Horn and N. J. Podraza, "Optical properties and microstructural evolution of vanadium oxide prepared by pulsed-DC magnetron sputtering," *Journal of Applied Physics,* p. 112, 2012.

[100] T. Schimert, C. Hanson, J. Brady, T. Fagan, M. Taylor, W. McCardel, R. Gooch, M. Gohlke and A. J. Syllaios, "Advances in small-pixel, large-format α-Si bolometer arrays," *Infrared Technology and*

Applications XXXV, vol. 7298, p. 72980T, 7 May 2009.

[101] P. Topart, F. Picard, S. Ilias, C. Alain, C. Chevalier, B. Fisette, J. E. Paultre, F. Généreux, M. Legros, J.-F. Lepage, C. Laverdière, L. N. Phong, J.-S. Caron and Y. Desroches, "Heterogeneous MEMS device assembly and integration," in *Proc. SPIE 8975, Reliability, Packaging, Testing, and Characterization of MOEMS/MEMS, Nanodevices, and Nanomaterials XIII, 89750E*, 2014.

[102] M. Yazici, H. Kayahan, O. Ceylan and Y. Gurbuz, "A new unit cell design with automatic input stage selection capability for increased SNR," in *Proc. SPIE 8704, Infrared Technology and Applications XXXIX, 870409*, 2013.

[103] M. U. Pralle, J. E. Carey, H. Haddad, C. Vineis, J. Sickler, X. Li, J. Jiang, F. Sahebi, C. Palsule and J. McKee, "IR CMOS: infrared enhanced silicon imaging," in *Proc. SPIE 8704, Infrared Technology and Applications XXXIX, 870407*, 2013.

[104] P. Robert, J. Tissot, D. Pochic, V. Gravot, F. Bonnaire, H. Clerambault, A. Durand and S. Tinnes, "Easy to use uncooled ¼ VGA 17 µm FPA development for high performance compact and low-power systems," in *Proc. SPIE 8353, Infrared Technology and Applications XXXVIII, 83531F*, 2012.

[105] M. L. Hai, M. Hesan, J. Lin, Q. Cheng, M. Jalal, A. J. Syllaios, S. Ajmera and M. Almasri, "Uncooled silicon germanium oxide (SixGeyO1-x-y) thin films for infrared detection," in *Proc. SPIE 8353, Infrared Technology and Applications XXXVIII, 835317*, 2012.

[106] Y. Jin, H. A. Basantani, A. Ozcelik, T. N. Jackson and M. W. Horn, "High-resistivity and high-TCR vanadium oxide thin films for infrared imaging prepared by bias target ion-beam deposition," in *Proc. SPIE 8704, Infrared Technology and Applications XXXIX, 87043C*, 2013.

[107] M. H. Unewisse, B. I. Craig, R. J. Watson, O. Reinhold and K. C. Liddiard, "Growth and properties of semiconductor bolometers for infrared detection," in *SPIE Proceedings 2554*, 1995.

[108] M. Moreno, A. Torres and A. Kosarev, "Uncooled microbolometers with GexSi1-x thermo-sensing layer deposited by plasma with different device configurations," in *SPIE Proceedings*, 2010.

[109] "New paints and coatings with specific properties in the near and the far infrared," IPS Innovations, 2007. [Online]. Available: http://www.ips-innovations.com/new_paints_ref.htm.

Vita
Hitesh Basantani

Hitesh Arjun Basantani was born in Kuwait on April, 24th 1987, to parents of Indian decent Meena Basantani and Arjun Basantani. They moved to New Delhi, India for a few years during the Gulf War of 1990 before returning back to Kuwait in 1992. Hitesh graduated from the Carmel School of Kuwait in 2004. He moved to The Penn State University for his B.S. and M.S. degree in Engineering Science and Mechanics, which he obtained in 2009 and 2011 respectively. His Master's thesis was on the development of vanadium oxide thin films for microbolometer application.

Following the obtaining of his M.S. degree, he stayed at Penn State for his Ph.D and was the first Super User for the Penn State Nanofabrication Facility. Here he worked on magnetron and low energy ion beam deposition systems. His Ph.D. work was on temperature sensing materials and devices.

In July of 2014, Hitesh accepted a position at Intel within the Intel Mask Operations Unit and will be moving to Hillsboro, OR with his fiancée Jennifer Ober.